PROBING THE INTERSTELLAR MEDIUM USING LABORATORY SAMPLES

A thesis submitted to the University of Manchester for the degree of Doctor of Philosophy in the Faculty of Engineering and Physical Sciences

2010

Ashley King

School of Earth, Atmospheric and Environmental Sciences

CONTENTS

Total Word Count: 48,006

i. List of Figures

Additional Data

Chapter 5

ii. List of Tables

PROBING THE INTERSTELLAR MEDIUM USING LABORATORY SAMPLES

Ashley King
The University of Manchester
submitted for the degree of Doctor of Philosophy, September 2010.

The aim of this thesis is to investigate the effects of interstellar processing using presolar samples. Dust in the interstellar medium is predicted to have experienced grain-grain and grain-gas collisions, cosmic-ray bombardment, or the formation of ices on their surfaces. Each process is likely to have altered presolar grains. The grains are extracted from meteorites and can be analyzed in the laboratory to try and understand these processes.

The main analytical tool used in this research was a new time-of-flight secondary ion mass spectrometry instrument equipped with a Au-cluster primary ion source. Analysis of presolar grains required that a rigorous experimental procedure was developed. A depth-profiling technique for the analysis of micron-sized samples was produced and the limitations of the technique considered. Secondary ion mass spectrometry suffers from matrix effects, so homogeneous silicate glass standards were analyzed. The use of Au-cluster primary ions was shown to enhance practical secondary ion yields relative to those with Au^+, consistent with increased sputter rates. Relative sensitivity factors for major and trace elements in the standards were obtained using both normal and delayed secondary ion extraction techniques.

Depth-profiles of Li, B, Mg, Al, K, Ca, Ti, V, Cr and Fe were obtained from eleven presolar SiC grains. In some SiC grains, the abundances of several elements were up to orders-of-magnitude higher in the outer ~200nm relative to the grain cores. This was attributed to the implantation of interstellar matter, accelerated to velocities of ~1000kms^{-1} by supernovae shockwaves. Other SiC grains contained homogeneously distributed trace elements, or evidence of elemental zoning, which could be explained by condensation processes around the grains' parent stars. These grains must have experienced minimal processing in the interstellar medium. It is suggested that the two populations represent SiC grains whose residence times in the interstellar medium significantly differed, consistent with previous findings of noble gas and Li isotopic studies.

A further study investigated carbonaceous grains isolated from the Murchison meteorite using a size and density procedure adapted for presolar graphite. No graphite grains were found and possible reasons for this are discussed. The structural and isotopic natures of thirty-three carbonaceous grains were determined by correlated, multi-instrument analyses. The grains contained solar C, N and O isotopic compositions. Deuterium was enriched in the grains with δD values up to +333 ± 110‰. These enrichments suggest exchange of H with cold interstellar gas in the outer part of the early solar nebula or interstellar medium. Raman spectroscopic and transmission electron microscopic analysis showed the grains to be composed of carbon more structurally disordered and amorphous than most carbonaceous phases observed in extra-terrestrial samples. It is argued that amorphization of the grains occurred through solar wind ion irradiation in the proto-solar nebula. This model is supported by previous studies of terrestrial

soot and carbon-rich ices irradiated by H^+ and He^+ ion doses of ~10^{15} – 10^{16} ions cm^{-2}. Implantation and mixing of H^+ ions is likely to have diluted the grains' original H isotopic composition.

DECLARATION

No portion of the work referred to in the thesis has been submitted in support of an application for another degree or qualification of this or any other university or other institute of learning.

COPYRIGHT STATEMENT

i) The author of this thesis (including any appendices and/or schedules to this thesis) owns certain copyright or related rights in it (the "Copyright") and s/he has given The University of Manchester certain rights to use such Copyright, including for administrative purposes.

ii) Copies of this thesis, either in full or in extracts and whether in hard or electronic copy, may be made **only** in accordance with the Copyright, Designs and Patents Act 1988 (as amended) and regulations issued under it or, where appropriate, in accordance with licensing agreements which the University has from time to time. This page must form part of any such copies made.

iii) The ownership of certain Copyright, patents, designs, trade marks and other intellectual property (the "Intellectual Property") and any reproductions of copyright works in the thesis, for example graphs and tables ("Reproductions"), which may be described in this thesis, may not be owned by the author and may be owned by third parties. Such Intellectual Property and Reproductions cannot and must not be made available for use without the prior written permission of the owner(s) of the relevant Intellectual Property and/or Reproductions.

iv) Further information on the conditions under which disclosure, publication and commercialisation of this thesis, the Copyright and any Intellectual Property and/or Reproductions described in it may take place is available in the University IP Policy (see http://www.campus.manchester.ac.uk/medialibrary/policies/intellectual-property.pdf) in any relevant Thesis restriction declarations deposited in the University Library, The University Library's regulations (see http://www.manchester.ac.uk/library/aboutus/regulations) and in The University's policy on presentation of Theses.

THE AUTHOR

The author graduated from The University of Manchester in June 2007 with a first class MEarthSci degree in Geology with Planetary Science. Since September 2007 the author has been engaged in the research presented in this thesis.

ACKNOWLEDGEMENTS

Firstly, I would like to thank my supervisors Ian Lyon and Torsten Henkel for their continual guidance and encouragement (and criticism), and without whose enthusiasm this PhD could never of happened. Ian was ever present throughout my undergraduate degree and took me on for my final year project, allowing me access to all the expensive equipment he had hoarded down in the TOFSIMS lab. I've thoroughly enjoyed his "hit it with a spanner and see" approach, which has provided me with ample experience of what should and shouldn't be done in the lab. In contrast Torsten is much more of a perfectionist. I am extremely grateful not only for the amount of time and effort he has put into helping me, and for never once complaining when I had/was a problem, but also for his friendship. A special mention must also go to Detlef Rost, who has always been on hand with helpful thoughts and comments. We've wasted many hours discussing, watching and listening to our hobbies and I look forward to seeing the mighty Hannover 96 sometime in the future.

I would like to thank the Isotope group, in particular Ray Burgess, Chris Ballentine, Sarah Crowther, Karen Theis, Angela Walker, Julia Cartwright and Ilya Strashnov. Jamie Gilmour has acted as a supervisor throughout my time in Manchester and I knew he was there if I needed him. Without the input of Henner Busemann the carbonaceous grains may have been a dead end. He is thanked for his advice, expertise and assistance with collecting and analyzing the Raman and NanoSIMS data, and for providing IOM samples and World Cup betting opportunities. Maria Schonbachler is thanked for taking the time to read and examine transfer reports and her excellent barbeque skills. Dave Blagburn and Bev Clementson made sure the labs (and Torsten) were kept in order. All the members of cake club have kept me well fed over the years, whilst Fat Back Five have helped to remove any excess.

Thanks must go to Vicky Fawcett at the School of Chemical Engineering for teaching me how to use the Raman spectrometer, Christelle Guillermier and Ian Franchi at the Open University for allowing me access to the NanoSIMS, and

Martin Lee at The University of Glasgow for TEM analysis. The Science and Technology Facilities Council funded the PhD.

A huge thank-you must go to my mum and sister, who provide so much love and support and no little amusement. Thanks to all my grandparents for putting up with me.

Ever since I've known her, Ceri Middleton has displayed an incredible desire to get the most out of life. She is by far the most caring person I have ever met. Unfortunately she is also one of the cleverest, meaning I rarely get away with anything. She made my time here in Manchester the best of my life and I'd like to thank her for being my friend and an inspiration.

Jenny Claydon always puts a smile on my face, and has a sense of fun and dry wit that continues to keep me entertained. Over the last few months she has listened to all of my grumblings, and always responded with words of support and encouragement. She is extremely loyal and amazingly patient. I hope the smile remains on her face.

For Dad

Chapter 1

Introduction and Literature Review

1.1 INTRODUCTION

The Solar System formed from an interstellar molecular cloud that collapsed under its own gravity approximately 4.6 billion years ago. The gravitational collapse, possibly triggered by a nearby supernova explosion (Cameron and Truran 1977, Boss 1995, Boss et al. 2010), of this dense, cold region of gas and dust, formed a proto-Sun surrounded by a flattened disc of material. As temperatures in the disc cooled, the first solids in the form of calcium-, aluminium-rich inclusions (CAIs), began to condense. Dust particles orbiting the proto-Sun began to collide and accrete together to create dust aggregates, flash-heating of which likely formed chondrules. For detailed reviews see Boss and Goswami (2006), Montmerle et al. (2006) and Russell (2007).

Over time much of the material in the disc was swept up into the early Sun. The continuing accretion of CAIs, chondrules and newly formed grains produced larger bodies known as planetesimals (>1km diameter), cemented together by a fine-grained (~1μm) matrix consisting largely of metals and silicate materials. The formation of the Solar System was completed as these planetesimals accreted to form the planets, asteroids and Edgeworth-Kuiper bodies that we see today.

For many years it was believed that Solar System formation resulted in the processing and complete homogenization of the dust and gas contained within the presolar molecular cloud (e.g. Suess 1965). However, the discovery of isotopic anomalies in the noble gases Xe (Reynolds and Turner 1964) and Ne (Black and Pepin 1969) within primitive meteorites indicated incomplete homogenization and the potential survival of presolar material in the least altered meteorites.

Lewis et al. (1987) were the first to isolate a presolar phase from its host meteorite. This phase, nanodiamonds, was quickly followed by the extraction of presolar SiC (Bernatowicz et al. 1987) and graphite (Amari et al. 1990). Other presolar phases discovered since include corundum (Al_2O_3) (Huss et al. 1993, Nittler et al. 1997), hibonite ($CaAl_{12}O_{19}$) (Choi et al. 1999), silicon nitride (Si_3N_4) (Nittler et al. 1995), spinel ($MgAl_2O_4$) (Nittler et al. 1994a; 1994b), silicates (Nguyen and Zinner 2004, Nagashima et al. 2004), plus refractory carbide sub-grains (e.g. TiC) (Bernatowicz et al. 1991, Croat et al. 2005, Stroud and Bernatowicz 2005).

Presolar grains are present not only in some meteorites but also other primitive Solar System materials, such as interplanetary dust particles (IDPs) (Messenger et al. 2003) and cometary samples returned by the Stardust mission (McKeegan et al. 2006).

Analysis of presolar grains finds them to be comprised of materials with isotopic compositions that vary by up to orders-of-magnitude from solar. For example, $^{12}C/^{13}C$ ratios in presolar SiC grains range from 1 – 7000 compared to the solar value of 89 (Zinner et al. 1987; 1989, Alexander 1993, Hoppe et al. 1994, Nittler et al. 2006). These huge anomalies cannot be produced in the Solar System by radioactive decay, cosmic-ray induced spallation or mass fractionation. Instead the anomalies are explained by nucleosynthesis in stars.

Presolar grains are condensates of material from dying stars. Before their discovery all knowledge of stars and interstellar dust came from astronomical observations. The grains formed in the extreme environments around their parent stars before passing through the interstellar medium (ISM) and into the presolar molecular cloud. They then survived the formation of the Solar System, were incorporated into meteorite parent bodies and delivered to Earth, where this "stardust" can then be studied in the laboratory (Figure 1.1). Presolar grains provide a wealth of information regarding a range of different environments and processing events.

1.1.1 Stellar Environments

Presolar grains contain material produced by their parent stars. They each carry a signature of the nucleosynthetic processes that took place within those stars. Their isotopic compositions indicate that they must have formed in a variety of stellar environments, including asymptotic giant branch (AGB) stars, novae and supernovae. Analysis of the isotopic compositions of these grains can provide insights into how nucleosynthesis occurs in these very different stellar environments. This data can then be used to constrain astrophysical models of stellar evolution, nucleosynthesis and galactic chemical evolution (GCE) (Gallino et al. 1990; 1994, Lugaro et al. 1999; 2003, Travaglio et al. 1999, Savina et al. 2004, Yin et al. 2006, Barzyk et al. 2007).

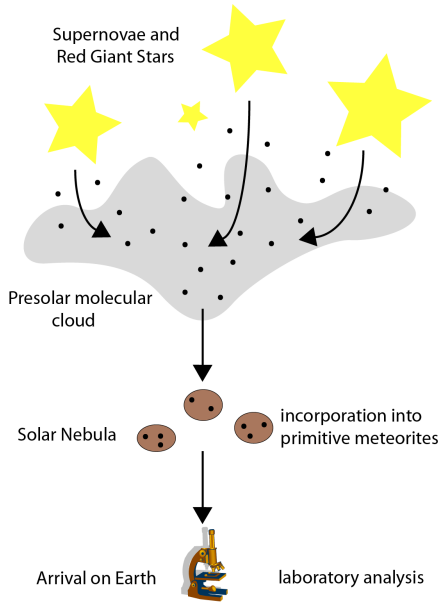

Figure 1.1 Presolar grains formed around asymptotic giant branch (AGB), red giant, novae and supernovae stars before being ejected into the ISM. They were present in the presolar molecular cloud before surviving the formation of the Solar System and becoming incorporated into primitive meteorites. Meteorites, and their constituent parts, fall to Earth and can be studied in the laboratory (adapted from Lodders and Amari 2005).

Grain morphologies are dependent upon the physical (pressures and temperatures) and chemical conditions in circumstellar shells and stellar outflows. For example, despite synthetic SiC forming >250 polytypes (which are sensitive to formation conditions), only two of these have been observed in presolar SiC (cubic 3C and hexagonal 2H), placing limits upon the conditions found around stars (Daulton et al. 2002; 2003). The composition of the source

gas from which the grains condensed played a significant role in determining the mineralogy of presolar grains and their trace element contents.

1.1.2 Interstellar Medium

After formation, grains are driven into the ISM by stellar winds and outflows. The ISM consists of many different regions that differ in temperature, density and chemical composition.

Whilst in the ISM presolar grains may have experienced several different forms of processing. These include, exposure to UV radiation, bombardment with high energy cosmic-rays, passing through shockwaves generated by nearby supernovae, grain-grain collisions or formation of ices on their surfaces. Each process is expected to have at least partially altered the grains prior to their arrival in the presolar molecular cloud.

Evidence of interstellar processing may include pitting or etching on the surfaces of grains, amorphization of grains, the implantation of interstellar material and structurally or chemically distinct surfaces/rims around grains. The grains are likely to have experienced more than one form of processing in the ISM resulting in an overlap of these different affects.

The major aim of this research is to determine the mechanisms by which presolar grains were processed in the ISM, and begin to establish the extent to which they have been altered. This will further our understanding of the material that provided the initial building blocks of the Solar System.

1.1.3 Early Solar Nebula

Most of the dust present within the presolar molecular cloud was heated, processed and homogenized. The small percentage of presolar grains that did survive Solar System formation represents the effects of processing in the early solar nebula. Studying the size, abundances and mineralogy of presolar grains in a range of primitive Solar System materials can help identify what type of, and to

what extent, processing occurred, and help determine the homogeneity of the disc.

Variations in the sizes and abundances of presolar grains in different meteorite groups may result from pre-accretionary events. In the disc, presolar grains are likely to have suffered from varying degrees of accretionary heating, shock heating, radial mixing and initial grain-grain collisions.

On meteorite parent bodies the grains will have been exposed to aqueous alteration and thermal metamorphism, both of which can alter and destroy presolar grains. Presolar grain abundances can therefore be used to constrain the alteration histories of primitive meteorites.

1.2 STELLAR FORMATION AND EVOLUTION

Stars are born when interstellar molecular clouds containing gas and dust suffer collapse as the result of gravitational instability. Instabilities may be triggered by events such as molecular cloud collisions or supernovae shockwaves. The collapsing gas collides with itself, releasing large quantities of energy in the form of heat, increasing temperatures and pressures in the cloud. Continued collapse drives further increases in temperature and opacity until the material starts to glow and a proto-star is created.

The life of a star is dependent upon its starting mass, and to a lesser extent its initial metallicity (abundance of elements heavier than He). As the proto-star finishes collapsing it will reach a maximum core temperature related to its mass. In proto-stars with a mass ≤ 0.1 of the solar mass ($M_{\odot}$), core temperatures and pressures fail to reach those required for thermonuclear reactions to begin. Lacking a source of energy (although the largest can fuse deuterium) these stars, known as brown dwarfs, quickly cool.

Proto-stars with masses $>0.1M_{\odot}$ have core temperatures and pressures high enough to kick-start thermonuclear reactions and hence further evolution. These new stars enter the main sequence, where they will spend the majority of their lifetime. A star's main sequence stage is driven by the competing forces of gravitational collapse and radiation pressure. Inward collapse of the star is countered by the radiation and gas pressure produced by thermonuclear reactions, such that the two opposing forces reach a hydrostatic equilibrium.

Astronomical observations allow us to study the formation and evolution of stars. Stellar evolution is summarized by the Hertzsprung-Russell diagram (Figure 1.2), which shows the relationship between a stars luminosity and effective temperature.

The following is a brief review of stellar evolution and nucleosynthesis. For a more detailed description the reader is referred to Rolfs and Rodney (1988) and Meyer and Zinner (2006).

1.2.1 H-burning

H-burning generates the radiation pressure that prevents a main sequence star from collapsing. This is where ^{1}H is fused to form ^{4}He and occurs through one of two processes; the proton-proton chain (p-p chain) or the CNO cycle.

The p-p chain is more efficient at low core temperatures and is therefore the major energy source in low-mass stars. In the p-p chain, two protons are fused together to create a deuterium atom (plus a positron and neutrino, see below). Deuterium is then available for fusion with further protons, producing ^{3}He, which subsequently fuses with a second ^{3}He and generates ^{4}He plus two protons. This branch, known as ppI, dominates ^{4}He production in low-mass stars, although it should be noted that two alternative paths (ppII and ppIII) also become available once ^{3}He is created.

i) $p + p \rightarrow D + \upsilon_e + e^+$
ii) $D + p \rightarrow {}^{3}He + \gamma$
iii) $^{3}He + {}^{3}He \rightarrow {}^{4}He + p + p$

Second generation stars (i.e. initial gas of higher metallicity) contain ^{12}C, which provides a starting point for the CNO cycle. The cycle begins with the fusion of ^{12}C with ^{1}H to produce ^{13}N, which quickly β-decays to ^{13}C. The ^{13}C fuses with ^{1}H to form ^{14}N, which in turn fuses with ^{1}H to produce ^{15}O. The ^{15}O β-decays to ^{15}N, which combines with ^{1}H to produce ^{12}C and ^{4}He. Again, a second path is available (ON cycle), where the fusion of ^{15}N with ^{1}H produces ^{16}O before leading, via ^{17}F and ^{17}O, back to ^{15}N and ^{4}He production.

Stars progress along the main sequence in relative stability until the fuel available for H-burning is exhausted. As reaction rates increase with temperature, larger, and therefore hotter, stars consume their fuel at a greater rate than low-mass stars. The typical lifetime of a $1M_{\odot}$ star is ~10 billion years, whereas a $0.2M_{\odot}$ star will reside on the main sequence for ~200 billion years, and a $40M_{\odot}$ star for just one million years. Once H-burning can no longer be sustained the star must find alternative sources of energy.

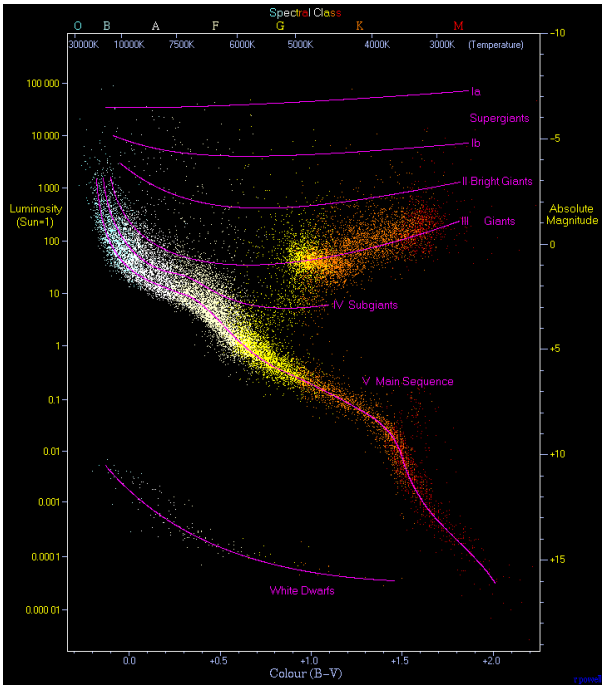

Figure 1.2 The Hertzsprung-Russell diagram represents the relationship between absolute magnitude, surface temperature and luminosity throughout the evolutionary stages of a star. Stars spend the majority of their lifetime on the main sequence before evolving to become red giant branch (RGB) and AGB stars, and white dwarfs (from Richard Powell; http://en.wikipedia.org/wiki/File:HRDiagram.png).

1.2.2 Red Giant Branch

When H-burning ceases, a lack of energy production ends hydrostatic equilibrium and gravitational collapse begins to dominate. However, as a star contracts its internal temperatures and pressure increase until H-burning is triggered in a shell around a now inert H-depleted, He-rich core (Figure 1.3). H-burning in the shell increases the luminosity of the star, whilst the outer envelope becomes convective and expands up to 10 – 50$R_{\odot}$. Surface temperatures therefore decrease and the star moves into the red giant branch (RGB) phase.

During the RGB phase the first "dredge-up" occurs (Iben and Renzini 1983, Boothroyd and Sackmann 1999). The convecting outer envelope of the star penetrates down into the H-burning shell. By this method, the products of H-burning are transported into the previously unprocessed outer envelope. Astronomical observations of RGB stars allow us to witness the first dredge-up event through changes in C and O isotopic compositions (decreased ^{12}C and increased ^{17}O) at the star's surface (Busso et al. 1999, Abia et al. 2008).

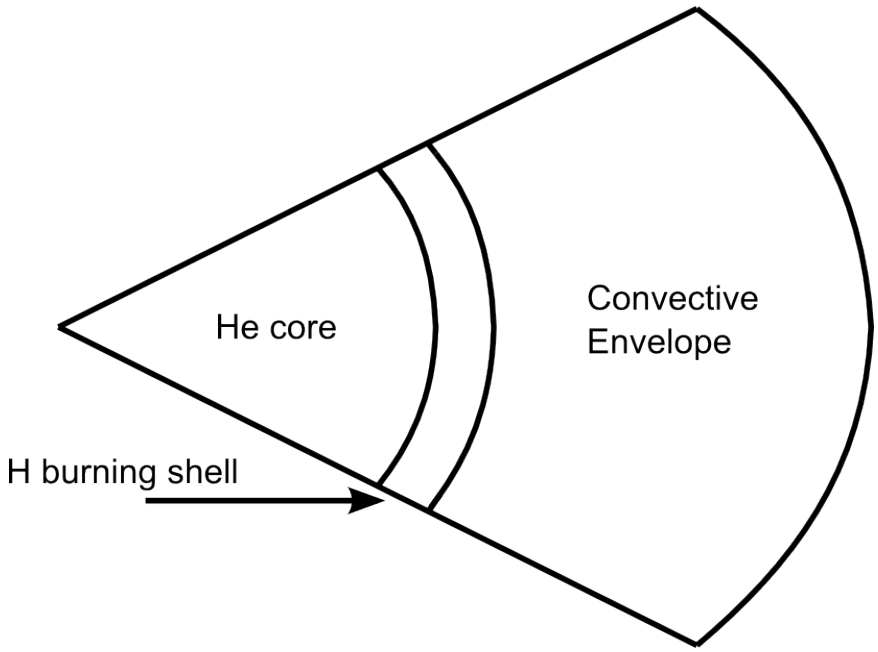

Figure 1.3 Internal structure of a star during the RGB phase. The convective envelope transports the products of H-burning to the stellar surface. Image not drawn to scale (after Lattanzio and Boothroyd (1996)).

As He is produced by H-burning in the shell, the mass of the inert He core grows. Eventually it builds up sufficient mass to reach core temperatures and densities high enough for the He to ignite. This "He-flash" sees ^{4}He fused into ^{12}C through the triple α process;

$$^{4}He + {}^{4}He + {}^{4}He \rightarrow {}^{12}C$$

If stable He-burning is maintained, ^{12}C may additionally undergo fusion to ^{16}O in the core;

$$^{12}C + {}^{4}He \rightarrow {}^{16}O + \gamma$$

During the He-buring phase the star will lose ~10% of its mass through stellar winds. As the supply of He becomes exhausted the star will again contract. This creates a new He-buring shell around a C-O rich core. The new input of energy causes the outer envelope to expand. In stars >3.5$M_{\odot}$ a second dredge-up takes place, whereby the products of H-burning are transported to the stellar surface. This is typically characterized by an increase in the ^{14}N/^{15}N ratio by a factor of 6 – 7 (Iben and Renzini 1983, Boothroyd and Sackmann 1999, Busso et al. 1999).

On the Hertzsprung-Russell diagram (Figure 1.2) the star moves away from the RGB and back towards the main sequence.

1.2.3 Asymptotic Giant Branch

Burning in the AGB phase alternates between He and H shells, which are separated by a He-intershell, and surround an inert C-O rich core (Figure 1.4).

The H-burning shell produces He that is deposited into the inactive He-intershell. This causes the temperature and density of the He-shell to increase, forcing rapid He-burning to occur for a short period. The He-intershell becomes convective and moves the products of nucleosynthesis to the interface between the H and He-shells.

When the He-shell is ignited the resulting higher temperatures cause the overlying shells to expand. Expansion of the H-shell causes it to cool and H-burning stops. Decreasing temperatures also stop He-shell burning. The lack of energy production causes collapse until new H-shell burning begins. This process may be repeated many times (10 – 100 cycles) and the star is now referred to as a thermally pulsing (TP) AGB star.

During the TP-AGB phase stars suffer further mass loss through stellar winds, providing suitable conditions for the formation of dust containing isotopic and elemental signatures that reflect the composition of the star at this point (see Section 1.3.1). AGB stars are the largest contributors to our presolar grain collection (Alexander 1996).

Stars may also undergo a third dredge-up at the end of a pulse (Iben and Renzini 1983, Busso et al. 1999). An inactive H-burning shell allows the convective outer envelope to transport material synthesized in the He-shell i.e. ^{12}C, towards the stellar surface. Stars may undergo several third dredge-up events during the TP-AGB phase, each of which causes the stellar surface to become increasingly C-rich (i.e. increasing the C/O ratio).

In stars whose masses are >6$M_{\odot}$ hot bottom burning (HBB) can take place (e.g. Sugimoto 1971). In these stars, temperatures at the base of the convective envelope exceed those required for partial H-burning. This involves proton captures on ^{12}C, causing the ^{12}C to be transformed into ^{14}N. In addition, during HBB He can also be converted, through ^{7}Be, into ^{7}Li (e.g. Cameron and Fowler 1971). The major effect of HBB is to alter the chemical composition of a star by preventing a build-up of C at its surface; thus delaying its development into a C-rich star.

When the abundance of He in the shell has been significantly depleted so that He-burning can no longer be sustained, a star will again suffer gravitational collapse. The temperature of the convective outer envelope starts to decrease, providing suitable conditions for the condensation of dust (see Section 1.3). The AGB stage is completed as material from the convective outer envelope is ejected into space (the planetary nebula phase).

Stars whose mass is <8$M_{\odot}$ are not large enough to produce the temperatures and densities required for further element synthesis. They eject so much material during the planetary nebula phase that their lives end as electron degenerate C-O white dwarves.

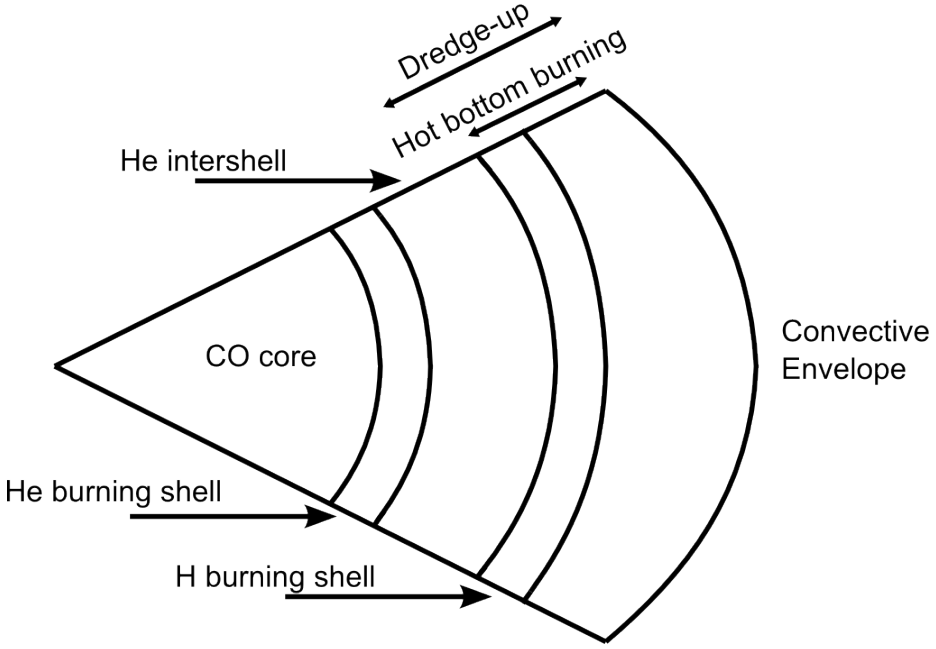

Figure 1.4 Internal structure of a star during the AGB phase. Burning alternates between He and H shells separated by a He-intershell. Hot Bottom Burning (HBB) occurs in stars whose masses are >6$M_{\odot}$. Image not drawn to scale (adapted from Lattanzio and Boothroyd (1996)).

1.2.4 Novae and Supernovae

In some instances white dwarf stars are found in closed binary systems with another star. In this case the white dwarf may accrete H-rich material from the other star, increasing its own temperature and density. This allows nuclear reactions to take place, eventually leading to explosive mass loss in a nova outburst.

In stars $>8M_{\odot}$ elements heavier than C and O may be synthesized. Collapse causes temperatures and pressures in the core to increase until C-burning is initiated.

The input of energy from C-burning increases a star's temperature. He-burning is then ignited in a new shell (causing expansion to a supergiant star) and the products of C-burning accumulate in a new inert core. Eventually C-burning can no longer be sustained and the star will cool and contract until temperatures are high enough for Ne-burning.

New H and He-burning shells are ignited and propagate outwards as increasingly heavier elements are burnt and the star develops an "onion shell" appearance (Figure 1.5). Each stage of burning produces less energy than the previous one, causing the star to exhaust its supply of fuel at an ever greater rate. Once the Fe-peak elements (i.e. ^{56}Ni, ^{56}Fe) are reached, there are no heavier elements a star can synthesize without requiring more energy than the reaction releases. Further energy production is therefore prevented and the star's core will rapidly collapse under gravity.

Due to electron degeneracy pressure the core can initially withstand the collapse. However at the core's surface Si-burning continues to create heavier elements. These elements are continuously added to the core until its mass exceeds the Chandreskar limit of $1.4M_{\odot}$. Above this limit electron degeneracy pressure can no longer support the core against gravitational collapse. Protons and electrons are forced to create neutrons and a neutron degenerate core, or neutron star, is formed.

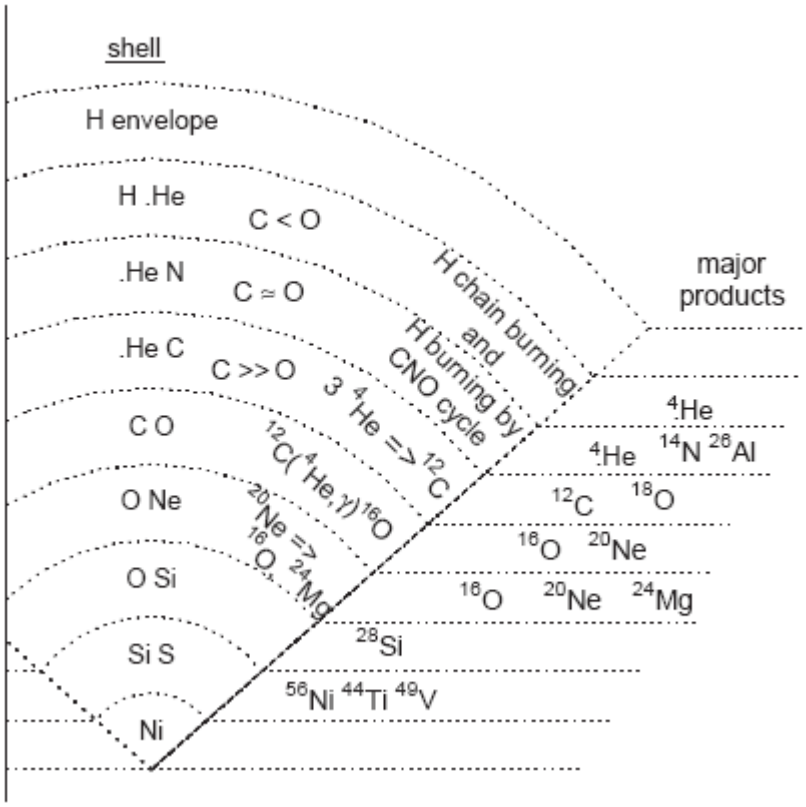

Figure 1.5 Onion shell model of nucleosynthesis in massive stars. For each shell the elements that are burnt and the resulting nuclear products are labeled (from Lodders and Amari (2005)).

As the core collapses gravitational potential energy is released. Collapse also forces together nuclei in the core, resulting in densities comparable with nuclear matter. Nuclear matter is nearly incompressible and hence further collapse is prevented. Instead the core "bounces" back with an outward moving shockwave. The shockwave causes the outer shells to become a hot plasma, where neutron capture by heavy elements (>^{56}Fe) may take place, before the shells are swept out into interstellar space as a Type II supernova explosion.

In the largest stars, where the core is >3$M_{\odot}$, even neutron degeneracy pressure cannot support the core's weight and the core will continue to collapse to a singularity. The gravity of this singularity, better known as a black hole, is so strong that nothing within the Schwarzchild radius can escape.

1.2.5 S- and R-process Nucleosynthesis

S- and r- process nucleosynthesis are responsible for the formation of nearly all stable isotopes heavier than ^{56}Fe. Both processes are neutron capture reactions, whereby "free" neutrons may be captured by seed nuclei dependent upon the neutron capture cross-section (i.e. probability of capturing a neutron of the nuclei). In s-process nucleosynthesis the time between these reactions is long (s for slow, ~10^4 years) due to low neutron densities. This means nearly all unstable nuclei undergo β-decay before the next neutron capture can occur. In contrast, the r-process occurs over short timescales, where the time between neutron captures is far less than the average β-decay half-life.

1.2.5.1 S-process

In the s-process, seed nuclei capture a neutron to produce new nuclei. The neutron flux is so low that stable nuclei can exist for 10^4 – 10^5 years before capture of a further neutron. If however the nuclei are unstable, there may be sufficient time between neutron captures for β-decay to new nuclei (Figure 1.6). Subsequent neutron captures and β-decays produce increasingly heavy isotopes until the heaviest stable isotope, ^{209}Bi, is reached (Figure 1.7). The s-process happens in environments with neutron densities of typically 10^6 – 10^{11}cm^{-3} (Lugaro et al. 2003).

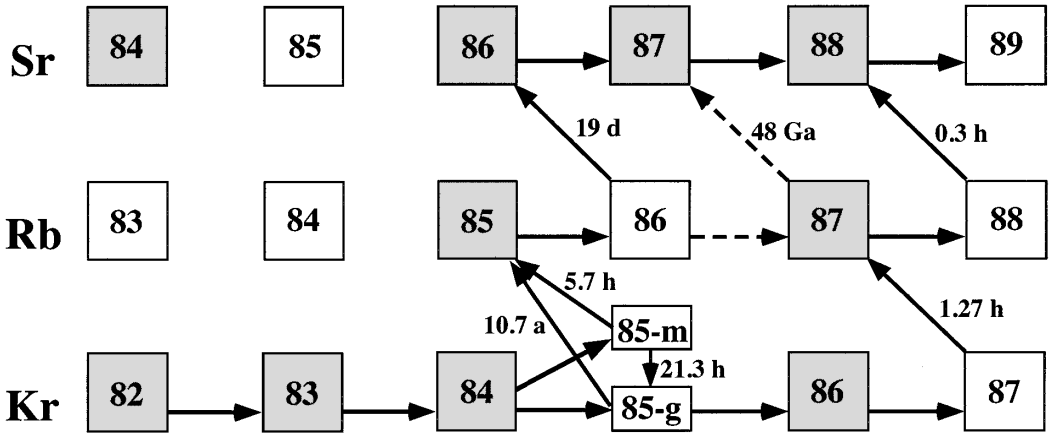

Figure 1.6 Example of the s-process in the Kr-Rb-Sr region of the chart of the nuclides. Stable isotopes are in shaded boxes. Arrows pointing right indicate capture of a neutron. Diagonal arrows indicate β-decay (from Nicolussi et al. 1998b).

If the neutron capture time and β-decay half-life are approximately the same then branching may occur (Gallino et al. 1996, Lugaro et al. 2003). The s-process will follow both paths from this point, resulting in distinctive s-process isotopic signatures. For example, s-process production of ^{86}Kr is influenced by the branching point found at ^{85}Kr. Such characteristics of s-process nucleosynthesis can be measured in presolar grains (e.g. Lewis et al. 1990; 1994).

Abundances of the isotopes are controlled by the ease with which they can be created (dependent upon the parent nucleus' neutron capture cross-section) and destroyed (e.g. by photodisintegration), and a dynamic equilibrium is reached. There is also a group of nuclides with particularly stable neutron configurations ("magic neutron numbers") and very small neutron capture cross-sections. These isotopes are unlikely to capture a neutron and are either stable, or have β-decay half-lives so long, that their abundances build up and elements to their right on the chart of the nuclides (i.e. Z=Z, N+1) are produced at exceptionally slow rates.

As there are ~10^4 years between neutron captures in the s-process, the environment in which it occurs must be stable for at least ~10^6 years. Also, as free neutrons are unstable particles that decay after ~15 minutes, for the s-process to continue they must be continuously produced. The s-process is predicted to predominantly occur in the He-burning shells of TP-AGB stars (Burbidge et al. 1957, Iben 1975).

1.2.5.2 R-process

Like the s-process, the r-process commences with seed nuclei capturing a neutron. However, the neutron density is so high that even isotopes with β-decay half-lives as short as 10^{-6} seconds may capture a neutron. This allows very neutron-rich nuclei to be formed. The r-process can occur either as a primary or secondary reaction. The primary (dominant) reaction involves seed nuclei and neutrons that were produced by nucleosynthesis in the source star. Secondary r-process utilizes pre-existing, non-processed nuclei already present in the star (i.e. second generation stars).

The extreme environments under which the r-process operates often contain abundant γ-rays that breakdown nuclei through photodisintegration. This leads to pseudo-equilibrium between the formation and destruction of nuclei.

The r-process fuses neutrons to highly neutron rich nuclei until eventually a nuclide with a magic neutron number is reached (Figure 1.7). As no further neutrons can be added, the nuclei must instead wait at this point for β-decay to take place. The resulting nuclei (Z+1) rapidly captures a neutron, returning to a stable neutron configuration that will again β-decay to Z+2 and so on towards more stable isotopes. This continues until the binding energy is large enough to breakthrough this bottle-neck and return to rapid neutron captures.

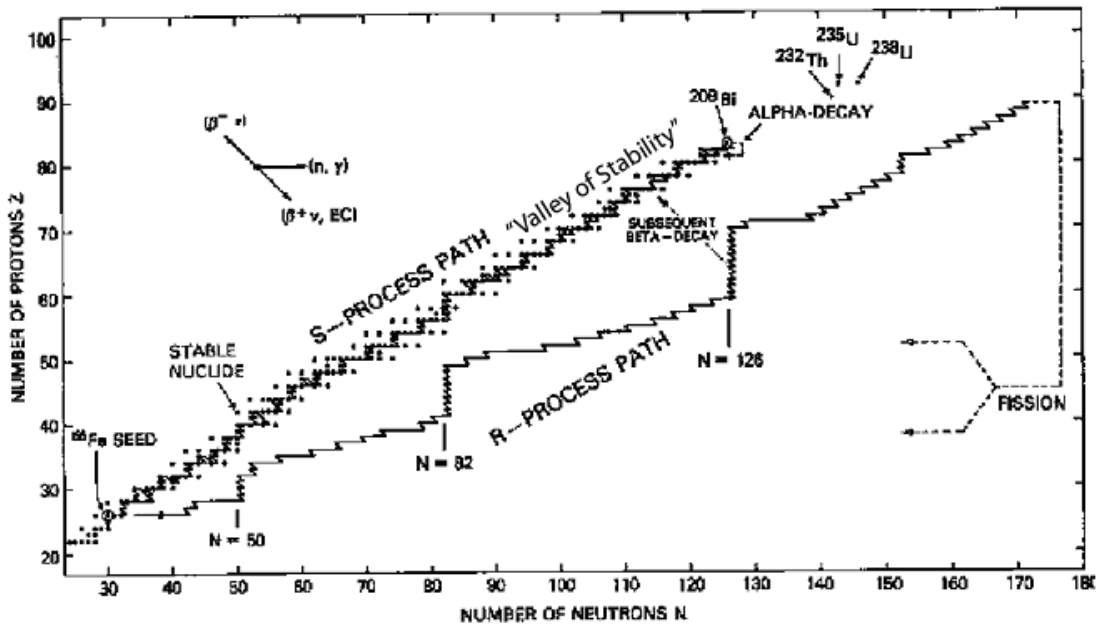

Figure 1.7 S- and r- process pathways on the chart of the nuclides. Dependent upon the neutron density, neutrons are added to seed nuclei either slowly or rapidly, producing heavier nuclei. The s-process proceeds along the stable nuclei, whilst the r-process builds neutron-rich nuclei away from the "valley of stability". Magic neutron numbers occur at N=50, 82 and 126 (from Rolfs and Rodney (1988)).

The r-process occurs in environments with neutron densities typically in excess of $10^{20}cm^{-3}$ (Montes et al. 2007). Candidate sites for the r-process include Type II supernovae, merging neutron stars and rotating stellar cores (Cowan and Thielemann 2004). At the point when the high neutron density ceases to exist, nuclear "freeze out" occurs and the short-lived, neutron-rich nuclei produced by the r-process rapidly decay back towards the "valley of stability".

1.3 PRESOLAR GRAINS

This research aims to identify evidence of interstellar processing on presolar grains by studying their outer surfaces, structures and internal compositions.

1.3.1 Formation of Presolar Grains

Astronomical observations indicate the presence of dust in the circumstellar shells of AGB stars, and within the ejecta of supernovae explosions (e.g. Gauba and Parthasarathy 2004, Lagadec et al. 2007). Chemical and physical conditions in these environments must therefore be favourable for the condensation of stellar dust.

Dust is only expected to condense at temperatures <2000K (Lodders and Fegley 1995), which are likely to be only found in the outer regions of the circumstellar shell. Typical pressures in circumstellar envelopes are between 10^{-3} – 10^{-7} bars (Lodders and Fegley 1995).

A major influence upon the formation of dust in stellar environments is the C/O ratio of the parent star. The C/O ratio of AGB stars varies from 0.5 to 1.76 (Lodders and Fegley 1995). Those with C/O >1 are classed as C-rich stars, whilst C/O <1 defines them as O-rich. Spectroscopic observations show that carbonaceous phases, such as SiC and graphite, condense in the envelopes of C-rich stars (e.g. Treffers and Cohen 1974). In comparison, silicates and oxides of major elements dominate the dust condensing around O-rich stars.

The density of the circumstellar shell also plays a critical role. Typical mass loss rates for AGB stars are estimated at ~$10^{-5}M_{\odot}$ per year (e.g. Zijlstra et al. 2006). Stars that are experiencing significant mass loss provide environments that are dense enough for seed nucleation and subsequent grain growth. Condensed grains are driven out of circumstellar shells and into the ISM by stellar winds and radiation pressure from the star. Some of the dust is destroyed around stars through grain-grain collisions or evaporation from falling back onto the central star.

1.3.2 Interstellar Processing

To be present in primitive meteorites, presolar grains must have travelled from their parent star to the early solar nebula via the ISM. The ISM contains ~99% ions and molecules in the gas phase and ~1% dust. In the ISM the dust may have been altered by a variety of processes including interactions with galactic cosmic-rays, sputtering by, and potential implantation of, ions and atoms, grain-grain and grain-gas collisions, and vaporization and re-condensation. Evidence of this processing should be recorded on the grains surfaces and within their outer rims.

Grain sputtering and collisions are expected to produce cratering affects on the surfaces of presolar grains (Jones et al. 1996). However, Bernatowicz et al. (2003) reported a lack of evidence for any such processing on the surfaces of 81 pristine SiC grains (see Section 1.3.3). This led to the suggestion that either the residence time of grains in the ISM is very short, or the grains were protected from sputtering by surface coatings. Expected residence times for dust in the ISM are >500Myr (Jones et al. 1996), whilst calculated cosmic-ray exposure ages for presolar SiC range from <50Myr to >1Gyr (Lewis et al. 1994, Ott and Begemann 2000, Ott et al. 2005, Heck et al. 2009, Gyngard et al. 2009). Bernatowicz et al. (2003) noted that ~60% of the pristine SiC grains studied had amorphous coatings (<100nm thick) of an unknown material.

Infrared observations of dark clouds in the ISM indicate that dust grains are covered by icy mantles (Ehrenfreund and Charnley 2000). It has been proposed that simple ices, such as H_2O, CO, CO_2 and CH_3OH, can accrete onto grain surfaces in the ISM through grain surface reactions (Sandford and Allamandola 1993, Messenger et al. 2006, Nuth et al. 2006). Ice mantles form due to the efficient absorption of atoms and molecules from the interstellar gas, followed by surface diffusion and reactions with other surface atoms. These ices may then be processed, by photolysis and sublimation caused by exposure to UV photons and cosmic-rays, to form protective organic mantles. Bernatowicz et al (2003) could not rule out that the amorphous coatings seen on presolar SiC grains were not organic in nature.

Supernovae shockwaves in the ISM can result in the acceleration of interstellar gas and ions to velocities of 100s kms^{-1} (Jones et al. 1996). Significant ion irradiation of dust could produce amorphization of the outer rims of presolar grains. Material may also become implanted into the grains. Lyon et al. (2007) found that Li and B abundances in the outer ~0.5μm of some presolar SiC grains were higher than those within the grain cores. Lithium and B isotopic compositions were solar and it was concluded that Li and B ions had been implanted into the grains at high velocity by supernovae shockwaves in the ISM.

1.3.3 Discovery and Separation of Presolar Grains

The presence of presolar material in primitive meteorites was clearly indicated by the anomalous isotopic components Xe-HL (Reynolds and Turner 1964), Xe-S (Srinivasan and Anders 1978) and Ne-E (Black and Pepin 1969). Xe-HL is characterized by excesses in both the heavy and light Xe isotopes, predicted by r- and p-process nucleosynthesis respectively. Xe-S is enriched in ^{128}Xe, ^{130}Xe and ^{132}Xe; isotopes created through s-process nucleosynthesis. Ne-E comprises of almost pure ^{22}Ne, which is released at both low (L) and high (H) temperatures during stepped heating experiments (Amari et al. 1995b). Ne-E(H) is typically found alongside s-process Xe and Kr, inferring an origin in the He-shells of AGB stars (Gallino et al. 1990). Ne-E(L) is attributed to the rapid radioactive decay of ^{22}Na produced by explosive nucleosynthesis in novae and supernovae.

Although these isotopic anomalies are easily identifiable within meteorites, locating their carriers proved to be a far greater challenge. It took over 20 years of work before presolar nanodiamonds were isolated as the carrier of Xe-HL by Lewis et al. (1987). Presolar SiC was discovered to be the carrier of Xe-S and Ne-E noble gas signatures (Bernatowicz et al. 1987), while presolar graphite was found to contain Ne-E (Amari et al. 1990).

Nearly all presolar grains analyzed to date were extracted from their host meteorite using a series of harsh acid treatments. Astronomical observations predicted that much of the dust condensing around stars was carbonaceous and refractory. Refractory phases can survive treatment by hydrofluoric acid, plus

other strong acids and oxidizing reagents. These acids could therefore be used to dissolve >99% of the silicate meteorite matrix material, leaving residues of refractory minerals such as SiC.

This technique, often referred to as the *"Chicago procedure"*, is fully described by Amari et al. (1994) and shown in Figure 1.8. Briefly, Amari et al. (1994) started with a sample of the Murchison (CM2) carbonaceous chondrite. This was subjected to alternating treatments of HCl-HF and HCl in order to dissolve the silicates that dominate the meteorite matrix. Next, kerogen and sulphur were removed using KOH and nanodiamonds were extracted as a colloid. The sample only containing SiC, spinel and carbonaceous phases, was then density separated into five fractions. To isolate SiC, fractions of densities >2.3gcm^{-3} (the density of SiC is ~3.1gcm^{-3}) were heated in $HClO_4$, to destroy organics and graphitic carbon, and then in H_2SO_4 to dissolve spinel and chromite. Graphite is located in the untreated lower density fractions (1.6 – 2.2gcm^{-3}). Each density fraction was then further separated according to size. Most analyzed presolar SiC and graphite grains either came from these original residues or were isolated by a similar procedure.

A major disadvantage of this method is the loss of any non-refractory presolar materials. For example, presolar silicates, which are destroyed by acids, have recently been discovered in untreated meteorite matrix and IDPs (Nguyen and Zinner 2004, Nagashima et al. 2004, Nguyen et al. 2007, Messenger et al. 2003).

Nittler and Alexander (2003) separated presolar SiC grains using a procedure that included CsF instead of HF/HCl. They found a shift in the $^{12}C/^{13}C$ isotope distribution of their SiC grains compared to previous data, and suggested that there may be a population of SiC grains preferentially destroyed by the HF/HCL treatments.

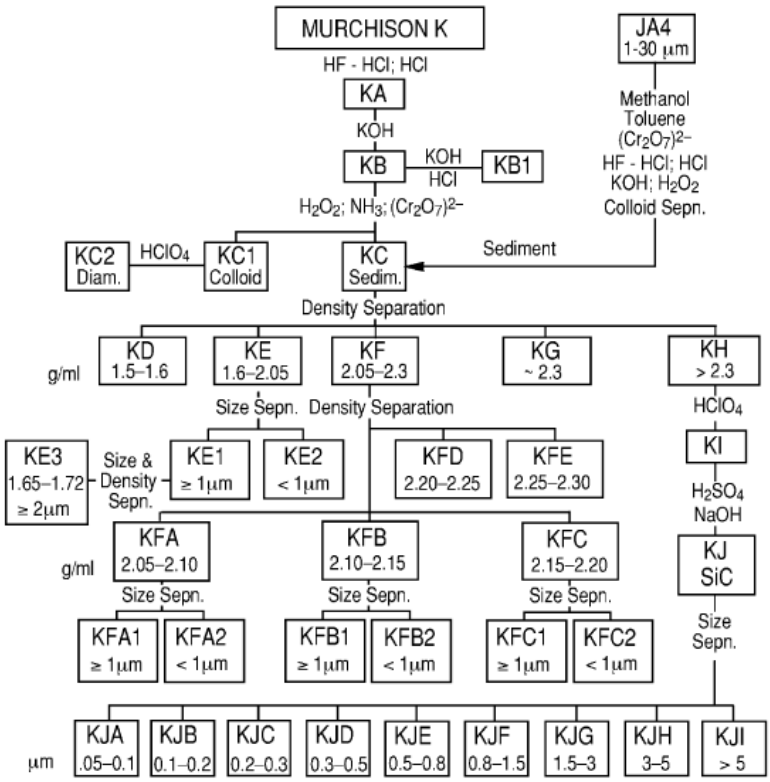

Figure 1.8 Flow-chart of the procedure used to separate presolar SiC grains from their host meteorites. Harsh acids dissolve the bulk (>99%) of the meteorite before grains are separated into fractions (here KJA-KJI) dependent upon their size and density (from Amari et al. (1994)).

There is also evidence that the use of harsh acids may alter the outer surfaces of presolar grains (Stephan et al. 1997, Henkel et al. 2007a). Henkel et al. (2007a) reported the loss of AlN inclusions, which are not resistant to acid treatments, from the outer regions of presolar SiC grains. Moreover, elevated abundances of elements such as Mg, K and Ca at grain surfaces were attributed to deposition of meteoritic matrix material in crystal defects potentially etched into grain surfaces by acid treatments.

These problems have led to attempts to study pristine presolar SiC grains. Bernatowicz et al. (2003) were the first to develop a non-acid, physical disaggregation technique. A 30mg sample of Murchison matrix was ultrasonicated to break up the material before separation by centrifugation into five size fractions. Using secondary electron microscopy (SEM) they then mapped the 1 – 3μm size fraction for SiC grains and located 81 pristine SiC

grains. As mentioned, ~60% of the grains were coated in an unknown amorphous material that had never previously been reported on acid extracted grains.

Tizard et al. (2005) further developed this idea of "gently separating" presolar SiC grains from meteorites. Starting with 32mg of Murchison matrix, this was crushed and broken down by cycles of freeze-thaw disaggregation. The disaggregated sample was separated into four size fractions before SiC grains were isolated by a density separation step. Silicon carbide grains were located by mapping with an electron microprobe and abundances were found to be enriched from 6ppm in Murchison whole rock to 0.67% in the 0.4 – 1.4μm size range.

1.3.4 Analysis of Presolar Grains

Since the late 1980's a wide range of analytical techniques and methods have been applied to the study of presolar grains. The earliest work focused upon noble gas concentrations in presolar grains (Lewis et al. 1990; 1994, Huss and Lewis 1994a; 1994b). However, the most important and widely used technique has been secondary ion mass spectrometry (SIMS).

SIMS is a destructive technique that involves sputtering a sample with primary ions in order to produce secondary ions representative of the sample composition. Most previous studies of SiC grains have used direct current (DC) beam ion probes that use magnets and electrical fields to separate the secondary ions (Zinner et al. 1989, Alexander 1993, Hoppe et al. 1994, Amari et al. 2000). These can provide both high spatial resolution and high mass resolution analyses, and have been vital in characterizing the isotopic and elemental compositions that prove the presolar nature of the grains.

Disadvantages of DC beam ion probes are high sample consumption and detection of only 5 – 7 isotopic species at a time. This means that grains must be typically >1μm in diameter to allow both major and trace element analysis, leading to a bias in the grain sizes analyzed. In presolar grain research there is an increasing need for multi-correlated analysis. The intention is to develop a more complete understanding of individual presolar grains, a task that requires multi-

elemental isotopic and abundance data alongside morphological and structural details (Nittler 2006).

One option is time-of-flight secondary ion mass spectrometry (TOFSIMS). In TOFSIMS a pulsed primary ion beam is used to generate secondary ions from the sample that are then separated according to their time-of-flight. The advantage of TOFSIMS is that an entire mass spectrum can be obtained in a single analysis. TOFSIMS will be the main technique used to analyze presolar grains in this research (see Chapter 2).

TOFSIMS has not been frequently used in the study of presolar grains. Stephan and Jessberger (1996) and Stephan et al. (1997) used TOFSIMS for high spatial resolution imaging, and major and trace element analysis, of presolar SiC, whilst Fahey and Messenger (2001) demonstrated its capability for measuring the Si isotopic compositions of presolar SiC grains. More recently, Henkel et al. (2007a) and Lyon et al. (2007) have used TOFSIMS to measure trace element abundances and isotopic compositions in presolar SiC grains extracted either using different chemical treatments or non-acid separation procedures.

New resonant ionization mass spectrometry (RIMS) instruments are now being utilized to study trace elements in presolar grains. The RIMS technique uses lasers to resonantly ionize a specific element in a sample; this boosts measurement sensitivity for that element. In particular it has been used to analyze the isotopic compositions of heavy elements thought to be produced by s-process nucleosynthesis (Nicolussi et al. 1997; 1998a; 1998b; 1998c, Savina et al. 2003; 2004, Barzyk et al. 2007).

Techniques such as SEM, transmission electron microscopy (TEM) and Raman spectroscopy have been widely used to investigate the morphology and structural characteristics of presolar grains (Bernatowicz et al. 1991, Zinner et al. 1995, Daulton et al. 2002; 2003, Stroud et al. 2002; 2003, Stroud and Bernatowicz 2005, Croat et al. 2005; 2008, Vollmer et al. 2009, Hynes et al. 2010a; 2010b, Nguyen et al. 2010). High resolution images of grains and the identification of sub-grain inclusions within them (Bernatowicz et al. 1991, Croat et al. 2005,

Stroud and Bernatowicz 2005) have provided insights into their formation in circumstellar shells.

1.3.5 Presolar SiC

To date, several thousand SiC grains have been studied and found to contain isotopic anomalies in almost every major and trace element within them.

The average presolar SiC grain size in the Murchison meteorite is ~0.4μm (Amari et al. 1994). Grains >60μm in diameter have been discovered, although those >10μm are extremely rare (Virag et al. 1992, Gyngard et al. 2009). Many presolar SiC grains are sufficiently large that isotopic and elemental compositions of single grains can be measured. They contain high trace element concentrations that allow for precise elemental and isotopic measurements to be made. Combined with their relatively high abundances in primitive meteorites (Table 1.1) and ease of extraction, this makes them ideal candidates for investigating interstellar processing (see Chapter 4).

Chondrite Group	SiC abundance (ppm by mass)
CI	14 – 49
CM	4 – 14
CR	0.6 – 60
CO	1 – 3
CV reduced	0.17 – 0.39
CV oxidized	0.006-0.2
CH	0.41
H 3.4	0.063
L 3.4/3.7	0.008 – 0.08
LL 3.0/3.1	0.39 – 1.52
EH 3-4	1.3 – 1.6

Table 1.1 SiC abundances in primitive meteorites (after Lodders and Amari (2005). Upper limits for CI and CR are from Davidson (2010) and Floss and Stadermann (2009).

1.3.5.1 Noble Gases

Presolar SiC is the carrier of the anomalous noble gas components Ne-E(H), Xe-S and Kr-S. Figure 1.9 shows the noble gas components as measured in bulk presolar SiC grain samples. Xenon in presolar SiC grains is enriched in the isotopes ^{128}Xe, ^{130}Xe and ^{132}Xe, Kr in the isotopes ^{82}Kr and ^{86}Kr. These enrichments are predicted by nucleosynthetic models of the s-process in stars. As

the s-process is expected to occur in the He-burning shells of AGB stars it is inferred that some presolar SiC was formed around AGB stars.

The s-process component (referred to as the G component) is often found mixed with a second noble gas component, the isotopic composition of which is similar to solar (Lewis et al. 1994). It is hence referred to as the normal, or "N", component. It is believed to originate in the outer envelopes of AGB stars where the products of nucleosynthesis are mixed to near solar compositions.

The inferred origin of presolar SiC grains around AGB stars is consistent with astronomical observations. Spectra from such stars contain an 11.3μm emission feature that is commonly interpreted as the presence of SiC dust (Treffers and Cohen 1974).

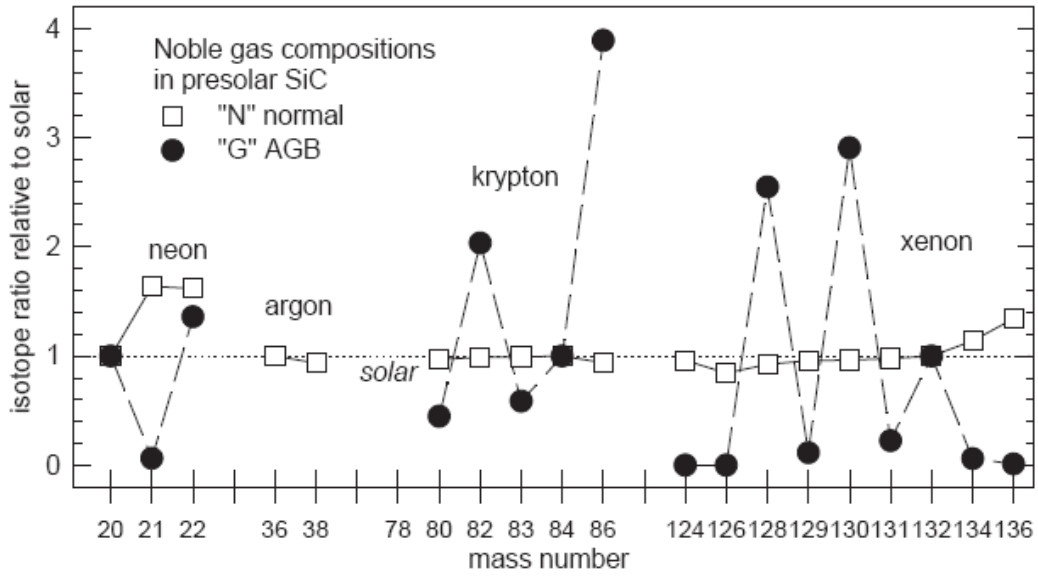

Figure 1.9 Noble gas components in bulk presolar SiC grain samples. Isotope ratios are plotted relative to solar (represented by the thinly dashed line). Krypton is enriched in its 82 and 86 isotopes, Xe in its 128, 130 and 132 isotopes. These patterns are predicted by s-process models occurring in AGB stars. Presolar SiC grains can therefore be linked to AGB stellar sources. Lewis et al. (1994) measured He, Ne, Ar, Kr and Xe, showing them to be a mixture of a highly anomalous "G" component, with the isotopic signature of the s-process, and "N" component, similar to solar (from Lodders and Amari (2005)).

1.3.5.2 C, N and Si

Figure 1.10 shows measured C and N isotopic ratios within presolar SiC grains, and Figure 1.11 shows their Si isotopic ratios. Based upon the large variations in C, N and Si isotopic compositions, presolar SiC grains can be divided into sub-

groups: *mainstream, A* and *B, X* grains, and *Y* and *Z*. Presolar SiC grains from novae (Amari et al. 2001c), and unusual grains with very extreme enrichments in ^{29}Si and ^{30}Si (Hoppe et al. 2010) have also been found. The discovery of distinct classes of presolar SiC indicates that at least several different stellar sources must have contributed SiC grains to the presolar molecular cloud (Alexander 1993, Hoppe et al. 1994).

The mainstream group makes up ~90% of all presolar SiC. Figure 1.10 shows that they typically contain ^{14}N/^{15}N ratios higher than the solar value (~272) and ^{12}C/^{13}C lower than solar (~89). Most of them are enriched in both ^{29}Si and ^{30}Si (relative to ^{28}Si) (Hoppe et al. 1994, Lugaro et al. 1999).

The other main diagnostic feature of mainstream presolar SiC grains is the presence of Xe-S and Kr-S, which combined with evidence from the other isotope systems (e.g. enrichments in ^{94}Zr or ^{86}Sr, isotopes produced by s-process nucleosynthesis), is consistent with formation around 1 – 3$M_{\odot}$ AGB stars of approximately solar metallcity (Nicolussi et al. 1997; 1998b, Lugaro et al. 2003).

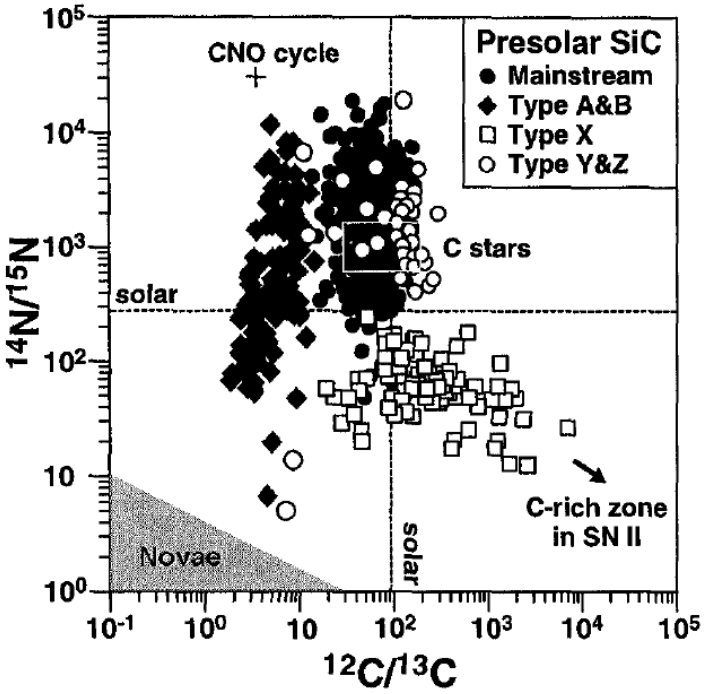

Figure 1.10 Measured C and N isotopic ratios within presolar SiC grains. The grains fall into distinct groups, mainstream, A and B, X, Y and Z. Isotopic ratios vary by orders-of-magnitude both between individual sub-groups and from solar values (dashed lines). Theoretical predictions for C-rich stars, novae, the C-rich zone of type II supernovae and burning by the CNO cycle are shown (from Hoppe (2001)).

On a Si three-isotope plot (Figure 1.11) the mainstream grains define a line of slope ~1.3, which is in disagreement with simple models of GCE (Clayton 1988, Timmes and Clayton 1996). Standard GCE models predict that the first stars formed in unseeded (only H, He and minor Li from the "Big Bang") molecular clouds and must therefore have produced primary isotopes, including ^{28}Si. The next generation of stars formed in a partially seeded (H, He plus some heavier elements) environment, allowing nucleosynthetic production of secondary isotopes, such as ^{29}Si and ^{30}Si. Therefore GCE dictates that ^{29}Si/^{28}Si and ^{30}Si/^{28}Si ratios will increase over time and should produce a line of unity on a three-isotope plot. It has been suggested that deviations from unity indicate that many stellar sources, whose initial compositions varied because of GCE, contributed SiC grains to the Solar System (Alexander 1993).

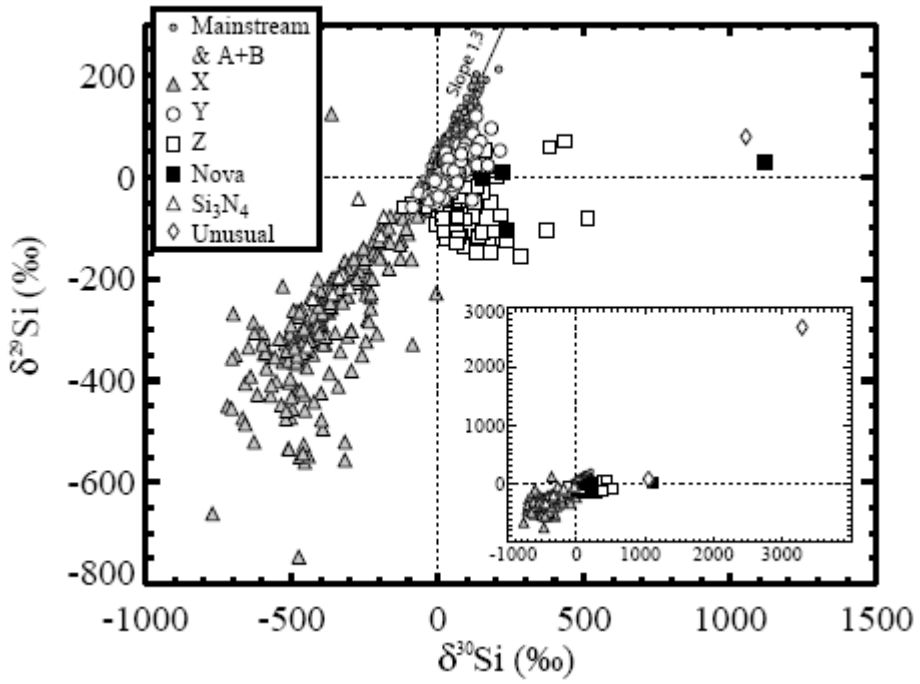

Figure 1.11 Silicon three-isotope plot for presolar SiC grains. The mainstream grains are enriched in ^{29}Si and ^{30}Si relative to ^{28}Si and define a line of slope *m = 1.3.* In contrast the X grains are depleted in ^{29}Si and ^{30}Si (from Nittler (2003)).

The issue is further complicated however, as the composition of each mainstream grain is believed to reflect that of its parent star. By definition the grains were created before the formation of the Sun. If this were true, according to GCE models, they should be depleted in ^{29}Si and ^{30}Si relative to the Sun (i.e. they

formed from more primitive material). Instead mainstream grains Si isotopic compositions suggest that they were formed *after* the Sun.

Potential solutions to these problems have included the evolution of ^{30}Si being faster in low metallicity stars (Alexander and Nittler 1999), an effect of mixing high and low metallicity gas in a presolar galactic merger (Clayton 2003), evolution of the star's orbits within the galaxy (Clayton and Timmes 1997) or inhomogeneous chemical evolution of the ISM (Lugaro et al. 1999).

The A and B sub-group (~3 – 4% of all presolar SiC) have $^{12}C/^{13}C$ <10 and a $^{14}N/^{15}N$ range of 40 – 12000. Their Si isotopic compositions are very similar to mainstream grains, although on the three-isotope plot they define a slope of ~1.5. Amari et al. (2001a) proposed that the A and B grains originated from C-rich J-type stars or CH stars. Unfortunately there is little astronomical data regarding these stars and current astrophysical models of them do not account for those A and B grains that have both low $^{12}C/^{13}C$ and $^{14}N/^{15}N$ ratios.

The X grains (~1%) have $^{12}C/^{13}C$ ratios often significantly higher than solar and $^{14}N/^{15}N$ ratios that are lower than solar (Figure 1.10). They also contain ^{28}Si excesses up to five times the solar value. These isotopic compositions cannot be explained by nucleosynthesis in AGB or C-rich stars. They are however qualitatively consistent with the explosive nucleosynthesis that takes place in Type II supernovae (Amari et al. 1992, Nittler et al. 1996, Clayton et al. 1997, Amari and Zinner 1996, Hoppe et al. 1996; 2000).

Further evidence for a Type II supernovae origin comes from excesses in the minor isotopes ^{26}Mg, ^{44}Ca and ^{49}Ti. Large $^{26}Mg/^{24}Mg$ excesses in X grains are attributed to the radioactive decay of ^{26}Al. From measured ^{26}Mg excesses, initial $^{26}Al/^{27}Al$ ratios of between 0.1 – 0.6 have been inferred (Amari et al. 1992, Hoppe et al. 1996; 2000). These are significantly different from the canonical $^{26}Al/^{27}Al$ ratio of the Solar System. An excess in $^{44}Ca/^{40}Ca$ has been attributed to the decay of ^{44}Ti, whilst those in $^{49}Ti/^{48}Ti$ are believed to come from ^{49}V (Hoppe and Besmehn 2002). As ^{44}Ti and ^{49}V can only be formed by explosive

nucleosynthesis in Type II supernovae, presolar SiC grains must have condensed in this environment.

The Y grains (~1%) have $^{12}C/^{13}C$ ratios >100 and $^{14}N/^{15}N$ ratios above solar (Amari et al. 2001b). Their Si isotopic compositions place them slightly to the right of the mainstream grains on a three-isotope plot (Figure 1.11) and indicate that they formed around AGB stars whose metallicities were 1/2 that of solar.

The Z grains contain C and N ratios that are similar to solar but often have excesses in ^{30}Si. It has been suggested that the Z grains originated in AGB stars of metallicities of up to a 1/3 of solar (Hoppe et al. 1997, Amari et al. 2001b). These stars contain less synthesized material within their envelopes. Nucleation effects therefore dictate that condensing SiC grains are smaller than those formed around stars of higher metallicity. Presolar SiC grains of type Z have been found to be particularly rare in the coarser SiC size fractions (Zinner 1998, Hoppe et al. 2010).

Amari et al. (2001c) have also measured five presolar SiC grains that have C and N isotopic ratios different to those seen in any other sub-group. These grains contain $^{12}C/^{13}C$ and $^{14}N/^{15}N$ ratios <20 and ^{30}Si excesses. This is a signature of high temperature H-burning and is believed to take place in novae.

1.3.5.3 Trace Elements

Presolar SiC grains contain several trace elements in substantial abundances. For example, Mg is found at levels of ~100ppm and Al can reach several mass percent (Amari et al. 1995a). The abundance of trace elements within presolar SiC reflects both the composition of the circumstellar gas in which they formed and the condensation process itself.

Amari et al. (1995a) measured trace element concentrations in 60 individual SiC grains and three SiC size-sorted aggregates. Elements more volatile than SiC were shown to be depleted in the grains (relative to solar) and refractory elements were generally enriched. In the mainstream grains heavy elements

(>Fe) produced by the s-process were enriched by up to 35 times the solar abundance.

Lodders and Fegley (1995) showed that their model of trace element condensation into SiC grains was consistent with the data of Amari et al. (1995a). Refractory compounds, such as SiC and TiC, condensed out from the circumstellar gas first. The more volatile elements, which could not condense at high temperatures, remained in the gas and formed compounds of carbides (ZrC, MoC), sulfides (MgS, CaS) and nitrides (AlN). As temperatures decreased these compounds began to condense in solid solution with SiC and TiC according to their volatility and compatibility within the crystal lattice structure.

Silicon carbide condenses over a range of temperatures (Lodders and Fegley 1995). This makes it possible for SiC grains originating from the same parent star to contain varying trace element abundances. As elements and their compounds condense the circumstellar gas becomes depleted in those elements. The first SiC grains to condense will therefore obtain their trace elements from a circumstellar gas differing in composition to those grains formed at lower temperatures.

Another factor that plays a role is whether an element condenses as a separate phase from SiC. For example, TiC is predicted to condense before SiC (Lodders and Fegley 1995). This causes a depletion of Ti in the gas and therefore also in the SiC grains. Similarly, any highly refractory elements that condense into the TiC prior to SiC (e.g. V) condensation will also be depleted in the SiC grains.

There is evidence that some trace elements may have been implanted into the grains. For example, Lyon et al. (2007) reported elevated Li and B abundances within the outer regions of grains and argued that this represented interstellar material implanted into the grains by supernovae shockwaves. Certainly, some noble gases also appear to have been implanted into SiC grains. Verchovsky et al. (2004) noted noble gas isotopic variations with SiC grain size, a feature they attributed to the implantation of two isotopically distinct noble gas components at different implantation energies in an AGB stellar environment.

Analytical constraints have restricted the ability to determine trace element abundances in presolar SiC grains. SIMS removes atoms from the surface of the sample and hence destroys the grain. When analyzing presolar SiC the first elements measured are often C, N and Si (for classification purposes - see Section 1.3.5.2). After this initial analysis the grain has been partly destroyed leaving less mass available for trace element measurements. In order to obtain significant trace element information alongside C, N and Si isotopic data, grains must have enough mass remaining for the trace element analysis. Current data regarding trace element abundances is biased towards larger grains.

Trace element analyses may also be biased if those elements are inhomogeneously distributed within the grains. High sample consumption during measurements with DC-beam ion probes means that data often represents an average over a large volume of the grain. Therefore in this research TOFSIMS will be used to measure the distribution of a range of trace elements in presolar SiC grains (see Chapter 4).

1.3.5.4 Structure and Morphology

Presolar SiC grains typically have euhedral shapes. Only two polytypes, cubic 3C (80%) and hexagonal 2H (3%), of presolar SiC have been observed (Daulton et al. 2002; 2003). Intergrowths (17%) between the two have also been noted. This is surprising as synthetic SiC forms several hundred different polytypes. The limited number of different polytypes that presolar SiC grains form allows constraints to be placed upon the environment in which they condensed. Thermochemical equilibrium calculations predict the formation cubic 3C and hexagonal 2H polytypes at low temperatures ($\leq$1633K), low pressures ($<10^{-4}$ bar) and when C/O $\geq$1.05 (Daulton et al. 2002; 2003). Such an environment is believed to exist in the stellar outflows of C-rich AGB stars.

In studying 81 pristine presolar SiC grains, Bernatowicz et al. (2003) reported that ~90% were of polytype cubic 3C. Polygonal depressions, believed to be primary growth features, were observed in crystal faces and suggested rapid formation times.

Approximately 60% of the grains were coated with an unknown amorphous material. It was speculated that these were silica rims, possibly created by oxidation in the early solar nebula (Mendybaev et al. 2001). Stroud and Bernatowicz (2005) reported evidence for the presence of silica rims, 10 – 30nm thick, on pristine presolar SiC grains, although it is still unknown whether these account for the amorphous coatings. Alternatively, it has been suggested that the grains may have acquired coatings consisting of organics and simple ices in the ISM or early solar nebula (see Messenger et al. 2006, Nuth et al. 2006).

TEM studies of pristine presolar SiC grains and those of type AB have revealed the presence of small sub-grains of TiC and AlN (Stroud and Bernatowicz 2005, Hynes et al. 2010a). An isotopic study of over 200 randomly selected presolar SiC grains also indicated that TiC sub-grains are likely to be present in nearly all the SiC sub-groups (Gyngard et al. 2006). This is not surprising as TiC is predicted to condense as a separate phase prior to the formation of SiC (see Section 1.3.5.3).

1.3.6 Presolar Graphite

Although often larger in size (>1μm diameter), and present in comparable abundances within meteorites to presolar SiC grains, fewer studies have been carried out on presolar graphite.

Presolar graphite is the carrier of Ne-E(L). Graphite grains are often divided into four sub-groups based upon their densities and C isotopic compositions. Low-density graphite is often of the "*cauliflower*" morphological type, consisting of aggregates of small grains. In contrast high-density graphite is often shaped like an "*onion*", with fine-grained crystalline core surrounded by concentric layers of carbon (Figure 1.12). Measurements have shown that with increasing density the abundance of minor elements such as H, N, O and Si decrease (Hoppe et al. 1995).

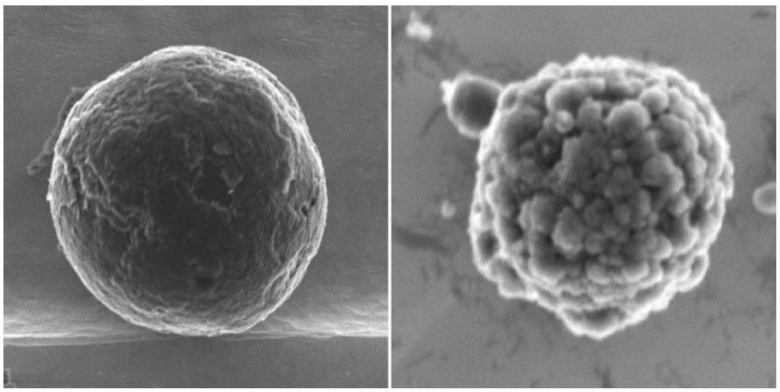

Figure 1.12 Representative SEM images of onion (left) and cauliflower (right) presolar graphite grains. Presolar graphite grains are typically >1µm in diameter (from Croat et al. (2008)).

Their $^{12}C/^{13}C$ ratios show a wide range, ~2 – 7000 (Hoppe et al. 1995, Bernatowicz et al. 1996), whereas N isotopic ratios are close to solar. Solar N ratios may reflect contamination (Hoppe et al. 1995). Silicon isotopic compositions are comparable to those observed in presolar SiC, although Wolf-Rayet and supernovae stars are thought to have contributed ~60% of presolar graphite grains (Hoppe et al. 1995). The presence of Xe-S and Kr-S indicates that at least some of the grains formed around AGB stars (Amari et al. 1995b).

Presolar graphite grains also contain small (typically 10's nm) sub-grains of predominantly TiC but also others phases such as Zr-Mo carbide (Bernatowicz et al. 1991; 1996, Croat et al. 2005; 2008). Many of these sub-grains are located within the core of the main graphite grain and may have acted as nucleation sites for graphite growth. Some sub-grains show no crystallographic relationship to the main graphite grain suggesting that they formed separately and were incorporated into the graphite at a later stage.

1.3.7 Presolar Nanodiamonds

Nanodiamonds are the most abundant presolar phase and are typically only ~2nm in size. This makes them too small for analysis of individual grains, so isotopic and elemental data must be obtained from bulk samples. They are therefore the least well understood presolar phase.

Presolar nanodiamonds are carriers of Xe-HL, indicating a supernova origin. This is further supported by the presence of isotopic anomalies in heavy elements such as Te and Pd (Maas et al. 2001). However, despite this evidence, nanodiamonds still remain controversial due to bulk analyses of $^{12}C/^{13}C$ ratios that are approximately solar (e.g. Lewis et al. 1987) and N isotopic compositions very similar to those seen in Jupiter's atmosphere (Owen et al. 2001). This suggests that a significant fraction of the nanodiamonds contained within primitive meteorites may have formed in the early Solar System and hence may not be presolar in origin.

1.3.8 Presolar Silicates

Despite being widely observed in the ISM and around young, AGB and massive stars (e.g. Malfait et al. 1998) presolar silicate grains were only recently discovered in primitive meteorites (Nguyen and Zinner 2004, Nagashima et al. 2004, Nguyen et al. 2007) and IDPs (Messenger et al. 2003). This is partly due to silicates being more susceptible than SiC and graphite to processing in the meteorite parent body, and also the need to dissolve silicates in the harsh acid treatments required for SiC and graphite extraction (see Section 1.3.3). A further problem is locating a presolar silicate amongst meteoritic material that is dominated by silicates formed in the Solar System.

The recent discovery of presolar silicates is the result of the high spatial resolution of the NanoSIMS (e.g. Nguyen et al. 2007). This allows silicate grains containing anomalous isotopic ratios to be easily identified in-situ from those with solar compositions. Initial measurements of presolar silicates have highlighted anomalous O isotopic ratios, which point towards origins around RGB and AGB stars (Nguyen et al. 2007).

1.3.9 Presolar Oxides

Presolar oxide grains, including corundum, hibonite, spinel and titanium oxide, may be extracted from meteorites with acid treatments similar to those used for SiC and graphite (Nittler et al. 1997; 2008). Presolar oxide grains have also been

analyzed in-situ by searching for isotopically anomalous grains within meteorite matrix material (Nguyen et al. 2003).

Presolar oxides are sub-divided into four groups (I-IV) in accordance with their O isotopic compositions (Figure 1.13). Their O isotopic compositions, along with elements such as Mg and Cr, indicate an origin around RGB stars, O-rich AGB stars and Type II supernovae (Zinner et al. 2005).

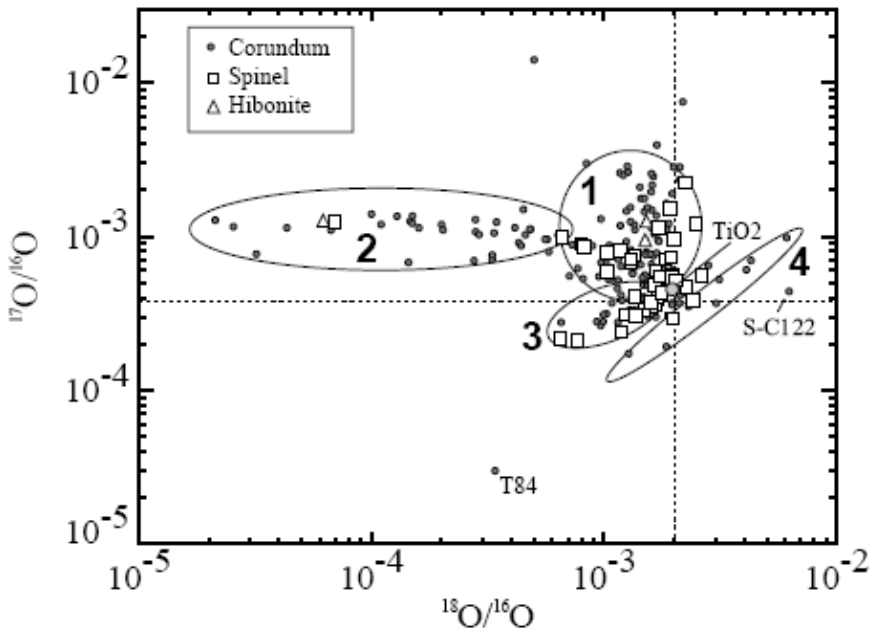

Figure 1.13 Presolar oxides can be divided into four groups based upon their O isotopic compositions. Groups 1-3 are believed to originate mainly from O-rich giant stars. The origin of group 4 is still unresolved (from Nittler (2003)).

1.3.10 Presolar Silicon Nitride

Few silicon nitride grains have been analyzed due to their rarity within primitive meteorites (~0.002ppm). Their isotopic compositions show ^{28}Si and ^{15}N excesses, characteristics also observed in SiC X grains. They also contain very high $^{26}Al/^{27}Al$ ratios consistent with a Type II supernovae origin (Nittler et al. 1995).

1.4 CARBON IN THE SOLAR SYSTEM

The major aim of this research is to investigate the processing of presolar grains in the ISM. This can be done by studying pristine presolar grains isolated from meteorites without acids. Therefore, one intention was to use the gentle separation procedure of Tizard et al. (2005) to isolate pristine presolar graphite. To date no presolar graphite grains have been located in the resulting size and density fractions. However, carbonaceous grains were present and subsequent analyses found them to contain evidence of processing in the early solar nebula. This work is presented in Chapter 5. Below is a summary of the current understanding of carbonaceous phases in primitive meteorites.

Carbon is found throughout the Solar System, and in the laboratory is now routinely analyzed within primitive meteorites (e.g. Brearley 1990, Amari et al. 1993, Alexander et al. 1998, Sephton 2002, Quirico et al. 2009), IDPs (e.g. Wopenka 1988, Flynn et al. 2003, Busemann et al. 2009) and cometary samples (e.g. Muñoz Caro et al. 2008, Rotundi et al. 2008).

It has a large molecular and isotopic diversity that suggests formation through a variety of processes. Carbon in primitive samples is therefore thought to reflect a mixture of different materials derived from either the ISM or early solar nebula, which were subsequently modified on meteorite parent bodies (for reviews see Botta and Bada 2002, Sephton 2002, Pizzarello et al. 2006).

In meteorites carbon is divided into soluble and insoluble fractions. Soluble organic carbon in carbonaceous chondrites (meteorites with a carbon-rich matrix) comprises of a complex suite of compounds that include species such as aromatic and aliphatic hydrocarbons (PAH), amino acids and small methane and formic acid molecules. However, most of the carbon, up to 99% in the Tagish Lake (ungrouped) meteorite (Pizzarello et al. 2001), is insoluble and can be extracted using HCL, HF and CsF acid treatments. The insoluble organic matter (IOM) is largely present as a complex, unstructured macromolecular material similar to terrestrial kerogens (e.g. Kerridge et al. 1987).

Analysis of the IOM shows it contains elemental and isotopic compositions that vary significantly between, and also sometimes within, chondrite classes. The differences are believed to represent the effects of parent body processing of a potentially common precursor material (e.g. Alexander et al. 2007).

Some IOM has retained large enrichments in D and ^{15}N acquired prior to accretion into meteorite parent bodies. These isotopic anomalies indicate that part of the IOM probably originated in the ISM or the cold outer regions of the early solar nebula (Robert and Epstein 1982, Yang and Epstein 1983, Kerridge et al. 1987, Busemann et al. 2006). At low temperatures (<50K) cosmic-ray ionization promotes ion-molecule reactions and isotopic mass fractionation, creating interstellar gas enriched in D and ^{15}N (Millar et al. 1989, Aikawa and Herbst 1999, Sandford et al. 2001). Interstellar ice analogs can be converted into refractory organic compounds by UV radiation (Strazzulla et al. 2003, Ferini et al. 2004), whilst similar materials have been astronomically observed around newly formed stars (Gibb and Whittet 2002).

In both acid extracted and untreated IOM residues there also exists a component of more structured carbon. Although this includes the isotopically anomalous presolar grains (e.g. SiC, graphite and nanodiamonds) described in Section 1.3, approximately 10% of IOM also consists of nano-metre sized aromatic carbon flakes, hollow or solid globules, and tubes (Garvie and Buseck 2004).

Garvie and Buseck (2004; 2006) and Garvie et al. (2008) have used SEM and TEM to study the globules and tubes in carbonaceous chondrite matrices. Spherical nano-globules occur ubiquitously throughout the carbonaceous chondrites. They are present as both single particles, or clustered together, and have either solid or hollow (possibly vesicular) cores. Most are <50nm in diameter although some individual particles up to ~2μm have been observed. The surfaces of globules are typically smooth or bumpy in appearance. Nano-tubes are less abundant than the globules. They appear “fluffy”, have hollow interiors and diameters of <100nm.

Nakamura-Messenger et al. (2006) used a NanoSIMS to obtain in-situ isotopic compositions of hollow nano-globules within Tagish Lake matrix material. The nano-globules contained large D and ^{15}N enrichments, which as mentioned above, are consistent with an interstellar or early nebula origin. As the nano-globules had walls, ~100 – 200nm thick, Nakamura-Messenger et al. (2006) proposed that they were created by UV radiation from icy mantles condensed onto grain surfaces. Exposure to radiation converted the mantles to organic phases whilst the interior grains were shielded. If the interior grains were pre-existing ice particles then they may have volatilized at a later stage leaving organic globules with hollow cores.

The heterogeneous compositions, sizes and distributions of nano-globules and tubes in carbonaceous chondrites indicate that, like most IOM, they formed from multiple sources. Indeed, Busemann et al. (2006) and Remusat et al. (2010) have reported organic materials within the same meteorite that contain both extreme D enrichments and lower δD values, possibly reflecting the mixing of many different sets of organic particles prior to accretion. However, currently there is still little information available regarding the nature of the carbonaceous particles in IOM and further investigations are required to establish their origins in the ISM or early solar nebula, and to determine the effects of processing on meteorite parent bodies.

1.5 THESIS AIMS AND OUTLINE

The main aim of this research is to investigate processing in the ISM using presolar grains extracted from primitive meteorites. As presolar grains condensed around stars prior to the formation of the Solar System, they must have been subjected to processing in the ISM and are expected to retain evidence of this.

One way to study the grains is to use TOFSIMS, which allows analysis of multiple elements within a grain during a single measurement. Subsequent measurements can be combined to give isotopic and elemental abundance depth-profiles from individual presolar grains. The distribution of trace elements within the grains may have been significantly altered by interstellar processing.

Most presolar grains are extracted from their host meteorite using harsh acid treatments. It has been argued that these treatments may also damage the surfaces of presolar grains. Any evidence of interstellar processing may therefore have been destroyed or altered by the acids, so ideally pristine presolar grains should be studied.

Constraining the affects of interstellar processing enables the complete history of individual presolar grains to be determined, and improves our understanding of the material from which the Solar System formed.

Chapter 2: Describes the analytical techniques used in this research, including the NanoSIMS, SEM, TEM and Raman spectroscopy. The main analytical tool used was a new TOFSIMS instrument equipped with a 25kV Au_n^+ liquid metal ion gun (LMIG). As a newly constructed instrument, experimental procedures had to be developed prior to the analysis of presolar grains.

Chapter 3: Is adapted from a paper published in *Rapid Communications in Mass Spectrometry*. In order to accurately determine elemental abundances in presolar grains using TOFSIMS, it is necessary to measure standards similar in structure and composition to the sample intended to be analyzed. This work describes measurements of a series of homogeneous silicate glasses, which were used to

calculate relative sensitivity factors (RSFs) in preparation for the analysis of presolar SiC grains. Au-cluster ion sources are rarely used for the analysis of inorganic samples and comparisons between different Au-cluster primary ion species are made.

Chapter 4: Is presented as a paper ready for submission. The paper describes depth-profiles of a range of trace elements in presolar SiC grains obtained using TOFSIMS, in presolar SiC grains. Presolar SiC grains experienced several different environments; the circumstellar regions of their parent stars, the ISM, the early solar nebula, and meteorite parent bodies, before arriving in the laboratory. The grains are likely to have undergone processing in each of these environments, evidence of which should be retained both on grain surfaces and within their internal structures and compositions.

Chapter 5: Is presented as a paper ready for submission. The paper describes the nature of amorphous carbonaceous grains separated from the Murchison meteorite according to their size and density. It should be noted that the separation procedure was performed by Sean Chapman at the University of Manchester. Based upon isotopic compositions measured using TOFSIMS and NanoSIMS, and structural characteristics determined by Raman spectroscopy and TEM analysis, possible origins of the amorphous carbonaceous grains are discussed.

Chapter 6: Provides a summary of the thesis, a discussion of the research's implications, and suggestions for future work.

Chapter 2

Methodology and Analytical Techniques

The investigation of presolar grains and carbonaceous phases in the Murchison meteorite required the application of a range of analytical techniques. TOFSIMS was the main means of analysis, full details of which are provided below. This section is followed by descriptions of the NanoSIMS, environmental SEM (ESEM), Raman and TEM techniques also used in this research.

2.1 TIME-OF-FLIGHT SECONDARY ION MASS SPECTROMETRY

TOFSIMS has been used in cosmochemistry since the early 1990's (e.g. Stephan et al. 1991). Its ability to detect an entire mass spectrum quasi-simultaneously at high spatial resolution makes it a useful tool for element mapping and analyzing isotopic and elemental abundance ratios in extra-terrestrial samples. As it is a destructive technique repeated measurements can be made to produce a depth-profile through a sample. TOFSIMS was the main analytical technique used in this study.

2.1.1 Secondary Ion Mass Spectrometry

Figure 2.1 provides a schematic description of a TOFSIMS instrument. During SIMS measurements samples are bombarded with high energy primary ions initiating the release of secondary particles from near-surface layers in a process known as sputtering. The secondary particles include electrons, atoms and molecules, of which ≤1% are ionized (Stephan 2001). The secondary ions can be extracted away from the sample surface, detected and used to produce secondary ion images. In TOFSIMS secondary ions of different isotopic species are separated according to their time-of-flight from the sample to the detector.

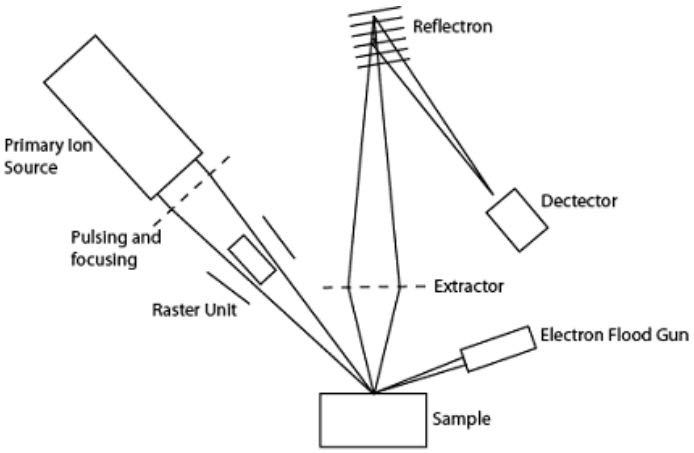

Figure 2.1 A schematic TOFSIMS instrument. A pulsed primary ion source bombards the sample, producing secondary ions that are extracted by acceleration in an electric field. The reflectron accounts for any spread in ion energies before they are mass separated.

Secondary ions are extracted away from the sample surface by acceleration in an electric field. The effects of acceleration on an ion species of mass (m) and charge (q) in an electric field with potential difference (V) is described as:

$$E = qV = \frac{1}{2}mv^2 \qquad \text{(Eq. 2.1)}$$

where E is the energy of an ion and v is its velocity.

As the ions leave the electric field they will therefore have a velocity of:

$$v = \left[\sqrt{\frac{2qV}{m}}\right] \qquad \text{(Eq. 2.2)}$$

The secondary ions are extracted into a field-free flight tube where those of different isotopic species are separated according to their mass-to-charge ratio (m/q):

$$\frac{m}{q} = \left(\frac{2V}{s^2}\right)t^2 \qquad \text{(Eq. 2.3)}$$

where t is the time taken by an ion to travel the length of the flight path (s).

Lighter ions have higher velocities and will arrive at the detector ahead of heavier ones. This enables all masses to be detected separately. The resulting

mass spectra consist of the ion *m/q* versus the number of secondary ions detected at each *m/q*.

Time focusing of secondary ions of any particular mass at the detector assumes mono-energetic ions (Eq. 2.1). However, the sputtering process releases secondary ions with a wide spread of kinetic energies (peaking at ~10 – 20eV) (Figure 2.2). This causes secondary ions of the same mass to have a range of velocities and therefore varying flight times in the flight tube.

This problem can be compensated by the introduction of a reflectron (Figure 2.1). The reflectron consists of a series of annular rings connected by a chain of resistors to produce an evenly graded electric field, plus a guard mesh at the top. An opposing voltage to that of the extraction field is used initially to decelerate secondary ions and then to invert their flight paths. Secondary ions of the same mass but higher energy (and hence velocity) penetrate deeper into the reflectron, taking longer to be reversed and delaying their arrival time at the detector relative to lower energy ions. In this way ions of the same mass but with different energies can be time-focused at the detector.

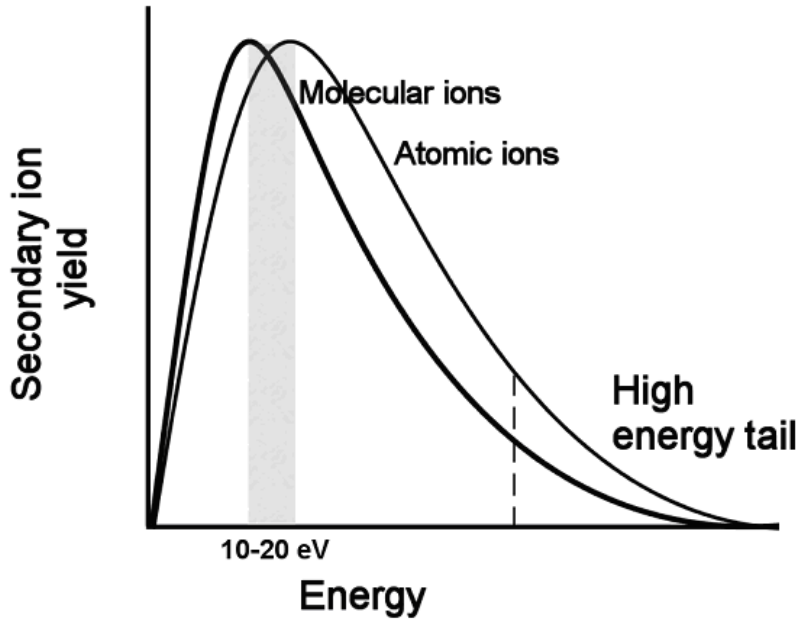

Figure 2.2 Typical energy spread of atomic secondary ions after sputtering (after Tizard (2005)).

Secondary ions are detected using a micro-channel plate detector (MCP). When a secondary ion strikes the MCP it is converted into an electrical pulse that is amplified and sent to a time-to-digital converter (TDC) on a computer. Electrical noise can be reduced by setting a threshold, over which a signal must be in order to be recorded. The TDC registers the arrival time of each pulse and converts them into a time-of-flight mass spectrum.

2.1.2 Primary Ion Gun

The primary ion beam is focused into a spot on the sample using an aperture and two lenses (Figure 2.3). The spot size of the primary ion beam is entirely determined by the size of the aperture through which it passes. The smaller the aperture, the smaller the spot size and hence increased spatial resolution of the secondary ion images. However smaller spot sizes lead to less beam current hitting the sample, which results in decreased secondary ion yields. For each measurement there must be a trade-off between the required spatial resolution and obtaining useful secondary ion intensities.

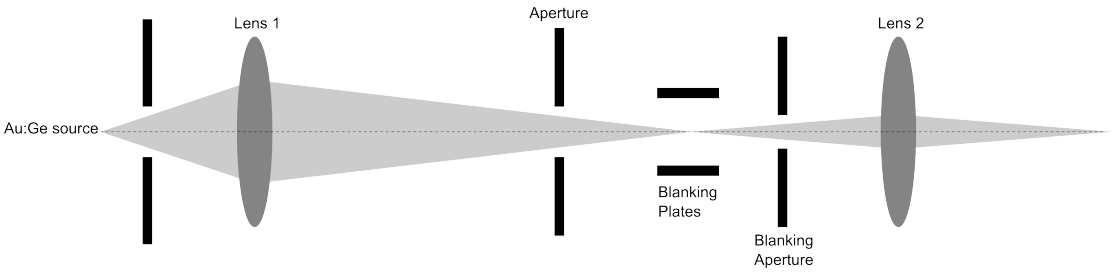

Figure 2.3 Schematic diagram of the TOFSIMS primary ion gun and optics. The spot size of the beam is controlled by the aperture and focused onto the sample using lens 2. The beam is pulsed by applying a voltage to the blanking plates.

TOFSIMS uses a pulsed primary ion beam with lengths of up to several tens of nanoseconds. If the time between two primary ion pulses is very short, then it is possible for the lightest (i.e. fastest) secondary ions produced by the second pulse to overtake the heaviest (i.e. slowest) from the initial pulse. These ions would then be incorrectly identified at the detector. The flight time of all secondary ions produced from a single primary ion pulse therefore dictates the maximum repetition rate (~10kHz) of a measurement.

Pulsing of the primary ion beam results in low duty cycles, typically ~10^{-4}, meaning long measurement times are required to achieve good counting statistics. However, this is partially compensated by the parallel detection of all secondary ions and also produces low sample consumption rates.

The primary ion beam is pulsed by sending it through two blanking plates (Figure 2.3). To blank the beam, i.e. prevent it from leaving the ion source, a potential difference between the plates is created by holding one plate at 200V and the other at ground. The beam is pulsed by applying pulses of 200V (the length of which can be altered to suit the operator's requirements) to the plate at ground potential. During the pulse there is a net field across the blanking plates of zero that allows the beam to pass through the chamber.

Rapid pulsing of the primary ion beam can degrade the spatial resolution of the ion focus on the sample. The spatial resolution can be improved by optimizing the ion source for "minimum motion". Achieving minimum motion involves lessening the movement of the primary ion beam on the sample during beam pulsing. This is done by centring the beam crossover focus between the blanking plates (using lens 1 on Figure 2.3) and correctly positioning the path of the primary ion beam through the blanking aperture until no movement in the image is observed when blanking and un-blanking the beam. Once minimum motion is complete, final focusing of the beam on the sample can be carried out and any stigmatism in the image can be corrected for.

Sample charging can cause the primary ion beam to be perturbed close to the sample surface and may also affect the extraction field and kinetic energies of secondary ions. To compensate for sample charging an electron flood gun may be used. Sample charging was not an issue in this study and charge compensation was never applied.

2.1.3 Mass Resolution

Mass resolution refers to the ability to discriminate between two different peaks in a mass spectrum ($m/\delta m$). Interferences in the spectrum can come from

hydrocarbons, oxides, hydroxides and hydrides along with isobaric interferences (nuclides of different elements with the same nominal mass). Typical hydrocarbons have δm (relative to an atomic species) of >0.01 daltons and hydrides δm ~0.007 daltons requiring $m/\delta m$ of <2000 and ~3000 respectively.

In TOFSIMS the mass resolution is determined by the resolution of the mass analyzer (R_{an}), the time resolution of the detector and electronics system (t_{reg}), and the length of the ionization event (i.e. length of the primary ion pulse) (t_p). The mass resolution of an instrument can be described as:

$$\frac{m}{\delta m} = \left[\frac{1}{R_{an}^2} + \frac{\delta t_{reg}^2 + \delta t_p^2}{c} \frac{1}{m} \right]^{-1/2} \qquad \text{(Eq. 2.4)}$$

where c is a constant dependent upon the length of the flight path and the secondary ion extraction voltage (from Stephan 2001).

For a given mass analyzer and detector, the mass resolution depends upon the length of the ionization event. Using shorter primary ion pulses will result in greater mass resolution. In theory mass resolutions of up ~10,000 are possible for the mass analyzer used in this research. However in practice, mass resolution was limited to 3000 – 4000. This may be due to several factors, including imperfect time-focusing of secondary ions in the reflectron, angular spread of secondary ions and the wide acceptance cone of the secondary ion extraction optics, or the topography of the sample.

Measurements can be performed using either a “normal” or “delayed” secondary ion extraction technique. In normal extraction the primary ions impact the sample whilst it is held at high potential. Secondary ions are extracted continuously for the duration of the primary ion pulse. High mass resolution is achieved using very short primary ion pulses (~2 – 3ns), which also lead to decreased secondary ion intensities.

In delayed secondary ion extraction, long primary ion pulses (~40ns) impact the sample whilst it is at ground potential. Secondary ions formed earlier in the pulse travel further from the sample than those formed towards the end. The sample

potential can then be switched on with an extremely fast rise-time (<10ns). This accelerates the secondary ions, with those formed earliest accelerated the least due to their greater height above the sample surface. The secondary ions are then time-focused at the detector by the two-stage reflectron. Delayed extraction enables high mass resolution and maintains useful secondary ion intensities. The longer pulse lengths of the primary ion beam also aid in obtaining high spatial resolution.

The use of delayed extraction creates mass fractionation across the secondary ion spectrum. During normal extraction the sample potential is on for the duration of the primary ion pulse. Under these conditions approximately every secondary ion of each mass is extracted into the TOF-analyzer and detected. In contrast, with delayed extraction the sample potential is switched on at the end of each primary ion pulse. The secondary ions therefore have a period of time in which they can become dispersed above the sample. Those no longer below the extraction cone are not extracted and detected. The result is that a smaller percentage of the lighter ions, which travel faster and become more dispersed, are extracted relative to heavier ions. The effects of this are discussed in Chapter 3.

When the achievable mass resolution is insufficient to resolve interferences, a peak deconvolution technique, such as that described by Stephan (2001), may be applied. This involves using an unperturbed isotope of the element that requires separation as an internal standard peak. For example, to separate the hydride peak $^{24}Mg^{1}H^{+}$ from $^{25}Mg^{+}$, the $^{24}Mg^{+}$ peak shape can be used as the internal standard. The peak is fitted to the low mass edge of the spectrum at 25amu. The $^{25}Mg/^{24}Mg$ isotopic ratio is given by the scaling factor between the two peaks.

2.1.4 Isotopic Ratios

Isotopic ratios are often given in the delta notation (δ). This shows the amount of deviation of the isotopic ratio in the sample compared to its known value in a standard. It is described as:

$$\delta\,(E) = \left[\frac{E_{\text{measured}}}{E_{\text{standard}}} - 1 \right] \times 1000 \qquad \text{(Eq. 2.5)}$$

where $\delta(E)$ is the isotope ratio in permil (‰), E_{measured} is the measured isotope ratio in the sample and E_{standard} the known isotope ratio of a standard.

As TOFSIMS collects an entire mass spectrum, it is possible to determine many isotopic ratios from a sample in a single analysis providing that interferences can be resolved. These isotopic ratios must, however, be corrected for mass fractionation.

Mass fractionation in a measurement is largely caused by the sputtering process. For any particular element in a sample its lighter isotopes will have weaker bonding energies than its heavier isotopes. When sputtered by high energy primary ions the lighter isotopes are more easily released from the sample surface. Also, for a given element's energy spectrum, the lighter isotopes will move faster than the heavier ones.

However, the situation is complicated by the matrix effect. The probability that a particular element is ionized during sputtering depends upon the chemical environment in which it is bound, the crystalline structure and orientation of a sample, and how the energy of the primary ions is dispersed within the sample. The relative ionization probabilities for different elements, and in some cases even different isotopes of the same element, can therefore vary significantly during analyses.

Further mass fractionation can also be caused in the instrument by variations in the transmission and detection efficiencies of secondary ion species.

To correct for mass fractionation it is necessary to measure a series of standards with well known isotopic compositions and similar in composition to the samples to be analyzed. Differences between the measured isotopic composition of the standard and the known values are attributed to mass fractionation effects. These deviations can then be used to correct isotopic ratios obtained from unknown samples.

In this study measured isotopic ratios were corrected for mass fractionation using the values of Henkel et al. (2007b), which provides a correction for a range of isotopic ratios based upon multiple analyses of several silicate standards.

2.1.5 Elemental Abundances

Due to matrix effects the ionization efficiency of any particular element varies for different sample types, making quantitative elemental abundances difficult to determine by SIMS.

In TOFSIMS it is most practical to determine elemental abundance ratios normalized to a reference element (usually Si). These ratios can be quantified using RSFs that are obtained by measuring standards with a known chemical composition as similar as possible to the sample to be analyzed. Standards must be very homogeneous and contain well known abundances of the elements of interest. RSFs can be expressed as:

$$RSF(E) = \frac{I(E)/I(E_{REF})}{A(E)/A(E_{REF})} \qquad \text{(Eq. 2.6)}$$

where E is the element of interest, E_{REF} the reference element, I the measured secondary ion intensity and A the atomic abundance in the standard.

Prior to measuring trace element abundances within presolar SiC grains in this study, an important step was to accurately determine RSFs for the elements of interest during analysis with Au^+ ions. This work is presented in Chapter 3.

Due to the lack of a SiC standard with a wide range of known trace element abundances, seven well characterized silicate standards were analyzed using Au^+ (along with Au_2^+ and Au_3^+) ions to obtain RSFs (relative to Si) for Li, B, O, Na, Mg, Al, K, Ca, Ti, V, Cr, Mn, Fe, Rb, Sr, Cs and Ba. These RSFs were used to calculate trace element abundances in analyzed presolar SiC grains. A SiC standard, for which only Al, Ca and Fe abundances are quantified, was also analyzed. The effects of using RSFs acquired from silicate and SiC materials to quantify trace element abundances in presolar SiC grains are discussed in Chapter 4.

2.1.6 Interstellar Dust Laser Explorer (IDLE3)

For this study a new TOFSIMS instrument, the *Interstellar Dust Laser Explorer (IDLE3)*, was used (Figure 2.4). This instrument was built within the Isotope Geochemistry and Cosmochemistry Group at the School of Earth, Atmospheric and Environmental Sciences, University of Manchester, U.K. Earlier versions of the instrument based upon the designs of Braun et al. (1998), were previously described by Henkel et al. (2006; 2007b).

IDLE3 is equipped with a 25kV Au_n^+ LMIG (Davies et al. 2003, Hill and Blenkinsopp 2004). A Wien filter allows a choice of primary ion species including Au^+, Au_2^+ and Au_3^+ (plus $AuGe^+$ and Ge^+ as the source is a Au:Ge alloy). Although not used in this study, the instrument also has a 5kV Ar/O duoplasmatron source and a fluorine excimer laser for post-ionization of secondary neutrals. Both ion sources were supplied by Ionoptika Ltd, Southampton, U.K.

The use of cluster ion species, such as Au_2^+ and Au_3^+, can produce significant secondary ion yield enhancements for high mass organic molecules (Benguerba et al. 1991, Davies et al. 2003). In Chapter 3 it is shown that Au_2^+ and Au_3^+ also boost secondary ion yields when analyzing inorganic samples but that this is counteracted by the lower primary ion currents achievable when using these primary ion species.

Secondary ions are extracted by biasing the sample stage from ground potential to 1400V. They are detected using a time-of-flight mass spectrometer (R-500 from Kore Technology, Ely, U.K.), consisting of a two-stage reflectron and a MCP detector biased to ±2.5kV for secondary ion post acceleration. The TDC has a time resolution of 250ps.

The LMIG can provide primary ion currents between 10pA to 10nA depending upon the primary ion species and aperture size selected. To obtain both high spatial resolutions and secondary ion intensities, all measurements of extra-terrestrial samples in this study were made using Au^+ primary ions through a

300µm aperture. This provided currents (DC) on the sample of ~1nA and a spatial resolution of ~0.5µm when the primary ion beam was pulsed.

Figure 2.4 highlights the main components of the IDLE3 instrument. Samples can be easily transferred and analyzed in the sample analysis chamber (SAC). The SAC is kept at pressures of ~10^{-9} mbar by an ion pump and Ti sublimation pump.

The LMIG can be operated in a direct-current (DC) mode. Sputtering with the DC-beam produces secondary electrons from the sample that can be used for imaging. Rastering the DC-beam over the sample can "clean" the sample surface. The subsequent removal of material allows depth-profiling through samples. There is an electron flood gun to compensate sample charging.

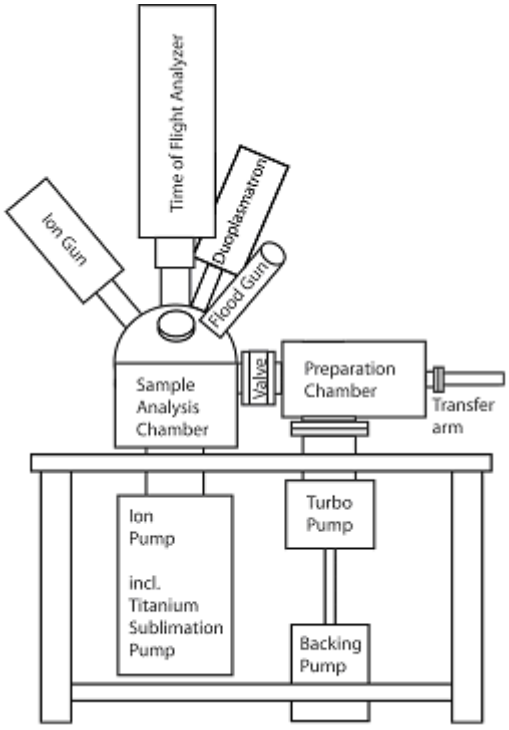

Figure 2.4 Sketch of IDLE3 highlighting its main components. Samples pass through the preparation chamber into the sample analysis chamber (SAC), where they can be bombarded by primary ions from the LMIG or duoplasmatron. Secondary ions are extracted into the time-of-flight analyzer (after Henkel et al. (2007b)).

2.1.7 Depth-Profiling

A major aim of this study is to determine the isotopic compositions and trace element distributions in presolar SiC grains using TOFSIMS. As IDLE3 had only

recently been built at the start of this research, time was spent developing a rigorous experimental procedure that could be used to analyze the grains. Initially this involved the measurement of silicate standards in order to calculate the RSFs needed to quantify elemental abundances in presolar SiC grains.

A depth-profiling technique was then tested in preparation for SiC analysis by applying it to a silicate grain (similar in size to presolar SiC grains) isolated from Murchison matrix material. Silicate grains were deposited upon cleaned (through ultrasonication in isopropanol and acetone) Au-foils and located using an ESEM, i.e. following the same procedure as that required to locate presolar SiC grains (see Chapter 4).

A DC-beam was rastered over a large area that included the silicate grain being analyzed, to remove hydrocarbons deposited on the sample surface and to also start sputtering into the grain. The sputter rate of Au^+ primary ions into silicate material was determined by sputtering a silicate glass with a known primary ion dose and measuring the depth of the resulting crater (see Chapter 3). Using this sputter rate, and by recording the primary ion beam current, the length of time the beam was applied and the field-of-view over which it was applied, it was possible to estimate the depth to which a grain had been sputtered. Although this estimate relies upon assuming sputter rates in silicate glass and SiC were similar, this was further calibrated by re-imaging grains that had been partially sputtered through using the ESEM.

Data was collected using a pulsed primary ion beam rastered over the silicate grain surface. The field-of-view over which the beam was rastered was set as small as possible so that the maximum amount of time was spent analyzing the grain. This meant that nearly all pixels in the resulting secondary ion image included mass spectra from the grain and not the surrounding Au-foil. The disadvantage was that any significant shift in the measurement could cause the grain to leave the field-of-view. Shifts could be caused by drifting of the sample stage or instabilities in the electronics moving the position of the primary ion beam. The size of the field-of-view was therefore often set slightly larger than the grain size to allow for this.

High mass resolution analyses were required to resolve interferences in the mass spectra. To maintain both high mass resolutions and the practical secondary ion intensities needed to measure trace elements in presolar SiC grains, long primary ion pulses combined with a delayed secondary ion extraction method were used (see Section 2.1.3).

After each SIMS measurement a grain was further sputtered using the DC-beam before the next measurement was started. This combination of sputtering with both the DC-beam and then the pulsed beam used for data collection, continuously removed material from the grain. Each grain was analyzed until it had been destroyed and a complete depth-profile had been obtained.

2.1.8 Data Processing

Data was acquired by rastering a pulsed primary ion beam over a field-of-view and collected using the "Bio-TOF" software (initially written by Nick Winograd, Penn State University, U.S.A., and since adapted by Andreas Wucher, University of Duisberg-Essen, Germany, and Torsten Henkel and Detlef Rost, University of Manchester, U.K.). In this software the number of pixels in each secondary ion image and the number of primary ion shots per pixel could be set. Each pixel in an image contained a complete mass spectrum and each image was recorded separately.

Data was processed offline using a combination of the "TOFCmd" software (written by Detlef Rost, University of Manchester, U.K.) and the "TSTSpec" software package (written by Thomas Stephan, University of Chicago, U.S.A.).

The secondary ion images were firstly loaded into TOFCmd. Each secondary ion frame was corrected for any shift due to stage movement, temperature changes or electronic instabilities that occurred during the measurement.

During a measurement the primary ion source emission could "drop-out", i.e. no primary ion current was hitting the sample so no secondary ion spectra were

collected during this time. The TOFCmd software could be used to remove any of these unwanted frames.

From the remaining frames a Region of Interest (ROI) was defined and only spectra from this area saved as an Ascii.txt file that could be opened in TSTSpec. When analyzing presolar SiC grains the application of a ROI ensured that no background signal from the Au-foil contributed to the grain spectrum.

In TSTSpec the mass spectrum was analyzed. A mass calibration was performed using well known undisturbed peaks such as $^{23}Na^{+}$. Each peak in the mass spectrum was assigned to a mass and the peak integral was corrected for background contribution by selecting areas left and right of the peak.

A dead time correction (~40ns, Stephan et al. 1993, Stephan 2001) was applied to account for the non-detection of secondary ions arriving in quick succession after another counted ion; an effect created by the response time of the mass spectrometer.

Measured isotopic and elemental abundance ratios were then extracted from TSTSpec for mass fractionation corrections and application of RSFs. If peak deconvolution techniques were required these could also be performed at this stage.

2.2 NanoSIMS

The recent development of the Cameca NanoSIMS ion probe has led to rapid progress in the field of cosmochemistry due to high spatial resolutions and high secondary ion transmission (for a review see Hoppe 2006). The NanoSIMS has been applied to a wide variety of extra-terrestrial samples including meteoritic matrix components (e.g. Mostefaoui et al. 2000, Bland et al. 2007, Ito and Messenger 2008, Remusat et al. 2009), presolar grains (e.g. Besmehn and Hoppe 2003, Zinner et al. 2003, Nguyen and Zinner 2004, Hoppe et al. 2010), IDPs (e.g. Floss et al. 2006, Busemann et al. 2009) and samples returned by the Stardust mission (e.g. McKeegan et al. 2006, Stadermann et al. 2008). Here, it has been used to determine the isotopic composition of the amorphous carbonaceous grains discussed in Chapter 5. The NanoSIMS is a commercial instrument and there are now several located at institutions across the world, including the Open University, U.K.

Like TOFSIMS, ion probes, such as the NanoSIMS, use a finely focused high energy primary ion beam to produce secondary ions from a sample surface. During ion microprobe analysis the primary ion beam is constantly applied to the sample (i.e. it is not pulsed) resulting in higher signal rates and better precision than can be achieved with TOFSIMS. The disadvantage of ion microprobes is that only several isotopic species of interest can be analyzed simultaneously so not all information can be obtained from a sample.

The NanoSIMS has two primary ion sources: a Cs^+ surface ionization source that can provide spot sizes on the sample of ~50nm, and an O^- duo-plasmatron source. Secondary ions are extracted away from the sample surface with electric fields towards a double-focusing mass spectrometer.

Isotopic species of interest are separated by the double-focusing magnetic sector mass spectrometer and then detected using electron multipliers. The NanoSIMS at the Open University is equipped with seven electron multipliers (six of which have adjustable positions) for detecting secondary ion signals. There is also a

photomultiplier for secondary electron imaging and several Faraday cups (not used in this study) for high precision measurements.

The NanoSIMS provides significantly improved spatial resolutions and secondary ion yields at high mass resolutions over older generations of ion probes (e.g. the Cameca IMS-3f). These improvements in the NanoSIMS are largely due to the co-axial design of the primary and secondary ion beams.

Figure 2.5 shows that in the NanoSIMS the primary ion beam impacts the sample with a normal angle of incidence. This allows the immersion lens of the NanoSIMS, which focuses the primary ion beam and collects the secondary ions, to be placed much closer to the sample surface than in previous ion probes. Smaller spot sizes are achievable, whilst focusing of the secondary ion beam takes place earlier. This decreases the energy spread of the secondary ions and leads to higher mass resolutions.

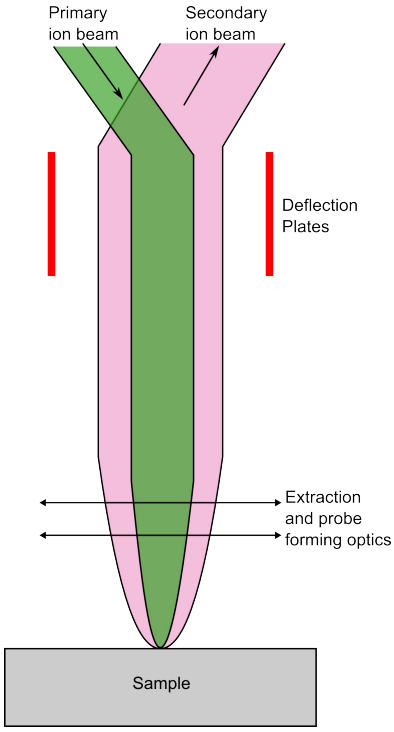

Figure 2.5 Schematic diagram of the co-axial design of the NanoSIMS. The primary ion beam impacts the sample at a normal angle of incidence, allowing the extraction optics to be placed closer to the sample surface (after Davidson (2010)).

Achievable mass resolutions for the NanoSIMS are $m/\delta m$ ~6000 making it suitable for determining the $^{2}D/^{1}H$, $^{13}C/^{12}C$, $^{15}N/^{14}N$ and $^{18}O/^{16}O$ ratios required in this work.

Analyses can be made either as spot measurements or by rastering the primary ion beam over a selected area. The field-of-view, number of pixels in each image and the number of scans acquired can be adjusted according to the requirements for the sample being analyzed. Secondary ion maps for each isotopic species analyzed are recorded for offline analysis. Full details of NanoSIMS measurements made as part of this study are provided in Chapter 5.

NanoSIMS data was processed using the "L'IMAGE" software (written by Larry Nittler, Carnegie Institution, U.S.A). In the software it is possible to remove anomalous scans, monitor secondary ion count rates over an entire measurement, combine all secondary ion images to give a total integrated image and calculate isotopic ratios and ratio images. Dead time corrections (~44ns) can be made and a shift correction applied to each individual scan. Davidson (2010) reported typical shifts in both the x and y directions of ~200nm during analyses lasting approximately one hour. The ROI of each image can be defined so that only "useful" spectra are used to calculate isotopic ratios.

As with TOFSIMS, isotopic ratios must be corrected for mass fractionation caused by factors such as differential sample sputtering, variations in transmission and the detection efficiencies of electron multipliers. Again this is done by measuring known standards that have well characterized isotopic ratios and are as similar as possible to the sample being analyzed. The analyses of standards and the mass fractionation corrections applied for NanoSIMS measurements in this study are fully described in Chapter 5.

2.3 ENVIRONMENTAL SCANNING ELECTRON MICROSCOPE (ESEM)

To obtain high resolution images of samples in this study it was necessary to use a SEM. The instrument used was a Phillips XL30 ESEM based in the School of Earth, Atmospheric and Environmental Sciences at the University of Manchester. It is equipped with detectors for secondary electrons, back scattered electrons (BSE) and energy dispersive X-ray (EDX) analysis. Although not used in this study the ESEM also has a cryo-stage and is able to operate at low vacuum pressures to enable analysis of biological samples.

A high energy electron beam focused onto the surface of a sample causes the release of secondary electrons and characteristic X-rays. Using differences in electric potential the secondary electrons can be directed towards a detector and used to produce secondary electron images of the sample. It is possible to achieve spatial resolutions of a few nanometres. Electrons from the beam may also be back-scattered by the sample and can be used to produce BSE images.

When the primary electron beam hits an atom within the sample it can eject an electron from the inner shell. An electron from a higher energy shell will "fall back" to fill this space, with the release of an X-ray. As the energy of these X-rays is characteristic of the atomic structure from which they originated (i.e. it represents the difference in energy between the two electron shells), energy dispersive X-ray analysis can provide quantitative elemental compositions of samples.

With the ESEM, EDX analysis was routinely used to determine the elemental composition of candidate presolar SiC grains and gently separated carbonaceous grains. High resolution images of all the grains of interest were acquired prior to any analyses. Often images of a grain were also recorded to show the effects of a particular analytical technique i.e. after TOFSIMS sputtering or Raman measurements. Electron beam energies during imaging and EDX analysis were kept low, typically 10 – 15kV, in order to minimise damage of the sample surface.

2.4 RAMAN SPECTROSCOPY

Raman spectroscopy can be used to determine the molecular structure of a sample. In cosmochemistry it has been used to study the nature of carbonaceous chondrites (Quirico et al. 2003; 2009, Matrajt et al. 2004, Bonal et al. 2006; 2007, Busemann et al. 2007), IDPs (Wopenka 1988, Muñoz Caro et al. 2006, Busemann et al. 2009, Davidson 2010) and cometary material (Muñoz Caro et al. 2008, Rotundi et al. 2008). As it is a relatively non-destructive technique, analyses may be combined with other analytical measurements. Here, Raman spectroscopy has been employed to characterize the crystalline structure of gently separated carbonaceous grains.

In Raman spectroscopy a laser is used to excite the sample surface. Photons of the fundamental laser frequency interact with vibrational modes of molecular bonds or crystal lattices producing inelastically scattered photons. These photons can be detected, with the interactions causing their energy to be shifted either up or down. Raman band positions are therefore given as shifts relative to the wavelength of the exciting laser. Raman analyses in this study were undertaken using a Horiba Scientific LabRAM 300 Raman microscope with a 632nm He:Ne exciting laser at the School of Chemical Engineering and Analytical Science, University of Manchester, U.K. The spectral resolution was ~1 – 2Δcm^{-1}.

Raman spectroscopy is a particularly useful tool for studying carbonaceous materials (e.g. Wopenka and Pasteris 1993). Raman spectra from carbon rich samples are dominated by two bands; the D ("disordered") and G ("graphitic") bands, which occur at positions of 1355cm^{-1} and 1581cm^{-1} respectively. The relative intensities of the bands, plus their central peak positions and peak widths provide information regarding the structural order of the carbon in the sample. For example, pure graphite only produces the G-band. The D-band is created by defects, crystal boundary effects, polycrystallinity and small domain sizes. An increase in D-band intensity is therefore an indication of increasing disorder within the carbon structure. If the carbon is significantly disordered then there is also a broadening of both the D and G band peak widths, while the presence of amorphous carbon causes the D and G bands to merge together. Figure 2.7 shows

examples of Raman spectra from crystallized graphite, through increasingly disordered, to finally amorphous carbon.

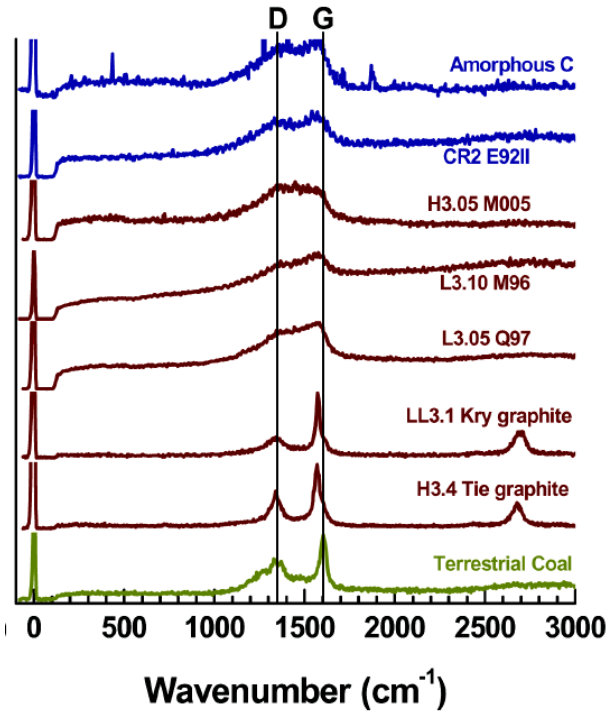

Figure 2.6 Raman carbon spectra of fragments of IOM from a selection of primitive chondrites, amorphous carbon and terrestrial coal. The carbon spectra become increasingly ordered from top to bottom (from Busemann et al. (2007)).

Collected Raman spectra were fitted using the Lorentzian profiles for the Raman D and G bands described by Busemann et al. (2007). Cosmic-rays hitting the detector during a measurement produced spikes in the Raman spectra that could be corrected for during the fitting procedure. Fluorescence can also be an issue in Raman studies and leads to steep, irregularly shaped backgrounds. In some cases fluorescence in the spectra prevented reliable fitting of the Raman band parameters and these spectra were excluded.

2.5 FOCUSED ION BEAM (FIB) AND TRANSMISSION ELECTRON MICROSCOPY (TEM)

TEM was used to investigate the internal structure of three carbonaceous grains and obtain very high resolution images of the grain cores. TEM requires that samples are electron transparent i.e. samples are thin enough for electrons to pass through them. It was therefore not possible to use TEM on grains and they instead had to be prepared as thin sections. These sections were produced using a Focused Ion Beam (FIB) system. Both FIB and TEM techniques were performed at the University of Glasgow, U.K.

In recent years FIB techniques have become widely used to prepare samples in cosmochemistry including presolar grains (e.g. Stroud et al. 2002; 2003, Stroud and Bernatowicz 2005), IDPs (e.g. Graham et al. 2008, Busemann et al. 2009) and meteoritic matrix components (e.g. Zega et al. 2007). Often a sample prepared using a FIB system is suitable for combined TEM/NanoSIMS/synchrotron studies. For a review of the FIB technique and its applications see Wirth (2004) and Lee (2010).

The grains were prepared as thin sections using an FEI Nova 200 DualBeam FIB system. As a DualBeam system this instrument is equipped with both an electron gun, for secondary electron imaging of the process, and a 30kV Ga^+ ion gun. The Ga^+ ion gun is primarily for the milling and polishing of samples but can also be used for sample imaging. There is also a platinum source gas injection system, which is used to coat samples in order to protect them from sputtering by the ion beam. The procedure used to cut the grains was as follows;

1. Deposition of Pt-strap on the grain surface. Due to the geometric nature of the grains there was a shadowing effect. Platinum was poorly deposited between the grain and the substrate on the grain side furthest from the direction in which the Pt was injected. This problem was overcome by rotating the sample so that the grain experienced similar levels of Pt deposition on both sides.

2. 30kV Ga^+ ion beam used to mill a trench on either side of the Pt-strap (destroying the uncoated sections of the grain). This produced a section through the grain approximately 0.5 – 1μm thick.

3. Section tilted to an angle of ~45° to the ion beam allowing it to be cut free at the base and along one edge.

4. Mo-needle welded to the Pt-strap on the side of the section not previously cut with the ion beam. Once the needle was securely attached this edge could also be cut free and the section lifted out and transported to a Cu TEM grid. It was then welded to the grid and the needle was cut free from the section.

5. Ion beam used to polish the section down to a thickness of ~100 – 200nm. Sputtering with the high energy ion beam can damage the sample and potentially lead to amorphization of its surface. The final polishing steps were therefore carried out using a 5kV ion beam to remove any "damaged" sample material.

An FEI Tecnai T20 TEM with a 200kV LaB_6 electron source and Gatan image filter was used to study the sections. TEM works by transmitting a beam of electrons through very thin samples to produce an image. Owing to the shorter wavelengths of electrons relative to photons it is possible to achieve image resolutions of a few angstroms.

Images were obtained using the bright field mode. Regions in the sample consisting of material of a higher atomic number, or which are thicker than others, transmit fewer electrons and therefore appear darker in the images. Electrons interacting with the sample also undergo Bragg scattering. It is therefore possible to obtain selected-area electron-diffraction (SAED) patterns from the sample. Crystalline materials produce characteristic diffraction patterns that can provide information regarding their internal structure. Diffraction patterns from crystalline and poly-crystalline materials are typically comprised of series of dots and rings, lacking in those from amorphous materials.

Chapter 3

Determination of relative sensitivity factors during secondary ion sputtering of silicate glasses by Au^+, Au_2^+ and Au_3^+ ions

Ashley King[1], Torsten Henkel[1], Detlef Rost[1], and Ian C. Lyon[1]

[1]The University of Manchester, School of Earth, Atmospheric and Environmental Sciences, Oxford Road, Manchester, M13 9PL, UK.

Adapted from: King A., Henkel T., Rost D. and Lyon I.C. (2010) Determination of relative sensitivity factors during secondary ion sputtering of silicate glasses by Au^+, Au_2^+, and Au_3^+ ions, *Rapid Communications in Mass Spectrometry* **24**; 15-20.

In recent years, Au-cluster ions have been successfully used for organic analysis in secondary ion mass spectrometry. Cluster ions, such as Au_2^+ and Au_3^+, can produce secondary ion yield enhancements of up to a factor of 300 for high mass organic molecules with minimal sample damage. In this study, the potential for using Au^+, Au_2^+, and Au_3^+ primary ions for the analysis of inorganic samples is investigated by analyzing a range of silicate glass standards. Practical secondary ion yields for both Au_2^+ and Au_3^+ ions are enhanced relative to those for Au^+, consistent with their increased sputter rates. No elevation in ionization efficiency was found for the cluster primary ions. Relative sensitivity factors for major and trace elements in the standards showed no improvement in quantification with Au_2^+ and Au_3^+ ions over the use of Au^+ ions. Higher achievable primary ion currents for Au^+ ions compared to Au_2^+ and Au_3^+ allow for more precise analyses of elemental abundances within inorganic samples, making them the preferred choice, in contrast to the choice of Au_2^+ and Au_3^+ for the analysis of organic samples. The use of delayed secondary ion extraction can also boost secondary ion signals, although there is a loss of overall sensitivity.

3.1 INTRODUCTION

The need for high spatial resolution analysis of biological materials has driven the development of primary ion sources that can deliver enhanced molecular secondary ion yields. One such example is the Au-cluster source, where Au_2^+ and

Au_3^+ ions have been shown to produce secondary ion yield enhancements for heavy organic molecules (Benguerba et al. 1991, Davies et al. 2003). In particular, Au_3^+ ions may produce high mass secondary ion yield enhancements of up to a factor of 60 relative to Au^+ ions, and a factor of 300 relative to Ga^+ (Davies et al. 2003) In most cases these increases can be attributed to the higher sputter yields achieved with Au-cluster ions, although for some samples increased ionization efficiency may play a role (Winograd 2005, Wucher 2006).

In order to utilize Au-cluster ion sources for inorganic analyses, an understanding of the sputtering and ionization process during Au^+, Au_2^+, and Au_3^+ measurements of such samples is required. This includes determining sputter rates, practical secondary ion yields (number of secondary ions per primary ion), and the effects of increased secondary ion cluster formation under Au-cluster bombardment.

Accurate quantification of elemental abundances in secondary ion mass spectrometry (SIMS) can be difficult to achieve as the composition and crystal structure of a sample can cause variations in sputter rates and secondary ion yields, the so-called matrix effect (Benninghoven et al. 1987, Wilson et al. 1989). It is therefore necessary to analyze standards of similar chemical composition and known elemental abundances to determine sensitivity factors relative to a major element. These relative sensitivity factors (RSF) may be expressed as:

$$RSF(E) = \frac{I(E)/I(E_{REF})}{A(E)/A(E_{REF})} \qquad \text{(Eq. 3.1)}$$

where E is the element of interest, E_{REF} the reference element, I the measured secondary ion intensity and A the atomic abundance in the standard.

We have measured seven silicate glass standards: six MPI-DING standards, prepared by Jochum et al. (2000; 2006), and a NIST glass, SRM 610, in order to determine practical secondary ion yields and RSFs for a range of major and trace elements when using Au-cluster SIMS. As the abundances of Li, Mg, V, Cr, Cs, and Ba are not included on the original NIST certificate for SRM 610, these were

instead taken from Pearce et al. (1997). Sputter rates for Au^+, Au_2^+, and Au_3^+ ions have also been determined using standard SRM 610.

3.2 EXPERIMENTAL PROCEDURE

The standards were prepared as thin sections mounted in resin on two glass slides. One slide contained MPI-DING standards KL2-G (Kilauea tholeiitic basalt glass), ATHO-G (Iceland rhyolite glass), and T1-G (Italian Alps quartz diorite glass). The other contained standards GOR132-G (Gorgona Island komatiite glass), StHs6/80-G (St. Helens andesitic ash glass), ML3B-G (Mauna Loa tholeiitic basalt glass), and NIST glass SRM 610 (quartz glass matrix containing ~500ppm of 61 elements).

Standards were coated with a ~20nm layer of gold to ensure uniform electrical potential at the sample surface. Prior to analysis, a 1.1nA direct current (DC)-beam was applied to large areas (up to 200μm × 200μm) of the standard to firstly sputter through this coating, and secondly to ensure that the analyzed area was in sputter equilibrium.

For this study a new time-of-flight secondary ion mass spectrometry (TOFSIMS) instrument, built to the same design as our previously described *Interstellar Dust Laser Explorer (IDLE)* was used (Henkel et al. 2006; 2007b, see Chapter 2). This new instrument is equipped with a 25kV Au_n^+ liquid metal ion gun (LMIG) constructed by Ionoptika Ltd (IOG 25Au) (Davies et al. 2003, Hill and Blenkinsopp 2004).

The primary ion species were selected by mass using a Wien filter. Each standard was analyzed with Au^+, Au_2^+, and Au_3^+ ions with nominal currents (DC) of 1.1nA, 0.13nA, and 0.094nA, respectively. The secondary ions were detected using a time-of-flight mass spectrometer (R-500 from Kore Technology), consisting of a two-stage reflectron and micro-channel plate detector (MCP) with secondary ion post-acceleration of 2.4kV.

Sputter rates for Au-cluster ions in silicate glasses were determined by using DC beams of Au^+, Au_2^+, and Au_3^+ to sputter uncoated 20µm × 20µm areas on SRM 610. The primary ion (PI) dose for the Au^+ beam was 9.36×10^{16} PI/cm^2 (beam applied for 45s). For Au_2^+ the dose was 2.96×10^{16} PI/cm^2 (120s) and for Au_3^+ it was 5.43×10^{16} PI/cm^2 (300s). The depths of the resulting craters were measured using an atomic force microscope (AFM).

SIMS measurements involved rastering a pulsed primary ion beam over 20µm × 20µm areas and recording each scan separately. These scans contained 128 × 128 pixels, with 30 primary ion shots per pixel and each pixel containing a complete mass spectrum.

High mass resolution (*m/δm ~3000*) was achieved by using "delayed extraction". Here, primary ion pulses, ~40ns long, hit the sample whilst it is at ground potential. Secondary ions formed early in the pulse travel further from the sample than those formed at the end. The sample potential is then switched to 1.5kV at ~60ns after the start of the primary ion pulse. The secondary ions are accelerated towards the extractor, with those formed earliest being accelerated the least as they are now at a lower potential relative to earth. The secondary ions are then time-focused at the detector using the two-stage reflectron. Using delayed extraction therefore allows high mass resolutions to be achieved despite using long primary ion pulses in order to boost secondary ion count rates. Longer pulse lengths also provide better spatial resolution for analyses as this normally deteriorates slightly when the primary ion beam is switched rapidly to produce very short pulses.

Disadvantages of the delayed extraction technique may include fractionation between different masses, along with varying peak-shapes and a change in mass resolution over the mass range. Therefore all standards, except T1-G and SRM 610, were also measured using Au^+ ions and "normal extraction". Here, primary ions hit the sample in short time pulses (~2 – 3ns), with the sample already at high potential. Secondary ions are continuously extracted for the duration of the primary ion pulse.

RSFs for Au^+, Au_2^+, and Au_3^+ using delayed extraction, as well as Au^+ with normal extraction were calculated according to Eq. 3.1, with Si used as the reference element. Measurements using Au_2^+ and Au_3^+ with normal extraction were not made due to much lower secondary ion signals and hence the long measurement times required. In some instances, several locations on the same standard were analyzed (marked in Tables 3.2 – 3.4 with *). In such cases, the presented RSFs for these standards are geometric means of those measurements.

3.3 RESULTS

The depths of the craters produced by DC sputtering of SRM 610 were 28 ± 5nm for Au^+, 21 ± 3nm for Au_2^+, and 33 ± 3nm for Au_3^+. These give sputter rates in silicate glass of 0.30 ± 0.05nm for 10^{15} PI/cm^2 for Au^+, 0.71 ± 0.11nm for Au_2^+, and 0.61 ± 0.05nm for Au_3^+.

Cluster ion sources are known to produce an increase in cluster secondary ion formation, which lowers the number of atomic secondary ions detected (Sun et al. 2005, Henkel et al. 2009). As the standards consist mainly of Si it may be expected that more Si-cluster ions will form compared to minor elements, when sputtered with Au_2^+ and Au_3^+ ions.

The total fraction of Si-ions detected as $^{28}Si^+$ (reference element for the RSFs) decreased with increasing Au-cluster size (Table 3.1). The decrease was a factor of 1.52 ± 0.29 (1σ) between Au^+ and Au_2^+, and 1.84 ± 0.34 (1σ) between Au^+ and Au_3^+ and can be attributed to the observed increase in Si present as Si-cluster ions (Si_n^+), oxides and hydroxides. Most other elements also formed more clusters in the Au_2^+ and Au_3^+ spectra, although the effects were less significant (Table 3.1).

Table 3.1 also contains practical secondary ion yields (number of secondary ions per primary ion) for major elements (Na, Mg, Al, Si, K, Ca, Ti, V, Cr, Mn, and Fe), determined from analyses of KL2-G with Au^+, Au_2^+, and Au_3^+ ions. As each element in the standard has a different concentration (e.g. Si is much more abundant than other elements), practical secondary ion yields have been normalized by each element's atomic percent abundance in the standard.

Figure 3.1 shows the practical secondary ion yields for Au_2^+ and Au_3^+ relative to those for Au^+ (corrected values from Table 3.1), versus the first ionization energy (FIE) of the major elements. The data have also been corrected in order to take into account the increased presence of cluster secondary ions for each element when using Au_2^+ and Au_3^+ (i.e. for Si this correction is a factor of 1.52 ± 0.29 for Au_2^+ and 1.84 ± 0.34 for Au_3^+, see above). On average, the practical secondary ion yields increased by a factor of 2.16 ± 0.28 for Au_2^+, and 2.58 ± 0.81 for Au_3^+, relative to Au^+.

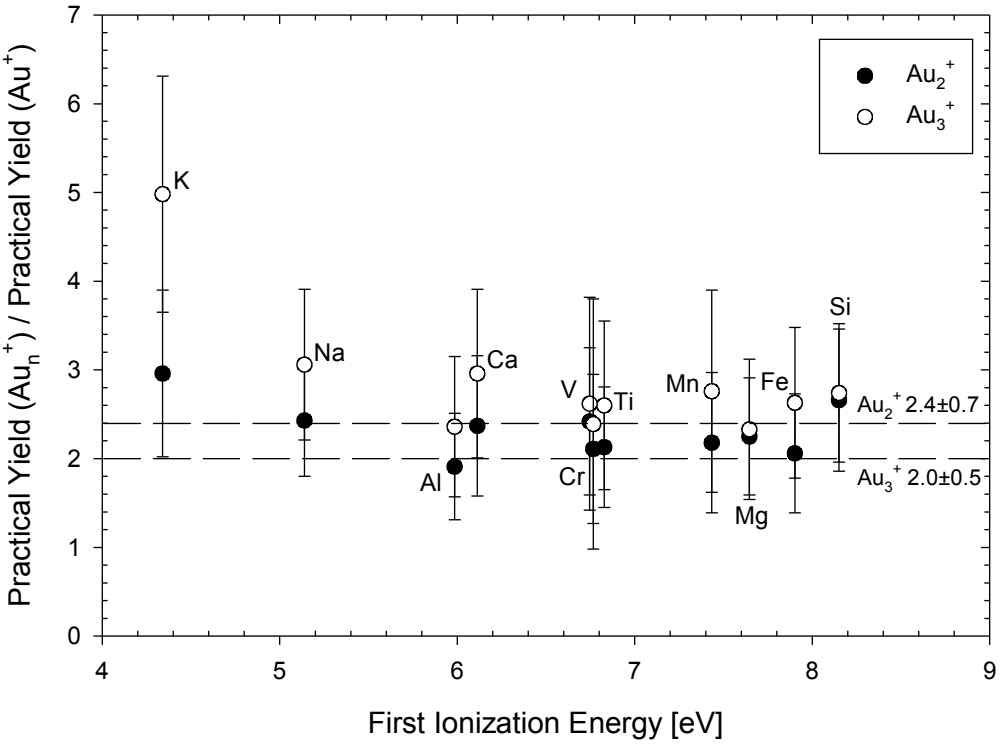

Figure 3.1 Practical secondary ion yields for Au_2^+ and Au_3^+ (relative to Au^+) versus FIE. The data for each element have been corrected for the increased presence of cluster secondary ions when using Au_2^+ and Au_3^+. Dashed lines and associated values represent the relative increase in sputter rate measured for Au_2^+ and Au_3^+ ions. Error bars are 1σ.

Tables 3.2 – 3.5 list RSFs for all standards analyzed using Au^+, Au_2^+, and Au_3^+ ions and delayed extraction, and Au^+ ions with normal extraction. Geometric means have been calculated for each data set as they are more suitable for ratios, such as the RSFs. Geometric standard deviations are also provided (both absolute and relative values) and reflect the variability of RSFs across the measured standards.

In Tables 3.2 – 3.5, RSFs deviating more than 3σ from the geometric mean of a data set were considered to be potentially anomalous. Reasons for such anomalous data are described below and, if appropriate, these outliers were excluded from that particular data set and were not used to calculate RSFs.

In Table 3.2, anomalous values for Na, Al, K, and Ca were all associated with the measurement of standard StHs6/80-G. Secondary ion images of this standard show that all four elements were heterogeneously distributed relative to Si within the measured area. Therefore, all data for these elements acquired from this standard have subsequently been excluded.

An anomalous RSF value also occurred for the Au^+ measurement of Sr in SRM 610 (Table 3.2). Strontium was not found to be heterogeneous within the measured area, nor were molecular interferences apparent in the mass spectrum. The anomalous value is therefore unexplained and has been retained in the data set.

RSFs for the major elements during delayed extraction displayed little variation across the standards when analyzed with Au^+ ions (Table 3.2). Relative standard deviations for most of these elements ranged between 10 – 40%. Titanium was an exception with a slightly higher relative standard deviation of 69%. Under normal extraction conditions the relative standard deviations for most of these elements were between 10 – 78% (although Na had a relative standard deviation up to 169%, see Table 3.3).

The trace elements (Li, B, Rb, Sr, Cs, and Ba), by definition, are found in lower abundances within the standards. The relative standard deviations for trace element RSFs from Au^+ ions with delayed extraction were between 19 – 182%. However, most elements (Rb, Sr, Cs, and Ba) were actually between 19 – 60%. Using normal extraction, most trace elements were between 26 – 86% (while Li and Rb extended this range up to 215%).

Table 3.1 Practical secondary ion yields (number of secondary ions/number of primary ions) from Au^+, Au_2^+, and Au_3^+ analysis of KL2-G. Each practical yield has been normalized by the elements atomic percent abundance in the standard. The Au_n^+/Au^+ ratios for each element have also been corrected for the increased presence of cluster secondary ions when using Au_2^+ and Au_3^+. Errors are 1σ.

	Au^+ ($\times10^{-5}$)	Au_2^+ ($\times10^{-5}$)	Au_3^+ ($\times10^{-5}$)	Au_2^+/Au^+	Cluster ions	Corrected value	Au_3^+/Au^+	Cluster ions	Corrected value
Na	469 ± 22	1130 ± 51	1420 ± 59	2.41 ± 0.22	1.01 ± 0.17	2.43 ± 0.63	3.03 ± 0.27	1.01 ± 0.19	3.06 ± 0.85
Mg	66.1 ± 3.3	136 ± 6	133 ± 5	2.06 ± 0.19	1.09 ± 0.22	2.25 ± 0.66	2.01 ± 0.18	1.16 ± 0.29	2.33 ± 0.79
Al	129 ± 7	244 ± 12	245 ± 11	1.89 ± 0.20	1.01 ± 0.21	1.91 ± 0.60	1.90 ± 0.19	1.24 ± 0.29	2.36 ± 0.79
Si	27.6 ± 1.5	48.4 ± 2.5	41.1 ± 1.9	1.75 ± 0.19	1.52 ± 0.29	2.66 ± 0.80	1.49 ± 0.15	1.84 ± 0.34	2.74 ± 0.78
K	1400 ± 72	3880 ± 198	6460 ± 306	2.77 ± 0.28	1.07 ± 0.23	2.96 ± 0.94	4.61 ± 0.46	1.08 ± 0.18	4.98 ± 1.33
Ca	154 ± 8	345 ± 19	435 ± 22	2.24 ± 0.24	1.06 ± 0.24	2.37 ± 0.79	2.82 ± 0.29	1.05 ± 0.23	2.96 ± 0.95
Ti	68.1 ± 3.9	143 ± 8	169 ± 9	2.09 ± 0.24	1.02 ± 0.21	2.13 ± 0.68	2.48 ± 0.27	1.05 ± 0.27	2.60 ± 0.95
V	66.8 ± 4.5	158 ± 14	172 ± 23	2.37 ± 0.37	1.02 ± 0.19	2.42 ± 0.83	2.57 ± 0.52	1.02 ± 0.26	2.62 ± 1.20
Cr	74.3 ± 7.7	152 ± 14	166 ± 41	2.05 ± 0.40	1.03 ± 0.21	2.11 ± 0.84	2.23 ± 0.78	1.07 ± 0.26	2.39 ± 1.41
Mn	63.3 ± 3.8	134 ± 9	168 ± 13	2.12 ± 0.27	1.03 ± 0.24	2.18 ± 0.79	2.65 ± 0.36	1.04 ± 0.29	2.76 ± 1.14
Fe	45.4 ± 2.6	92.6 ± 5.5	117 ± 7	2.04 ± 0.24	1.01 ± 0.21	2.06 ± 0.67	2.58 ± 0.30	1.02 ± 0.21	2.63 ± 0.85

Table 3.2 RSFs for Au^+ ions obtained using delayed extraction. All elements were measured as positive secondary ions. Data used to calculate geometric means is shown in bold. For reasons of exclusion see text. nd indicates insufficient counts in the mass spectrum and * indicates standards analyzed in more than one location, so given values are the geometric means.

	Li	B	O	Na	Mg	Al	Si	K	Ca	Ti	V	Cr	Mn	Fe	Rb	Sr	Cs	Ba
KL2-G	**0.68**	**2.36**	**0.00098**	**16.39**	**2.85**	**4.35**	**1**	**53.09**	**5.46**	**3.10**	**2.57**	**2.51**	**2.19**	**1.67**	**54.40**	**4.12**	nd	**3.85**
ATHO-G	**1.23**	**1.85**	**0.00045**	**18.97**	**4.75**	**5.97**	**1**	**37.55**	**10.00**	**5.87**	**2.62**	**4.33**	**3.37**	**2.07**	**54.15**	**5.22**	**9.39**	**3.05**
T1-G	**3.96**	**3.23**	**0.00065**	**23.67**	**3.28**	**5.21**	**1**	**62.44**	**7.78**	**3.79**	**3.08**	**2.99**	**3.09**	**2.28**	**32.46**	**5.37**	**32.35**	**2.98**
GOR132-G*	**21.64**	**2.05**	**0.00094**	**40.78**	**5.05**	**4.90**	**1**	**72.95**	**9.50**	**4.00**	**3.02**	**3.20**	**2.79**	**1.89**	nd	nd	**24.43**	nd
StHs6/80-G	**4.67**	nd	**0.00069**	338.35	**5.17**	20.43	**1**	427.68	60.32	**4.06**	**3.13**	**3.66**	**2.26**	**1.40**	**27.59**	**4.85**	**22.79**	**2.72**
ML3B-G*	**5.70**	**7.87**	**0.00092**	**21.44**	**4.47**	**4.90**	**1**	**41.24**	**7.37**	**3.27**	**3.14**	**4.07**	**2.79**	**1.93**	**50.41**	**4.75**	nd	**4.54**
SRM 610	**4.64**	**0.85**	**0.0013**	**28.90**	**4.99**	**5.87**	**1**	**45.93**	**13.85**	**4.08**	**5.87**	**5.50**	**3.40**	**4.44**	**67.38**	**16.75**	**19.31**	**4.76**
Geometric Mean	3.66	2.41	0.00081	23.89	4.27	5.17	1	50.81	8.63	3.95	3.22	3.64	2.81	2.10	45.57	5.95	20.08	3.57
Lower Stdev	2.36	1.17	0.00023	6.14	0.84	0.54	0	10.48	2.16	0.69	0.73	0.78	0.42	0.60	12.28	2.23	6.82	0.69
Upper Stdev	6.66	2.28	0.00031	8.26	1.05	0.60	0	13.21	2.88	0.83	0.94	1.00	0.50	0.85	16.81	3.57	10.33	0.86
Rel Lower Stdev (%)	65	49	28	26	20	10	0	21	25	21	23	21	15	29	27	38	34	19
Rel Upper Stdev (%)	182	95	39	35	25	12	0	26	33	69	29	27	18	40	37	60	51	24

Table 3.3 RSFs for Au^+ ions using normal extraction (see Table 3.2 for details of data presentation).

	Li	B	O	Na	Mg	Al	Si	K	Ca	Ti	V	Cr	Mn	Fe	Rb	Sr	Cs	Ba
KL2-G	**9.16**	**6.95**	**0.0013**	**17.33**	**3.09**	**4.67**	**1**	**41.53**	**4.72**	**2.60**	**2.37**	**2.35**	**1.52**	**1.46**	**30.86**	**2.73**	nd	**1.58**
ATHO-G	**5.00**	**3.65**	**0.0013**	**6.38**	**6.53**	**4.98**	**1**	**15.51**	**6.15**	**2.63**	**6.13**	**7.52**	**2.29**	**1.65**	**7.84**	**3.06**	**27.38**	**1.41**
GOR132-G*	**85.33**	**1.40**	**0.0015**	**76.70**	**7.79**	**6.11**	**1**	**56.61**	**9.34**	**3.56**	**4.41**	**3.23**	**1.85**	**1.51**	nd	nd	**30.54**	nd
StHs6/80-G	**22.32**	nd	**0.0013**	113.99	**4.64**	4.65	**1**	103.60	4.31	**1.56**	**1.79**	**1.94**	**0.91**	**0.76**	**9.71**	**1.40**	**7.79**	**0.59**
ML3B-G	**84.01**	**4.20**	**0.0011**	**57.23**	**8.53**	**6.96**	**1**	**70.28**	**12.14**	**2.54**	**3.17**	**4.28**	**1.97**	**1.10**	**45.40**	**2.59**	nd	**1.85**
Geometric Mean	23.60	3.49	0.0013	26.39	5.74	5.61	1	40.01	7.57	2.49	3.25	3.43	1.63	1.25	18.07	2.35	18.67	1.25
Lower Stdev	16.10	1.54	0.00013	16.60	1.79	0.83	0	17.57	2.32	0.58	1.15	1.30	0.45	0.31	9.49	0.61	8.63	0.45
Upper Stdev	50.68	2.75	0.00015	44.72	2.59	0.97	0	31.32	3.34	0.76	1.78	2.09	0.61	0.41	19.99	0.83	16.04	0.70
Rel Lower Stdev (%)	68	44	10	63	31	15	0	44	31	23	35	38	27	25	53	26	46	36
Rel Upper Stdev (%)	215	79	11	169	45	17	0	78	44	30	55	61	38	33	111	35	86	56

Table 3.4 RSFs for Au_2^+ ions using delayed extraction (see Table 3.2 for details of data presentation).

	Li	B	O	Na	Mg	Al	Si	K	Ca	Ti	V	Cr	Mn	Fe	Rb	Sr	Cs	Ba
KL2-G	**2.04**	nd	**0.0016**	**20.17**	**3.19**	**4.56**	**1**	**71.94**	**6.64**	**3.70**	**3.55**	**3.53**	**2.51**	**1.91**	**58.11**	**5.79**	nd	**3.70**
ATHO-G	**5.36**	**2.84**	**0.00077**	**60.99**	**10.76**	**13.23**	**1**	**303.93**	**72.99**	**7.75**	nd	nd	**5.87**	**11.11**	**330.36**	**89.83**	nd	**21.01**
T1-G	**13.63**	**10.59**	**0.0010**	**68.60**	**4.37**	**9.27**	**1**	**218.72**	**14.97**	**6.01**	**6.50**	**23.29**	**4.91**	**4.61**	**100.06**	**20.89**	nd	**5.63**
GOR132-G	**27.83**	**2.72**	**0.0082**	**170.41**	**18.50**	**11.26**	**1**	**441.30**	**49.97**	**9.54**	**11.15**	**8.73**	**5.91**	**4.99**	nd	nd	**81.85**	nd
StHs6/80-G	**16.70**	nd	**0.0042**	187.00	**14.25**	12.31	**1**	424.18	53.23	**12.93**	**19.80**	**29.59**	**17.85**	**9.26**	**240.07**	**38.55**	nd	**15.42**
ML3B-G*	**30.05**	nd	**0.0057**	**207.20**	**10.77**	**13.29**	**1**	**328.23**	**47.77**	**5.09**	**7.48**	**6.41**	**4.78**	**4.26**	**193.69**	**10.10**	nd	**9.61**
SRM 610	**36.59**	**2.46**	**0.0065**	**152.07**	**24.27**	**9.40**	**1**	**333.06**	**49.82**	**12.37**	**19.54**	**13.52**	**7.98**	**9.26**	**409.54**	**42.75**	**75.37**	**20.25**
Geometric Mean	13.37	3.77	0.0029	87.64	10.05	9.61	1	247.65	30.86	7.50	9.52	11.07	6.04	5.62	182.20	23.78	78.54	10.46
Lower Stdev	8.31	1.70	0.0017	48.24	4.99	2.92	0	110.33	17.59	2.63	4.36	5.75	2.55	2.44	89.67	14.31	3.17	5.01
Upper Stdev	21.99	3.09	0.0041	107.31	9.90	4.20	0	198.98	40.92	4.05	8.06	11.96	4.43	4.31	176.59	35.95	3.31	9.61
Rel Lower Stdev (%)	62	45	59	55	50	30	0	45	57	35	46	52	42	43	49	60	4	48
Rel Upper Stdev (%)	164	82	143	122	99	44	0	80	133	54	85	108	73	77	97	151	4	92

Table 3.5 RSFs for Au_3^+ ions using delayed extraction (see Table 3.2 for details of data presentation).

	Li	B	O	Na	Mg	Al	Si	K	Ca	Ti	V	Cr	Mn	Fe	Rb	Sr	Cs	Ba
KL2-G	nd	nd	**0.0013**	**28.80**	**3.65**	**5.44**	**1**	**138.71**	**9.99**	**5.30**	**3.52**	**4.62**	**3.73**	**2.82**	**118.10**	**12.23**	nd	**8.33**
ATHO-G	nd	nd	**0.00081**	**38.66**	**8.18**	**11.47**	**1**	**435.57**	**53.76**	**10.48**	nd	nd	**4.64**	**2.41**	**703.82**	**42.97**	nd	**62.68**
T1-G	**12.34**	nd	**0.0020**	**77.91**	**5.33**	**10.01**	**1**	**288.26**	**17.20**	**7.77**	**10.77**	nd	**5.78**	**5.18**	**114.30**	**19.47**	nd	**11.38**
GOR132-G	**79.43**	**1.96**	**0.0025**	**27.67**	**13.14**	**9.98**	**1**	**411.06**	**32.83**	**6.36**	**5.73**	**5.61**	**2.80**	**4.22**	nd	nd	**71.09**	nd
StHs6/80-G	**76.38**	nd	**0.0066**	362.78	**12.99**	11.33	**1**	525.29	35.64	**6.82**	**11.10**	**11.66**	**6.68**	**5.15**	**66.75**	**10.97**	nd	**4.85**
ML3B-G	nd	nd	**0.0057**	**23.70**	**6.12**	**7.15**	**1**	**63.52**	**22.15**	**6.80**	**5.13**	**5.17**	**3.88**	**4.51**	nd	**30.92**	nd	nd
SRM 610	**50.06**	**0.62**	**0.0050**	**192.43**	**22.05**	**11.69**	**1**	**590.99**	**47.60**	**3.95**	**7.48**	**17.93**	**5.29**	**7.85**	**119.87**	**41.83**	**78.90**	**27.89**
Geometric Mean	44.00	1.10	0.0027	35.56	8.67	8.97	1	254.03	26.15	6.52	6.73	7.75	4.52	4.30	101.94	22.93	74.89	15.17
Lower Stdev	23.34	0.48	0.0014	12.26	3.79	2.16	0	136.17	11.59	1.60	2.26	3.19	1.08	1.32	22.16	9.69	3.80	9.05
Upper Stdev	49.70	0.86	0.0029	18.72	6.74	2.84	0	293.51	20.83	2.12	3.40	5.42	1.43	1.91	28.32	16.78	4.01	22.46
Rel Lower Stdev (%)	53	44	53	34	44	24	0	54	44	25	34	41	24	31	22	42	5	60
Rel Upper Stdev (%)	113	78	111	53	78	32	0	116	80	33	50	70	32	44	28	73	5	148

For Au_2^+, during delayed extraction, the relative standard deviations for most of the major elements were 30 – 99%, although those for O, Na, Ca, and Cr were all above 100%. For the trace elements B, Rb, Cs, and Ba the range was 4 – 97%. Lithium was higher at 164%, and Sr was also high at 151% (Table 3.4). For Au_3^+ the relative standard deviations ranged between 24 – 80% for the major elements (excluding O at 111% and K at 116%), and 5 – 78% for most trace elements (excluding Li at 113% and Ba at 148%, see Table 3.5).

RSFs for the major elements obtained using Au_2^+ and Au_3^+ ions were significantly higher than those from Au^+. On average, the increase between Au_2^+ and Au^+ was a factor of 2.8 (calculated as a geometric mean with lower and upper limits of 1.7 – 4.7). For Au_3^+ the average increase in RSFs was a factor of 2.4 (0.9 – 6.2) relative to Au^+.

Figure 3.2 shows RSFs obtained using Au^+ with delayed extraction, normalized to those from Au^+ with normal extraction, versus element mass. As only five of the seven standards were analyzed using normal extraction only the corresponding data from the delayed extraction measurements have been used to calculate the delayed RSFs plotted in Figure 3.2.

There is a systematic difference between the two sets of RSFs. In general, for the elements lighter than Si (Li, B, O, Na, Mg, and Al) the ratio between RSFs obtained using delayed extraction and those using normal is <1, while for the elements heavier than Si (K, Ca, Ti, V, Cr, Mn, Fe, Rb, Sr, Cs, and Ba) this ratio is >1.

As the initial kinetic energies of secondary ions are very similar, it can be assumed that their velocities are proportional to the inverse square-root of their mass. The dispersion of the secondary ions above the sample surface is proportional to their velocity and hence any elemental fractionation should be proportional to the square-root of elemental mass. The data in Figure 3.2 has therefore been fitted with a square-root function, which fits reasonably well to the data.

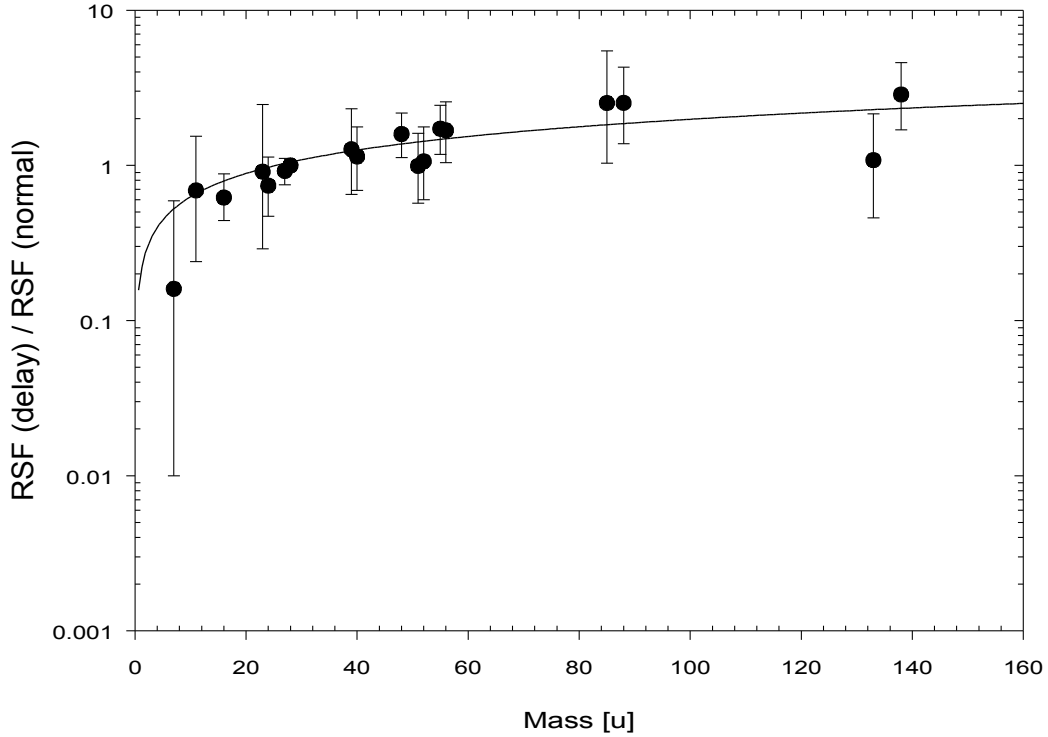

Figure 3.2 RSFs for delayed extraction relative to RSFs for normal extraction, versus element mass. The data is taken from the standards KL2-G, ATHO-G, GOR132-G, StHs6/80-G, and ML3B-G and has been fitted with a square-root function ($f(x) = a\sqrt{x}$). For elements lighter than Si the ratio is typically <1, and for heavier elements >1. Error bars are 1σ.

3.4 DISCUSSION

The observed increase in the sputter rate of Au_2^+ ions relative to Au^+ by a factor of 2.4 ± 0.7 explains the enhancement in practical secondary ion yields for the major elements analyzed with Au_2^+, as seen in Figure 3.1. There appears to be no significant change in ionization efficiencies.

For Au_3^+ there is an increase by a factor of 2.0 ± 0.5 in sputter rate relative to Au^+. Again, the practical secondary ion yield increases for nearly all major elements agree within error with this change in sputter rate. The exception is K (Figure 3.1), which has a practical secondary ion yield increase of 4.98 ± 1.33 times greater than that of Au^+. Although we cannot fully exclude that this is linked to its low FIE and potentially changing ionization efficiencies this seems unlikely as there is still an overlap for the 2σ errors.

RSFs for major and trace elements in silicate glasses obtained using Au^+ primary ions were less variable across the standards than those from Au_2^+, or Au_3^+. Figure 3.3 shows that the standard deviations for RSFs measured in different silicate standards when using Au^+ are comparable to those reported for other primary ions sources such as Ga^+ (Henkel et al. 2007b). There appears to be no improvement, and similarly no deterioration, in the quantification of elemental abundances in the standards when using Au^+ rather than Ga^+ ions.

The size of the increases in RSFs observed between Au_2^+ and Au_3^+ relative to the Au^+ are comparable, within error, to the size of the decrease in the total fraction of Si-ions detected as $^{28}Si^+$. As Si is used as the reference element, the higher RSFs measured for Au_2^+ and Au_3^+ can be explained by their calculation from lower total atomic Si-ion numbers. In comparison the other elements only showed minimal cluster ion formation.

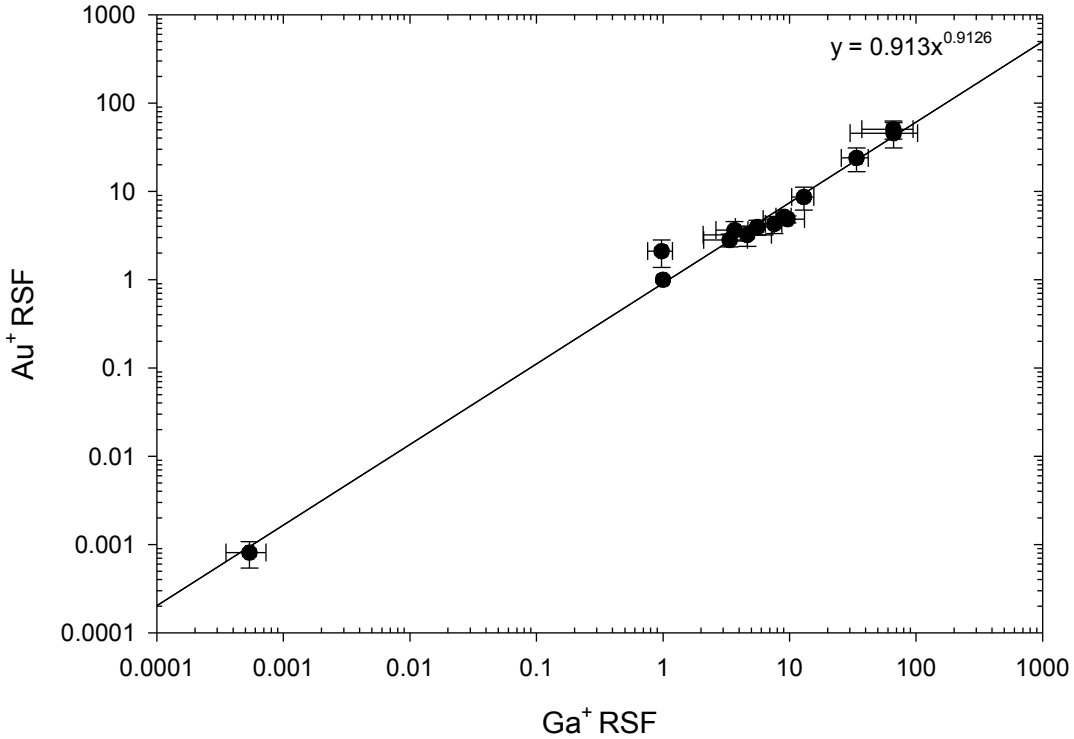

Figure 3.3 Comparison of RSFs obtained using Au^+ (this study) and Ga^+ (Henkel et al. 2007b) Error bars are 1σ and reflect the variations observed between the silicate glasses.

The systematic changes between RSFs determined using delayed and normal extraction shown in Figure 3.2 are caused by the variations in the number of

secondary ions extracted by each method. Under normal extraction conditions, the sample potential is switched on for the duration of the primary ion pulse. To a good approximation, every secondary ion of each mass is extracted into the TOF-analyzer and detected.

During delayed extraction the sample potential is switched on after the primary ion pulse. This provides the resulting secondary ions a period of time during which they can travel away from the sample surface. When the sample potential is then switched on, only secondary ions directly below the extractor are accelerated into the TOF-analyzer. As the lighter ion species travel faster, they are more dispersed and a smaller fraction of the secondary ions are actually extracted. The heavier the ion species the less dispersed the secondary ions are, with the result of a greater percentage of the respective secondary ion species being extracted.

For Si, the number of secondary ions per primary ion was 2.76×10^{-4} during delayed extraction and 3.98×10^{-4} with normal extraction. This indicates that ~30% of Si-ions were lost using delayed extraction. For the elements lighter than Si this percentage is higher, with as much as ~95% of Li-ions lost during delayed extraction. Heavy elements such as Rb, Sr, Cs, and Ba appear to suffer no loss with delayed extraction.

3.5. CONCLUSION

Higher order Au-cluster ions are routinely used in the analysis of organic samples by SIMS as they can produce significant secondary ion yield increases for high mass organic molecules. In contrast, no improvement was found for the ionization efficiencies of inorganic secondary ions. An increase in sputter rate (by approximately a factor of 2) is outweighed by the lower primary ion currents (approximately a factor of 8 less) for Au-clusters compared to atomic Au^+. This makes Au^+ the preferred choice for analysis of elemental abundances within inorganic samples.

The use of Au_2^+ and Au_3^+ ions causes a significant increase in the formation of Si-cluster ions. If Si is used as the reference element this results in elevated RSFs for Au_2^+ and Au_3^+ relative to those for Au^+.

Chapter 4

Trace element depth-profiles in presolar silicon carbide grains

Ashley King[1], Torsten Henkel[1], Detlef Rost[1], and Ian C. Lyon[1]

[1]The University of Manchester, School of Earth, Atmospheric and Environmental Sciences, Oxford Road, Manchester, M13 9PL, UK.

Adapted from: King A., Henkel T., Rost D. and Lyon I.C. (2010) Trace element depth-profiles in presolar silicon carbide grains, submitted to Meteoritics and Planetary Science.

We have analyzed 11 presolar SiC grains from the Murchison meteorite with time-of-flight secondary ion mass spectrometry. The Si isotopic compositions of the grains indicate that they are probably of an AGB star origin. The average abundances of Mg, Fe, Ca, Al, Ti and V are strongly influenced by their condensation behaviour into SiC in circumstellar environments. Elements such as Mg, Fe, Ca and Al are depleted in the grains due to their volatility relative to SiC. Depth-profiles of Li, B, Mg, Al, K, Ca, Ti, V, Cr and Fe in the SiC grains show that trace elements do not always occur homogenously within the grains and we find evidence for two distinct populations of presolar SiC. In some SiC the trace element distributions can be explained by condensation processes around the grains' parent stars. These grains must have experienced only minimal processing before their arrival in the presolar molecular cloud, probably due to short residence times in the interstellar medium. The second population of SiC grains contain elevated abundances of several elements within their outer ~200nm. This is attributed to the implantation of energetic ions accelerated to ~1000kms^{-1} by shockwaves in the interstellar medium. These grains may have spent a longer period of time in the interstellar medium, hence increasing the probability of them passing through a shockfront. Distinct populations of presolar SiC grains, whose residence times in the interstellar medium differ, are consistent with previous findings of noble gas studies.

4.1 INTRODUCTION

Presolar grains are dust that condensed in the environments of dying stars. The grains travelled through the interstellar medium (ISM), survived the formation of the Solar System and are present within primitive meteorites. Nanodiamonds were the first type of presolar dust isolated from meteorites (Lewis et al. 1987). This was soon followed by the extraction of presolar SiC (Bernatowicz et al. 1987) and graphite (Amari et al. 1990) grains. Other presolar phases discovered since include oxides (Al_2O_3, spinel and hibonite; Huss et al. 1993, Nittler et al. 1994b; 1997, Choi et al. 1999), silicon nitride (Nittler et al. 1995) and silicates (Messenger et al. 2003, Nguyen and Zinner 2004, Nagashima et al. 2004).

Presolar SiC is the most extensively studied presolar phase, with abundances in the Murchison (CM2) meteorite of ~6ppm. Isotopic anomalies in C, N and Si define several distinct populations. Most grains (~90%) are "mainstream" and condensed in stellar envelopes around asymptotic giant branch (AGB) stars of 1 – $3M_{\odot}$ (Zinner et al. 1989, Alexander 1993, Hoppe et al. 1994, Lugaro et al. 2003). The A and B grains (~4%) are likely to come from J-type carbon stars (Amari et al. 2001a), whilst X grains (~1%) are from supernovae (Amari et al. 1992, Nittler et al. 1996, Hoppe et al. 2000), and Y (Amari et al. 2001b) and Z grains (Hoppe et al. 1997) (~1%) are from low metallicity AGB stars.

Many SiC grains are >0.5μm in diameter, making them suitable for measurements of trace element abundances along with isotopic analyses. Despite this, there have been few quantitative studies of trace element abundances and distributions within presolar SiC grains (Amari et al. 1995a, Huss et al. 1997, Hoppe et al. 2000; 2010, Kashiv et al. 2001; 2002, Henkel et al. 2007a, Lyon et al. 2007, Knight et al. 2008). As stellar condensates the SiC grains must have experienced several different environments and processing events before arriving in the laboratory. Each event may have influenced the abundance and distribution of the trace elements contained within the grains.

The grains condensed in gaseous envelopes around stars, and abundances of elements such as Al, Mg, Ti, V and Fe within them directly reflect compositions

and condensation processes in these environments. Amari et al. (1995a) showed that elements (e.g. Al, Mg, Ca, Fe) and compound species more volatile than SiC are depleted in the grains. Also, as elements condense they are removed from the circumstellar gas. This causes the gas to become depleted in those elements, altering its composition over time. Silicon carbide is known to condense over a range of temperatures (Lodders and Fegley 1995). Therefore, grains condensing at higher temperatures acquire trace elements in different concentrations to those that formed later at lower temperatures.

Trace element compositions can also be affected by whether a compound species condenses in solid solution with SiC or as a separate phase. For example, TiC condenses separately before SiC, resulting in the presence of TiC sub-grains in some presolar SiC grains (Stroud and Bernatowicz 2005, Hynes et al. 2010a). Similarly, MgS and CaS have been calculated to condense as coatings on the surfaces of presolar SiC grains (Zhukovska and Gail 2008), with the presence of MgS used to explain the 30μm emission feature observed around some stars (Forrest et al. 1981, Goebel and Moseley 1985).

In the ISM the grains are subjected to grain-grain or grain-gas collisions, and ion implantation. The grains are predicted to display the effects of this sputtering on their surfaces (Jones et al. 1996). Lyon et al. (2007) presented Li and B isotopic compositions, and Li/Si and B/Si abundance ratios in 11 acid-extracted and 10 pristine (isolated using the gentle separation procedure of Tizard et al. (2005)) presolar SiC grains. The Li/Si and B/Si ratios in some grains were found to be elevated at, or near the surface, to depths of ~200 – 300nm. This was interpreted as evidence for the implantation into the grains of Li and B ions accelerated by supernova shockwaves in the ISM.

However, Bernatowicz et al. (2003) studied 81 pristine presolar SiC grains and found no evidence of any cratering on the grain surfaces. They did report that ~60% of the grains had amorphous, potentially organic coatings, indicating that grain surfaces may have been shielded from sputtering in the ISM. It has been suggested that grains could have been protected by ices accreting onto their

surfaces that were then broken down into organic mantles by exposure to UV and cosmic-ray exposure (Sandford and Allamandola 1993, Gibb and Whittet 2002).

Alternatively, the residence time of presolar SiC grains in the ISM was very short and they did not experience significant sputtering. Attempts have been made to estimate the time of formation of presolar SiC grains by determining cosmic-ray exposure ages using either noble gas analyses (Lewis et al. 1994, Ott and Begemann 2000, Ott et al. 2005, Heck et al. 2009) or Li isotopic compositions (Gyngard et al. 2009). Calculated cosmic-ray exposure ages have a wide range, from <50Myr to >1Gyr. The longer exposure ages (>500Myr) are consistent with expected grain survival times in the ISM (Jones et al. 1996).

Trace element abundances in presolar SiC grains may also be affected by contamination in the laboratory. This could arise from the meteorite matrix or through the acid extraction procedure. Henkel et al. (2007a) reported the apparent deposition of meteoritic matrix material in crystal defects etched into grain surfaces by the harsh acids used to isolate the grains (Amari et al. 1994). Knight et al. (2008) measured abundances of trace elements, including Ti, V, Cr, Mn, Fe, Pb and W, in SiC grains isolated using standard acid treatments, and with cleaned acids. They found that using cleaned acids caused a decrease in contamination of W and Pb on grain surfaces.

Most previous studies of trace elements in presolar SiC have used direct current (DC) beam ion probes (Zinner et al. 1989, Alexander 1993, Hoppe et al. 1994, Amari et al. 1995a; 2000). The use of a DC-beam means that sample consumption is high during an analysis, so that data represents an average over a large volume of a grain. These ion probes use magnetic and electric fields to separate the secondary ions and often only 5 – 7 isotopic species can be measured in a single analysis. Generally the first measurements are for C, N and Si isotopic compositions, leaving only a small amount of material remaining for trace element analyses.

Attempts have been made to determine trace element abundances in individual SiC grains using synchrotron x-ray fluorescence (SXRF) (Kashiv et al. 2001;

2002, Knight et al. 2008). This method has the advantage of being non-destructive, so other analytical techniques may be later applied to the same grains. It also does not suffer from the matrix effects associated with secondary ion mass spectrometry (SIMS). Several s-process elements, such as Rb, Sr, Y and Zr, have been successfully measured using SXRF. The disadvantages include measured concentrations representing the bulk grain, beam diameters of ~2.5μm and a need to coat the samples with aluminium oxide.

In this study we have used time-of-flight secondary ion mass spectrometry (TOFSIMS). TOFSIMS allows for comprehensive studies of samples, with a complete mass spectrum for either positive or negative secondary ions acquired in a single analysis. Isotopic ratios and trace element abundances can be obtained at the same time providing a more efficient sample usage. High spatial resolution analyses can be achieved although with a loss of signal. TOFSIMS uses a pulsed primary ion beam with low duty cycle and a high transmission TOF mass spectrometer, so sample consumption during a single measurement is low. This makes it suitable for high resolution depth-profiling of individual presolar grains. The effects of heterogeneities such as sub-grains on trace element abundances, not detected using DC ion probes or SXRF, may potentially be analyzed.

We have undertaken a series of systematic TOFSIMS analyses to measure trace element abundances and distributions in presolar SiC grains. The resulting depth-profiles can help to constrain the effects of any processing experienced by the grains in circumstellar envelopes, the ISM and the Solar System. Here we present data for 11 acid-extracted presolar SiC grains. For each grain complete depth-profiles for a range of trace elements have been obtained.

4.2 EXPERIMENTAL PROCEDURE

4.2.1 Samples

Silicon carbide grains from two residues of the Murchison (CM2) meteorite were analyzed.

Four of the analyzed grains came from the KJG acid residue prepared according to the "Chicago procedure" (Amari et al. 1994). These grains were received as a deposit spread upon a Au-foil. Grains from this sample were then transferred onto a new, cleaned (through ultrasonication in isopropanol and acetone), high-purity (>99.999%) Au-foil, upon which a copper finder-grid (Agar H15, 3.05mm, 125mesh) had been imprinted, by pressing the foils together. These grains are referred to as AK-KJG.

The other seven grains analyzed were extracted by John Arden using a procedure similar to that described by Amari et al. (1994). Murchison matrix material was treated with HF/HCl to produce the sample "MM". Some of this was then oxidized using $Cr_2O_7^-$ followed by $HClO_4$ to give a new sample, "MM1". Kerogen and sulphur were removed to leave a SiC and spinel rich residue named "MM2". A small aliquot of the MM2 residue, suspended in a 1:1 isopropanol/water mixture, was distributed upon a second high purity gold foil with imprinted finder-grid. These grains are referred to as AK-MM2.

Silicon carbide grains on both foils were located using a Phillips XL30 environmental secondary electron microscope (ESEM). Energy dispersive X-ray (EDX) analysis was used to confirm the composition of grains as SiC. Electron beam energies were kept low (10 – 15kV) to minimize potential damage on the grain surfaces. The grains were imaged using the ESEM and their locations relative to the finder-grid recorded. The average major-axis diameter of the AK-KJG grains was 1.60μm. The AK-MM2 grains were slightly larger at 2.01μm. Grains were named according to their sample name, grid location (letters A-Z, numbers 0-9) and numbered sequence within each grid area.

4.2.2 Analytical Procedure

The SiC grains were analyzed with high mass resolution and high spatial resolution in two separate rounds of measurements. These were performed using our "IDLE" (*Interstellar Dust Laser Explorer*) TOFSIMS instruments. The instruments is based upon the designs of Braun et al. (1998) and previous versions have been described by Henkel et al. (2006; 2007b).

The AK-KJG grains were analyzed using "IDLE2", which at the time was equipped with a 25kV Ga^+ liquid metal ion gun (LMIG) (IOG25 from Ionoptika Ltd, Southampton, UK). We then built a new instrument, "IDLE3", equipped with a 25kV Au_n^+ LMIG (IOG 25Au from Ionoptika Ltd, Southampton, UK, Davies et al. 2003, Hill and Blenkinsopp 2004, see Chapter 2). The AK-MM2 grains were analyzed using this second instrument. The analytical procedure (outlined below) used was the same for both sets of grains.

Grains were analyzed by rastering a pulsed primary ion beam over their surfaces. The primary ion beam was typically applied over a 7μm × 7μm area, although this could be adjusted according to grain size. Sputtered secondary ions were extracted from the sample and analyzed using a TOF mass spectrometer (R-500 from Kore Technology, Ely, UK). Positive secondary ions were detected and a single analysis often lasted several hours in order to achieve good counting statistics for low abundance elements within the grains.

The measurements operated in a scanning mode, with each scan recorded separately. The scans could then be combined to give a total secondary ion image. Scans often contained 64 × 64 pixels, with 150 primary ion shots per pixel and each pixel containing a complete mass spectrum (1 – 300amu).

Raw data was collected for offline analysis. The region of interest was defined using the $^{28}Si^+$ secondary ion image to mark the grain area and produce a total spectrum for the grain. As only spectra from the region of interest were selected for further analysis this ensured that the background signal from the Au-foil contributing to the spectrum was minimal. During long measurements the position of the primary ion beam could shift by up to a few micrometres due to temperature changes or electronic instabilities. A shift correction was therefore applied prior to combining the individual scans.

4.2.3 Mass Resolution

Accurate determination of isotopic ratios and quantification of trace element abundances within presolar SiC grains required that high mass resolution (e.g.

m/δm ~3500 at ^{28}Si) was achieved, so that hydride and oxide interferences could be resolved throughout the spectrum. In TOFSIMS high mass resolutions can be obtained by using very short primary ion pulses (~2 – 3ns) (Stephan 2001). However, using such short pulses results in low secondary ion signals and may degrade the spatial resolution of analyses due to the rapid switching of the primary ion beam. Instead we used a delayed secondary ion extraction technique to achieve high mass resolutions.

During delayed extraction, primary ion pulses ~40ns long hit the sample whilst it was at ground potential. Secondary ions formed earlier in the pulse traveled further from the sample than those formed towards the end. The sample potential was then switched to 1.4kV accelerating the secondary ions towards the extractor, with those formed earliest accelerated the least due to their greater height above the sample surface. The secondary ions were then focused at the detector using a two-stage reflectron. The major advantage of delayed extraction was that high mass resolutions (*m/δm* of 3000 – 4000) could be achieved despite using long primary ion pulses to boost secondary ion signals. Also, as the primary ion pulses were long compared to the switching time, this helped to maintain sub-micron spatial resolutions of the focused ion beam.

Even at high mass resolutions the Si-isotope analysis was affected by a significant interference on the ^{29}Si-peak from $^{28}SiH^{+}$. We therefore used the peak deconvolution technique described by Stephan (2001) to determine the Si isotope ratios. The same technique was also used to derive δ^{26}Mg values. This method involves fitting the peak shape of the major isotope (i.e. ^{28}Si) to that of the minor isotope. The isotope ratio is given by the scaling factor between the two peaks.

Isotopic ratios were corrected for instrumental mass fractionation using an average of multiple analyses of silicate standards and these values are given by Henkel et al. (2007b).

4.2.4 Element Quantification

In SIMS, measured elemental abundances can vary when analyzed in samples of different mineralogy due to matrix effects (Benninghoven et al. 1987). In order to quantify elemental abundances in presolar SiC grains it is therefore necessary to calculate Relative Sensitivity Factors (RSFs) from standards of similar composition.

We have previously calculated RSFs for Ga^+, Au^+, Au_2^+ and Au_3^+ primary ions (Henkel et al. 2007b, King et al. 2010, see Chapter 3) using a series of silicate glasses (MPI-DING standards (Jochum et al. 2000; 2006)) and NIST reference material SRM 610, that have a wide range of known trace element concentrations. For this study the SiC standard SRM 112b, for which only abundances of Al, Ca and Fe are quantified, was also measured for comparison.

Figure 4.1 shows that RSFs measured in SiC with Au^+ primary ions were elevated (on average by a factor of ~7) relative to their respective values in the silicate glasses. This indicates that RSFs from the silicate glasses need correcting for quantification of elemental abundances in presolar SiC.

It has been shown that sputtering with cluster primary ions can lead to an increased presence of cluster secondary ion species in the mass spectrum (e.g. Lyon et al. 2010, King et al. 2010). For example, during sputtering of silicate glass we observed an increase of O cluster ion species (e.g. SiO^+, SiO_2^+, Si_2O^+, $Si_2O_2^+$ etc), whilst for SiC we instead saw C cluster species (e.g. SiC^+, SiC_2^+, Si_2C^+, $Si_2C_2^+$ etc). In both cases Si tended to partition into cluster species, resulting in a decrease in the practical secondary ion yield (number of secondary ions per primary ion) for Si^+.

The practical secondary ion yield for Si in SiC was determined to be 3.09×10^{-5} ($\pm6.45\times10^{-6}$). This is a factor of 8.93 (±1.92) lower than the yield for Si in silicate glasses (2.76×10^{-4} ($\pm$ 1.5×10^{-4}) from King et al. 2010). As the bond between Si and C is stronger than that for Si and O (Krantzman et al. 2007; 2008), it is anticipated that the loss of Si ions is less severe during analyses of silicate

materials than SiC. We therefore attribute lower yields for Si to the increased formation of $Si_mC_n^+$ clusters when analyzing SiC.

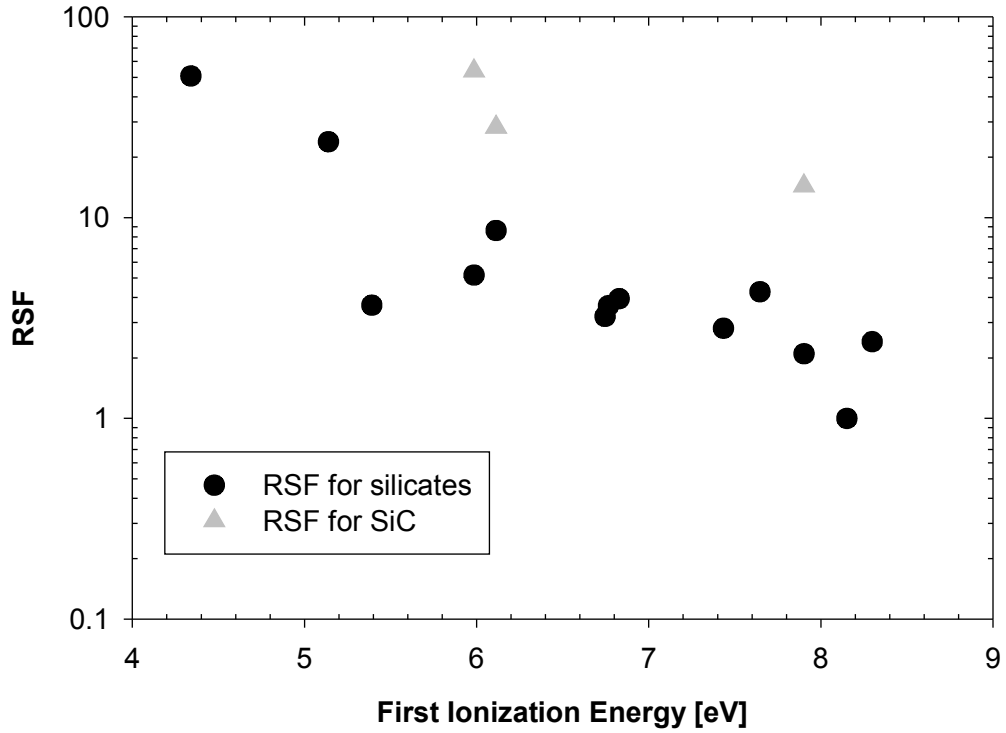

Figure 4.1 Comparison of RSFs obtained from analysis of several silicate glasses (data from King et al. 2010, see Chapter 3) and SiC standard SRM 112b. The RSFs for Al (5.99eV), Ca (6.11eV) and Fe (7.90eV) in SiC are on average a factor of 7 higher than those in silicate glass.

Table 4.1 compares practical secondary ion yields for Al, Ca and Fe obtained during sputtering of SiC and silicate glasses. In contrast to Si there was no significant difference in the yields for Al, Ca and Fe.

Sample	**Silicon** ($\times 10^{-5}$)	**Aluminium** ($\times 10^{-5}$)	**Calcium** ($\times 10^{-5}$)	**Iron** ($\times 10^{-5}$)
Silicate	27.6 ± 1.5	129 ± 7	154 ± 8	45.4 ± 2.6
SiC	3.1 ± 0.7	151 ± 26	101 ± 18	38.1 ± 5.9
Silicate/SiC	**8.9 ± 1.9**	**0.86 ± 0.15**	**1.53 ± 0.29**	**1.19 ± 0.20**

Table 4.1 Practical secondary ion yields (number of secondary ions/number of primary ions) for Si, Al, Ca and Fe during Au^+ analysis of silicate glasses (data from King et al. 2010, see Chapter 3) and SiC standard SRM 112b. Practical yields have been normalized by the element's atomic percent abundance in the standards. Errors are 1σ.

The RSFs for trace elements in silicate glasses given by Henkel et al. (2007b) and King et al. (2010) are normalized to Si. If a factor of 8.93 more Si is detected during analysis of silicates than SiC, then the resulting RSFs will be lower by the

same amount. Elemental abundances relative to Si measured within our SiC grains were therefore quantified according to Eq. (4.1) using the well characterized RSFs for the analyzed elements (Li, B, Mg, Al, K, Ca, Ti, V, Cr and Fe) in silicate glass, and then correcting the calculated abundances for the change in Si yield by a factor of 8.93. The errors on the RSFs used for quantification were typically ~30%.

$$E / E_{REF} = \frac{I(E)/I(E_{REF})}{RSF_E} \qquad \text{(Eq. 4.1)}$$

where E is the element of interest, E_{REF} the reference element (Si), I the measured secondary ion intensity, and RSF the known sensitivity factor for the element of interest.

4.2.5 Depth-Profiling Procedure

Sputtering during SIMS measurements is a destructive process that removes atoms from the surfaces of samples. The longer a grain is sputtered the more material is removed. Subsequent measurements therefore sample material from a greater depth within that grain and a depth-profile can be produced.

Each grain was initially sputtered using a DC-beam that was rastered over a 50 – 100μm area containing the grain for ~1 – 2 minutes. This was sufficient to both remove hydrocarbons, which may have become deposited on the sample during handling or in the ultra-high vacuum environment, and to start sputtering into the grain. The initial sputtering removed an estimated 10 – 30nm from the surface of the grains. This "cleaning" was followed by TOFSIMS measurements using a pulsed primary ion beam (see Section 4.2.2).

The low duty cycle of the pulsed beam produces a lower sputter rate than that of the DC-beam. However, measurements with the pulsed beam often lasted several hours so a significant amount of material was still removed from the grain. The grain was then cleaned again with a DC-beam before the next measurement was started. This procedure was repeated until approximately half of the grain had been sputtered away. At this point some grains were removed, re-imaged using

the ESEM, and then returned to the TOFSIMS for analysis until they had been completely sputtered away.

By carefully recording the primary ion beam current, length of time the beam was applied, field-of-view for each cleaning step and measurement, and using known sputter rates (King et al. 2010, see Chapter 3), it was possible to estimate the depth to which a grain had been sputtered. These depths were checked by comparing them with the amount of the grain remaining when it was re-imaged in the ESEM.

To test whether this procedure was a reliable method for measuring trace element depth-profiles in presolar SiC, we firstly applied it to a silicate grain (1.2μm × 0.7μm) that had been separated from Murchison matrix material. The resulting depth-profile is shown in Figure 4.2. Initially as the grain was sputtered away, most trace element abundances increased slightly, with the largest variation being a factor of ~6 observed for Fe. However, after this the abundances of all trace elements remained relatively constant across the profile. On average the trace element abundances only varied by a factor of ~2.2 from this point.

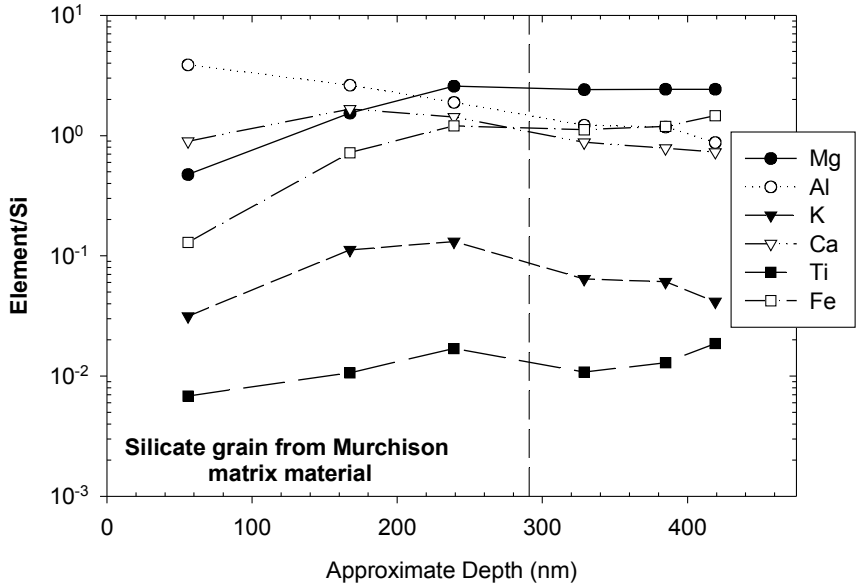

Figure 4.2 Trace element depth-profile through a silicate grain from Murchison matrix. The grain was depth-profiled using the procedure outlined in the text. The dashed vertical line indicates where the grain was removed from the TOFSIMS and re-imaged using the ESEM. As the grain was sputtered away trace element abundances displayed little variation with depth. The abundances did increase slightly during the first measurement but after this depth only varied on average by a factor of ~2.2 across the rest of the profile.

At ~290nm the grain was removed from the TOFSIMS and re-imaged using the ESEM. The abundances for all of the elements in the measurements immediately after this were very similar to those before removal. This indicated that re-imaging using the ESEM and extra sample handling resulted in no significant contamination on the grain surface.

4.2.6 Limitations of Depth-Profiling

For accurate depth-profiling, samples should ideally be flat. Rough samples lead to the detection of secondary ions from different depths in the sample during the same measurement. The depth resolution of our analyses is therefore affected by the rough surfaces of the SiC grains. This also leads to the primary ion beam hitting the grain at varying angles of incidence, resulting in differential sputtering of the surface (Rost et al. 1999). Preferential sputtering of any sub-grains, known to be present in some SiC grains (e.g. Stroud and Bernatowicz 2005, Hynes et al. 2010a), would further degrade the depth resolution. Depths given for our trace element profiles are only estimates, with the error on the known sputter rate probably around 20% (King et al. 2010).

The apparent distribution of trace elements shown in our depth-profiles may also have been affected by primary ion beam mixing of layers with different elemental compositions. The Au^+ primary ions used in this study have energies of 25kV when impacting into a grain surface and they are implanted to depths of tens of nanometres. This creates collisions between the primary ions and atoms in the grain, which become transported to greater depths. Layers in a grain containing different elemental abundances could therefore have become mixed, giving an "average" signal. We often observed variations in elemental abundance that appeared to change smoothly rather than displaying a clear transition between layers during the analyses.

Evidence has suggested that some SiC grains contain outer layers enriched in some elements due to implantation in the ISM (Lyon et al. 2007). Depth-profiling through any such enriched outer layer is difficult as only the initial data will represent the outer region of a grain. Eventually enough material will be

sputtered away so that the grain core is exposed. If the thickness of the outer region is less than the spatial resolution of the primary ion beam then it cannot be resolved from the grain core.

Lyon et al. (2007) measured peaks in Li and B abundances at depths of ~200 – 300nm, smaller than the spatial resolution of our analyses. Elemental abundances from any enriched outer regions in the SiC grains will therefore contribute to those recorded for the core. This is particularly an issue if there is a strong gradient in elemental abundances between the outer regions and core and means that core abundances in this study are likely upper limits.

In an attempt to account for this effect we have produced a simple geometrical model (described in the additional data, Section 4.6) that assumes depth-profiling through a spherical grain of 1μm diameter with an outer region, the thickness of which can be varied, enriched in any chosen element. The abundance of the element is taken as 1 in the enriched outer region and 0 in the grain core. In an ideal situation, when sputtering through this grain the depth-profile should show a clear transition between the two layers of differing composition. In reality primary ion beam mixing prevents this and the abundance in the core is elevated due to a contribution from the enriched outer region. The model indicates that the variation measured between the core and enriched region will be determined by the thickness of the enriched region relative to the grain core. The thicker the outer region, the higher abundances in the grain core will appear.

It is important to note that this is a simple model that assumes a spherical grain and constant sputtering rate. It therefore does not take into account other depth-profiling issues such as irregular grain shapes, preferential sputtering, crystal orientation or heterogeneous inclusions, and provides only an indication as to the depth-profiles we might observe.

4.3 RESULTS

4.3.1 Isotopes

Individual Si, Mg, Li and B average isotopic values for each grain are given in Table 4.2.

The measured $\delta^{29}Si$ and $\delta^{30}Si$ values were within the range -32‰ to +296‰. Figure 4.3 shows that most of the grains were clearly enriched in both ^{29}Si and ^{30}Si isotopes. This is consistent with the grains belonging to the mainstream SiC family having originated around 1 – $3M_{\odot}$ AGB stars (Zinner et al. 1989, Hoppe et al. 1993; 1994, Lugaro et al. 2003).

However, it is clear from Figure 4.3 that compared to the well defined Si-isotopic systematics of mainstream presolar SiC grains (e.g. data taken from Hoppe et al. 1994 in Figure 4.3) our data is biased towards ^{29}Si, with $\delta^{29}Si$ values at the upper end of those measured previously. This is likely due to an insufficient deconvoultuion of the $^{28}SiH^{+}$ interference from the ^{29}Si-peak. Lyon et al. (2007) showed that the presence of the $^{28}SiH^{+}$ interference can add a 20 – 30‰ uncertainty to the $\delta^{29}Si$ value when using the peak deconvolution technique.

Nevertheless, enrichments in both the ^{29}Si and ^{30}Si isotopes, plus the fact that >99% of SiC within the Murchison meteorite is presolar in origin (Amari et al. 1994), suggests that the grains reported here are presolar. Regardless of the $^{28}SiH^{+}$ interference, we would still expect to observe a difference between SiC grains of type X, which are depleted in ^{29}Si and ^{30}Si, and mainstream grains. Within the analytical uncertainties we cannot determine between mainstream, A, B, Y or Z SiC grains but as the mainstream grains make up ~90% of all presolar SiC our grains likely belong to this group.

A further argument against a possible X grain origin is that the $\delta^{26}Mg$ values were in the range -155‰ to +92‰, with 1σ errors on average of ~50‰. Within the analytical uncertainty none of the grains contained a significant ^{26}Mg-excess which could be attributed to the decay of ^{26}Al, a characteristic of SiC X grains.

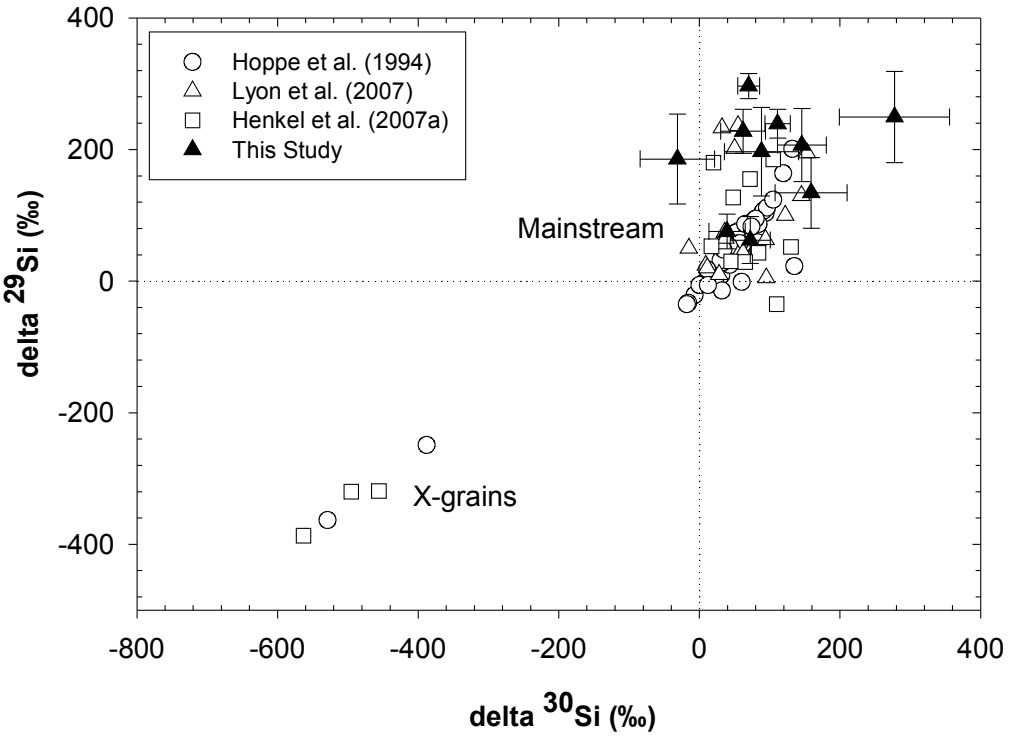

Figure 4.3 Three-isotope plot of the Si isotopic compositions (expressed as δ values) measured in presolar SiC grains as part of this study. Dotted lines indicate the solar composition. The compositions are compared to previous studies using both DC-SIMS (Hoppe et al. 1994) and TOFSIMS (Henkel et al. 2007a, Lyon et al. 2007). Mainstream SiC grains, as all of those in this study appear to be, are characterized by enrichments in ^{29}Si and ^{30}Si relative to solar. Error bars are 1σ.

Table 4.2 also provides Li and B isotopic compositions in the analyzed SiC grains. No significant ^{7}Li/^{6}Li and ^{11}B/^{10}B isotopic anomalies were detected, with all ratios within 3σ of the solar values of ~12 and ~4 respectively.

4.3.2 Average Grain Data

Elemental abundance data for Li, B, Mg, Al, K, Ca, Ti, V, Cr and Fe relative to Si for each grain is presented in Table 4.2. An element's "average" (calculated as a geometric mean) abundance within a grain is also provided, along with the size of each grain and the calculated depth sputtered to during each individual measurement.

Figure 4.4 shows the average abundances, relative to Si and normalized to CI abundances (Anders and Grevesse 1989), of Mg, Fe, Ca, Al, Ti and V compared

to data measured using DC-SIMS by Amari et al. (1995a) (in 60 KJH grains), and using TOFSIMS by Henkel et al. (2007a). The abundances of these elements are influenced by their condensation behavior into the SiC structure (Amari et al. 1995a, Lodders and Fegley 1995). For example, Figure 4.4 shows that Mg, Fe, Ca and Al are always heavily depleted relative to Si and CI, reflecting their (and subsequent compound species) increased volatility relative to SiC.

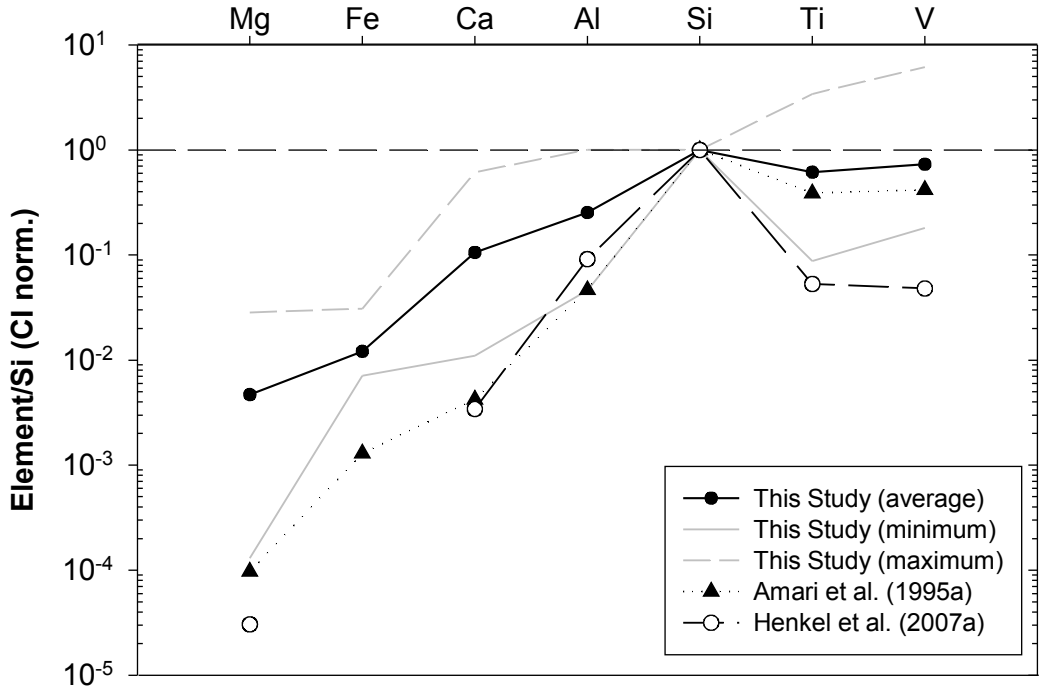

Figure 4.4 Comparison of the average abundances of Mg, Fe, Ca, Al, Ti and V in individual presolar SiC grains analyzed by TOFSIMS in this study and Henkel et al. (2007a), and DC-SIMS by Amari et al. (1995a). The maximum and minimum abundances measured in this study are also shown. Abundances are relative to Si and normalized to CI. Elements more volatile than SiC, such as Mg and Fe, are depleted in the grains.

Our average abundances for Mg, Fe, Ca and Al were all approximately an order-of-magnitude higher than those measured by Amari et al. (1995a) and Henkel et al. (2007a). However, Amari et al. (1995a) did measure similarly high abundances of Mg, Fe, Ca and Al in some individual SiC grains, whilst the lower range of our measured abundances were comparable to the average abundances reported by both Amari et al. (1995a) and Henkel et al. (2007a).

The average abundances of Ti and V were similar to those reported by Amari et al. (1995a), with the lower limit close to the average Ti and V abundances measured by Henkel et al. (2007a).

The average Li/Si and B/Si ratios for the grains were ~10^{-3} and ~10^{-4} respectively. Hoppe et al. (2001) measured B/Si ratios of 10^{-3} – 10^{-5} in mainstream SiC grains from the Murchison meteorite. Huss et al. (1997) measured Li/Si ratios of 10^{-4} – 10^{-6} in SiC grains from the Orgueil meteorite, at least an order-of-magnitude greater than those reported here, whilst in large (>5μm) presolar SiC grains Gyngard et al. (2009) measured Li abundances as low as ~10^{-8}. In contrast Lyon et al. (2007) did measure Li/Si up to ~10^{-2} in the outer regions of both acid and gently separated SiC grains.

High abundances of Li may be the result of contamination from the meteorite matrix or laboratory. The Li/Si ratio in bulk meteorite matrix is ~10^{-5} (Curtis et al. 1980). During depth-profiling of a silicate grain from the Murchison matrix no Li (or B) was reliably detected. This suggests that the high abundances measured in the SiC grains cannot be due to contamination with the matrix material. Furthermore, secondary ion images from the analyses of the SiC grains showed measured Li to be strongly localized to the grains, with no significant contribution arising from the surrounding Au-foil. We therefore argue that the measured Li abundances are not from contamination and must have been produced prior to the grains incorporation into the meteorite parent body.

4.3.3 Depth-Profiles

Due to the variety of factors that can affect the elemental composition of presolar SiC grains, trace element depth-profiles for individual grains are complex. Full descriptions and figures of individual grains' depth-profiles are provided in the additional data (Section 4.6.2). Increases and decreases of elemental abundances in the depth-profiles occur either near the grain surface, (i.e. the surface exposed to the primary ion beam during the first few measurements), the grain core, or the far side of the grain (i.e. the surface closest to the Au-foil).

Seven of the grains produced symmetrical trace element depth-profiles, the other four asymmetrical. This is either a true reflection of the distribution of trace elements within some grains, or indicates that in some instances cleaning steps with the DC-beam (see Section 4.2.5) were too large and information was lost from the grains.

The grains have been grouped according to whether any significant variation in their trace element abundances occurred either near the grain surface or below it (summarized in Table 4.3). In three grains, elemental abundances showed little variation with depth and these have been grouped separately. Each group is described below and representative depth-profiles for each group are shown in Figure 4.5.

4.3.3.1 Grain Surface

The grains AK-KJG-D-1, AK-KJG-D-2, AK-KJG-M-1, AK-MM2-G-2 and AK-MM2-delta-2 had depth-profiles where the highest trace element abundances were observed near the grain surfaces. The abundances then decreased as the grain cores were exposed by primary ion beam sputtering.

As the far side of grains AK-KJG-D-2, AK-KJG-M-1 and AK-MM2-G-2 were reached, the elemental abundances then began to rise again. This resulted in symmetrical depth-profiles with abundances in the outer regions of these grains higher than those measured in the grain cores (i.e. Figure 4.5). Elemental abundances in the grain cores were often a factor 3 – 4 lower than those at the grain surfaces, although in one case the Mg/Si and Fe/Si ratios in AK-KJG-G-2 were up to a factor of 20 lower.

Table 4.2 Elemental abundances and approximate depths sputtered to during TOFSIMS measurements of presolar SiC grains. Elemental abundances are given as atomic-% relative to Si. Errors on the RSFs used for quantification are ~30%. Errors for the isotopic compositions are 1σ. A gap indicates that no data was obtained, either due to unresolved interferences or lack of counts in the mass spectra. Values given in bold are the geometric mean abundances for each element within a grain. Values given in italics have been excluded from the interpretation of depth-profiles (see text and Section 4.4.2) although these data points are still included on Figures 4a.3 – 4a.13.

Grain Name	Grain Size (μm)	$^{7}Li/^{6}Li$	$^{11}B/^{10}B$	$\delta^{29}Si$	$\delta^{30}Si$	$\delta^{26}Mg$	Approx Depth (nm)	Li/Si (× 10^{-2})	B/Si (× 10^{-2})	Mg/Si (× 10^{-2})	Al/Si (× 10^{-2})	K/Si (× 10^{-2})	Ca/Si (× 10^{-2})	Ti/Si (× 10^{-2})	V/Si (× 10^{-2})	Cr/Si (× 10^{-2})	Fe/Si (× 10^{-2})
							42	0.024	0.0028	0.085	0.41	0.44	0.34	0.036	0.011	0.037	0.32
MM2-G-1	2.9 × 0.4	15.1 ± 1.6	4.5 ± 0.8	296 ± 19	70 ± 15	-1 ± 21	153	0.51		0.86	49.46	3.26	2.93	3.69	0.67	1.13	1.23
							398	0.41	0.013	2.23	3.56	8.47	2.43	1.01	0.76	0.15	5.79
							621	0.49	0.0088	0.73	8.41	10.38	3.54	3.35	0.18	0.12	2.82
								0.22	**0.0069**	**0.59**	**4.96**	**3.34**	**1.71**	**0.82**	**0.18**	**0.17**	**1.59**
							61	0.056	0.0040	1.81	3.25	1.52	1.25	0.40	0.016	0.53	2.58
							167	0.18	0.0054	0.16	0.94	0.46	0.33	0.16	0.0040	0.17	0.84
MM2-G-2	1.1 × 0.5	14.0 ± 1.2	4.6 ± 2.6	228 ± 33	62 ± 32	13 ± 19	256	0.17	0.0021	0.33	1.54	0.50	0.23	0.12	0.0042	0.078	0.60
							343	0.31	0.011	2.69	3.56	2.00	0.44	0.093	0.018	0.10	0.16
							430	0.37	0.013	2.76	3.88	0.61	1.27	0.11	0.014	0.23	0.14
							523	0.35	0.0099	3.98	2.69	1.32	1.35	0.36	0.016	0.23	3.39
								0.20	**0.0063**	**1.19**	**2.36**	**0.91**	**0.64**	**0.17**	**0.010**	**0.18**	**0.68**
							31	0.39	0.010	2.48	3.74	2.87	0.93	0.067	0.022	0.61	
							84	0.41		2.71	3.51	2.91	0.094	0.043	0.025	0.39	
MM2-M-1	1.4 × 0.9	17.2 ± 1.9		185 ± 68	-32 ± 53	4 ± 20	125	0.056		4.04	3.78	1.84	0.50	0.074	0.036	0.36	
							179	0.0095	0.0046	3.09	1.85	1.07	0.66	0.048		0.19	
							249	0.26		5.11	1.88	0.24	1.41	0.040	0.012	0.38	
							350	0.29		1.88	2.70	1.63	2.33	0.14	0.020	0.25	
								0.14	**0.0069**	**3.05**	**2.78**	**1.36**	**0.68**	**0.062**	**0.022**	**0.34**	
							62	0.41	0.013	1.62	3.44	0.71	0.22	0.020		0.26	
							179	0.42	0.0094	1.00	1.37	1.16	0.51	0.033	0.0036	0.27	
MM2-N-1	1.8 × 1.0	13.9 ± 0.8	2.4 ± 1.5	207 ± 55	146 ± 35	24 ± 15	411	0.21	0.010	4.32	2.23	0.85	1.34	0.054	0.0060	0.11	
							659	0.28	0.0079	3.54	3.48	1.09	1.50	0.086	0.011	0.16	
							785	0.15	0.0036	2.31	2.25	1.11	0.69	0.099	0.0066	0.019	
							920	0.27		4.14	3.20	0.33	1.12	0.049	0.0028	0.027	
								0.27	**0.0081**	**2.48**	**2.53**	**0.81**	**0.75**	**0.049**	**0.0053**	**0.093**	

Table 4.2 Continued.

Grain Name	Grain Size (µm)	$^{7}Li/^{6}Li$	$^{11}B/^{10}B$	$\delta^{29}Si$	$\delta^{30}Si$	$\delta^{26}Mg$	Approx Depth (nm)	Li/Si ($\times 10^{-2}$)	B/Si ($\times 10^{-2}$)	Mg/Si ($\times 10^{-2}$)	Al/Si ($\times 10^{-2}$)	K/Si ($\times 10^{-2}$)	Ca/Si ($\times 10^{-2}$)	Ti/Si ($\times 10^{-2}$)	V/Si ($\times 10^{-2}$)	Cr/Si ($\times 10^{-2}$)	Fe/Si ($\times 10^{-2}$)
							14	0.0023	0.0037	2.65	0.030	0.0098	0.0094	0.010		0.023	0.58
							190	0.45		0.47	3.12	3.46	0.88	0.16	0.025	0.32	2.43
MM2-delta-1	2.0 × 1.4	12.7 ± 1.4	2.9 ± 1.9	197 ± 67	88 ± 53	-81 ± 61	466	0.33	0.0018	0.096	0.34	0.12	0.067	0.033		0.078	0.49
							705	0.037	0.0012	0.12	0.63	0.20	1.25	0.10		0.14	0.33
							910	0.050	0.0047	0.10	0.47	0.082	0.84	0.041		0.036	0.45
								0.057	**0.0025**	**0.27**	**0.39**	**0.15**	**0.23**	**0.047**	**0.025**	**0.079**	**0.64**
							30	0.15	0.0033	3.29	9.31	0.26	3.41	0.35	0.011	0.22	3.49
							98	0.097	0.0039	2.43	17.13	0.65	5.46	0.88	0.014	0.25	3.13
							157	0.13	0.0038	4.12	16.92	0.72	5.14	1.24	0.015	0.38	1.53
							206	0.028		3.10	17.51	1.79	2.45	1.60		0.11	2.66
MM2-delta-2	2.4 × 1.6	13.5 ± 0.8	4.4 ± 1.6	75 ± 26	39 ± 26	15 ± 17	294	0.17	0.00061	3.96	18.74	1.39	1.32	6.16	0.018	0.074	1.00
							489	0.11	0.0021	0.14	1.00	0.98	0.57	0.034	0.0046	0.24	1.58
							677	0.16	0.0026	0.27	0.38	0.31	0.61	0.036		0.044	0.51
							801	0.23	0.00089	0.17	0.36	0.27	0.68	0.0090	0.0012	0.024	0.26
							1079	0.34	0.0030	0.047	1.08	0.84	0.40	0.35	0.0088	0.12	0.81
								0.13	**0.0021**	**0.79**	**3.70**	**0.65**	**1.45**	**0.29**	**0.0079**	**0.12**	**1.25**
							106	0.056	0.0059	4.52	0.27	0.65	0.12	0.024	0.011	0.085	0.57
							371	0.11		0.48	8.83	1.53	0.25	0.018	0.044	0.23	2.02
MM2-5-1	3.9 × 0.6	13.5 ± 2.2		62 ± 36	72 ± 28	35 ± 20	668	0.087		0.15	11.23	1.45	0.15		0.071	0.029	0.67
							826	*0.12*		*0.31*	*3.77*	*1.07*	*9.14*	*0.10*	*0.29*	*0.16*	*1.15*
							867	*0.058*	*0.0022*	*0.15*	*0.85*	*0.20*	*0.97*	*0.090*	*0.030*	*0.050*	*0.14*
								0.080	**0.0059**	**0.70**	**3.00**	**1.13**	**0.17**	**0.021**	**0.033**	**0.083**	**0.92**

Table 4.2 Continued.

Grain Name	Grain Size (μm)	$^{7}Li/^{6}Li$	$^{11}B/^{10}B$	$\delta^{29}Si$	$\delta^{30}Si$	$\delta^{26}Mg$	Approx Depth (nm)	Li/Si (× 10^{-2})	B/Si (× 10^{-2})	Mg/Si (× 10^{-2})	Al/Si (× 10^{-2})	K/Si (× 10^{-2})	Ca/Si (× 10^{-2})	Ti/Si (× 10^{-2})	V/Si (× 10^{-2})	Cr/Si (× 10^{-2})	Fe/Si (× 10^{-2})
							21	0.074	0.013	1.56	1.52	14.56	59.34	0.65	0.048	3.59	16.85
							70	0.076		0.26	0.84	0.44	0.52	1.10		1.85	6.17
							160	0.17		0.65	0.42	0.34				1.63	
							300	0.060		0.37	0.35	0.15	0.15	0.88		0.34	2.52
KJG-D-1	1.3 × 1.1	10.2 ± 3.1		249 ± 69	277 ± 78	-155 ± 191	460	0.056		0.41	0.37	0.23		1.83			2.84
							587	0.0065		0.014	2.11	0.30	0.42	0.35		0.34	1.68
							670	0.0091	0.0042		3.95	0.21	0.26	0.54	0.032	0.48	1.91
							787	0.0081		0.0084	2.19	0.15	0.14	0.55		0.21	1.55
							870				1.68	0.095	0.10	0.57		0.31	1.56
							1077	0.0030		0.017	2.27	0.16	0.20	0.43	0.038	0.36	1.70
								0.025	**0.0074**	**0.13**	**1.17**	**0.32**	**0.44**	**0.68**	**0.039**	**0.62**	**2.78**
							51	0.24	0.22	1.12	0.44	0.83	2.10			5.10	
							129	0.24		0.89	0.77	1.12	3.75			3.79	
KJG-D-2	2.0 × 1.5	13.7 ± 4.2		237 ± 164			145	0.041		0.12	0.96	6.62	2.08	0.028		0.63	
							232	0.061		0.19	0.74	2.27	1.32				
							294	0.070			0.64	2.30	1.20				
							366	0.34		2.17	1.67	1.89	5.81			6.54	
								0.12	**0.22**	**0.55**	**0.80**	**1.98**	**2.31**	**0.028**		**2.98**	

Table 4.2 Continued.

Grain Name	Grain Size (μm)	$^{7}Li/^{6}Li$	$^{11}B/^{10}B$	$\delta^{29}Si$	$\delta^{30}Si$	$\delta^{26}Mg$	Approx Depth (nm)	Li/Si (× 10^{-2})	B/Si (× 10^{-2})	Mg/Si (× 10^{-2})	Al/Si (× 10^{-2})	K/Si (× 10^{-2})	Ca/Si (× 10^{-2})	Ti/Si (× 10^{-2})	V/Si (× 10^{-2})	Cr/Si (× 10^{-2})	Fe/Si (× 10^{-2})
							34	0.0042	0.0020	0.010	1.09	0.050	0.049	0.33	0.0084	0.022	0.60
							79	0.0039		0.021	2.62	0.034	0.070	0.56	0.010		0.98
							124	0.0020		0.021	2.53	0.033	0.068	0.53	0.013	0.19	0.95
							152	0.0031		0.019	2.48	0.024	0.055	0.64	0.019	0.21	0.83
							237	0.0016		0.0095	2.05	0.024	0.055	0.46	0.020	0.21	0.85
							345	0.0019		0.0082	1.71	0.018	0.058	0.55	0.030	0.22	0.82
							465	0.0011		0.014	1.43	0.016	0.056	0.54	0.033	0.22	0.86
KJG-M-1	1.6 × 1.5	17.2 ± 4.0		239 ± 22	111 ± 18	48 ± 161	528	0.0012		0.013	1.26	0.016	0.074	0.53	0.021	0.21	0.85
							560	0.00094		0.014	1.10	0.019	0.076	0.53	0.026	0.21	0.86
							610	0.0013	0.00046	0.011	1.27	0.020	0.095	0.46	0.023	0.19	0.85
							755	0.0020		0.012	1.37	0.016	0.057	0.34	0.013	0.23	0.87
							826	0.0017		0.012	1.68	0.019	0.073	0.52	0.040	0.23	0.92
							912	0.0045		0.017	1.78	0.016	0.075	0.54	0.020	0.26	0.91
							947	0.0027			1.49	0.020	0.083	0.49	0.049	0.18	0.62
							1001	0.0030	0.0016	0.017	2.26	0.024	0.079	0.37	0.027	0.22	0.79
								0.0021	**0.0011**	**0.014**	**1.67**	**0.022**	**0.067**	**0.49**	**0.021**	**0.18**	**0.83**
							22	0.0056		0.23	7.01	8.43	1.06	0.62	0.017	0.51	
							92	0.042	0.0014	0.92	5.85	1.25	4.35	0.45	0.0071	1.20	
							224	0.067		1.05	9.01	1.48	5.62	0.54		1.58	
KJG-6-1	1.5 × 1.1	13.5 ± 1.3		134 ± 54	159 ± 51	92 ± 48	397	0.084		0.97	9.30	1.99	5.18	1.00	0.024	1.46	
							570	0.16		0.97	10.11	1.69	5.06	0.61	0.024	1.17	
							750	*0.0086*		*0.044*	*2.98*	*0.19*	*0.15*	*0.17*		*0.068*	
							895	0.18		1.45	10.20	3.02	7.01	0.88		1.80	
							1183	0.10	0.0034	0.24	9.17	0.83	2.21	0.56	0.031	0.32	
								0.063	**0.0022**	**0.68**	**8.52**	**2.01**	**3.75**	**0.65**	**0.018**	**0.99**	

In the grains AK-KJG-D-1 and AK-MM2-delta-2 elemental abundances did not increase again at the far side of the grains. Instead the abundances either continued to decrease or flattened until the rest of the grain had been sputtered away.

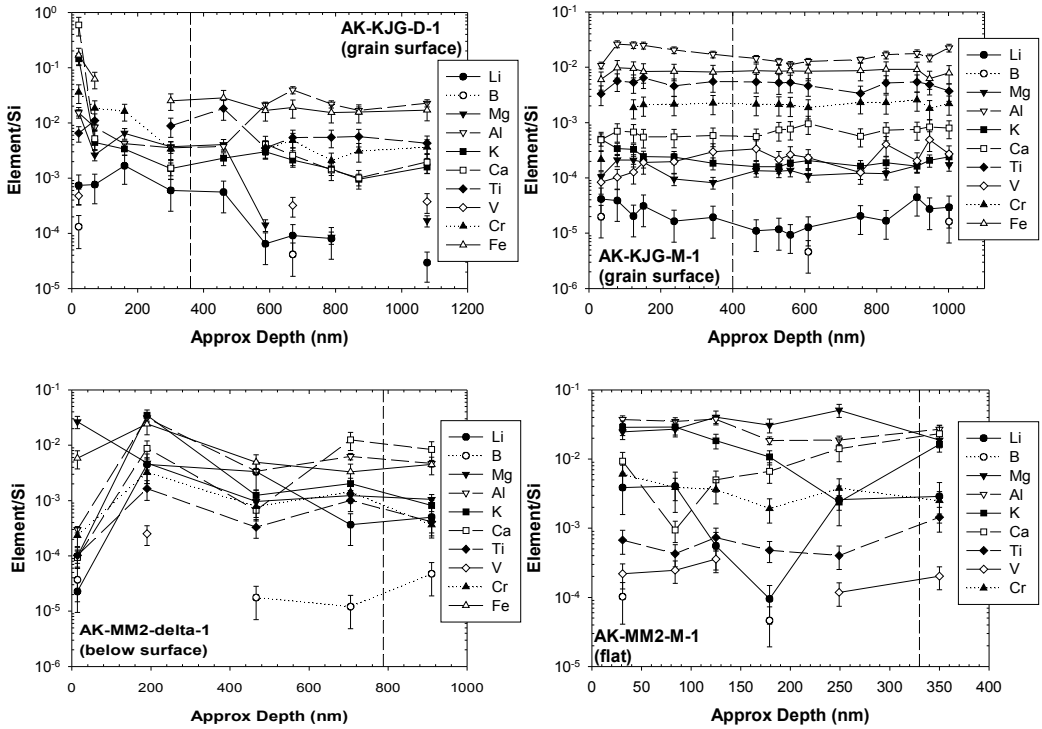

Figure 4.5 Representative trace element depth-profiles. In some presolar SiC grains variations in trace element abundances occurred from the grain surface. For example trace element abundances in AK-KJG-D-1 (top left) and AK-KJG-M-1 (top right) were high at the surface and decreased in the grain core. In other grains, such as AK-MM2-delta-1 (bottom left) where abundances rose to a peak at ~200nm, variations in trace element abundance took place below the surface. The trace elements in several grains showed no abundance variations with depth e.g. AK-MM2-M-1 (bottom right). Dashed vertical lines indicate where a grain was removed and re-imaged using the ESEM. Trace element depth-profiles for all 11 analyzed grains are provided in Section 4.6.2.

For AK-KJG-D-1 and AK-MM2-delta-2, elemental abundances decreased by a factor of 5 – 10 between the surface and core of the grains. The exceptions were Mg/Si and Al/Si in AK-MM2-delta-2, and Li/Si in AK-KJG-D-1, which fell by factors of 25 and 60 respectively. Also, in grain AK-KJG-D-1 the K/Si and Ca/Si ratios decreased sharply from the grain surface before remaining constant throughout the rest of the grain.

Variation?	Symmetrical	Asymmetrical
At Surface	AK-KJG-D-2 AK-KJG-M-1 AK-MM2-G-2	AK-KJG-D-1 AK-MM2-delta-2
Below Surface	AK-MM2-N-1	AK-MM2-G-1 AK-MM2-delta-1
Flat	AK-KJG-6-1 AK-MM2-M-1 AK-MM2-5-1	

Table 4.3 Summary of the main characteristics of each presolar SiC grains trace element depth-profile. The grains either have symmetrical or asymmetrical depth-profiles. They are grouped according to whether any significant changes in trace element abundances occur either at, or below, the grain surfaces.

4.3.3.2 Below the Grain Surface

The grains AK-MM2-G-1, AK-MM2-N-1 and AK-MM2-delta-1 each had depth-profiles where the major changes in elemental abundances occurred below the grain surface.

In AK-MM2-N-1 the lowest abundances were measured at the grain surface. Abundances increased as the grain was sputtered away and the core became exposed. At the far side of the grain the abundances then decreased, resulting in a symmetrical depth-profile with the highest elemental abundances found within the grain core. The Mg/Si, Ca/Si and V/Si abundances were higher in the core by a factor of 3 – 6.

Trace element abundances observed at the grain surfaces in AK-MM2-G-1 and AK-MM2-delta-1 increased as the grains were sputtered away. They continued to rise until peaks in abundances were measured at depths of ~150 – 200nm. During subsequent analyses through the grain cores and the far side of the grains, the abundances decreased from these peak values.

For AK-MM2-G-1 the Al/Si, Ti/Si, V/Si and Cr/Si increased, on average, by a factor of 80, to a peak, before falling by a factor of 15 throughout the rest of the grain. For AK-MM2-delta-1 the increase was even more extreme, with Li/Si, Al/Si, K/Si and Ca/Si rising by an average factor of 190, before falling by up to a

factor of 40. The Ti/Si, Cr/Si and Fe/Si ratios also peaked in AK-MM2-delta-1, although the following decreases in the grain core were less than a factor of 10.

4.3.3.3 Flat Depth-Profiles

Grains AK-KJG-6-1, AK-MM2-M-1 and AK-MM2-5-1 all had "flat" depth-profiles. These are profiles where the majority of elemental abundances showed very little variation with depth. They rarely changed by any more than a factor of 2, similar to the differences measured when depth-profiling through a meteoritic silicate grain (see Section 4.2.5). The small variations measured in these SiC grains were not significant and were mainly within the errors of the RSFs used to quantify the elemental abundances.

4.4 DISCUSSION

4.4.1 Average Abundance Patterns

Amari et al. (1995a) and Lodders and Fegley (1995) suggested that average elemental abundance patterns reflect the volatility of an element and its compound species relative to SiC. Our average elemental abundance patterns for Mg, Fe, Ca, Al, Ti and V (Figure 4.4) match qualitatively with those measured by Amari et al. (1995a) and Henkel et al. (2007a). The patterns show that the more volatile elements (Mg, Fe, Ca and Al) are depleted in the grains relative to Si.

Our average elemental abundances of Ti and V (relative to Si and CI) are close to 1, similar to the abundances measured by Amari et al. (1995a). Figure 4.4 shows that the Ti and V abundances of Henkel et al. (2007a) were approximately an order-of-magnitude lower.

Around stars, Ti is predicted to condense as TiC prior to the condensation of SiC (Lodders and Fegley 1995). This should result in a depletion of Ti in the gas and subsequently in SiC grains. Strong correlations between the abundances of Ti and V in presolar SiC suggest that V condenses into TiC (Amari et al. 1995a). However, as abundances of Ti in the source gas are expected to be very low, its

condensation as TiC is restricted by nucleation effects. The Ti and V will instead condense into SiC producing the abundances measured in this study and by Amari et al. (1995a).

Generally, the lowest Ti and V abundances are found in presolar SiC grains of type X that originate from supernovae (Amari et al. 1995a, Henkel et al. 2007a). Gas surrounding a supernova is expected to be enriched in Si so that other elements appear depleted in condensed SiC grains. The X grains comprise only ~1% of all presolar SiC grains but the data of Henkel et al. (2007a) shown on Figure 4.4 was obtained from thirteen presolar SiC grains, three of which were of type X. Depletions in Ti and V measured by Henkel et al. (2007a) in these three grains causes the average Ti and V abundances to appear lower than our data and that of Amari et al. (1995a).

The average elemental abundance patterns of Amari et al. (1995a), Henkel et al. (2007a), and those presented in this work, indicate that the condensation behavior of each element in stellar atmospheres must play a major role in controlling their abundances in presolar SiC grains.

The range of our average elemental abundances for Mg, Fe, Ca, Al, Ti and V are comparable to those of Amari et al. (1995a) and other similar studies (Huss et al. 1997, Hoppe et al. 2000). To measure trace element abundances Amari et al. (1995a) used DC-SIMS, which sputters a much larger volume of each grain during a single analysis than the TOFSIMS technique used here (and also in the study of Henkel et al. 2007a), which has a depth-resolution of tens of nanometres. In the Amari et al. (1995a) study, trace element measurements were also made after some previous sputtering of the grains had taken place to determine isotopic compositions (Hoppe et al. 1994). The data of Amari et al. (1995a) therefore represented an average elemental abundance over a large volume of each analyzed grain. However, trace element depth-profiles of individual grains show that the elements are clearly not homogeneously distributed within SiC grains.

Below we discuss how processes such as contamination, stellar condensation and interstellar processing could have influenced the distribution of trace elements in presolar SiC grains and compare the expected effects to the measured trace element depth-profiles.

4.4.2 Contamination

The elements Mg, K, Ca and Fe are major constituents of meteorite matrix material. Recent evidence indicates that the use of harsh acid treatments to extract presolar SiC grains from meteorites can etch grain surfaces, leading to a high density of surface pits (e.g. Bernatowicz et al. 2003). The acids may also at least partially dissolve non-acid resistant phases in SiC such as AlN (Stephan et al. 1997, Henkel et al. 2007a).

Henkel et al. (2007a) suggested that depletions of Al at the surfaces of grains plus correlations between the abundances of Al, Mg, K and Ca were caused by the dissolution of AlN and subsequent deposition of meteoritic matrix material in crystal defects. This could lead to high abundances of Mg, K, Ca and Fe at SiC grain surfaces. During analysis of pristine SiC, Stroud and Bernatowicz (2005) noted an apparent in-filling of surface pits by meteorite matrix minerals.

The acids used to isolate the grains have also been found to be a source of trace element contamination. Knight et al. (2008) measured higher abundances of W and Pb in SiC grains isolated using standard acids than those isolated with cleaned acids. The abundances of Ti, V, Cr, Mn and Fe were less affected.

If contamination by the acids or meteorite matrix was an issue in this study we would expect it to affect all SiC grains from the same separation equally, although potentially the effects could vary between the KJG and MM2 samples. All grains from the same separation would probably have similar surface abundances of any contaminating elements. However, we measured orders-of-magnitude differences in the Mg, K, Ca and Fe abundances near the surfaces of SiC grains from each separation. For example, the K/Si ratio at the surface of AK-KJG-D-1 was 0.14 but for AK-KJG-M-1 it was 5×10^{-4}. Similarly, for AK-

MM2-5-1 the Mg/Si ratio was 0.05 at the surface, compared to 8.5×10^{-4} in AK-MM2-G-1.

Structural characteristics could make it more or less difficult for particular SiC grains to retain contamination. The grains in this study were all of similar sizes and did not appear significantly different in morphology from one another. It is possible that some grains had a higher density of surface pits that could allow an increased take-up of meteorite matrix material. However, if these were etched into the grains by the acids, again we would expect all grains from the same separation to be affected in a similar manner.

During depth-profiling of a silicate grain we observed no significant variation in trace element abundances in the immediate measurements after the grain had been re-imaged in the ESEM (see Section 4.2.5). However, trace element abundances in the SiC grains AK-KJG-6-1 and AK-MM2-5-1 did decrease noticeably in the first measurements after re-imaging, before returning to values comparable to those previously recorded in the grains.

If this were the result of surface contamination from handling we would expect the trace element abundances to increase rather than the observed decrease. The interaction of the electron beam may have altered the chemical environment (e.g. oxidation state) on the grain surfaces, leading to a change in ionization efficiency. In either case, all analyzed grains should have been affected similarly but this was not apparent in any of the other depth-profiles. Nevertheless, as elemental abundance decreases in AK-KJG-6-1 and AK-MM2-5-1 occurred in the measurements immediately after re-imaging by the ESEM, we cannot rule out that this was an artefact of the experimental procedure and the data has been excluded.

If any contamination occurred, either from the extraction process or sample handling, it probably affected all SiC grains from the same separation equally. As very different surface abundances were measured, the large variations must be the result of condensation effects around the grains parent stars or interstellar processing.

4.4.3 Condensation

Elements that condensed in solid solution with SiC are likely to be homogeneously distributed within the grains. However, SiC grains condensed from the cooling gas around expanding stars. This could have produced not only variations in trace element abundances between grains, but also elemental zoning within individual grains. At the time of initial SiC growth, higher temperatures would have prevented the condensation of more volatile species causing the grains to be depleted in these trace elements. As the stellar gas cooled, newly condensed elements became available for incorporation into the outer regions of SiC grains. In this scenario some SiC grains may contain higher trace element abundances within their outer regions than in the grain cores.

Compound species that condensed as separate phases, rather than in solid solution with SiC, resulted in the presence of sub-grains in some presolar SiC grains (Stroud and Bernatowicz 2005, Hynes et al. 2010a). Sputtering of any internal sub-grains, such as TiC or AlN, would produce apparent inhomogeneous distributions of those trace elements in presolar SiC. Similarly, MgS and CaS coatings are predicted to condense on SiC (Zhukovska and Gail 2008), although if present are likely to have been at least partially removed by alteration on meteorite parent bodies or through the acid extraction process, and could lead to grain surface enrichments of Mg, Ca and S.

4.4.4 Interstellar Medium

Dust is expected to have passed through several shockfronts during residence in the ISM. Interactions between the shockwaves and ions in the interstellar gas would have caused those ions to be accelerated to the same velocity as the shockwave. The accelerated ions may have then become implanted into the grains, resulting in peaks in elemental abundances below the grain surfaces. Evidence of such implantation was presented by Lyon et al. (2007), who measured elevated abundances of Li and B to depths of ~200 – 300nm in presolar SiC grains.

The estimated residence times of some presolar SiC grains in the ISM are <50Myr (Lewis et al. 1994, Ott and Begemann 2000, Ott et al. 2000, Heck et al. 2009, Gyngard et al. 2009) and most damage or alteration to grains in this environment is caused by the fastest shockwaves (>250kms^{-1}). Jones et al. (1996) estimated that as the interval between fast shockwaves is ~10^8 years, approximately 10% of dust in the ISM will have never experienced a fast shockwave.

This theory is partly supported by the lack of cratering observed by Bernatowicz et al. (2003) on pristine presolar SiC. The presence of amorphous coatings on some grains suggests that they may have protected the grains from sputtering in the ISM. Grains that were shielded in the ISM, or had short ISM residence times, may not display any effects of interstellar processing.

4.4.5 Profiles with Variations beneath the Grain Surface

In grain AK-MM2-G-1 the elements Al, Ti, V and Cr, and in grain AK-MM2-delta-1 the elements Li, Al, K, Ca, Ti, Cr and Fe, showed peaks in abundance at depths within the grains. Unfortunately B was not always reliably detected in measurements and its profiles are incomplete.

The depths at which abundance peaks occur in grains AK-MM2-G-1 and AK-MM2-delta-1, ~150 – 200nm, are well below the grain surfaces and are comparable to those reported by Lyon et al. (2007). Whereas elemental abundances in grains AK-MM2-G-1 and AK-MM2-delta-1 increased by up to a factor of 190, the largest variation measured when depth-profiling a meteoritic silicate grain was only a factor of ~6. We therefore conclude that the peaks in abundance are not contamination or sputtering artefacts and reflect true variations within the grains.

The peaks in trace element abundances may have been caused by the sputtering of any TiC or AlN sub-grains or inclusions present within the SiC grains. There was no evidence of any such grains in the secondary ion images, although they

may not have been sufficiently resolved since many sub-grains are <200nm in size, smaller than the spatial resolutions achieved in the measurements.

An argument against the TiC or AlN origin for the abundance peaks is that they are unlikely to contain significant abundances of elements such as Li or K, which also peak at depths within grains AK-MM2-G-1 and AK-MM2-delta-1. Additionally, the possibility of AlN and TiC being present at the same depth within two different grains is unlikely.

The peaked depth-profiles appear to support the scenario whereby elements may be implanted into presolar SiC grains by supernova shockwaves. Calculations using the SRIM code (Ziegler 2004) indicate that the implantation of Li, Al, Ca, Ti, Cr ions etc to depths of 150 – 200nm in SiC requires implantation velocities on the order of 1000kms^{-1} (Figure 4.6). This is towards the upper end of the range expected for supernovae shockwaves (Jones et al. 1996, Ellison et al. 1997).

Lyon et al. (2007) argued that the relative uniformity of ^{7}Li/^{6}Li ~12 recorded within a range of extra-terrestrial samples (e.g. Sephton et al. 2004, Chaussidon et al. 2006, Seitz et al. 2007), and observed spectroscopically in local star-forming regions (Knauth et al. 2003), could only be achieved by mixing of several sources on a molecular cloud scale. This led them to conclude that the implantation of Li ions into presolar SiC grains must have taken place as a shockwave passed through an interstellar molecular cloud. The presolar SiC reported here also contain solar Li isotopic compositions, supporting the model outlined by Lyon et al. (2007).

The grain AK-MM2-N-1 contained a peak in elemental abundances at a depth of ~500 – 600nm. As the grain was ~1μm in diameter this peak occurred within the grain core rather than just below the grain surface. Elemental abundances at the surface were depleted relative to the core.

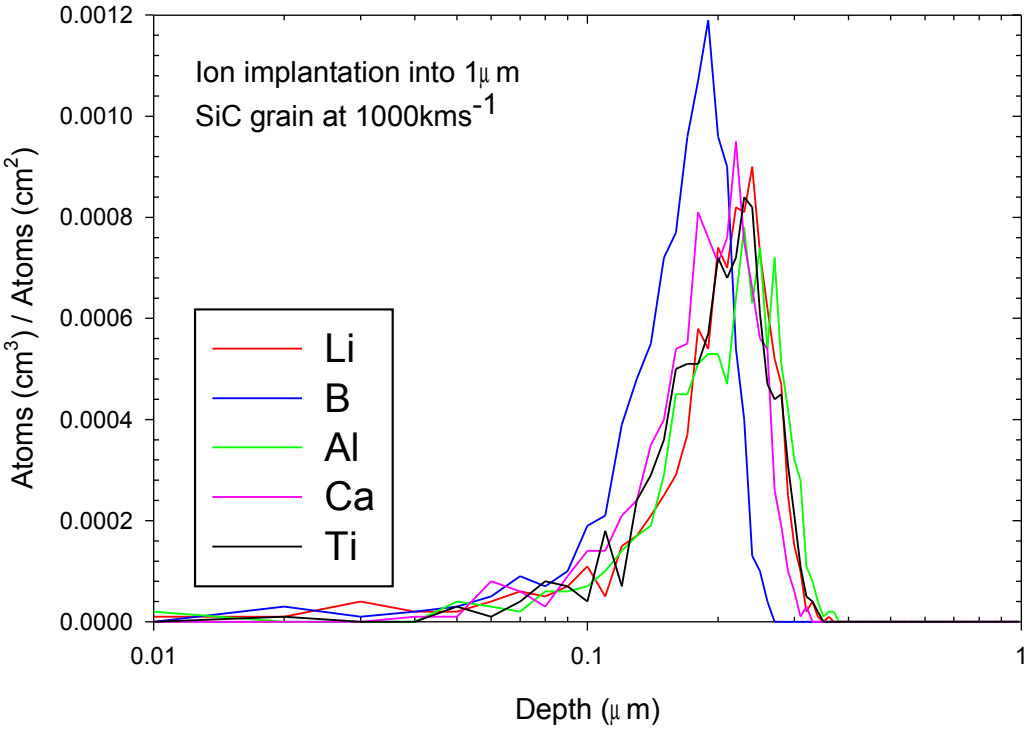

Figure 4.6 SRIM calculations simulating the implantation of Li, B, Al, Ca and Ti ions into a 1μm SiC grain at a velocity of 1000kms^{-1}. The ions impact the SiC at normal angle of incidence. At this velocity most ions are implanted into the SiC to a depth of ~200nm, consistent with peaks in elemental abundances observed in some presolar SiC grains. Lower implantation velocities would lead to implantation to shallower depths. The same calculation for Mg, K, Cr, V and Fe ions produces the same result.

Like the profiles in grains AK-MM2-G-1 and AK-MM2-delta-1, potentially this peak would have been caused by ion implantation. However, an implantation depth of >500nm is larger than those measured both in this study and by Lyon et al. (2007). It would require shockwaves with velocities of several 1000's kms^{-1}. Shocks with such extreme velocities are rare in the ISM, indicating that ion implantation is unlikely to be the cause of high abundances in the core of AK-MM2-N-1.

If the depth profile for AK-MM2-N-1 is not due to processing in the ISM or alteration and contamination in the laboratory this leaves us with the stellar environment. For this grain we cannot exclude sputtering of a sub-grain, which is likely to be either TiC or AlN in composition. The Al abundance remains flat

throughout the grain but the Ti abundance does increase slightly in the grain core.

As discussed, SiC grains formed at high temperatures would have initially acquired low abundances of trace elements in their cores, before cooling of the source gas allowed condensation of new elements in their outer regions. However, this situation would have produced grains with higher trace element abundances in the outer layers than in the core, the opposite of what is observed in AK-MM2-N-1.

Alternatively, some grains may have condensed in, or been transported to, chemically inhomogeneous regions, such as high density knots or jets, of the circumstellar shell. Silicon carbide grains can condense at temperatures as low as ~1000K (Lodders and Fegley 1995). We may hypothesize therefore that AK-MM2-N-1 may have formed in a cooler region, allowing the condensation of many trace elements, before moving to an area containing gas of differing composition.

4.4.6 Profiles with Variations from the Grain Surface

In AK-KJG-D-2, AK-MM2-G-2 and AK-MM2-delta-2 trace element abundances were highest within the outer 50 – 200nm before decreasing in the grain cores. In AK-KJG-D-1 and AK-KJG-M-1 they dropped from the grain surface to lower abundances in the core.

The spatial resolution of the primary ion beam hampered the resolving of the enriched outer regions from the grain cores (see Sections 4.2.6 and 4.6.1). Abundances recorded in the cores must therefore be upper limits due to mixing of the layers during analyses of the core. Using our geometrical model we can infer that decreases in trace element abundances of a factor of ~4, which were typically measured between the outer regions and cores of grains AK-KJG-D-2, AK-KJG-M-1, AK-MM2-G-2 and AK-MM2-delta-2, should be consistent with abundance enrichments to depths of ~200nm. Enrichments to this depth were observed in grains AK-KJG-D-2 and AK-MM2-delta-2, although not in AK-

KJG-M-1 and AK-MM2-G-2, possibly due to irregular sputtering or grain morphologies.

In grain AK-KJG-D-1 trace element abundances decreased by orders-of-magnitude within the first 50nm. As this decrease is much larger than that predicted by our geometrical model it suggests that the high abundances were only present upon the very surface of this grain. The size of the decrease between the surface and grain core was more consistent with that observed after peaks in elemental abundance in grains AK-MM2-G-1 and AK-MM2-delta-1.

Elemental zoning due to condensation of SiC in a cooling gas could have produced the trace element depth profiles seen in grains AK-KJG-D-1, AK-KJG-D-2, AK-KJG-M-1, AK-MM2-G-2 and AK-MM2-delta-2. A test for this explanation is that Li and B, which due to their high volatilities are unlikely to condense into SiC in any significant quantities, should not display the same profiles as elements that clearly do condense into SiC, such as Al and Ca.

In AK-MM2-G-2 and AK-MM2-delta-2 Li and B profiles are relatively flat through the grains with no abundance decreases in the cores. Condensation in a cooling gas can therefore be used to explain the trace element depth profiles in these grains. For AK-KJG-D-1, AK-KJG-D-2 and AK-KJG-M-1 the Li abundance was high in the outer regions of the grains and decreased in the cores. This suggests that these profiles are not the result of changing condensation environments.

AK-KJG-D-2 and AK-KJG-M-1 have outer regions, up to ~200nm thick that are enriched in several elements. This depth is similar to the implantation depths reported by Lyon et al. (2007). In AK-KJG-D-1 trace element enrichments at the grain surface indicate implantation at lower velocities.

If the trace elements were implanted, our data suggest that peaks in these elemental abundances should be present below the grain surfaces, which are not seen in AK-KJG-D-1, AK-KJG-D-2 and AK-KJG-M-1. However, in Lyon et al.

(2007), peaks in Li and B abundances in some SiC grains did occur at the surface rather than below it.

Prior to implantation some grains may have acquired surface coatings that partially protected them from sputtering. These coatings are likely to have been removed on the meteorite parent body or by the acids used in the extraction process. The acids may have also altered or damaged the grains so that we no longer analyze their original surfaces.

4.4.7 Flat Profiles

The abundances of most of the analyzed elements in grains AK-KJG-6-1, AK-MM2-M-1 and AK-MM2-5-1 did not show any significant variation with depth. Elemental abundances within the grains were largely consistent with those measured in other SiC grains. The homogeneous distribution of elements is most likely due to their condensation in solid solution with the SiC in the atmospheres of their parent stars.

The lack of any significant variations in most elemental abundances with depth suggests that these grains suffered only minimal alteration prior to their arrival in the laboratory, although they must have spent some time in extreme environments around their parent stars, the ISM and the early solar nebula.

As discussed, any coating on the grain surfaces may have shielded AK-KJG-6-1, AK-MM2-M-1 and AK-MM2-5-1 from sputtering. However, despite potential coatings we still observe the effects of ion implantation in the grains AK-KJG-D-1, AK-KJG-D-2 and AK-KJG-M-1, so would expect to also see them for AK-KJG-6-1, AK-MM2-M-1 and AK-MM2-5-1.

It seems that grains AK-KJG-6-1, AK-MM2-M-1 and AK-MM2-5-1 must have spent only a short period of time in the ISM and did not experience any significant processing. The unaltered grains make up ~30% of our sample size, higher than the 10% of unprocessed dust predicted by Jones et al. (1996), although only 11 grains have been analyzed in this study. Unfortunately within

the analytical uncertainties we detected no Li isotopic anomalies that could be used to calculate cosmic-ray exposure ages for the grains.

4.4.8 Implications

Based upon our interpretations of trace element depth-profiles, presolar SiC grains can be separated into two distinct populations. The grains AK-KJG-6-1, AK-MM2-G-2, AK-MM2-M-1, AK-MM2-N-1, AK-MM2-delta-2, and AK-MM2-5-1 have trace element distributions consistent with those expected for condensation processes around parent stars. In contrast, the SiC grains AK-KJG-D-1, AK-KJG-D-2, AK-KJG-M-1, AK-MM2-G-1, and AK-MM2-delta-1 clearly display the effects of significant processing in the ISM, with peaks in trace element abundances attributed to ion implantation.

For ion implantation into SiC to occur, high velocity shockwaves are required. The likely source of these in the ISM is supernovae explosions. At least one grain contains evidence of ion implantation at lower velocities. This grain was either hit by the same shockfront as the other grains, although after the front had begun to decelerate, or the grain experienced a different shockwave.

The two populations may reflect the large variations in ISM residence times previously determined for other presolar SiC grains (Lewis et al. 1994, Ott and Begemann 2000, Ott et al. 2000, Heck et al. 2009, Gyngard et al. 2009). As mentioned, cosmic-ray exposure ages indicate that some grains spent <50Myr in the ISM compared to others there for >1Gyr. It seems reasonable to assume that the grains present in the ISM for the longest periods of time are more likely to have experienced at least one, if not more, shockfronts fast enough to implant ions below their surfaces. Grains that do not contain the products of ion implantation probably did not experience a significant shockwave, perhaps because they were only in the ISM for a short time.

Using Si isotopic compositions, Alexander (1993) calculated that 10 – 100 AGB stars must have contributed SiC grains to the presolar molecular cloud. Combined with the wide range of cosmic-ray exposure ages measured in presolar

SiC, this suggests that not all the SiC grains were formed at the same place or time, and that not all grains resided in the ISM for the same period of time. The distribution of trace elements within SiC grains appear to be consistent with this model, with some grains apparently having experienced very little processing in their histories, whilst others must have been altered in the ISM.

4.5 SUMMARY

We have produced complete depth-profiles of Li, B, Mg, Al, K, Ca, Ti, V, Cr and Fe in 11 acid-extracted presolar SiC grains. The average elemental abundance patterns of Mg, Fe, Ca, Al, Ti and V indicate that condensation processes heavily dictate the abundances of these elements in presolar SiC.

We find evidence for two distinct populations of SiC grains based upon the distribution of trace elements within them. The grains in one group contain either homogenous trace element distributions, or evidence of elemental zoning. These are explained by condensation processes around the grain's parent stars. Silicon carbide grains belonging to the other group have enrichments of several trace elements to depths of up to ~200nm. These are attributed to the implantation of ions at velocities of ~1000kms^{-1}. Supernova shockwaves in the ISM are the suggested source of implantation.

The two populations suggest that some SiC grains experienced no, or only minimal, processing prior to arrival in the presolar molecular cloud, whereas others must have passed through high velocity shockwaves. With previous calculations of residence times ranging from <50Myr to >1Gyr, it is suggested that the youngest grains may never have seen a significant shockfront during their time in the ISM.

4.6 ADDITIONAL DATA

4.6.1 A geometrical model to estimate the effects of primary ion beam mixing when there is a steep elemental abundance gradient between two layers in a grain

Figure 4a.1 shows the set-up of our geometrical model. The model assumes a spherical grain of diameter 1μm. The model grain has an outer rim with an elemental abundance of 1 and inner core with an abundance of 0. The thickness of the outer rim is altered to show the effects of thicker or thinner enriched layers. If such a grain were to be sputtered by a primary ion beam the initial secondary ion signal would only come from the rim.

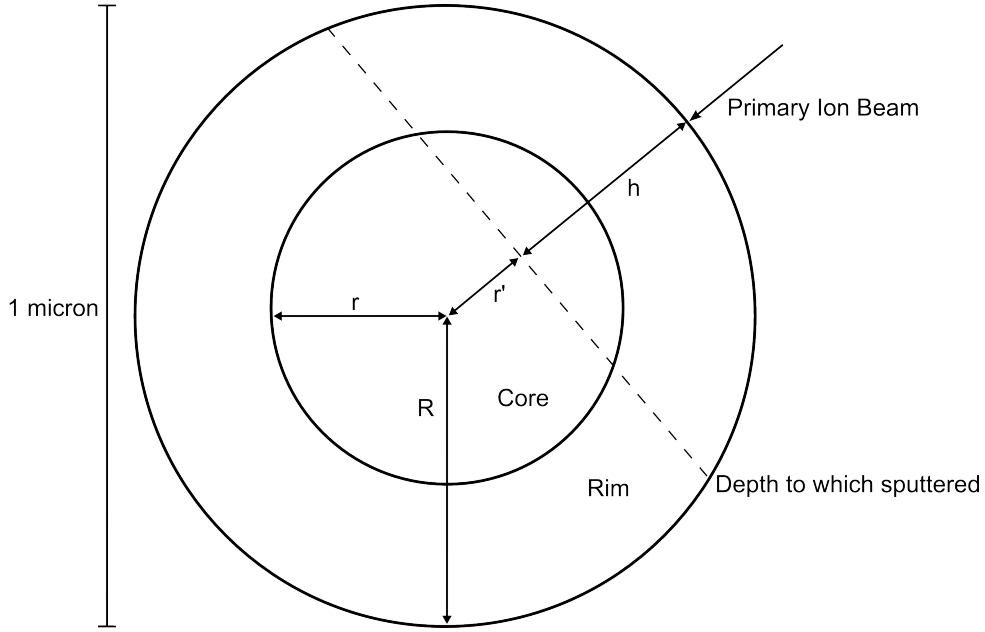

Figure 4a.1 Set-up of our geometrical model that shows the effects of primary ion beam mixing when a spherical grain has an outer rim enriched in an element relative to the core. The primary ion beam impacts the grain at an angle of 45°. Initial sputtering is through the rim until enough material is removed so that part of the grain core becomes exposed to the primary ion beam. If the thickness of the rim is less than the achievable spatial resolution then the secondary ion signal will now come from both the core and rim.

Eventually enough material would be sputtered so that the core becomes exposed. If the spatial resolution is not sufficient to resolve the two regions, then during analysis of the core the overall signal is a combination of both that from the rim and also the core. Initially the ratio of exposed rim to core would be high, providing a signal dominated by the rim abundance of 1. As the grain continued to be sputtered the rim/core ratio decreases and an increased fraction of the signal would come from the core.

If R is the radius of the model grain, r the radius of the grain core, r' the changing radius of the core during sputtering and h is the depth to which sputtered, then this effect can be described as;

when $h > R\text{-}r$:-

$$r' = R - h \qquad \text{(Eq. 4a.1)}$$

Observed from the primary ion beam the area of the exposed grain core is given by:-

$$\pi (r^2 - r'^2) \qquad \text{(Eq. 4a.2)}$$

and the area of the exposed grain rim:-

$$\pi (R^2 - r^2) \qquad \text{(Eq. 4a.3)}$$

The fraction of exposed outer rim relative to the total area during sputtering is given by:-

$$\frac{(R^2 - r^2)}{(R^2 - r'^2)} \qquad \text{(Eq. 4a.4)}$$

The results of our model are shown in Figure 4a.2. It is important to note that this is a simple model that assumes a spherical grain. The model also assumes that the sputtering rate remains constant throughout the measurements. It therefore does not take into account irregular grain shapes or a changing crystallography, which could lead to preferential sputtering.

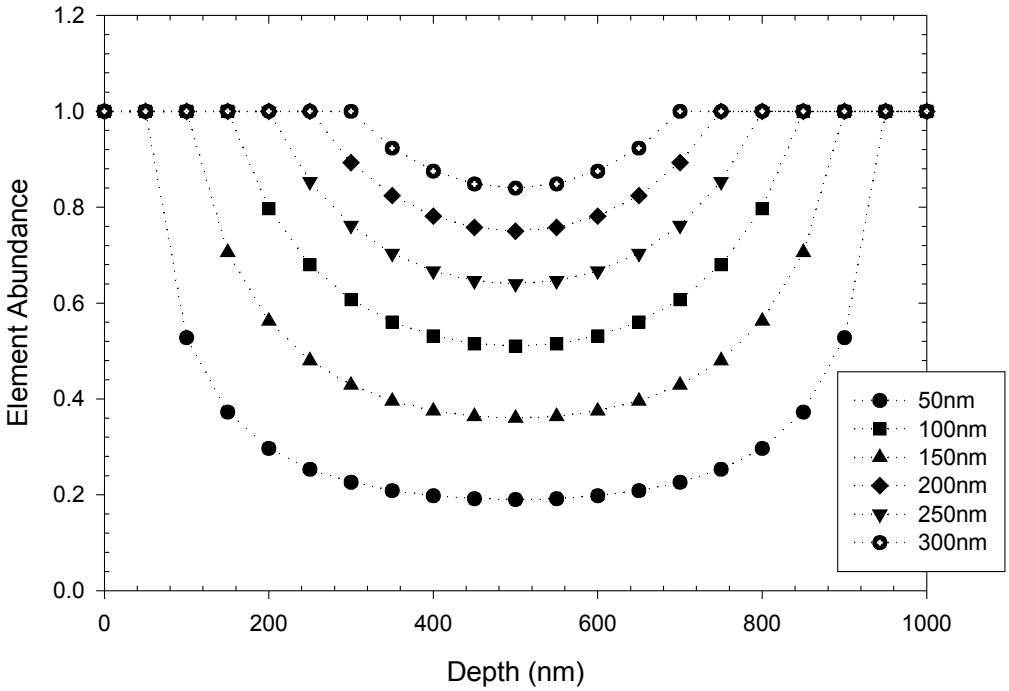

Figure 4a.2 Geometrical model to show the effects of primary ion beam mixing when a grain has an outer rim enriched in an element relative to the grain core. The element abundance represents the fraction of outer rim exposed to the primary ion beam during sputtering (see Eq. 4a.4). In the model the thickness of the enriched outer rim is changed (intervals between 50 – 300nm) to show how abundances measured in the grain core are upper limits determined by the amount of signal acquired from the rim/core in a single analysis.

4.6.2 Trace element depth-profiles within individual presolar SiC grains

AK-MM2-G-1

The Al/Si, Ti/Si, V/Si and Cr/Si ratios all rose from the grain surface (on average by a factor of 80) to a peak at ~150nm depth. The abundances of these elements then decreased, by up to a factor of 15, as we sputtered towards the grain core. Li/Si also peaked at this depth but its abundance did not drop within the core of the grain.

The Mg/Si and Fe/Si ratios did not show similar peaks in abundance. Instead their abundances in the grain core were approximately a factor of 20 greater than in the outer regions of the grain.

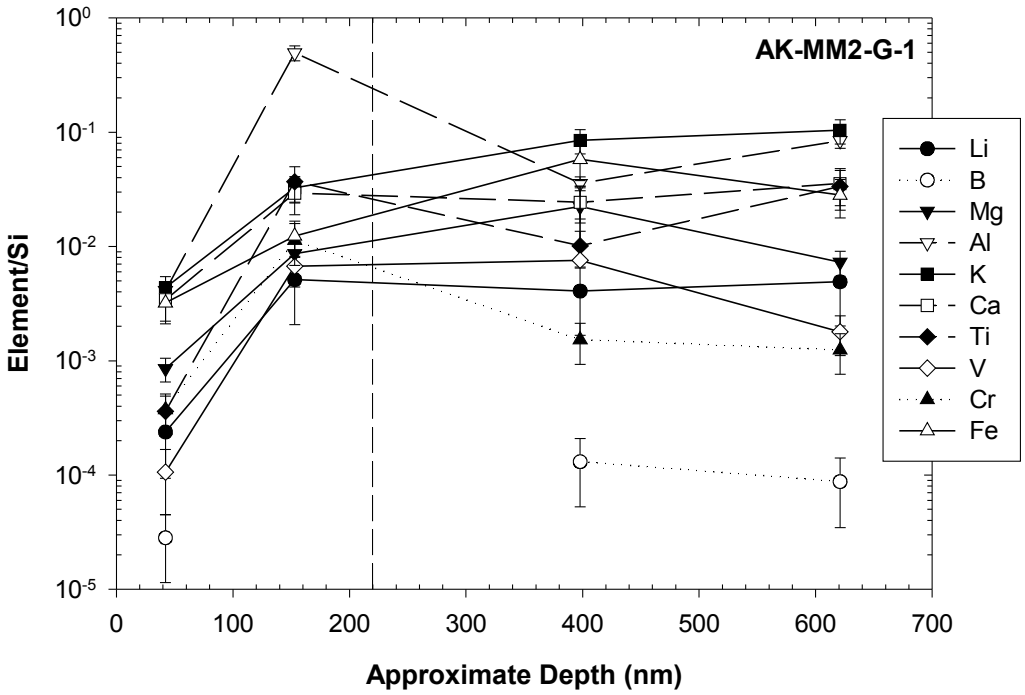

Figure 4a.3 Trace element depth-profile through presolar SiC grain AK-MM2-G-1. Dashed vertical lines indicate where the grain was removed from the TOFSIMS and re-imaged using the ESEM. Depth-profiles do not always start from 0nm as some material was sputtered away during the secondary ion imaging used to locate the grains in the TOFSIMS. Error bars are 1σ.

AK-MM2-G-2

The abundances of Mg, Ca, Ti, V, Cr and Fe were high within the outer 50nm before falling to a minimum in the grain core. For Mg/Si and Fe/Si this decrease was approximately a factor of 20, whilst for others, such as Ti/Si and V/Si, it was only around a factor of 4. The abundances of all of these elements then increased by similar amounts as the far side of the grain was exposed, producing symmetrical depth-profiles.

In contrast the K depth-profile did not display such a dip. The K/Si ratio peaked in the centre of the grain (increasing by a factor of 4) before decreasing at the far side.

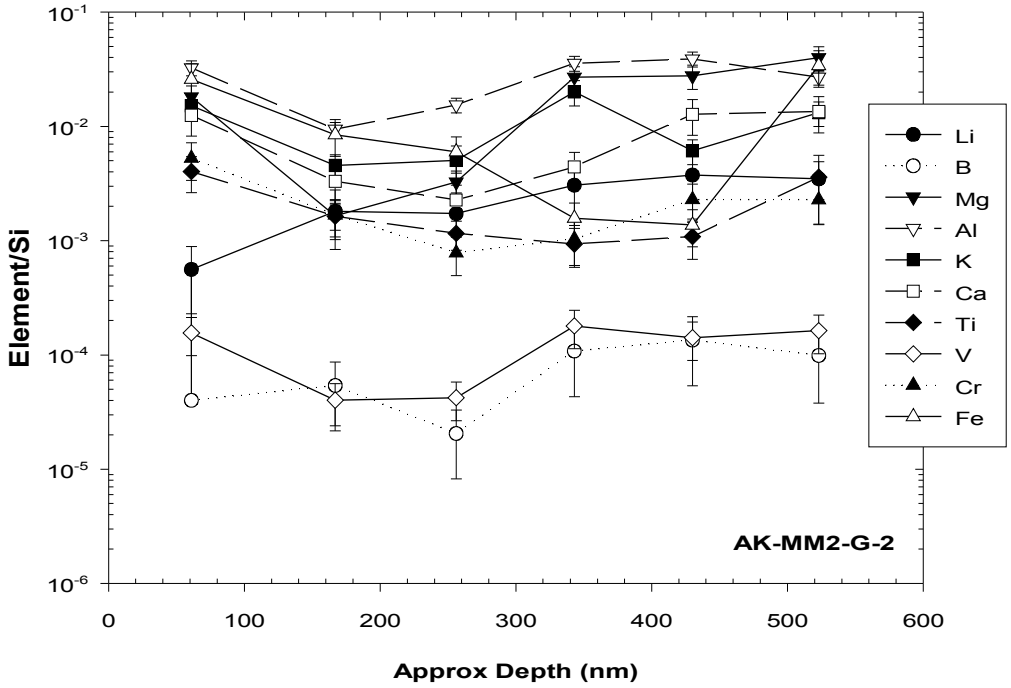

Figure 4a.4 Trace element depth-profile through AK-MM2-G-2 (see Figure 4a.3 for presentation details).

AK-MM2-M-1

Lithium had a symmetrical depth-profile, with a grain core abundance of a factor of 40 lower than that seen near the grain surface. K/Si had a similar depth-profile. However, the minimum K/Si ratio was not observed exactly in the grain core, rather towards the far side of the grain (~250nm).

The Ca/Si ratio fell by a factor of 10 from the grain surface before rising again by a comparable amount and then remaining similar throughout the rest of the grain. The abundances of the other elements did not vary significantly within the grain.

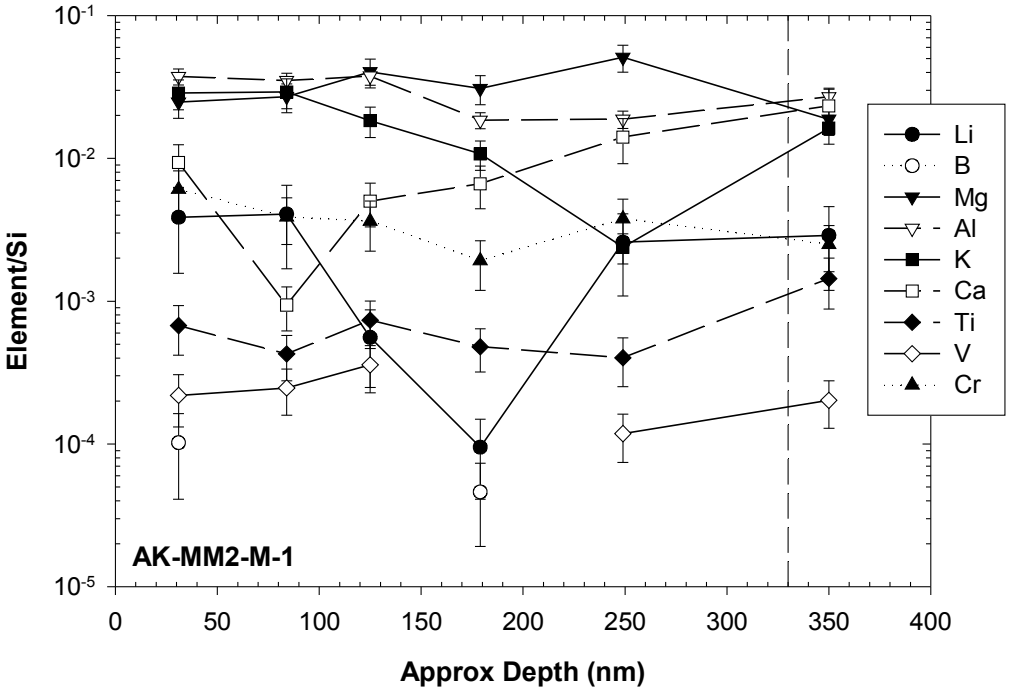

Figure 4a.5 Trace element depth-profile through AK-MM2-M-1 (see Figure 4a.3 for presentation details).

The Mg/Si, Ca/Si and V/Si were higher in the core than the surface by factors of ~6. With the exception of Cr/Si, which decreased by a factor of 8 at ~800nm, the other elements had "flat" depth-profiles, with no significant variations in their abundances as the grain was sputtered away.

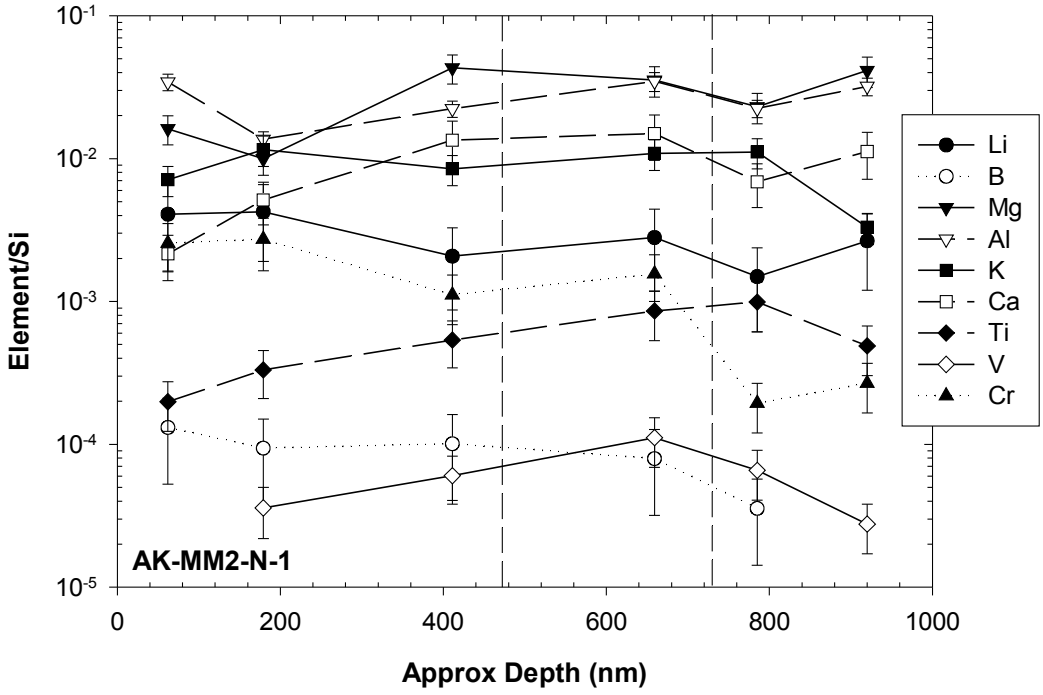

Figure 4a.6 Trace element depth-profile through AK-MM2-N-1 (see Figure 4a.3 for presentation details).

AK-MM2-delta-1

The Li/Si, Al/Si, K/Si and Ca/Si ratios all increased (on average by a factor of 190) from the grain surface to a peak at ~200nm. Their abundances then fell, by a factor of 10 – 40, as the core of the grain was reached. Interestingly the Ca/Si ratio appeared to rise again to a second corresponding peak at a depth of ~700nm.

The Ti/Si, Cr/Si and Fe/Si ratios also peaked at ~200nm, although the subsequent abundance decrease in the grain core was less severe (up to a factor of 10).

The Mg/Si ratio was highest at the grain surface. It then decreased throughout the grain. The Mg abundance at the far side of the grain was approximately a factor of 25 less than the initial value.

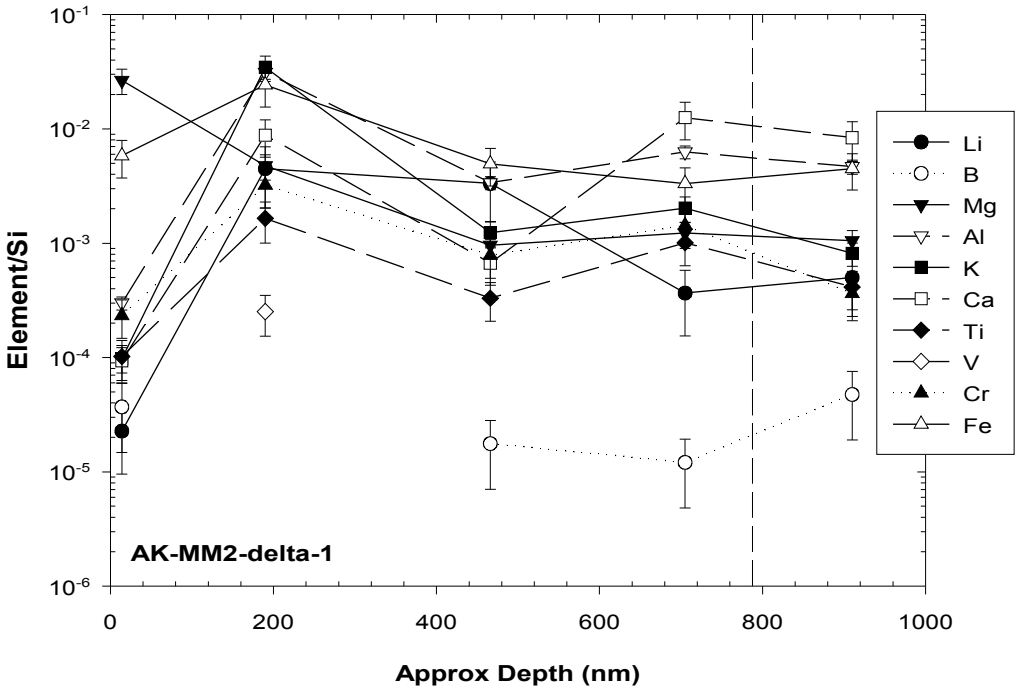

Figure 4a.7 Trace element depth-profile through AK-MM2-delta-1 (see Figure 4a.3 for presentation details).

AK-MM2-delta-2

The Ti/Si ratio increased from the grain surface (by a factor of 20) to a peak at ~300nm. The Ti abundance then decreased by a factor of ~700 in the grain core. This may have been caused by sputtering of a small TiC sub-grain, although if so, it was not observed in the secondary ion images. K/Si rose to a peak at ~200nm but its abundance then fell only slightly in the grain core.

The Li/Si ratio was constant throughout the grain except for a dip in abundance (by a factor of 6) seen at ~200nm.

The Mg/Si, Al/Si, Ca/Si, Cr/Si and Fe/Si ratios were high at the grain surface and remained so during the first five measurements. From this point their abundances then decreased as the grain was sputtered away, eventually falling to a value up to a factor of 25 lower than those observed during the first ~200nm.

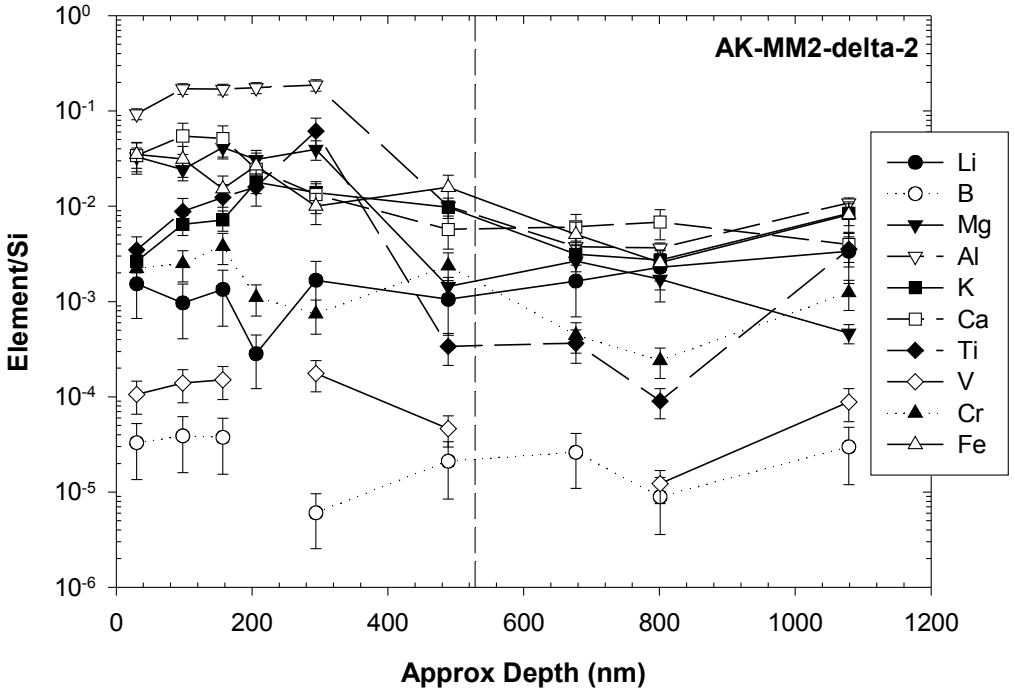

Figure 4a.8 Trace element depth-profile through AK-MM2-delta-2 (see Figure 4a.3 for presentation details).

AK-MM2-5-1

The abundances of most elements remained consistent throughout the grain until showing a dramatic decrease at a depth of ~820nm. This occurred during the two measurements immediately after the grain had been removed from the TOFSIMS and re-imaged using the ESEM. Although no effect on measured trace element abundances was observed when testing the depth-profiling technique on a meteoritic silicate grain, it seems likely that this decrease is an effect of either sample handling or ESEM analysis and is not a true variation in elemental abundances at this depth within the grain (see Section 4.4.2). The data from these two measurements has been excluded from the data set.

The Al/Si ratio was higher within the core relative to the outer parts of the grain by a factor of 40. The Mg/Si ratio was highest at the grain surface before decreasing as the grain was sputtered away. The abundance at the far side was a factor of 30 lower than the original exposed surface. For V the opposite occurred, with V/Si lowest at the near side surface and a factor of 25 greater at the far side.

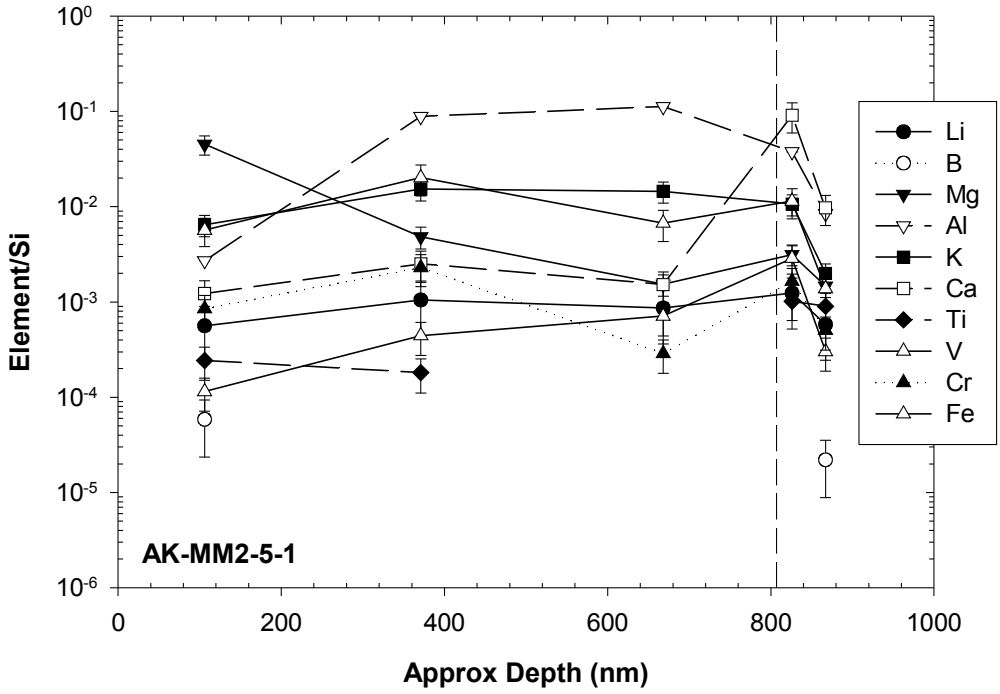

Figure 4a.9 Trace element depth-profile through AK-MM2-5-1 (see Figure 4a.3 for presentation details). Data obtained after the grain was re-imaged has been excluded from Table 4.2 but is still shown in the figure.

AK-KJG-D-1

The Li, Mg, Ti, Cr and Fe abundances were highest at the surface before decreasing as the grain was sputtered away. The largest decrease was observed for Li/Si, which fell by a factor of 60, whilst the smallest was a factor of 5 for Ti/Si.

The K/Si and Ca/Si ratios decreased sharply within the first two measurements by factors of 30 and 115 respectively. The K/Si and Ca/Si ratios then remained constant.

The Al/Si ratio was flat throughout the first 400nm of the grain before rising by a factor of 10. The Al/Si ratio then stayed at this higher value as the rest of the grain was sputtered away.

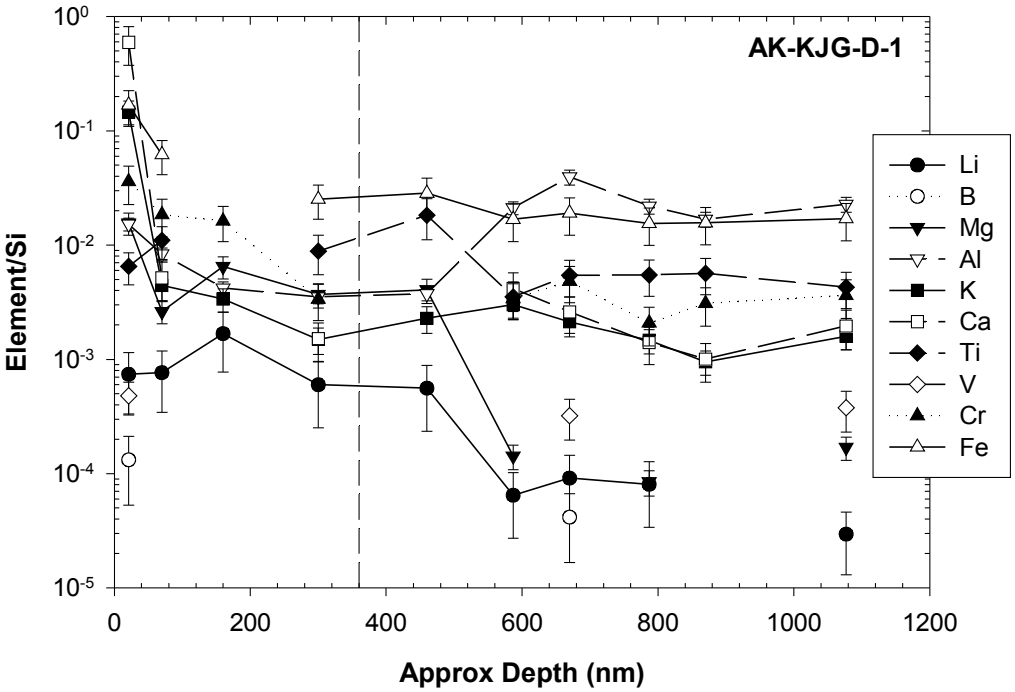

Figure 4a.10 Trace element depth-profile through AK-KJG-D-1 (see Figure 4a.3 for presentation details).

AK-KJG-D-2

The Li/Si, Mg/Si, Ca/Si and Cr/Si ratios were highest within the outer 150nm of the grain. Their abundances then fell by a factor 3 – 7 in the grain core before showing an increase at the far side of the grain.

The K/Si ratio rose to a peak at ~150nm. This increase, which was by a factor of 6, was then followed by a decrease by a factor of 4 within the grain core.

The Al/Si ratio showed very little variation as the grain was sputtered away.

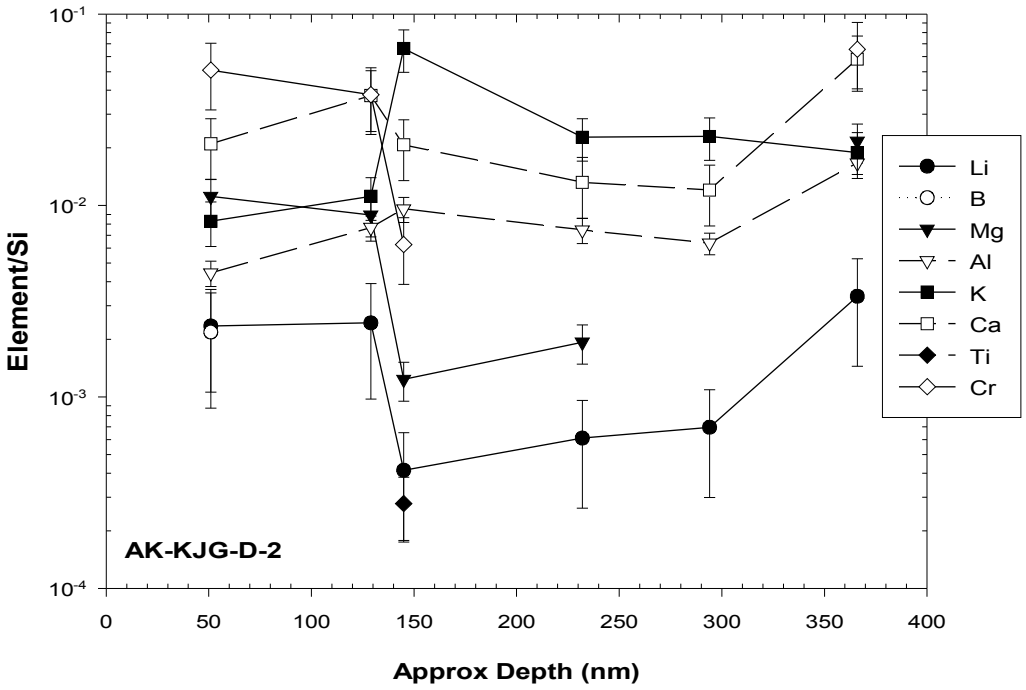

Figure 4a.11 Trace element depth-profile through AK-KJG-D-2 (see Figure 4a.3 for presentation details).

AK-KJG-M-1

The elements Li, B, Mg, Al and K all had symmetrical depth-profiles where abundances in the grain core were lower than those at the outer surfaces of the grain. For Li/Si and B/Si the decrease between the surface and the core was a factor of 4. For Mg/Si, Al/Si and K/Si it was a factor of 3.

The Ca, Ti, Cr and Fe abundances remained constant throughout this grain. This produced flat depth-profiles for these elements.

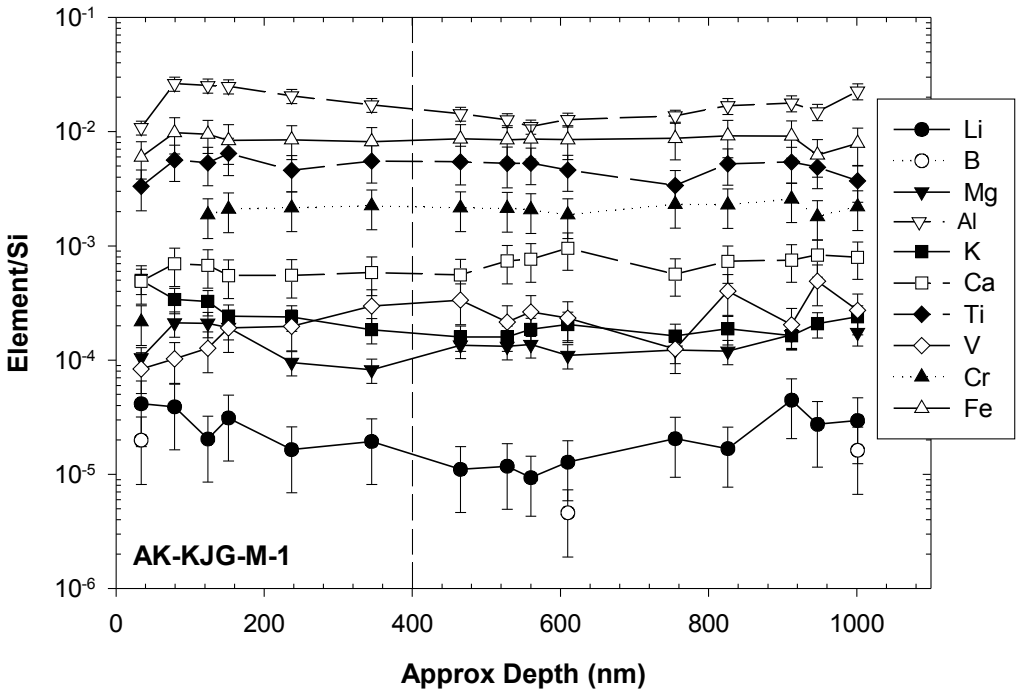

Figure 4a.12 Trace element depth-profile through AK-KJG-M-1 (see Figure 4a.3 for presentation details).

AK-KJG-6-1

The Li/Si, by a factor of 8, and Mg/Si and Ca/Si by a factor of 4, all rose from the surface abundance before remaining consistent throughout the grain. The K/Si ratio decreased from the grain surface by a factor of 7 before flattening out. All elements (excluding B and V for which there were insufficient counts) displayed a significant dip (by up to a factor of 35) in their abundances at a depth of ~700nm. This depth corresponds with when the sample was removed from the TOFSIMS and re-imaged using the ESEM.

A similar decrease in abundance after re-imaging was observed for grain AK-MM2-5-1 (see above), although not during the analysis of a meteoritic silicate grain using the same analytical procedure. Whereas the abundance decreases occurred at the far side of grain AK-MM2-5-1, here there was sufficient material left for further measurements. The abundances of all elements increased to the values measured before the sample was re-imaged within two measurements, supporting the idea that the decrease is the result of sample handling or ESEM analysis. The data from this measurement has therefore been excluded.

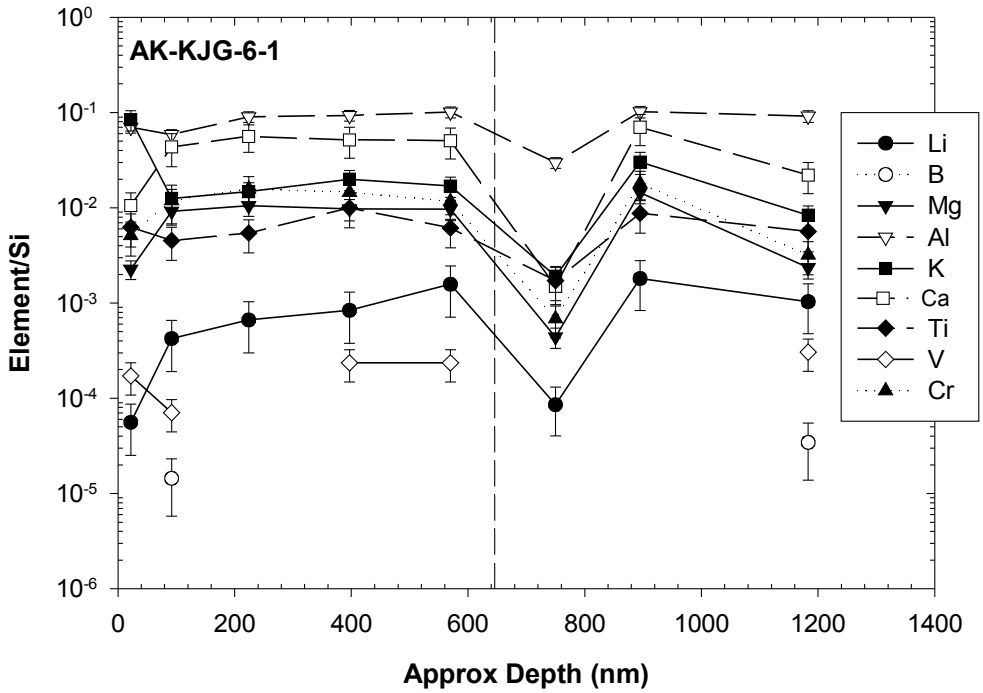

Figure 4a.13 Trace element depth-profile through AK-KJG-6-1 (see Figure 4a.3 for presentation details). Data obtained after the grain was re-imaged has been excluded from Table 4.2 but is still shown in the figure.

Chapter 5

Amorphous carbon grains in the Murchison meteorite

Ashley King[1], Torsten Henkel[1], Sean Chapman[1], Henner Busemann[1], Detlef Rost[1], Christelle Guillermier[2], Martin Lee[3], Ian Franchi[2] and Ian C. Lyon[1]

[1]The University of Manchester, School of Earth, Atmospheric and Environmental Sciences, Oxford Road, Manchester, M13 9PL, UK.
[2]The Open University, Planetary and Space Sciences Research Institute, Walton Hall, Milton Keynes, MK7 6AA, U.K.
[3]The University of Glasgow, Department of Geographical and Earth Sciences, Gregory Building, Lilybank Gardens, Glasgow, G12 8QQ, U.K.

Adapted from: King A., Henkel T., Chapman S., Busemann H., Rost D., Guillermier C., Lee M., Franchi I. and Lyon I.C. (2010) Amorphous carbon grains in the Murchison meteorite, to be submitted to Meteoritics and Planetary Science.

A study of micron-sized carbonaceous grains from the Murchison meteorite was undertaken. The structural and isotopic nature of 33 grains were determined by using scanning and transmission electron microscopy, Raman spectroscopy, time-of-flight secondary ion mass spectrometry and NanoSIMS analysis. The grains contain solar $^{13}C/^{12}C$, $^{15}N/^{14}N$ and $^{18}O/^{16}O$ isotopic ratios. Deuterium is enriched in the grains with δD values up to +333 ± 110‰. Raman characteristics and TEM observations of their internal structure show them to be composed of highly disordered and amorphous carbon. We hypothesize that the grains may have acquired their amorphous structure through irradiation in the proto-solar nebula, a scenario supported by previous studies of terrestrial soot irradiated by H^+ and He^+ ion fluences of ~10^{15} – 10^{16} ions cm^{-2}. The deuterium enrichments suggest exchange of H with cold interstellar gas in the outer part of the early nebula, although formation in the interstellar medium cannot be excluded. If the amorphization of the grains was caused by irradiation with solar wind H ions, then this is likely to have substantially lowered any original δD composition.

5.1 INTRODUCTION

Determining the nature of carbon in extra-terrestrial samples helps to constrain the mechanisms by which carbonaceous materials were formed and processed in the interstellar medium (ISM) or early solar nebula.

Carbonaceous material is present within primitive meteorites (for reviews see Botta and Bada 2002, Sephton 2002, Pizzarello et al. 2006), interplanetary dust particles (IDPs) (e.g. Rietmeijer 1998, Bradley 2003) and cometary dust returned by the Stardust mission (Sandford et al. 2006, Muñoz Caro et al. 2008, Rotundi et al. 2008). Analysis of these samples indicates that the carbon exists in a variety of molecular structures and is isotopically diverse, consistent with its formation and processing through several different mechanisms (for a review see Pizzarello et al. 2006).

In carbonaceous chondrites, 70 – 99% of the carbon occurs as a complex macromolecular (kerogen-like) material, often referred to as insoluble organic matter (IOM).

Enrichments in D and ^{15}N suggest that at least part of the IOM either formed in the ISM or the cold outer regions of the proto-solar nebula (Robert and Epstein 1982, Yang and Epstein 1983, Kerridge et al. 1987, Busemann et al. 2006). The enrichments can be produced through ion-molecule reactions or catalytic mass fractionation processes at low temperatures (Millar et al. 1989, Aikawa and Herbst 1999, Sandford et al. 2001, Charnley and Rodgers 2008). Differences in the size of the enrichments observed between carbonaceous chondrite classes are likely to have been caused by varying degrees of parent body alteration (Alexander et al. 1998; 2007).

The amount of parent body processing is also reflected in the structural characteristics of the IOM. Much of the carbon present in IOM is structurally disordered (Matrajt et al. 2004, Bonal et al. 2006; 2007, Busemann et al. 2007, Quirico et al. 2009). However, several studies using Raman spectroscopy have shown that the most disordered carbon is found within the most primitive

meteorites i.e. those which underwent the least amount of alteration (Quirico et al. 2003, Bonal et al. 2006; 2007, Busemann et al. 2007). Heating can cause the graphitization of carbon. Therefore meteorite parent bodies that experienced increased levels of thermal metamorphism contain carbon of greater structural order.

Similar studies of primitive IDPs and cometary samples have found them to also contain carbon of a highly disordered nature (Wopenka 1988, Muñoz Caro et al. 2006; 2008, Sandford et al. 2006, Rotundi et al. 2008, Busemann et al. 2009).

Within the IOM there exists a carbon component that is presolar in origin. Nanodiamonds and spherical graphite grains contain isotopic anomalies in C, N, Ne and Xe that are up to several orders-of-magnitude different from solar ratios, but similar to those observed in a range of stellar environments (Amari et al. 1993; 1995b, Hoppe et al. 1995, Zinner et al. 1995). Irregularly shaped carbonaceous grains in meteorites typically contain elements with solar isotopic compositions (Amari et al. 1993, Zinner et al. 1995).

Presolar grains are isolated from meteorites using a series of harsh HF/HCl treatments (Amari et al. 1994). Recently, evidence has suggested that the use of such acids can alter or damage the surfaces of presolar grains (Stephan et al. 1997, Henkel et al. 2007a). This has led to the development of non-acid extraction procedures in order to provide pristine samples for analysis (Bernatowicz et al. 2003, Tizard et al. 2005).

Amorphous carbon has been reported in IOM extracted from carbonaceous chondrites and several ordinary chondrites (Busemann et al. 2007). It has also been detected as carbon flakes and nano-tubes in untreated meteorite residues (Garvie and Buseck 2004; 2006), hollow nano-globules in meteorite matrix (Nakamura-Messenger et al. 2006, Aoki and Akai 2008, Garvie et al. 2008), IDPs (Wopenka 1988, Muñoz Caro et al. 2006, Busemann et al. 2009, Davidson 2010) and cometary materials (Sandford et al. 2006, Muñoz Caro et al. 2008, Rotundi et al. 2008).

On Earth, amorphous carbon is not usually observed in kerogen-like materials (Wopenka and Pasteris 1993). However, Court et al. (2006; 2007) showed that increased exposure to ionizing irradiation in U-rich environments leads to greater radiolytic alteration of terrestrial organics. It was found that the most altered organics contained the most disordered and amorphous carbon, similar to that found in primitive extra-terrestrial samples.

In the ISM or early solar nebula, amorphous carbon may have been produced by ion irradiation of carbonaceous phases from cosmic-rays or high energy solar wind.

Investigations into the effects of ion irradiation at low temperatures on carbon-ices such as benzene (C_6H_6), methane (CH_4) or butane (C_4H_{10}) show that the ices can be converted, firstly into refractory residues and then, under increasing amounts of irradiation, amorphous carbon (Strazzulla et al. 2003, Ferini et al. 2004). Comparisons between the Raman spectra obtained from frozen hydrocarbons (Baratta et al. 2004) and terrestrial soot (Brunetto et al. 2009), used as analogs for extra-terrestrial samples, before and after irradiation with H^+ and He^+ ion fluences of $\sim 10^{15} - 10^{16}$ ions cm^{-2}, show that even highly ordered crystalline graphite can be altered to an amorphous phase.

Brearley (1990) also found small volumes of amorphous carbon within carbon-rich aggregates associated with Fe, Ni metal in ordinary chondrites. It was argued that Fischer-Tropsch reactions, which convert CO gas to hydrocarbons through hydrogenation in the presence of a catalyst, could have produced aggregates of Fe, Ni metal embedded in carbonaceous materials in the early solar nebula.

Here, we report combined secondary electron microscopy (SEM), transmission electron microscopy (TEM), isotopic and Raman analyses of a set of amorphous carbonaceous grains isolated from the Murchison meteorite.

5.2 EXPERIMENTAL PROCEDURE

We have previously developed a gentle separation procedure in order to isolate pristine presolar SiC grains from host meteorites according to their size and density characteristics (Tizard et al. 2005). The grains described here were discovered in size and density separations carried out following an adapted version of the Tizard et al. (2005) procedure. The intention was to study pristine presolar graphite, although the grains reported here were not graphite grains.

5.2.1 Adapted Gentle Separation Procedure

One-hundred and sixteen mg of Murchison matrix material, free from chondrules and calcium-, aluminium-rich inclusions (CAIs), were crushed using a stainless steel mortar and pestle. The sample was then dispersed in ultra-pure water and further broken down using freeze-thaw disaggregation. The sample underwent 138 freeze-thaw cycles by alternately dipping it between liquid N_2 (for 90s) and hot water (45°C for 60s). A small deposit of the disaggregated sample was examined using an environmental SEM (Philips XL30), and grain sizes were predominantly <20μm. The remaining sample was dried and then suspended in a 1:1 mixture of water and isopropanol.

Next, the sample was separated according to grain size using a fixed-angle rotor centrifuge. A size separation timetable was calculated according to Stokes' law and assuming a grain density of $1.6 gm^{-3}$ (see Tizard et al. 2005 for details). Size fractions were selected as: A >20μm, B = 7 – 20μm, C = 1 – 7μm, and D <1μm, by the corresponding time intervals and g-forces of 465s (at 1g), 633s (at 6g), and 620s (at 300g) (see Figure 5.1).

The largest size separation was carried out first. After each size separation the sedimented grains were siphoned from the sample. The size separation step was then repeated for both the sedimented grains and those still in suspension. Each size separation was repeated for a minimum of four times before all of the sediments from the separation step were added together, and similarly the

suspensions accumulated. The size-separated samples were dried before the next separation step was begun.

The size fractions B and C were separated by density using a series of organic heavy liquids (*Cargille Laboratories*) of densities 1.6, 2.05, 2.15 and 2.26gcm^{-3} (as presolar graphite grains have densities of 1.6 – 2.2gcm^{-3}).

Starting with the lowest density, the heavy liquid was introduced to the size fractions and mixed thoroughly by agitation in an ultrasonic bath for 15 minutes. The fractions were then centrifuged again according to a timetable calculated from Stokes' law. Following centrifugation, the heavy liquid was removed from the fraction, leaving behind only the sedimented grains. The sediment and floating separation underwent thorough washing in isopropanol and water, whilst also being agitated in the ultrasonic bath.

The density step was repeated twice more, with washing after each repeat separation, for both the sediment and floating separation. The next heavy liquid was then introduced and the process repeated until both size fractions had been separated into four density separations (see Figure 5.1).

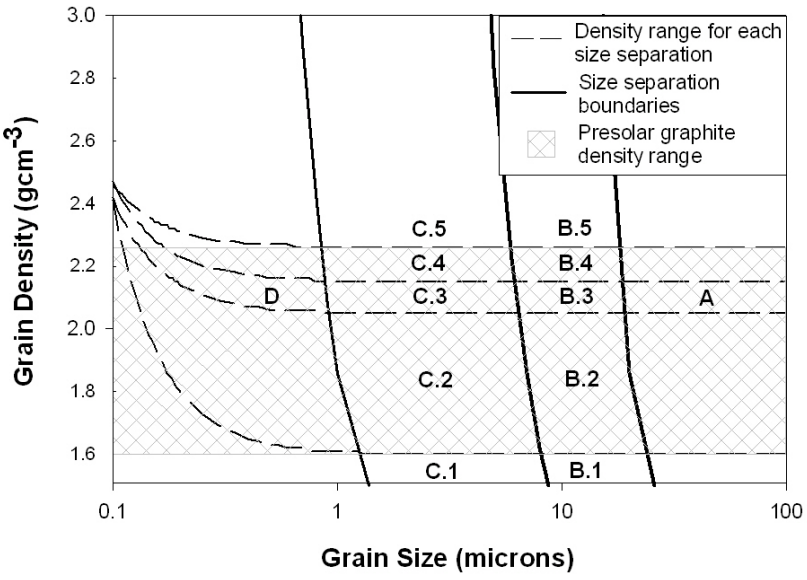

Figure 5.1 Final size and density fractions from the gentle separation procedure adapted for presolar graphite. Only the size fractions B and C were separated according to density. All of the grains discussed in this work came from the fractions B4 and C4.

To determine whether the heavy liquids contained any carbonaceous grains a small deposit of the 2.15gcm^{-3} heavy liquid was deposited onto a Au-foil and inspected using the ESEM. The heavy liquid appeared as a residue on the foil; however no visible grains were discovered. This residue was rarely seen in the final size and density fractions, indicating that the washing procedure was effective.

5.2.2 Samples

Two small aliquots from the size and density fraction B4 (7 – 20μm, 2.15 – 2.26gcm^{-3}), and one from C4 (1 – 7μm, 2.15 – 2.26gcm^{-3}) (initially selected as they were fractions likely to contain presolar graphite, see Figure 5.1), were deposited over three cleaned (through ultrasonication in isopropanol and acetone), ultra-pure (>99.999%) Au-foils with Cu-finder grids (Agar H15, 3.05mm, 125mesh) imprinted upon them.

No presolar graphite grains were located in the B4 and C4 fractions. In the size and density separations of Tizard et al. (2005), the SiC abundances in one separation was enriched by a factor of ~1000 from the Murchison whole rock abundance of ~6ppm to 0.67%.

In the B4 and C4 fractions in this study only ~2000 grains were on each foil. Assuming that the Murchison presolar graphite abundance of ~5ppm (Huss et al. 2003) was similarly enriched by a factor of 1000, we would expect ~11 of the 2000 grains to be presolar graphite grains. However, in another separation of Tizard et al. (2005), the enrichment factor was only ~360. A similar sized enrichment in the graphite separations would result in only ~4 out of the 2000 grains expected to be presolar graphite.

Carbonaceous grains within the samples, from herein referred to as B4a, B4b and C4a, were located using ESEM and energy dispersive X-ray analysis (EDX). Electron beam energies were kept relatively low (10 – 15kV) in order to minimize damage on grain surfaces. Ten carbonaceous grains were located in

sample B4a, 14 in B4b and 9 in C4a. Some examples of the grains are shown in Figure 5.2.

The positions of carbonaceous grains relative to the finder-grid were recorded and high resolution images taken. Grains were named according to their sample, grid location (letters A-Z, numbers 0-9) and numbered sequence within each grid area.

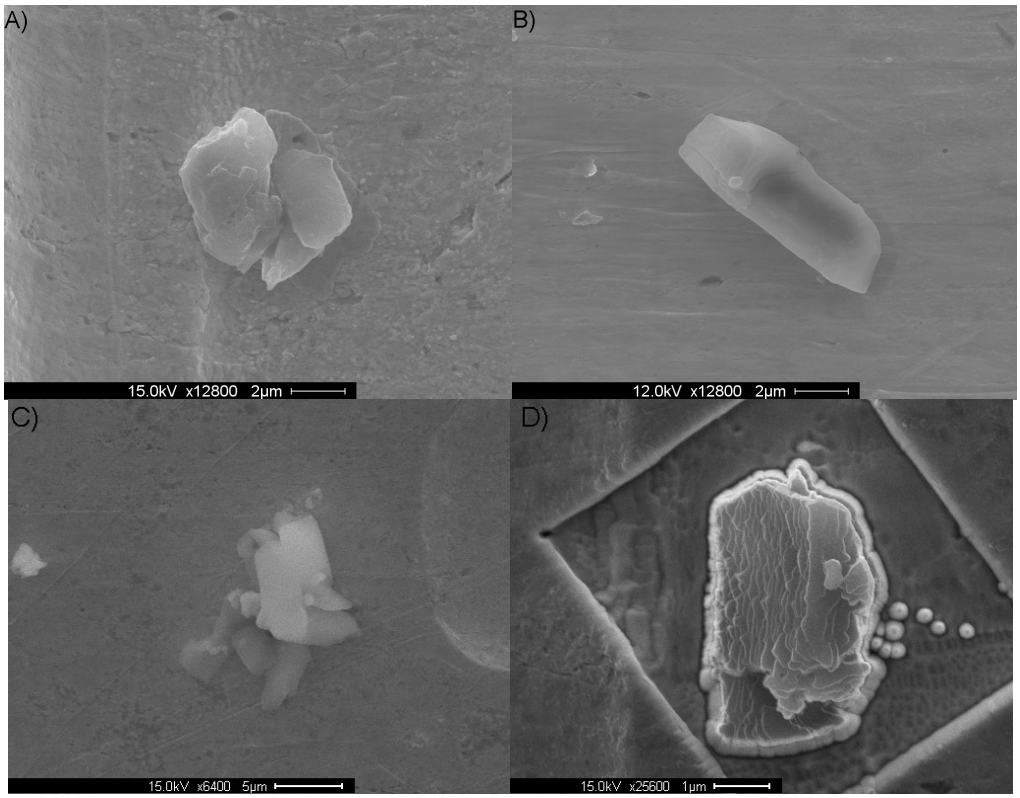

Figure 5.2 Three different carbonaceous grain morphologies were identified in both the B4 and C4 fractions. (A) B4a-Q-1 represents a "Flake". These grains were relatively flat and often hexagonal or disc shaped. (B) B4a-X-1 represents an "Elongated" grain that had a smooth surface. (C) B4b-1-6 is an example of a "Blocky" grain. These grains were very irregular and occasionally angular in appearance. (D) B4b-1-1 after SIMS analysis examination of the grain cores showed them to be platy with layers of carbonaceous material.

5.2.3 TOFSIMS

Secondary ion mass spectrometry (SIMS) uses high energy primary ions to sputter secondary ions from a sample. Time-of-flight secondary ion mass spectrometry (TOFSIMS) uses a pulsed primary ion beam and TOF mass spectrometer, allowing for the simultaneous detection of all secondary ion

species (either positive or negative ions) during a single analysis (for review see Stephan 2001). The elemental and isotopic compositions of samples can be analyzed together at sub-micron spatial resolution. Sample consumption rates are low, so samples may be depth-profiled or analyses combined with other analytical techniques.

Six of the carbonaceous grains from B4a, and all from C4a, were analyzed for $^{12}C/^{13}C$, $^{14}N/^{15}N$ and $^{16}O/^{18}O$ isotopic compositions using a TOFSIMS instrument equipped with a 25kV Au_n^+ liquid metal ion gun (LMIG) (IOG 25Au from Ionoptika Ltd, Southampton, UK, Davies et al. 2003, Hill and Blenkinsopp 2004) at the University of Manchester. Previous versions of this instrument, which instead utilized a Ga^+ LMIG, have been described in detail by Henkel et al. (2006; 2007b).

Measurements involved rastering a pulsed Au^+ primary ion beam over grain surfaces. The field-of-view of each measurement was adjusted according to the grain size. Sputtered negative secondary ions were extracted away from the sample and separated using a TOF mass spectrometer (R-500 from Kore Technology, Ely, UK). The measurements were run in a scanning mode, with each scan recorded separately and then combined to give a total secondary ion image. Scans contained 64 x 64 pixels, with 150 – 400 primary ion shots per pixel. Each pixel contained a complete negative secondary ion mass spectrum.

A delayed secondary ion extraction technique was used. This bunches together secondary ions of the same species by delaying their extraction, done by switching on the sample potential, until the end of a long primary ion pulse. In this way high mass resolutions ($m/\delta m$ ~3000) could still be achieved despite using long primary ion pulses to boost sensitivity.

The achieved mass resolution was insufficient to fully resolve the $^{12}C^1H$ interference from ^{13}C. Attempts were made to separate the $^{12}C^1H$ interference from the ^{13}C peak using the peak deconvolution method described by Stephan (2001). The low mass edge of the peak at mass 13 was fitted to the ^{12}C peak, with the scaling factor between the peaks giving the $^{12}C/^{13}C$ ratio. However, as the

$^{12}C^{1}H$ interference was of similar size to the ^{12}C peak it was not possible to use the deconvolution method.

Despite requiring greater mass resolutions (*m/δm* ~4300 to resolve $^{12}C^{15}N$ from $^{13}C^{14}N$) the C and N isotopic ratios were determined by measuring CN^-. The $^{12}C/^{13}C$ and $^{14}N/^{15}N$ ratios were calculated from peaks at mass 26 ($^{12}C^{14}N$), and mass 27 ($^{12}C^{15}N$ and $^{13}C^{14}N$). The $^{12}C^{14}N$ peak was fitted to the left edge of the peak at mass 27 and the scaling factor between the two peaks gave the $^{14}N/^{15}N$ ratio. Similarly, the $^{12}C^{14}N$ was also fitted to the right edge of the peak at mass 27 to give the $^{12}C/^{13}C$ ratio.

Offline data processing involved removing any unwanted (due to noise or loss of primary ion current) scans, applying shift corrections before combining scans, deadtime corrections, and defining regions of interest (ROIs). Mass fractionation corrections were determined by analyzing terrestrial graphitic grains, comparable in size to the carbonaceous grains and assumed to have solar $^{12}C/^{13}C$ (89), $^{14}N/^{15}N$ (272) and $^{16}O/^{18}O$ (499) isotopic compositions, under the same conditions.

5.2.4 NanoSIMS

The NanoSIMS can provide high signal rates and spatial resolutions down to 50nm (for a review see Hoppe 2006). Mass resolutions up to *m/δm* ~6000 make it suitable for the accurate determination of isotopic ratios in samples. However, as the secondary ions are separated using a double-focusing magnetic sector mass spectrometer, often only seven isotopic species are detected during an analysis.

The $^{2}D/^{1}H$, $^{12}C/^{13}C$, $^{14}N/^{15}N$ and $^{16}O/^{18}O$ isotopic compositions of carbonaceous grains from B4b were measured using the Cameca NanoSIMS 50L at the Open University, Milton Keynes. Measurements were made in a scanning mode by rastering a Cs^+ primary ion beam over the grain surfaces, with the field-of-view dictated by the grain size.

In the first round of measurements negative secondary ions of ^{12}C, ^{13}C, ^{16}O, ^{18}O, $^{12}C^{14}N$ and $^{12}C^{15}N$ were collected simultaneously in six electron multiplier detectors. Secondary electrons were also collected for imaging during a measurement. The primary ion beam current was ~2pA and recorded scans contained 512 × 512 pixels.

All grains were initially analyzed without pre-sputtering. Four grains (B4b-1-3, B4b-1-4, B4b-5-1 and B4b-7-1) were then analyzed a second time following pre-sputtering with a de-focused beam that had a current of 400pA. This ensured that the cores of the grains, where isotopic ratios could not be affected by any potential contamination with the organic heavy liquids used in the grain separation procedure, were definitely analyzed.

The grains were then analyzed using Raman spectroscopy (see Section 5.2.5) before a second round of NanoSIMS measurements. Negative secondary ions of ^{1}H, ^{2}D and ^{12}C were collected using a primary ion beam current of ~20pA. Scans from these measurements contained 256 × 256 pixels.

Data was processed offline, with any unwanted scans (due to noise) removed, shifts between scans corrected, deadtime corrections applied, ROIs defined, and isotope ratio images produced.

Mass fractionation of all isotopic ratios was corrected with measurements of well characterized terrestrial samples and insoluble organic matter (IOM) (extracted from the meteorites Allende, Murchison, EET 92042 and GRO 95577, Alexander et al. 2007).

It should be noted that the $^{12}C/^{13}C$ isotopic ratios were not corrected for quasi-simultaneous arrival (QSA) of C secondary ions. During NanoSIMS analysis the probability that more than one C secondary ion will arrive at the detector at the same time is not negligible (Slodzian et al. 2004). When the C secondary ion count rate of the standard differs from that of the sample, as was the case here, then QSA may have an affect of several percent on the measured $^{12}C/^{13}C$ ratio. However, as presolar graphite grains typically contain $^{12}C/^{13}C$ ratios orders-of-

magnitude different from solar, QSA should not have restricted our ability to distinguish grains of presolar origin.

5.2.5 Raman Spectroscopy

Raman spectroscopy provides a relatively non-destructive method by which the structure of a sample can be determined. In Raman spectroscopy, photons of the fundamental laser frequency interact with vibrational modes of molecular bonds or crystal lattices producing inelastically scattered photons. These photons can then be detected, with the interactions causing their energy to be increased or decreased. Raman band positions are therefore given as shifts relative to the wavelength of the exciting laser.

Carbonaceous materials produce two major bands; the D ("disordered") and the G ("graphitic"), which occur at positions of 1355cm^{-1} and 1581cm^{-1} respectively (see Wopenka and Pasteris 1993). Depending upon the level of disorder in the carbon, minor D-bands, such as D_2 at ~1620cm^{-1}, D_3 at ~1500cm^{-1} and D_4 at ~1200cm^{-1}, may also occur in the spectrum (Sadezkey et al. 2005). We have not attempted to resolve the minor D-bands in this study. However, it should be noted that these secondary bands can affect the position of the major D and G bands; in particular the D_2-band causes a broadening of the G-band and a shift in its position to higher values.

The relative intensities of the major D and G bands, plus their central peak positions and peak widths, can provide information regarding the structural order of the carbon in the sample. Pure graphite produces only the G-band. The presence of increasing disorder within the carbon structure, either through defects, crystal boundary effects, polycrystallinity or small domain sizes, is indicated by an increasing D-band intensity (e.g. Tuinstra and Koenig 1970).

Raman analyses of all carbonaceous grains were acquired after they had been analyzed either by TOFSIMS or in the NanoSIMS. This allowed us to analyze the interior of grains rather than their outer surfaces, which may have been coated. Four grains from fraction B4a not sputtered during SIMS analyses were

also analyzed for comparison, but only two of these yielded usable Raman spectra (see below).

Spectra were obtained using a Horiba Scientific LabRAM 300 Raman microscope with a 632nm He:Ne exciting laser at the School of Chemical Engineering and Analytical Science, University of Manchester. A 10x objective was used and the spot size of the laser was ~140μm with a power of ~70mW. Most grains were sufficiently far apart, so that despite the large spot size, only spectra from the grain of interest were recorded. However, in two cases (* in Table 5.3) grains had to be analyzed as pairs.

Spectra were collected as spot measurements in the spectral range 800 – 1800cm^{1}. Three spot measurements were taken from each grain analyzed. Reported D and G band values are the mean of the three measurements with 1σ errors.

Spectra were fitted with Lorentzian profiles for the Raman D and G bands with a linear background using custom software (written in the IDL programming language (Research Systems, Inc.)) and following the method described in Busemann et al. (2007).

Peak fitting was attempted for each spectrum collected. However, spectra with steep and irregularly shaped backgrounds, due to fluorescence resulting from the irradiation of the carbonaceous grains by the laser, could not be reliably fitted and were therefore excluded. Any spectra whose fitting errors were >100% for the D and G band peak widths or central positions were also excluded. For several grains no useful Raman spectra were obtained, either due to the fitting criteria or a lack of Raman-active carbon. Spikes in the spectra from cosmic-rays hitting the detector during a measurement were automatically corrected during fitting.

For calibration, and to compare spectra from our instrument to that obtained in other laboratories, a terrestrial graphitic grain, along with well characterized IOM fragments from the meteorites Murchison (CM2), EET 92042 (CR2), Leoville

(CV3.0) and Allende (CV3.2) (Alexander et al. 2007, Busemann et al. 2007), were also analyzed. The determined D and G band parameters (peak widths (Γ) and central peak positions (ω)) are presented in Table 5.1.

The IOM fragments, plus the carbonaceous grains in B4b, were pressed into the Au-foil prior to any analyses. It should be noted that high pressures (i.e. >5GPa) can produce significant upward shifts in Raman band positions (Huang et al. 2010a; 2010b). However, such pressures were never applied to the IOM and carbonaceous grains, so any pressure induced shift is not thought to be an issue here.

Sample	ω_G	Γ_G	ω_D	Γ_D	D/G
Murchison (CM2)	1571.8 ± 0.8	123.7 ± 2.7	1323.9 ± 0.4	245.7 ± 1.3	1.93 ± 0.05
EET92042 (CR2)	1581.4 ± 2.5	135.3 ± 9.2	1335.7 ± 2.5	286.6 ± 7.3	1.82 ± 0.19
Leoville (CV3.0)	1600.3 ± 3.1	82.4 ± 10.9	1344.8 ± 3.3	224.2 ± 10.0	2.23 ± 0.4
Allende (CV3.2)	1592.0 ± 0.6	75.5 ± 1.8	1329.6 ± 0.4	107.8 ± 1.2	1.78 ± 0.06
Terrestrial Graphite	1581.3 ± 0.2	41.9 ± 0.5	1330.8 ± 0.2	55.4 ± 0.6	1.07 ± 0.02

Table 5.1 D and G band Raman data collected from well characterized IOM from the Murchison, EET92042, Leoville and Allende meteorites. A terrestrial graphite grain was also analyzed. Errors are 1σ.

Busemann et al. (2007) reported that IOM extracted from the most primitive meteorites (e.g. CM-type) produced the largest Γ_D, ω_D, and Γ_G values, and lowest ω_G values, reflecting the disordered nature of the carbon in the IOM. In contrast, IOM from more thermally altered meteorites (e.g. CV) showed the opposite trend in D and G band parameters.

In this study, carbon in the IOM from the primitive meteorites, Murchison and EET 92042, was more disordered than that present in the altered meteorites, Leoville and Allende. Measured D and G band parameters for the IOM were comparable to those reported by Busemann et al. (2007). Rotundi et al. (2008) performed a similar test at five different Raman laboratories. Results for Γ_D, Γ_G and ω_G from the different laboratories were comparable, relative to the large variations between the meteoritic IOM samples, indicating that the experimental set-ups did not cause the trend.

Analysis of the terrestrial graphitic grain produced much narrower Γ_D and Γ_G values than any of the IOM measured here; consistent with it's much more ordered nature (see Figure 5.3).

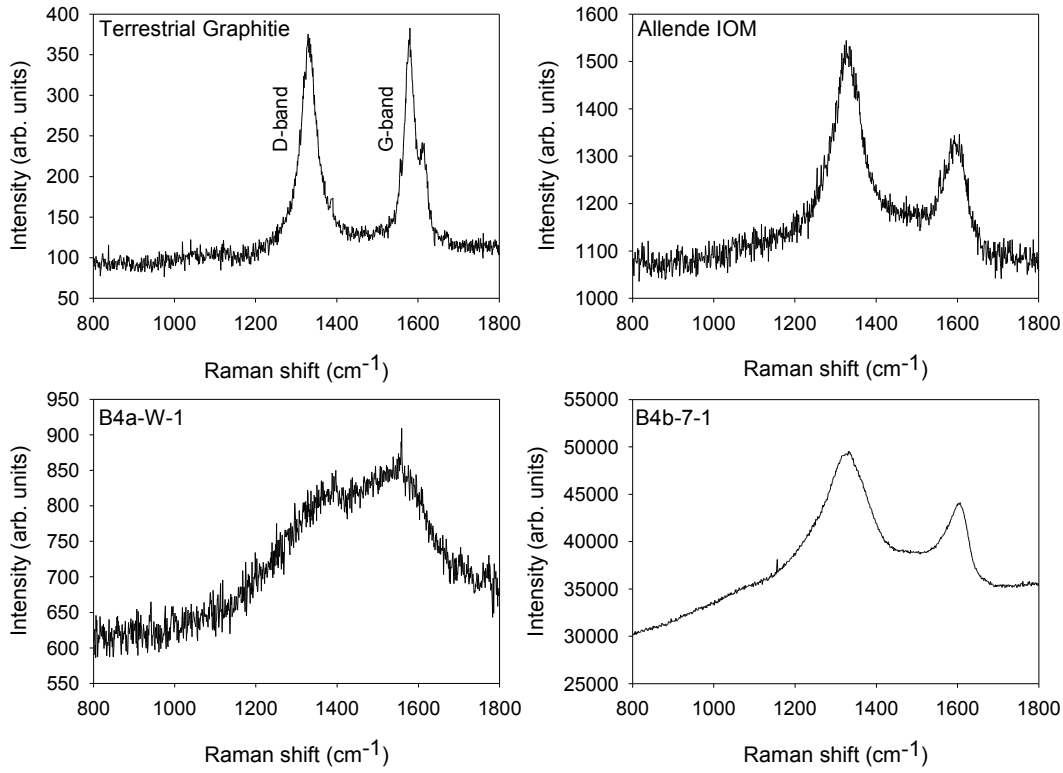

Figure 5.3 Comparison of Raman spectra obtained in this study from a terrestrial graphite grain (top left), IOM extracted from Allende (top right), amorphous carbonaceous grain B4a-W-1 (bottom left), and grain B4b-7-1 containing more ordered carbon (bottom right). Both B4a-W-1 and B4b-7-1 are highlighted on Figures 5.4, 5.5 and 5.7. The narrow G-band for the terrestrial graphitic grain indicates that it contained the most ordered carbon. In contrast grain B4a-W-1 had broad overlapping D and G bands that almost formed a single peak.

We note that the D-band peak positions appeared to be shifted to lower values, for both the IOM measurements and the terrestrial graphite, than previously observed by Busemann et al. (2007). It is known that the D-band peak position can vary with exciting photon energy (Ferrari and Robertson 2001, Negri et al. 2004). For example, Rotundi et al. (2008) measured IOM with three different exciting wavelengths, 512nm, 532nm and 632nm and showed that the use of increasingly longer wavelengths could shift the D-band peak position to lower values but has little affect on the G-band position. The reported downshift in ω_D was ~5 – 8cm^{-1} between the 532nm and 514nm excitation wavelengths, although

Ferrari and Roberston (2001) showed downshifts >20cm^{-1} in some carbonaceous samples.

As Busemann et al. (2007) used a 532nm laser we attribute our lower D-band peak positions to the use of a longer exciting wavelength in this study, although the position of the D-band does not influence our overall interpretation of the data.

In summary, the D and G band parameters and observed trends measured in meteoritic IOM and a terrestrial graphitic grain, lead us to conclude that our experimental set-up did not cause carbonaceous phases to appear more disordered than they really were.

5.2.6 TEM

TEM uses a high energy electron beam to obtain high resolution images from electron transparent samples. Electrons interacting with the sample also undergo Bragg scattering, producing diffraction patterns characteristic of the sample's crystalline structure (for reviews see Wirth 2004, Lee 2010).

Three carbonaceous grains, B4a-Q-1, B4a-X-1 and C4a-D-1, were analyzed using TEM. The grains were prepared as electron transparent sections using an FEI Nova 200 DualBeam Focused Ion Beam (FIB) system at the University of Glasgow.

Protective straps of Pt were deposited onto the grain surfaces to minimize damage from implantation during ion sputtering. Sections, up to ~4μm in size, were extracted from the grains and milled down to thicknesses of 100 – 200nm using a 30kV Ga^+ ion beam. As sputtering with the high energy beam could damage the section and potentially lead to amorphization of its surface, the final polishing steps were carried out using a 5kV ion beam to remove any "damaged" sample material.

An FEI Tecnai T20 TEM with a 200kV LaB_6 electron source and Gatan image filter (also at the University of Glasgow) was used to study the three sections. Images were obtained using the bright field mode and a selected-area electron-diffraction pattern (SAED) was collected from the central region of each section.

5.3 RESULTS

5.3.1 Grain Abundances, Sizes and Morphologies

Based upon the total number of grains for which EDX spectra were collected in each fraction, the abundance of the carbonaceous grains in B4 (B4a and B4b combined) is 0.13% and 0.22% for C4.

The B4 and C4 fractions also contain a large percentage of silicate grains from the meteorite matrix. Silicate grains have densities >2.2gcm^{-3}, the upper end of the density range of graphite (1.6 – 2.2gcm^{-3}), and should not be widely present within the B4 and C4 fractions (2.15 – 2.26gcm^{-3}). Grains of density >2.26gcm^{-3} should be sedimented after the first density step and extracted from the separation, leaving only grains of density <2.26gcm^{-3}. However, it appears that some of the densest material must have remained in the separation, placing it into the supposedly lower density fractions.

Carbonaceous grain sizes in B4 ranged from 1 – 13μm, with an average long axis diameter of 6.3μm. For C4 the grain sizes ranged from 1 – 7μm, with an average long axis diameter of 2.6μm.

The average carbonaceous grain size in B4 was larger than that within the C4 fraction indicating that the size separation was successful. Approximately 90% of the C4 carbonaceous grains fell into their expected size range of 1 – 7μm. In contrast only ~40% of the B4 grains were within the range of 7 – 20μm, with the rest having long axis diameters of <7μm. This is likely due to the use of a fixed-angle centrifuge, which can lead to some deviation from Stokes' law when size separating the grains (see Tizard et al. 2005 for details). The centrifuge causes grains to become pushed outwards to the walls of the tube, whilst grains will also

sediment in bulk rather than as single particles. Smaller grains may therefore sediment in a faster time than that calculated from Stokes' law. This was partly combated with repeated separations for each size fraction; however it seems an increased number of repetitions are required.

We have divided the carbonaceous grains into three groups based upon their morphology (see Figure 5.2). The grains were either regarded as: (1) "Flakes", small grains with smooth surfaces, (2) "Elongated", long grains, again usually with smooth surfaces, or (3) "Blocky", which had angular or irregular appearances.

Many of the grains appeared to be similar in morphology to the non-round, isotopically normal, grains described by Amari et al. (1993) and Zinner et al. (1995) in presolar graphite acid residues. Those grains were reported to be either hexagonal or irregular shapes, including blocky grains and elongated particles they referred to as "potatoes", and often had smooth surfaces.

Table 5.2 summarizes the abundances of each morphological group within the fractions B4a, B4b and C4a. Each of the morphologies was represented in all of the fractions, and for B4a and B4b they were found in relatively similar abundances. In C4a the blocky grains dominated, comprising almost 70% of the carbonaceous grains. Overall however, the flakes and blocky grains were most abundant in the fractions at ~40%, whilst the elongated grains made up just over 20% of all carbonaceous grains.

Morphology	B4a	B4b	C4a	Total
Flakes (F)	4 (40%)	7 (50%)	2 (22%)	13 (40%)
Elongated (E)	3 (30%)	4 (29%)	1 (11%)	8 (24%)
Blocky (B)	3 (30%)	3 (21%)	6 (67%)	12 (36%)

Table 5.2 Summary of the distribution of carbonaceous grain morphologies in the size and density fractions B4 and C4.

5.3.2 Isotopic Ratios

The measured H, C, N and O isotopic ratios of the carbonaceous grains are presented in Table 5.3. The C, N and O isotopic compositions of nearly all of the

carbonaceous grains were within 1σ error of the solar values. They did not contain the large anomalies that are commonly associated with presolar graphite grains (Amari et al. 1993; 1995b, Hoppe et al. 1995, Zinner et al. 1995), indicating that they are not stellar condensates.

The $^{12}C/^{13}C$ ratios obtained using TOFSIMS were lower (average of 85 ± 5) than those from the NanoSIMS measurements (average of 90 ± 0.7). Despite using a peak deconvoltion technique (see Section 5.2.3) it appears that there was still some contribution from $^{12}C^{15}N$ to the $^{13}C^{14}N$ peak resulting in systematically lowered $^{12}C/^{13}C$ ratios. The NanoSIMS measurements were performed at sufficient mass resolutions so that this was not an issue. However, all of the $^{12}C/^{13}C$ ratios acquired using TOFSIMS were within 3σ of solar suggesting that they are unlikely to be presolar in origin.

The grain B4a-W-1 had a $^{14}N/^{15}N$ ratio of 103 ± 44. Enrichments in ^{15}N are predicted to occur through low temperature ion-molecule reactions in the cold outer regions of the early solar nebula or the ISM (Millar et al. 1989, Aikawa and Herbst 1999, Sandford et al. 2001, Charnley and Rodgers 2008).

The grains were enriched in D relative to SMOW (Standard Mean Ocean Water), with δD values between +134 to +333‰, and 1σ errors on average ~110‰. Bulk δD values in Murchison matrix are ~ −30‰ (Pearson et al. 2001, Eiler and Kitchen 2004), although D enrichments are found in Murchison IOM, with δD of around +780‰ (Alexander et al. 2007).

After SIMS sputtering, the remaining grains were examined again using the ESEM. Most of the grains had an apparent platy structure, with layers of carbonaceous material (see Figure 5.2).

5.3.3 Raman Spectroscopy

Average D and G band parameters, and D/G intensity ratios for the carbonaceous grains, are provided in Table 5.3. Due to the fitting criteria, or lack of Raman-active carbon, useful Raman spectra were not obtained from every grain.

Table 5.3 Summary of morphology, isotopic compositions and Raman characteristics of carbonaceous grains. The grains belong to either the "Flakes" (F), "Elongated" (E) or "Blocky" (B) morphological groups. Isotopic compositions were acquired using TOFSIMS (TOF) and NanoSIMS (Nano) analysis and have been corrected for mass fractionation (but not QSA). As part of the NanoSIMS analysis the grains B4b-1-3, -1-4, -5-1 and -7-1 were pre-sputtered using a de-focused 400pA primary ion beam. * indicates that due to the large spot size of the exciting laser these grains were analyzed as pairs. A space in the table indicates that no data was obtained (i.e. not all grains were analyzed for H isotopes and the fitting criteria meant no useful Raman spectra were collected from some grains). Errors are 1σ.

Name	Size (µm)	Morphology	Technique	$^{12}C/^{13}C$	$^{14}N/^{15}N$	$^{16}O/^{18}O$	δD (‰)	ω_G	Γ_G	ω_D	Γ_D	D/G
B4a-C-1	9 x 3	E										
B4a-D-1	11 x 4	E										
B4a-E-1	7 x 3	F						1593.5 ± 1.8	92.7 ± 5.7	1346.4 ± 1.6	155.3 ± 4.9	1.51 ± 0.13
B4a-G-1	1 x 1	B						1574.4 ± 2.8	191.2 ± 9.6	1346.8 ± 2.6	257.6 ± 7.0	1.44 ± 0.13
B4a-J-1	8 x 8	B	TOF	90 ± 2	287 ± 42	432 ± 61		1565.5 ± 0.5	141.2 ± 2.0	1358.8 ± 0.9	265.3 ± 2.2	1.13 ± 0.03
B4a-Q-1	6 x 5	F	TOF	81 ± 3	206 ± 44	513 ± 96		1557.9 ± 0.9	181.7 ± 3.1	1352.1 ± 1.4	254.8 ± 3.5	0.96 ± 0.03
B4a-W-1	3 x 2	F	TOF	79 ± 8	103 ± 44	690 ± 213		1546.6 ± 1.8	165.8 ± 5.5	1363.8 ± 2.8	214.9 ± 7.0	0.84 ± 0.06
B4a-W-2	6 x 5	F	TOF	77 ± 5	159 ± 45	426 ± 55		1557.0 ± 0.7	148.4 ± 2.5	1358.3 ± 1.2	250.0 ± 3.0	0.98 ± 0.03
B4a-W-3	10 x 8	B	TOF	82 ± 2	248 ± 41	546 ± 77		1566.9 ± 1.0	153.3 ± 3.5	1357.0 ± 1.5	232.0 ± 4.1	0.96 ± 0.04
B4a-X-1	7 x 3	E	TOF	90 ± 2	214 ± 41	503 ± 51						
B4b-0-1	3 x 2	F	Nano	90.7 ± 1.1	279 ± 3	517 ± 15	177 ± 115					
B4b-1-1	5 x 3	B	Nano	91.7 ± 1.1	278 ± 3	497 ± 15						
B4b-1-2	7 x 3	E	Nano	90.4 ± 1.1	275 ± 3	516 ± 15	203 ± 113	1566.5 ± 1.2	221.0 ± 3.7	1345.1 ± 2.3	281.4 ± 5.5	0.67 ± 0.03
B4b-1-3	6 x 3	F	Nano	90.4 ± 1.1	277 ± 4	517 ± 15	287 ± 113					
B4b-1-4	5 x 3	F	Nano	91.1 ± 1.1	274 ± 4	513 ± 15	333 ± 116					
B4b-1-5	4 x 2	F	Nano	90.8 ± 1.1	271 ± 3	501 ± 15	230 ± 113					
B4b-1-6	9 x 2	E	Nano	90.5 ± 1.1	268 ± 3	504 ± 15	286 ± 113	1571.1 ± 2.5	180.5 ± 8.5	1341.3 ± 2.4	210.0 ± 7.3	1.19 ± 0.10
B4b-1-7	13 x 8	B	Nano	92.8 ± 1.1	274 ± 3	503 ± 15	314 ± 113					
B4b-5-1	9 x 4	E	Nano	89.9 ± 1.1	272 ± 4	511 ± 15	235 ± 114					
B4b-6-1	6 x 5	F	Nano	90.3 ± 1.1	277 ± 3	509 ± 15	134 ± 117	1592.0 ± 0.8	109.6 ± 2.6	1355.4 ± 0.8	217.5 ± 2.6	1.39 ± 0.05
B4b-6-2	6 x 3	E	Nano	90.6 ± 1.1	273 ± 3	511 ± 15	246 ± 113					
B4b-7-1	4 x 2	B	Nano	91.4 ± 1.1	277 ± 4	517 ± 15	275 ± 114	1595.1 ± 0.1	59.5 ± 0.4	1322.1 ± 0.1	213.1 ± 0.4	1.81 ± 0.01
B4b-9-1	2 x 1	F	Nano	90.6 ± 1.1	271 ± 4	507 ± 15	321 ± 114	*1585.3 ± 2.1	*152.3 ± 7.7	*1344.4 ± 2.8	*263.6 ± 8.0	*1.18 ± 0.10
B4b-9-2	5 x 2	F	Nano	90.1 ± 1.1	265 ± 5	499 ± 17	144 ± 113	*1585.3 ± 2.1	*152.3 ± 7.7	*1344.4 ± 2.8	*263.6 ± 8.0	*1.18 ± 0.10
C4a-D-1	3 x 2	B	TOF	84 ± 2	287 ± 46	591 ± 73		1554.2 ± 0.7	132.7 ± 2.5	1353.3 ± 1.2	267.9 ± 2.9	1.12 ± 0.04
C4a-E-1	2 x 1	B	TOF	88 ± 3	519 ± 107	511 ± 86		1556.6 ± 2.7	173.2 ± 9.8	1345.5 ± 4.0	294.1 ± 9.2	1.24 ± 0.13
C4a-E-2	2 x 1	F	TOF	87 ± 2	545 ± 101	555 ± 81		1547.7 ± 2.1	143.5 ± 7.3	1367.7 ± 4.1	251.3 ± 9.4	0.95 ± 0.10
C4a-G-1	2 x 2	B	TOF	89 ± 3	279 ± 48	607 ± 174		1542.0 ± 1.5	145.1 ± 5.4	1343.5 ± 3.0	293.9 ± 6.7	1.05 ± 0.07
C4a-H-1	7 x 3	E	TOF	83 ± 2	269 ± 43	553 ± 51		1562.7 ± 3.9	170.0 ± 12.9	1357.8 ± 3.6	207.9 ± 10.7	0.97 ± 0.14
C4a-L-1	4 x 3	B	TOF	88 ± 2	254 ± 45	471 ± 125		1565.4 ± 1.3	207.2 ± 4.4	1345.0 ± 2.0	257.1 ± 5.1	0.83 ± 0.04
C4a-Q-1	1 x 1	B	TOF	87 ± 3	335 ± 52	548 ± 109		1551.8 ± 2.0	141.2 ± 6.8	1360.3 ± 3.0	195.5 ± 8.8	0.88 ± 0.08
C4a-R-1	1 x 1	F	TOF	96 ± 2	275 ± 45	552 ± 81		*1549.9 ± 2.5	*152.8 ± 9.1	*1368.8 ± 4.6	*284.6 ± 9.6	*1.18 ± 0.14
C4a-R-2	2 x 1	B	TOF	78 ± 4	231 ± 44	538 ± 67		*1549.9 ± 2.5	*152.8 ± 9.1	*1368.8 ± 4.6	*284.6 ± 9.6	*1.18 ± 0.14

The majority of grains (including B4a-G-1, which had not been sputtered) had very broad Γ_D and Γ_G values that were consistent with the presence of highly disordered carbon. In many cases the D and G bands overlapped, a common feature of amorphous carbon (e.g. Ferrari and Robertson 2001). Figure 5.3 compares typical Raman spectra obtained from a terrestrial graphite grain, meteoritic IOM, amorphous carbonaceous grain B4a-W-1, and the more ordered grain B4b-7-1. It shows how, with increasing disorder of the carbon, the intensity of the D band relative to the G increases, and both the D and G bands become broader.

Figures 5.4 and 5.5 plot the peak widths as a function of peak position for both the D and G bands in the carbonaceous grains respectively. Also included on Figures 5.4 and 5.5 are D and G band data from meteoritic IOM (Busemann et al. 2007), IDPs (Busemann et al. 2009) and cometary materials (Rotundi et al. 2008).

Figure 5.4 shows that the grains had Γ_D and ω_D values comparable to carbonaceous phases present in meteoritic IOM, IDPs and cometary materials. However, our analyses of IOM from Murchison and EET 92042, Leoville and Allende, gave ω_D values 10 – 20cm^{-1} lower than those measured in the same samples by Busemann et al. (2007), which we attributed to our use of a longer exciting wavelength (see Section 5.2.5). The ω_D values of the carbonaceous grains may therefore have also been downshifted by a similar amount.

Nearly all carbonaceous grains plot in the top left of Figure 5.5, with Γ_G values often higher and ω_G values lower than any previously reported for extra-terrestrial samples. Three grains, B4a-E-1 (not sputtered), B4b-6-1 and B4b-7-1, had G band characteristics similar (lower Γ_G and higher ω_G – bottom right of Figure 5.5) to those measured in other primitive samples.

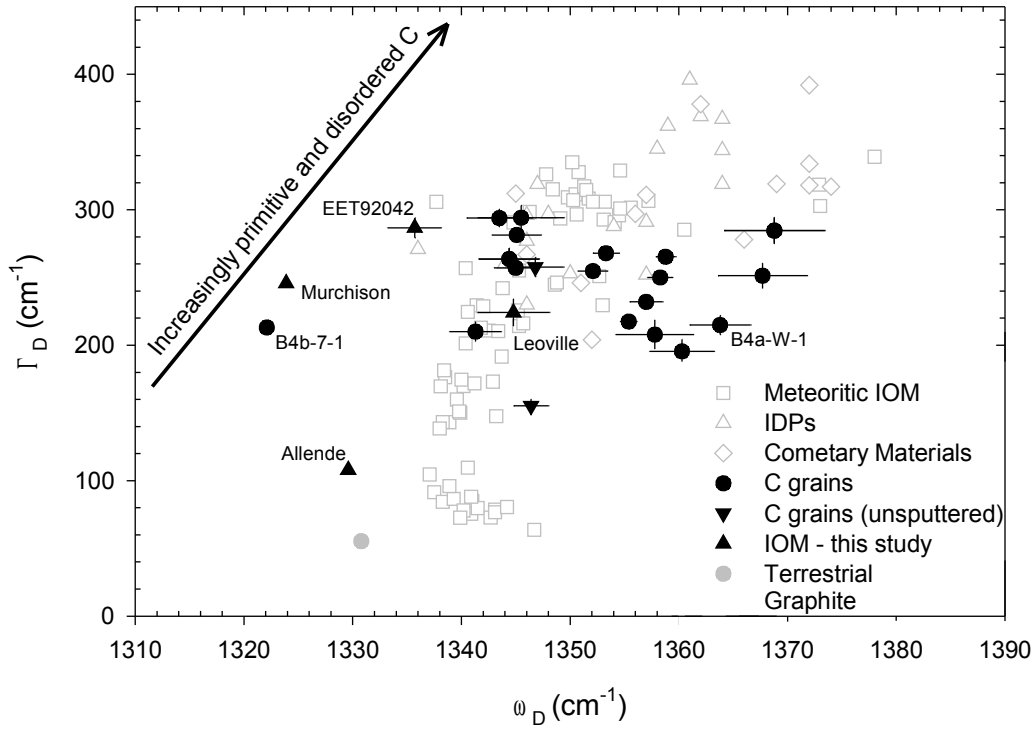

Figure 5.4 D-band characteristics of Raman spectra collected as part of this study (closed symbols) from carbonaceous grains (including those not analyzed by SIMS), IOM (from Murchison, EET92042, Leoville and Allende) and a terrestrial graphite grain. The data are compared to that previously obtained (open symbols) from meteoritic IOM (Busemann et al. 2007), IDPs (Busemann et al. 2009) and cometary materials returned by the Stardust mission (Rotundi et al. 2008). The Γ_D and ω_D values for the carbonaceous grains were comparable to those from primitive extra-terrestrial samples. A downshift of 10 – 20cm^{-1} in ω_D values for the IOM from Murchison, EET 92042 and Allende measured here is attributed to our use of a longer exciting wavelength (632nm) than the other studies. The ω_D values for the carbonaceous grains may therefore also have been downshifted by a similar amount.

We tested whether contamination with organic heavy liquids could produce the bands observed for the carbonaceous grains. Several terrestrial graphitic grains were centrifuged in heavy liquid and washed thoroughly following the same procedure used for the gentle separation. The Raman spectra from these "treated" grains were identical to those obtained from terrestrial graphite not washed in heavy liquid. This indicated that the use of the organic heavy liquids did not significantly alter the grain's Raman characteristics.

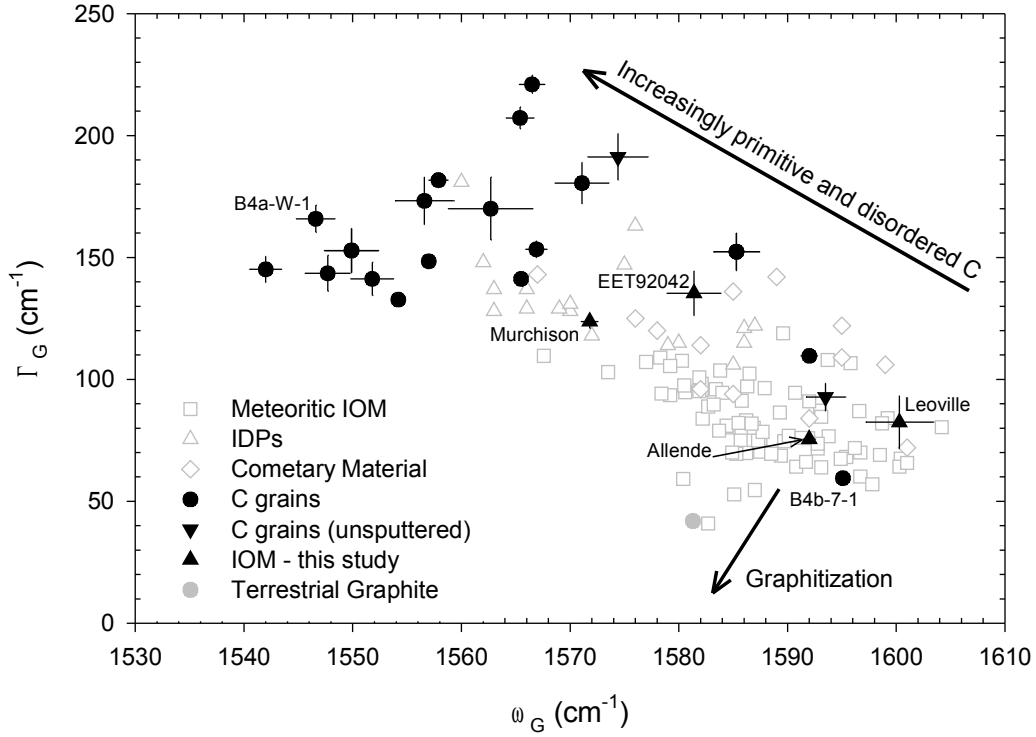

Figure 5.5 G-band characteristics of Raman spectra collected as part of this study (closed symbols) from carbonaceous grains (including those not analyzed by SIMS), IOM (from Murchison, EET92042, Allende and Leoville) and a terrestrial graphite grain. The data are compared to that previously obtained (open symbols) from meteoritic IOM (Busemann et al. 2007), IDPs (Busemann et al. 2009) and cometary materials returned by the Stardust mission (Rotundi et al. 2008). Most carbonaceous grains had Γ_G values higher, and ω_G lower, than those measured in other primitive extra-terrestrial samples.

5.3.4 TEM

Further evidence for the amorphous nature of the carbonaceous grains came from the TEM analysis. Figure 5.6 shows TEM images of the three grains prepared using the FIB. The grains are featureless and lack any internal structure. The SAED patterns obtained from each grain contain only very weak rings (Figure 5.6), consistent with them having no crystalline structure and therefore being amorphous.

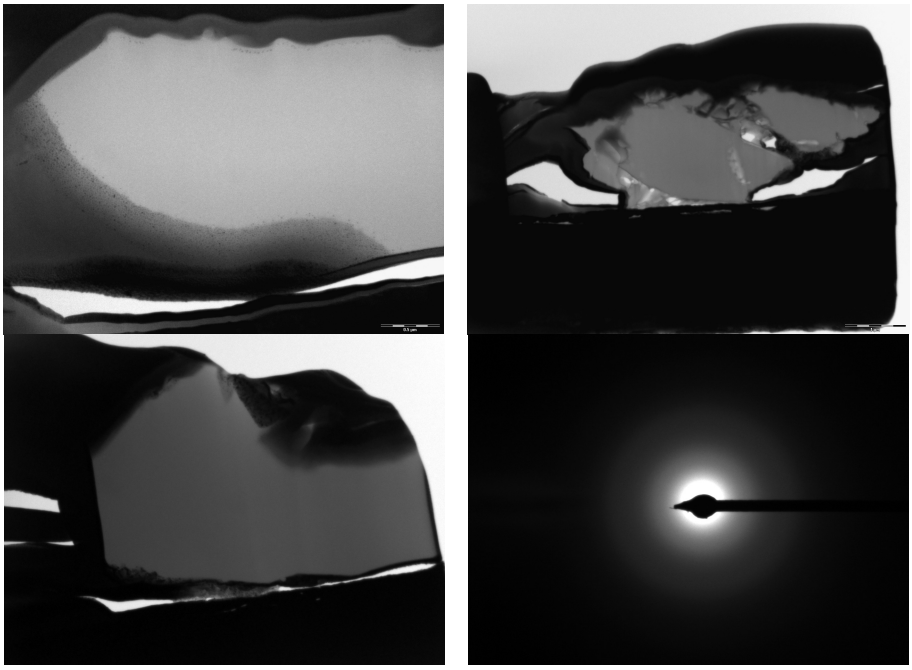

Figure 5.6 TEM images from three carbonaceous grains, B4a-X-1 (top left), B4a-Q-1 (top right) and C4a-D-1 (bottom left – scale is the same as for B4a-Q-1 image). The grains are the light coloured material in the centre of the images, and are surrounded by Pt above and Au-foil below, i.e. darker regions. The grains lacked any internal structure, as indicated by SAED patterns from the central regions of the sections (e.g. bottom right).

5.4 DISCUSSION

5.4.1 Contamination

We must first consider whether the grains are the result of contamination. A possible source is from the organic heavy liquids. As previously mentioned, heavy liquid deposited onto a clean Au-foil and examined with the ESEM yielded no carbonaceous grains. The only other items that came into contact with the Murchison sample were a stainless steel mortar and pestle, plastic test tubes and pipette, and the Au-foil. We would not expect any of these items to produce such highly disordered and amorphous carbonaceous material, which is uncommon in terrestrial samples (Wopenka and Pasteris 1993).

Another major argument against contamination is that the grains are slightly enriched in D relative to SMOW, again not an expected feature of terrestrial materials (e.g. Hoefs 1980).

We conclude therefore that the carbonaceous grains are not contaminants introduced by the gentle separation procedure or any other laboratory process prior to analysis.

5.4.2 Effects of SIMS and Raman Analyses

The carbonaceous grains were analyzed either by TOFSIMS or NanoSIMS prior to any Raman spectroscopic measurements. Sputtering by high energy primary ion beams causes ion implantation (Au^+ from the TOFSIMS, Cs^+ from the NanoSIMS) into the outer tens of nanometres of a sample, leading to amorphization within its top layers. The SIMS analysis may therefore have perturbed the Raman spectra of the grains towards a more disordered nature.

Raman spectra from two carbonaceous grains not analyzed by SIMS were compared to those from grains that had been. One of the grains (B4a-G-1) had Γ_G and ω_G consistent with those grains analyzed by SIMS, whilst the other (B4a-E-1) contained less disordered carbon (higher ω_G and lower Γ_G).

The Raman spectra of B4a-E-1 were comparable with those seen in other primitive samples but also carbonaceous grains B4b-6-1 and B4b-7-1, both of which were analyzed by NanoSIMS. As the peak widths and peak positions of B4a-E-1 are within the range measured in the sputtered grains, and B4a-G-1 contains highly disordered carbon, similar to that observed in grains analyzed by SIMS, it appears that the SIMS measurements have not had a major influence on the Raman characteristics of the carbonaceous grains.

Furthermore, Zinner et al. (1995) performed Raman spectroscopy on presolar graphite grains after SIMS measurements so that grain cores were analyzed rather than potentially coated or altered outer surfaces. The grains still displayed Raman spectra consistent with graphite rather than shifting towards amorphous carbon, indicating that the SIMS had little effect on carbon structure of the grains.

TEM analysis also indicates that the SIMS measurements have not caused the amorphization of the carbonaceous grains. Sputtering by the primary ion beam is only expected to cause amorphization of the outer layers of a sample. However, the TEM images and diffraction patterns indicate that the cores of sections up to 4μm in diameter are also lacking crystalline structure and are amorphous.

Laser induced thermal alteration of samples can be an issue in Raman spectroscopy. Thermal alteration often causes carbonaceous materials to become more processed, decreasing Γ_G, and increasing ω_G, shifting them towards the bottom right corner of Figure 5.5. This is the region opposite to where the carbonaceous grains plot. Everall et al. (1991) and Kagi et al. (1994) have shown that the ω_G for graphite can also be shifted, by 10 – 20cm^{-1}, to lower values by laser induced heating. However, the ω_G we obtained from well characterized IOM and a terrestrial graphitic grain are not significantly down-shifted relative to previous studies (e.g. Busemann et al. 2007). We therefore conclude that the ω_G values of the carbonaceous grains have not been affected by laser induced alteration in our experimental set-up.

5.4.3 Amorphous Carbon

Ruling out the possibility that the carbonaceous grains are terrestrial contamination, and that their disordered and amorphous structure is the result of any analytical technique, we may discuss how the grains may have been formed and processed prior to arrival in the laboratory.

Brearley (1990) suggested that amorphous carbon, located alongside Fe, Ni metal particles within carbon-rich aggregates in ordinary chondrites, was formed by a combination of Fischer-Tropsch reactions and the direct precipitation of elemental carbon onto metal grains at low temperatures within the early solar nebula. The resulting amorphous carbon should therefore contain evidence of metals such as Fe and Ni.

Several carbonaceous grains from the B4a fraction were measured by TOFSIMS analyzing positive secondary ions. No Fe-rich “hotspots” were present in the

resulting secondary ion images. This was consistent with the ESEM analyses, which also found no signs of metals within the grains, suggesting their formation via a different process.

Rotundi et al. (1998) produced amorphous carbon through arc discharge between two amorphous carbon electrodes in an inert Ar atmosphere. Most of the carbon consisted of chain-like aggregates of amorphous carbon, but also poorly graphitized carbon and Buckminster-fullerenes. The grains were tens of nanometres in size, inconsistent with the carbonaceous grains reported here.

Ion irradiation, from cosmic-rays or high energy solar winds, is predicted to be a major cause of the amorphization of extra-terrestrial samples (e.g. Bradley 1994). Ion irradiation leads to a disordering of the carbon structure (breakdown of sp2 bonds) and therefore a shift of ω_G to lower, and Γ_G to higher values (i.e. towards the top left of Figure 5.5) (e.g. Baratta et al. 1996).

Brunetto et al. (2009) compared the Raman spectra of soot, used as an analogy for carbonaceous dust observed in the ISM, before and after irradiation with up to 400keV H^+, He^+ and Ar^{++} ions. Figure 5.7 compares the data of Brunetto et al. (2009) to that from the carbonaceous grains analyzed here.

Prior to irradiation the soot had high ω_G and low Γ_G (bottom right of Figure 5.7). Upon irradiation, with ion fluences of $\sim 10^{15}$ ions cm^{-2}, the soot became disordered and eventually amorphous (top left of Figure 5.7). It developed Raman characteristics comparable to primitive IDPs, and remarkably similar to those in the carbonaceous grains. The highly disordered and amorphous nature of the carbonaceous grains appears to be consistent with the ion irradiation of pre-existing more ordered carbon grains. Baratta et al. (2004) and Ferini et al. (2004) have shown that irradiation by 3 – 30keV He ions at fluences of $>10^{16}$ ions cm^{-2} can transform carbon ices, and even highly ordered graphite, to carbonaceous materials with $\omega_G < 1540 cm^{-1}$ and $\Gamma_G > 150 cm^{-1}$.

The effects of ion irradiation can be reversed by thermal metamorphism, which causes graphitization of carbon (Wopenka and Pasteris 1993). Much of the

carbonaceous material that accreted into meteorite parent bodies is likely to have been of a highly disordered nature. However, annealing of amorphous materials during meteorite parent body processing would result in an alteration of its Raman spectra towards a more ordered structure (Bonal et al. 2006; 2007, Busemann et al. 2007). It is therefore not surprising that amorphous carbon has only been observed in the most primitive samples that experienced the least amount of thermal metamorphism.

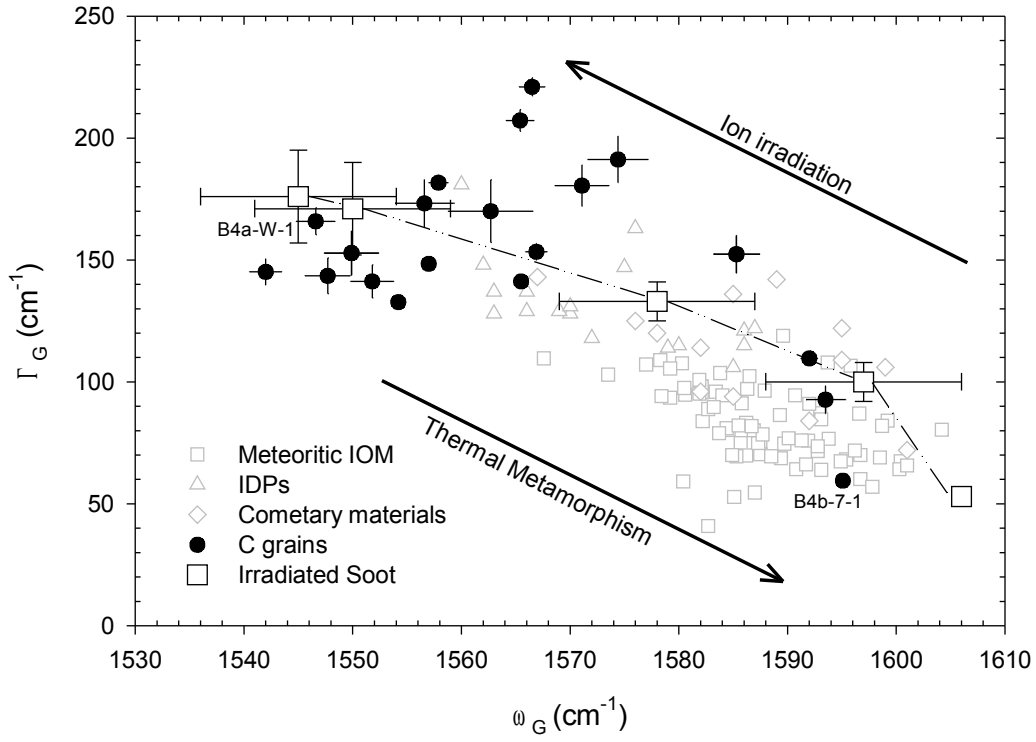

Figure 5.7 Comparison of Raman G-band characteristics from carbonaceous grains (closed symbol), meteoritic IOM (Busemann et al. 2007), IDPs (Busemann et al. 2009), cometary materials (Rotundi et al. 2008) and ion irradiated soot (data from Brunetto et al. 2009). The Γ_G and ω_G of the soot evolve as a function of ion fluence. Prior to irradiation the soot plots in the lower right-hand corner. Upon exposure to ion fluences $>10^{14}$ ions cm^{-2} the carbon becomes disordered (i.e. increasing Γ_G and decreasing ω_G) and shifts towards the top left. At ion fluences $>10^{15}$ ions cm^{-2} the carbon becomes highly disordered and amorphous and is similar to that observed in the carbonaceous grains, plus some IDPs and cometary material.

Three grains (B4a-E-1, B4b-6-1 and B4b-7-1) had ω_G and Γ_G values consistent with a more ordered carbon structure, typical of those reported for most extra-terrestrial carbonaceous samples. One scenario is that these grains were more thermally metamorphosed than the other carbonaceous grains. However, the Murchison parent body is not predicted to have experienced any significant

thermal alteration (Huss et al. 2006, Busemann et al. 2007, Cody et al. 2008). These grains must therefore have either experienced lower doses of ion irradiation, perhaps having formed after the other grains or through shielding in the nebula, or increased amounts of heating prior to their incorporation into the Murchison parent body.

5.4.4 Origins of Amorphous Carbonaceous Grains

The isotopic compositions of the carbonaceous grains exclude circumstellar environments as their source. Potentially, presolar graphite grains could be converted to amorphous carbon by ion irradiation in the ISM, but the grains would still be expected to retain isotopic anomalies from their stellar origins.

Organic particles or mantles on grains in the ISM can contain large D and ^{15}N enrichments from ion-molecule reactions and mass fractionation processes (Millar et al. 1989, Aikawa and Herbst 1999, Sandford et al. 2001, Charnley and Rodgers 2008). Similar processes may have also occurred at the outer edges of the collapsing cloud from which the solar nebula was formed. Temperatures in this region are predicted to have been as low as ~10K, allowing the condensation of gas molecules onto icy grains. It has been suggested that intense UV radiation in this environment could create D-rich ionized molecular H gas (Aikawa and Herbst 1999). Rapid H isotope exchange with the ionized gas would lead to extreme D enrichments in any organic mantles and icy grains.

Formation in the ISM or the outer proto-planetary disk has been used to explain extreme D and ^{15}N enrichments observed in IOM (Robert and Epstein 1982, Yang and Epstein 1983, Kerridge et al. 1987, Busemann et al. 2006), IDPs (Keller et al. 2000, Messenger 2000, Floss et al. 2006, Busemann et al. 2009) and nanoglobules (Nakamura-Messenger et al. 2006).

With the exception of B4a-W-1, extreme D and ^{15}N enrichments were not detected in the amorphous carbonaceous grains. However, the grains' slight D enrichments are comparable to those measured in some IDPs (Messenger 2000,

Floss et al. 2006, Busemann et al. 2009), indicating that they may have formed in similar environments.

Remusat et al. (2010) have argued that carbon-rich particles located in the matrices of carbonaceous chondrites, and containing a wide range of D enrichments, are remnants of organics synthesized in the cold regions of the early solar nebula. In their model, particles that remained in the outer disk underwent H isotopic exchange with the ionized gas, leading to extreme D enrichments. The inward transport of other carbonaceous particles caused them to spend less time in this environment, hence acquiring smaller D enrichments. In the inner regions of the disk, higher temperatures and gas densities shielded material from UV radiation. Further movement in the turbulent disk (Ciesla 2009) eventually led to mixing of all the carbonaceous particles in the meteorite parent body accretion zone of the early solar nebula.

A similar scenario was proposed by Muñoz Caro et al. (2006) to explain the formation of amorphous carbon in IDPs. They suggested that during the T-tauri phase of the early Sun, icy mantles on grains at the outer edge of the disk were processed by UV and ion irradiation until turbulent mixing transported the grains to the inner disk. Higher temperatures led to sublimation of volatiles, leaving behind amorphous carbon.

We could expect the amorphous carbonaceous grains to have a wide range of D compositions, similar to those observed in other primitive samples. This is not the case, with most of the carbonaceous grains having very similar δD values to one another, although only 13 of the carbonaceous grains have so far been analyzed for their H isotopic compositions. As discussed, B4a-W-1, for which D/H was not obtained, does have a ^{15}N enrichment and is therefore a possible candidate for containing an extreme D enrichment.

After formation the carbonaceous grains would have been exposed to UV and ion irradiation from the solar wind and cosmic-rays in the early solar nebula. During its T-tauri stage the Sun was more active, with estimates suggesting that the solar

wind may have been up to 1000 times stronger than present day conditions (Wood et al. 2002).

Today the solar wind (energy of 1keV), which consists largely of He^+ and H^+, has an ion flux of ~2×10^8 ions cm^{-2} s^{-1} at 1AU. Its strength decays as $1/R^2$, where R^2 is the distance from the Sun.

Assuming a 1000 times stronger solar wind in the early nebula (Wood et al. 2002), at 50AU the ion flux would have been ~8×10^7 ions cm^{-2} s^{-1}. The experimental work of Baratta et al. (2004) and Brunetto et al. (2009) shows that H^+ and He^+ ion fluences on the order of ~10^{15} – 10^{16} ions cm^{-2} are required to transform structurally ordered carbon to an amorphous phase. The carbonaceous grains therefore would have needed to spend only ~4 years in this environment to acquire the necessary irradiation dose. If the grains formed at a distance of 100AU then it would still only take ~16 years. An early solar wind only 100, or even 10 times stronger, obviously increases the required timescales, to 160 years or 1600 years respectively.

The calculations do not take into account the effects of solar flares, which provide doses of higher energy (>1MeV) particles, or cosmic-ray irradiation, events that occur in addition to the main solar wind. Models have predicted that even under current conditions, irradiation doses are high enough at 40 – 50AU to produce irradiation mantles several metres thick in Edgeworth-Kuiper belt objects (Gil-Hutton 2002). It therefore seems likely that micron-sized carbonaceous phases exposed to irradiation in the early solar nebula could have been converted to highly disordered and amorphous phases.

If amorphization of the carbonaceous grains was due to irradiation in the solar wind, then this could explain the lack of extreme D enrichments comparable to those seen in IOM and IDPs. The carbonaceous grains may have initially acquired similarly large D enrichments that were subsequently diluted by the implantation and mixing of H^+ ions from the solar wind.

5.5 SUMMARY

We have obtained isotopic ratios, alongside characteristic Raman spectra and TEM analysis, from 33 carbonaceous grains. The grains were isolated from the Murchison meteorite using a size and density procedure originally designed for the separation of pristine presolar graphite.

The C, N and O isotopic compositions suggest that the grains are not presolar in origin. The grains all contain slight D enrichments, with δD values up to +333‰, lower than bulk IOM from Murchison but similar to some IDPs. It is suggested that the carbonaceous grains may represent particles that formed in the cold, D rich outer regions of the early Solar System, or possibly the ISM.

Raman spectra of the carbonaceous grains indicate that they contain highly disordered and amorphous carbon. This is supported by the TEM analyses, which show that the cores of three examined grains lack any internal structure. Amorphous Raman spectra were also obtained from a carbonaceous grain not previously analyzed for its isotopic composition by SIMS. We therefore rule out amorphization of the grains due to SIMS measurements.

Amorphous carbon has previously been observed in meteoritic IOM, IDPs, cometary samples and nano-globules. Although amorphous carbon may be produced by Fischer-Tropsch reactions or arc discharge, we favour ion irradiation as the cause of amorphization. Ion irradiation has been shown to lead to the disordering of carbon, with a broadening and shift of the Raman G-band to lower wave numbers, and an overlap with the Raman D-band. The Raman spectra of the carbonaceous grains are consistent with materials produced by ion irradiation of carbon rich ices or soot with ion fluences of $\sim 10^{15} - 10^{16}$ ions cm^{-2}.

Even at large distances from the Sun, the early solar wind, possibly during the T-tauri phase, combined with solar flares and cosmic-rays, could have provided sufficient ion doses to convert ordered carbonaceous materials into more structurally disordered and amorphous carbon. The implantation and mixing of

solar H^+ ions is likely to have diluted any extreme D enrichment the grains originally had.

Chapter 6

Summary and Future Work

This chapter reviews the research presented in this thesis. A summary of each research topic is provided, followed by a discussion of the implications of the work and suggestions for future research.

6.1 ANALYTICAL DEVELOPMENTS

The main analytical tool used in this work was a newly constructed TOFSIMS instrument equipped with a 25kV Au_n^+ LMIG. In order to achieve the aim of this research, which was to investigate the effects of interstellar processing on presolar samples; it was necessary to measure a series of standards with this instrument. Data from these measurements was then used for calibration and quantification of extra-terrestrial samples.

Over recent years, Au-cluster primary ions have primarily been used for the analysis of organic samples, as they provide enhanced molecular secondary ion yields. In this research Au-cluster ions were used to study inorganic samples by analyzing a series of well characterized silicate glasses with Au^+, Au_2^+ and Au_3^+ primary ions.

Practical secondary ion yields for inorganic ions when sputtering with Au_2^+ and Au_3^+ were enhanced by a factor of ~2 relative to those for Au^+. This was attributed to a similar sized increase in sputter rate when analyzing with Au_2^+ and Au_3^+ ions, and not an increase in ionization efficiency for secondary ions. However, Au_2^+ and Au_3^+ primary ion beams provide a factor of ~8 lower currents on the sample, making them largely unsuitable for analysis of inorganic samples.

Analysis of the silicate glass standards allowed the determination of RSFs required for quantification of trace element abundances in presolar SiC grains. Ideally, standards should be as structurally and chemically similar as possible to

the sample intended for analysis. Therefore a SiC standard, for which only Al, Ca and Fe abundances were known, was also measured.

It was found that the increased formation of $Si_mC_n^+$ clusters and subsequent decrease in the abundance of $^{28}Si^+$ in the mass spectra, results in elevated RSFs when sputtering SiC. RSFs for trace elements in silicate glass therefore require correction if used to quantify elemental abundances in presolar SiC grains.

The effects of using a delayed secondary ion extraction technique were also investigated during analysis of the standards. During normal extraction, approximately every secondary ion is extracted and detected. Using delayed extraction introduces fractionation between masses in the spectrum. A smaller fraction of the lighter ions are extracted relative to the heavier ions, although this is compensated by the use of longer primary ion pulses.

A depth-profiling procedure for the analysis of micron-sized grains was developed. Initially applied to a meteoritic silicate grain, it was eventually used for obtaining trace element depth-profiles in presolar SiC grains. A DC beam was used to sputter material from a grain before measurements using a pulsed primary ion beam. By using known sputter rates, primary ion currents, length of time the primary ion beam was applied, and field-of-view over which it was applied, it was possible to estimate the amount of material removed from a grain. Re-imaging of grains with an ESEM aided in calibrating sputter depths. Limitations of the depth-profiling procedure have been considered and a simple model used to infer potential trace element depth-profiles.

6.2 TRACE ELEMENTS IN PRESOLAR SiC

Complete depth-profiles for the trace elements Li, B, Mg, Al, K, Ca, Ti, V, Cr and Fe have been obtained from 11 presolar SiC grains.

The average elemental abundances of Mg, Fe, Ca, Al, Ti and V were qualitatively consistent with those reported by DC beam ion probe studies. The elements Mg, Fe, Ca and Al were depleted relative to Si and CI abundances

(Anders and Grevesse 1989) in the presolar SiC grains. This is due to their high volatilities, meaning that they condense at much lower temperatures than SiC. In contrast, average Ti and V abundances in the grains were close to 1. Nucleation effects must have inhibited their formation as TiC so that they instead condensed in solid solution with SiC.

Elevated abundances of several elements within the outer ~200nm of some presolar SiC grains provide evidence that material was implanted into the grains by supernovae shockwaves in the ISM. However, some SiC grains display no effects of interstellar processing, and instead their trace element depth-profiles can be explained by condensation processes around the grains parent stars. Evidence was found of elemental zoning in grains resulting from changing chemical environments during SiC condensation.

The significant difference between the two populations of SiC grains is likely their residence times in the ISM. This is consistent with the findings of noble gas (Lewis et al. 1994, Ott and Begemann 2000, Ott et al. 2005, Heck et al. 2009**)** and Li isotopic studies (Gyngard et al. 2009), which have shown that some of grains resided in the ISM for <50Myr, whilst others were there for >1Gyr, before accretion into the presolar molecular cloud from which the Solar System formed. Fast shockwaves, the expected mechanism through which grain-grain and grain-gas collisions arise in the ISM, only occur every ~10^8 years, therefore the youngest grains are unlikely to have passed through a high velocity shockwave (Jones et al. 1996).

6.3 AMORPHOUS CARBONACEOUS GRAINS

Carbonaceous grains were separated as part of an attempt to isolate pristine presolar graphite grains from the Murchison meteorite according to their size and density characteristics. No presolar graphite grains were discovered, although this may be due to an insufficient number of grains mapped in the resulting size and density fractions. The carbonaceous grains that were found contributed up to 0.22% of the total number of grains in the mapped fractions. They have been

analyzed using TOFSIMS, NanoSIMS, ESEM, Raman spectroscopy, TEM and SEM.

The C, N and O isotopic compositions of the carbonaceous grains were close to the solar values, indicating that they were not presolar in origin. Nearly all of the grains were enriched in D, with δD values up to +333‰. Although similar to some δD values reported in IDPs, this is lower than the extreme D enrichments often measured in IOM and IDPs. The carbonaceous grains may have formed in the ISM, or the cold outer regions of the early solar nebula, where H isotopic exchange with ionized gas produced extreme D enrichments.

Raman spectroscopy showed the carbonaceous grains to contain highly disordered and amorphous carbon, with broad, and often overlapping, major D and G band features. The amorphous nature of the grains was confirmed by TEM analysis with no visible diffraction pattern. The grains consisted of carbon that was more structurally disordered than values reported for almost all IOM extracted from primitive meteorites, IDPs and cometary samples.

Previous studies have shown that amorphous carbon can be produced by Fischer-Tropsch reactions (Brearley 1990) or arc discharge (Rotundi et al. 1998). The morphological, textural and structural characteristics of the carbonaceous grains in this research were inconsistent with these processes and they were ruled out.

Ion irradiation by the solar wind and cosmic-rays is the proposed source of amorphization. Previous experiments have shown that irradiation of terrestrial soot and carbon-rich ices with ion fluences of ~10^{15} – 10^{16} ions cm^{-2} can produce carbon phases, whose Raman characteristics are very similar to those of the carbonaceous grains (Baratta et al. 2004, Brunetto et al. 2009).

Such doses could easily be provided by the solar wind, which is predicted to have been up to 1000 times more active during its T-tauri phase (Woods et al. 2002). It is shown that even at large distances from the Sun, the solar wind, in combination with solar flare events and cosmic-rays, could have converted

carbonaceous materials in the early solar nebula into more structurally disordered and amorphous carbon.

Amorphization of the carbonaceous grains due to irradiation in the solar wind may explain the lack of extreme D enrichments within them. Implantation and mixing of solar wind H^+ ions is likely to have severely lowered the $^2D/^1H$ ratios of the grains.

6.4 DISCUSSION AND FUTURE WORK

The major aim of this research was to investigate the effects of interstellar processing on presolar samples. One way in which this was done was by analyzing the distribution of trace elements in presolar SiC grains using TOFSIMS.

Presolar grains are expected to display the effects of processing in the ISM. Sputtering from high energy ions and grain-grain collisions should lead to cratering on grain surfaces. This cratering has not been observed on the faces of presolar SiC grains, leading to suggestions that the grains may have been shielded from sputtering by coatings of possibly organic phases or MgS/CaS (e.g. Bernatowicz et al. 2003). Although no signs of cratering are reported here, evidence for the implantation of matter into some SiC indicates that not all grains were completely protected.

However, the presence of any coatings on the SiC grains in this research cannot be entirely ruled out, with several of the grains containing no evidence for implantation. Most analyzed presolar SiC grains, including all of those reported here, were extracted from their host meteorite using harsh acid treatments. It is probable these treatments removed or altered any coatings originally present on the grains.

A significant step forward will be the analysis of pristine presolar SiC grains that should retain any coatings. This will allow the coatings to be identified and their effects on interstellar processing to be constrained. In this research TOFSIMS

has proven to be a useful tool for measuring a wide range of trace element abundances and isotopic compositions in individual micron-sized SiC grains. Several studies have already looked at pristine presolar SiC grains (Bernatowicz et al. 2003, Tizard et al. 2005, Stroud and Bernatowicz 2005, Lyon et al. 2007), and the depth-profiling procedure developed here should provide a comprehensive method by which a large amount of information can be extracted from rare pristine presolar samples.

In order for research into pristine presolar samples to progress, during this work an attempt was made to study pristine presolar graphite. Unfortunately no graphite grains were discovered. However, amorphous carbonaceous grains were present in size and density separations.

The carbonaceous grains were isotopically and structurally different to IOM present within the Murchison meteorite. This suggests that the parent body accreted a variety of different carbonaceous materials that were formed and processed by several mechanisms. This is unsurprising, as studies of the carbonaceous phases in meteorites find them to be a diverse collection of materials that reflect the wide range of processes that occurred in the early solar nebula. The carbonaceous grains reported here provide new insights into conditions in this environment.

The carbonaceous grains contained isotopic compositions that indicated they were not presolar in origin. It was argued that slight enrichments in D were due to the grains having formed in the outer regions of the early solar nebula before being transported to the inner regions of the disk. This is consistent with models that indicate a large-scale inward movement of materials in the early solar nebula (e.g. Ciesla 2009).

It appears ion irradiation from the solar wind and cosmic-rays has played an important role in processing materials in the Solar System. Carbonaceous materials in the early solar nebula exposed to irradiation would have become increasingly disordered. It could be expected that highly amorphous and disordered carbon should be widely present in extra-terrestrial samples.

However, it is often only observed in the most primitive materials, such as IDPs, cometary samples and very primitive meteorites. As thermal metamorphism increases the structural order of carbon, it reverses the effects of ion irradiation. Highly disordered and amorphous carbon should only be observed in the samples that experienced the least amount of heating.

To further constrain the origins of the amorphous carbonaceous grains, and hence conditions in the nebula, the size and density separation procedure needs to be applied to a wider number of meteorites. It is necessary to determine whether the grains are only present within Murchison, or can also be found in other meteorites. The abundances of the grains within different meteorite types could potentially be used as an indicator of the degree of parent body processing. Similarities and differences between the isotopic compositions and structural characteristics of carbonaceous grains isolated from other meteorites may give clues as to the exact location and method of formation.

REFERENCES

Abia C., de Laverny P. and Wahlin R. (2008) Chemical analysis of carbon stars in the Local Group, *Astronomy and Astrophysics* **481**; 161-168.

Aikawa Y. and Herbst E. (1999) Deuterium fractionation in protoplanetary disks, *Astrophysical Journal* **526**; 314-326.

Alexander C.M.O'D. (1993) Presolar SiC in chondrites: How variable and how many sources?, *Geochimica et Cosmochimica Acta* **57**; 2869-2888.

Alexander C.M.O'D. (1996) Dust production in the galaxy: The meteorite perspective In: *Astrophysical Implications of the Laboratory Study of Presolar Materials*: Edited by T.J. Bernatowicz and E. Zinner (American Institute of Physics (AIP), Woodbury, New York).

Alexander C.M.O'D. and Nittler L.R. (1999) The galactic evolution of Si, Ti, and O isotopic ratios, *Astrophysical Journal* **519**; 222-235.

Alexander C.M.O'D., Russell S.S., Arden J.W., Ash R.D., Grady M.M. and Pillinger C.T. (1998) The origin of chondritic macromolecular organic matter: A carbon and nitrogen isotope study, *Meteoritics and Planetary Science* **33**; 603-622.

Alexander C.M.O'D., Fogel M., Yabuta H. and Cody G.D. (2007) The origin and evolution of chondrites recorded in the elemental and isotopic compositions of their macromolecular organic matter, *Geochimica et Cosmochimica Acta* **71**; 4380-4403.

Amari S. and Zinner E. (1996) Supernova grains from meteorites In: *Astrophysical Implications of the Laboratory Study of Presolar Materials*: Edited by T.J. Bernatowicz and E. Zinner (American Institute of Physics (AIP), Woodbury, New York).

Amari S., Anders E., Virag A. and Zinner E. (1990) Interstellar graphite in meteorites, *Nature* **345**; 238-240.

Amari S., Hoppe P., Zinner E. and Lewis R.S. (1992) Interstellar SiC with unusual isotopic compositions: Grains from a supernova?, *Astrophysical Journal* **394**; L43-46.

Amari S., Hoppe P., Zinner E. and Lews R.S. (1993) The isotopic compositions and stellar sources of meteoritic graphite grains, *Nature* **365**; 806-809.

Amari S., Lewis R.S. and Anders E. (1994) Interstellar grains in meteorites: I. Isolation of SiC, graphite and diamond; size distributions of SiC and graphite, *Geochimica et Cosmochimica Acta* **58**; 459-470.

Amari S., Hoppe P., Zinner E. and Lewis R.S. (1995a) Trace element concentrations in single circumstellar silicon carbide grains from the Murchison meteorite, *Meteoritics and Planetary Science* **30**; 679-693.

Amari S., Lewis R.S. and Anders. E. (1995b) Interstellar grains in meteorites: III. Graphite and its noble gases, *Geochimica et Cosmochimica Acta* **59**; 1411-1426.

Amari S., Zinner E. and Lewis R.S. (2000) Isotopic compositions of different presolar silicon carbide size fractions from the Murchison meteorite, *Meteoritics and Planetary Science* **35**; 997-1014.

Amari S., Nittler L.R. and Zinner E. (2001a) Presolar SiC of type A and B: Their isotopic compositions and stellar origins, *Astrophysical Journal* **559**; 463-483.

Amari S., Nittler L.R., Zinner E., Gallino R., Lugaro M. and Lewis R.S. (2001b) Presolar SiC grains of type Y: Origin from low-metallicity asymptotic giant branch stars, *Astrophysical Journal* **546**; 248-266.

Amari S., Gao X., Nittler L.R. and Zinner E. (2001c) Presolar grains from novae, *Astrophysical Journal* **551**; 1065-1072.

Anders E. and Grevesse N. (1989) Abundances of the elements: Meteoritic and solar, *Geochimica et Cosmochimica Acta* **53**; 197-214.

Aoki T. and Akai J. (2008) Carbon materials in Antarctic and non Antarctic carbonaceous chondrites: high resolution transmission electron microscopy, *Journal of Mineralogical and Petrological Sciences* **103**; 173-182.

Barrata G.A., Arena M.M., Strazzulla G., Colangeli L., Mennella V. and Bussoletti E. (1996) Raman spectroscopy of ion irradiated amorphous carbons, *Nuclear Instruments and Methods in Physics Research B* **116**; 195-199.

Barrata G.A., Mennella V., Brucato J.R., Colangeli L., Leto G., Palumbo M.E. and Strazzulla G. (2004) Raman spectroscopy of ion irradiated interplanetary carbons dust analogues, *Journal of Raman Spectroscopy* **35**; 487-496.

Barzyk J.G., Savina M.R., Davis A.M., Gallino R., Gyngard F., Amari S., Zinner E., Pellin M.J., Lewis R.S. and Clayton R.N. (2007) Constraining the ^{13}C neutron soruce in AGB stars through isotopic analysis of trace elements in presolar SiC, *Meteoritics and Planetary Science* **42**; 1103-1119.

Benguerba M., Brunelle A., Della-Negra S., Depauw J., Joret H., Le Beyec Y., Blain M.G., Schweikert E.A., Ben Assayag G. and Sudraud P. (1991) Impact of slow gold clusters on various solids: nonlinear effects in secondary ion emission, *Nuclear Instruments and Methods in Physics Research B* **62**; 8-22.

Benninghoven A., Rüdenauer F.G. and Werner H.W. (1987) *Secondary Ion Mass Spectrometry* (Wiley, New York).

Bernatowicz T.J., Fraundorf G., Tang M., Anders E., Wopenka B., Zinner E. and Fraundorf P. (1987) Evidence for interstellar SiC in the Murray carbonaceous meteorite, *Nature* **330**; 728-730.

Bernatowicz T.J., Amari S., Zinner E.K. and Lewis R.S. (1991) Interstellar grains within interstellar grains, *Astrophysical Journal* **373**; L73-76.

Bernatowicz T.J., Cowsik R., Gibbons P.C., Lodders K., Fegley Jr. B., Amari S. and Lewis R.S. (1996) Constraints on stellar grain formation from presolar graphite in the Murchison meteorite, *Astrophysical Journal* **472**; 760-782.

Bernatowicz T.J., Messenger S., Pravdivtseva O., Swan P. and Walker R.M. (2003) Pristine presolar silicon carbide, *Geochimica et Cosmochimica Acta* **67**; 4679-4691.

Besmehn A. and Hoppe P. (2003) A NanoSIMS study of Si- and Ca-Ti isotopic compositions of presolar silicon carbide grains from supernovae, *Geochimica et Cosmochimica Acta* **67**; 4693-4703.

Black D.C. and Pepin R.O. (1969) Trapped neon in meteorites-II, *Earth and Planetary Science Letters* **6**; 395-405.

Bland P.A., Stadermann F.J., Floss C., Rost D., Vicenzi E.P., Kearsley A.T. and Benedix G.K. (2007) A cornucopia of presolar and early solar system materials at the micrometer size range in primitive chondrite matrix, *Meteoritics and Planetary Science* **42**; 1417-1427.

Bonal L., Quirico E., Bourot-Denise M. and Montagnac G. (2006) Determination of the petrologic type of CV3 chondrites by Raman spectroscopy of included organic matter, *Geochimica et Cosmochimica Acta* **70**; 1849-1863.

Bonal L., Bourot-Denise M., Quirico E., Montagnac G. and Lewin E. (2007) Organic matter and metamorphic history of CO chondrites, *Geochimica et Cosmochimica Acta* **71**; 1605-1623.

Boothroyd A.I. and Sackmann I-J. (1999) The CNO isotopes: Deep circulation in red giants and first and second dredge-up, *Astrophysical Journal* **510**; 232-250.

Boss A.P. (1995) Collapse and fragmentation of molecular cloud cores. II. Collapse induced by stellar shockwaves, *Astrophysical Journal* **439**; 224-236.

Boss A.P. and Goswami J.N. (2006) Presolar cloud collapse and the formation and early evolution of the solar nebula In: *Meteorites and the Early Solar System*: Edited by D.S. Lauretta and H.Y. McSween Jr. (The University of Arizona Press).

Boss A.P., Keiser S.A., Ipatov S.I., Myhill E.A. and Vanhala H.A.T. (2010) Triggering collapse of the presolar dense cloud core and injecting short-lived radioisotopes with a shockwave. I. Varied shock speeds, *Astrophysical Journal* **708**; 1268-1280.

Botta O. and Bada J.L. (2002) Extraterrestrial organic compounds in meteorites, *Surveys in Geophysics* **23**; 411-467.

Bradley J.P. (1994) Chemically anomalous, preaccretionally irradiated grains in interplanetary dust particles from comets, *Science* **265**; 925-929.

Bradley J.P. (2003) Interplanetary dust particles In: *Treatise on Geochemistry – vol 1. Meteorites, Comets, and Planets*: Edited by A.M. Davis (Elsevier).

Braun R.M., Blenkinsopp P., Mullock S.J., Corlett C., Willey K.F., Vickerman J.C. and Winograd N. (1998) Performance characterization of a chemical imaging Time-of-flight Mass Spectrometer, *Rapid Communications in Mass Spectrometry* **12**; 1246-1252.

Brearley A.J. (1990) Carbon-rich aggregates in type 3 ordinary chondrites: Characterization, origins and thermal history, *Geochimica et Cosmochimica Acta* **54**; 831-850.

Brunetto R., Pino T., Dartois E., Cao A-T., d'Hendecourt L., Strazzulla G. and Bréchigna Ph. (2009) Comparison of the Raman spectra of ion irradiated soot and collected extraterrestrial carbon, *Icarus* **200**; 323-337.

Burbidge E.M., Burbidge G.R., Fowler W.A. and Hoyle F. (1957) Synthesis of the elements in stars, *Reviews of Modern Physics* **29**; 547-650.

Busemann H., Young A.F., Alexander C.M.O'D., Hoppe P., Mukhopadhyay S. and Nittler L.R. (2006) Interstellar chemistry recorded in organic matter from primitive meteorites, *Science* **312**; 727-730.

Busemann H., Alexander C.M.O'D. and Nittler L.R. (2007) Characterization of insoluble organic matter in primitive meteorites by microRaman spectroscopy, *Meteoritics and Planetary Science* **42**; 1387-1416.

Busemann H., Nguyen A.N., Cody G.D., Hoppe P., David Kilcoyne A.L., Stroud R.M., Zega T.J. and Nittler L.R. (2009) Ultra-primitive interplanetary dust particles from the 26P/Grigg-Skjellerup dust stream collection, *Earth and Planetary Science Letters* **288**; 44-57.

Busso M., Gallino R. and Wasserburg G.J. (1999) Nucleosynthesis in asymptotic giant branch stars: Relevance for galactic enrichment and solar system formation, *Annual Review of Astronomy and Astrophysics* **37**; 239-309.

Cameron A.G.W. and Fowler W.A. (1971) Lithium and the s-process in Red Giant Stars, Astrophysical Journal 164; 111-114.

Cameron A.G.W. and Truran J.W. (1977) The supernova trigger for formation of the solar system, *Icarus* **30**; 447-461.

Charnley S.B. and Rodgers S.D. (2008) Interstellar reservoirs of cometary matter, *Space Science Reviews* **138**; 59-73.

Chaussidon M., Robert F. and McKeegan K.D. (2006) Li and B isotopic variations in an Allende CAI: Evidence for the in situ decay of short-lived ^{10}Be and for the possible presence of the short-lived nuclide ^{7}Be in the early solar system, *Geochimica et Cosmochimica Acta* **70**; 224-245.

Choi B-G., Wasserburg G.J. and Huss G.R. (1999) Circumstellar hibonite and corundum and nucleosynthesis in asymptotic giant branch stars, *Astrophysical Journal* **522**; L133-136.

Ciesla F.J. (2009) Two-dimensional transport of solids in viscous protoplanetary disks, *Icarus* **200**; 655-671.

Clayton D.D. (1988) Isotopic anomalies: Chemical memory of galactic evolution, *Astrophysical Journal* **334**; 191-195.

Clayton D.D. (2003) A presolar galactic merger spawned the SiC-grain mainstream, *Astrophysical Journal* **598**; 313-324.

Clayton D.D. and Timmes F.X. (1997) Placing the sun in galactic chemical evolution: Mainstream SiC particles, *Astrophysical Journal* **483**; 220-227.

Clayton D.D., Arnett D., Kane J. and Meyer B.S. (1997) Type X silicon carbide presolar grains: Type Ia supernova condensates?, *Astrophysical Journal* **486**; 824-834.

Cody G.D., Alexander C.M.O'D., Yabuta H., Kilcoyne A.L.D., Araki T., Ade H., Dera P., Fogel M., Militzer B. and Mysen B.O. (2008) Organic thermometry for chondritic parent bodies, *Earth and Planetary Science Letters* **272**; 446-455.

Court R.W., Sephton M.A., Parnell J. and Gilmour I. (2006) The alteration of organic matter in response to ionizing irradiation: Chemical trends and implications for extraterrestrial sample analysis, *Geochimica et Cosmochimica Acta* **70**; 1020-1039.

Court R.W., Sephton M.A., Parnell J. and Gilmour I. (2007) Raman spectroscopy of irradiated organic matter, *Geochimica et Cosmochimica Acta* **71**; 2547-2568.

Cowan J.J. and Thielemann F.K. (2004) R-process nucleosynthesis in supernovae, *Physics Today* **57**; 47-53.

Croat T.K., Stadermann F.J. and Bernatowicz T.J. (2005) Presolar graphite from AGB stars: Microstructure and s-process enrichment, *Astrophysical Journal* **631**; 976-987.

Croat T.K., Stadermann F.J. and Bernatowicz T.J. (2008) Correlated isotopic and microstructural studies of turbostratic presolar graphite from the Murchison meteorite, *Meteoritics and Planetary Science* **43**; 1497-1516.

Curtis D., Gladney E. and Jurney E. (1980) A revision of the meteorite-based cosmic abundances of boron, *Geochimica et Cosmochimica Acta* **44**; 1945-1953.

Daulton T.L., Bernatowicz T.J., Lewis R.S., Messenger S., Stadermann F.J. and Amari S. (2002) Polytype distribution in circumstellar silicon carbide, *Science* **296**; 1852-1855.

Daulton T.L., Bernatowicz T.J., Lewis R.S., Messenger S., Stadermann F.J. and Amari S. (2003) Polytype distribution of circumstellar silicon carbide: Microstructural characterization by transmission electron microscopy, *Geochimica et Cosmochimica Acta* **67**; 4743-4767.

Davidson J. (2010) NanoSIMS and beyond – presolar grains in primitive materials and early Solar System formation, *Ph.D. thesis*, Planetary and Space Sciences Research Institute, The Open University, Milton Keynes, U.K.

Davies N., Weibel D.E., Blenkinsopp P., Lockyer N., Hill R. and Vickerman, J.C. (2003) Development and experimental application of a gold liquid metal ion source, *Applied Surface Science* **203-204**; 223-227.

Ehrenfreund P. and Charnley S.B. (2000) Organic molecules in the interstellar medium, comets, and meteorites: A voyage from dark clouds to the early Earth, *Annual Review of Astronomy and Astrophysics* **38**; 427-483.

Eiler J.M. and Kitchen N. (2004) Hydrogen isotope evidence for the origin and evolution of the carbonaceous chondrites, *Geochimica et Cosmochimica Acta* **68**; 1395-1411.

Ellison D.C., Drury L.O'C. and Meyer J-P. (1997) Galactic cosmic rays from supernova remnants. II Shock acceleration of gas and dust, *Astrophysical Journal* **487**; 197-217.

Everall N.J., Lumsdon J. and Christopher D.J. (1991) The effect of laser-induced heating upon the vibrational Raman spectra of graphites and carbon fibres, *Carbon* **29**; 133-137.

Fahey A.J. and Messenger S. (2001) Isotopic ratio measurements by time-of-flight secondary ion mass spectrometry, *International Journal of Mass Spectrometry* **208**; 227-242.

Ferini G., Baratta G.A. and Palumbo M.E. (2004) A Raman study of ion irradiated icy mixtures, *Astronomy and Astrophysics* **414**; 757-766.

Ferrari A.C. and Robertson J. (2001) Resonant Raman spectroscopy of disordered, amorphous, and diamondlike carbon, *Physical Review B* **64**; 075414.

Floss C. and Stadermann F.J. (2009) High abundances of circumstellar and interstellar C-anomalous phases in the primitive CR3 chondrites QUE 99177 and MET 00426, *Astrophysical Journal* **697**; 1242-1255.

Floss C., Stadermann F.J., Bradley J.P., Rong Dai Z., Bajt S., Graham G. and Scott Lea A. (2006) Identification of isotopically primitive interplanetary dust particles: A NanoSIMS isotopic imaging study, *Geochimica et Cosmochimica Acta* **70**; 2371-2399.

Flynn G.J., Keller L.P., Feser M., Wirick S. and Jacobsen C. (2003) The origin of organic matter in the solar system: Evidence from the interplanetary dust particles, *Geochimica et Cosmochimica Acta* **67**; 4791-4806.

Forrest W.J., Houck J.R. and McCarthy J.F. (1981) A far-infrared emission feature in carbon-rich stars and planetary-nebulae, *Astrophysical Journal* **248**; 195-200.

Gallino R., Busso M., Picchio G. and Raiteri C.M. (1990) On the astrophysical interpretation of isotope anomalies in meteoritic SiC grains, *Nature* **348**; 298-302.

Gallino R., Raiteri C.M., Busso M. and Matteucci F. (1994) The puzzle of silicon, titanium, and magnesium anomalies in meteoritic silicon carbide grains, *Astrophysical Journal* **430**; 858-869.

Gallino R., Busso M. and Lugaro M. (1996) Neutron capture nucleosynthesis in AGB stars In: *Astrophysical Implications of the Laboratory Study of Presolar Materials*: Edited by T.J. Bernatowicz and E. Zinner (American Institute of Physics (AIP), Woodbury, New York).

Garvie L.A.J. and Buseck P.R. (2004) Nanosized carbon-rich grains in carbonaceous chondrite meteorites, *Earth and Planetary Science Letters* **224**; 431-439.

Garvie L.A.J. and Buseck P.R. (2006) Carbonaceous materials in the acid residue from the Orgueil carbonaceous chondrite meteorite, *Meteoritics and Planetary Science* **41**; 633-642.

Garvie L.A.J., Baumgardner G. and Buseck P.R. (2008) Scanning electron microscopical and cross sectional analysis of extraterrestrial carbonaceous nanoglobules, *Meteoritics and Planetary Science* **43**; 1-5.

Gauba G. and Parthasarathy M. (2004) Circumstellar dust shells of hot post-AGB stars, *Astronomy and Astrophysics* **417**; 201-215.

Gibb E.L. and Whittet D.C.B. (2002) The 6 micron feature in protostars: Evidence for organic refractory material, *Astrophysical Journal* **566**; L113-116.

Gil-Hutton R. (2002) Color diversity amongst Kuiper belt objects: The collisional resurfacing model revisited, *Planetary and Space Science* **50**; 57-62.

Goebel J.H. and Moseley S.H. (1985) MgS grain component in circumstellar shells, *Astrophysical Journal* **290**; L35-39.

Graham G.A., Teslich N.E., Kearsley A.T., Stadermann F.J., Stroud R.M., Dai Z., Ishii H.A., Hutcheon I.D., Bajt S., Snead C.J., Weber P.K. and Bradley J.P. (2008) Applied focused ion beam techniques for sample preparation of astromaterials for integrated nanoanalysis, *Meteoritics and Planetary Science* **43**; 561-569.

Gyngard F., Amari S., Jadhav M., Marhas K., Zinner E. and Lewis R.S. (2006) Titanium isotopic ratios in KJG presolar SiC grains from Murchison, *Meteoritics and Planetary Science* **41**; 5334.

Gyngard F., Amari S., Zinner E. and Ott U. (2009) Interstellar exposure ages of large presolar SiC grains from the Murchison meteorite, *Astrophysical Journal* **694**; 359-366.

Heck P.R., Gyngard F., Ott U., Meier M.M.M., Ávila J.N., Amari S., Zinner E.K., Lewis R.S., Baur H. and Wieler R. (2009) Interstellar residence times of presolar SiC dust grains from the Murchison carbonaceous meteorite, *Astrophysical Journal* **698**; 1155-1164.

Henkel T., Tizard J., Blagburn D. and Lyon I. (2006) Interstellar dust laser explorer (IDLE): A new instrument for submicron analyses of stardust – quantification of laser SNMS, *Applied Surface Science* **252**; 7117-7119.

Henkel T., Stephan T., Jessberger E.K., Hoppe P., Strebel R., Amari S. and Lewis R.S. (2007a) 3-D elemental and isotopic composition of presolar silicon carbides, *Meteoritics and Planetary Science* **42**; 1121-1134.

Henkel T., Tizard J., Blagburn D. and Lyon I. (2007b) IDLE-Interstellar Dust Laser Explorer: A new instrument for elemental and isotopic analysis and imaging of interstellar and interplanetary dust, *Review of Scientific Instruments* **78**; 055107.

Henkel T., Rost D. and Lyon I.C. (2009) Improvements in quantification accuracy of inorganic time-of-flight secondary ion mass spectrometric analysis of silicate materials by using C_{60} primary ions, *Rapid Communications in Mass Spectrometry* **23**; 3355-3360.

Hill R. and Blenkinsopp, P.W.M. (2004) The development of C_{60} and gold cluster ion guns for static SIMS analysis, *Applied Surface Science* **231-232**; 936-939.

Hoefs J. (1980) *Stable Isotope Geochemistry* (Springer-Verlag, Berlin), p. 140.

Hoppe P. (2001) Stardust in meteorites and its relevance to nuclear astrophysics, *Nuclear Physics A* **688**; 94c-101c.

Hoppe P. (2006) NanoSIMS: A new tool in cosmochemistry, *Applied Surface Science* **252**; 7102-7106.

Hoppe P. and Besmehn A. (2002) Evidence for extinct vanadium-49 in presolar silicon carbide grains from supernovae, *Astrophysical Journal* **576**; L69-72.

Hoppe P., Geiss J., Bühler F., Neuenschwander J., Amari S. and Lewis R.S. (1993) Fingerprints of carbon, nitrogen, and silicon isotopes in small interstellar SiC grains from the Murchison meteorite, *Geochimica et Cosmochimica Acta* **57**; 4059-4068.

Hoppe P., Amari S., Zinner E., Ireland T. and Lewis R.S. (1994) Carbon, nitrogen, magnesium, silicon and titanium isotopic compositions of single interstellar silicon carbide grains from the Murchison carbonaceous chondrite, *Astrophysical Journal* **430**; 870-890.

Hoppe P., Amari S., Zinner E. and Lewis R.S. (1995) Isotopic compositions of C, N, O, Mg, and Si, trace element abundances, and morphologies of single circumstellar graphite grains in four density fractions from the Murchison meteorite, *Geochimica et Cosmochimica Acta* **59**; 4029-4056.

Hoppe P., Strebel R., Eberhardt P., Amari S. and Lewis R.S. (1996) Type II supernova matter in a silicon carbide grain from the Murchison meteorite, *Science* **272**; 1314-1316.

Hoppe P., Annen P., Strebel R., Eberhardt P., Gallino R., Lugaro M., Amari S. and Lewis R.S. (1997) Meteoritic silicon carbide grains with unusual Si-isotopic compositions: Evidence for an origin in low-mass, low-metallicity asymptotic giant branch stars, *Astrophysical Journal* **487**; L101-104.

Hoppe P., Strebel R., Eberhardt P., Amari S. and Lewsi R.S. (2000) Isotopic properties of silicon carbide X grains from the Murchison meteorite in the size range 0.5–1.5μm, *Meteoritics and Planetary Science* **35**; 1157-1176.

Hoppe P., Lodders K., Strebel R., Amari S. and Lewis R.S. (2001) Boron in presolar silicon carbide grains from supernovae, *Astrophysical Journal* **551**; 478-485.

Hoppe P., Leitner J., Gröner E., Marhas K.K., Meyer B.S. and Amari S. (2010) NanoSIMS studies of small presolar SiC grains: New insights into supernova nucleosynthesis, chemistry, and dust formation, *Astrophysical Journal* **719**; 1370-1384.

Huang E-P., Huang E., Yu S-C., Chen Y-H., Lee J-S. and Fang J-N. (2010a) High-temperature and pressure Raman spectroscopy of diamond, *Materials Letters* **64**; 580-582.

Huang T., Shieh S.R., Akhmetov A., Liu X., Lin C-M. and Lee J-S. (2010b) Pressure-induced phase transition in $BaCrO_4$, *Physical Review B* **81**; 214117.

Huss G.R. and Lewis R.S. (1994a) Noble gases in presolar diamonds I: Three distinct components and their implications for diamond origins, *Meteoritics and Planetary Science* **29**; 791-810.

Huss G.R. and Lewis R.S. (1994b) Noble gases in presolar diamonds II: Component abundances reflect thermal processing, *Meteoritics and Planetary Science* **29**; 811-829.

Huss G.R., Hutcheon I.D., Fahey A.J. and Wasserburg G.J. (1993) Oxygen isotope anomalies in Orgueil corundum: Confirmation of presolar origin, *Meteoritics and Planetary Science* **28**; 369.

Huss G.R., Hutcheon I.D. and Wasserburg G.J. (1997) Isotopic systematics of presolar silicon carbide from the Orgueil (CI) chondrite: Implications for Solar System formation and stellar nucleosynthesis, *Geochimica et Cosmochimica Acta* **61**; 5117-5148.

Huss G.R., Meshik A.P., Smith J.B. and Hohenberg C.M. (2003) Presolar diamond, silicon carbide, and graphite in carbonaceous chiondrites: Implications for thermal processing in the solar nebula, *Geochimica et Cosmochimica Acta* **67**; 4823-4848.

Huss G.R., Rubin A.E. and Grossman J.N. (2006) Thermal metamorphism in chondrites In: *Meteorites and the Early Solar System*: Edited by D.S. Lauretta and H.Y. McSween Jr. (The University of Arizona Press).

Hynes K.M., Amari S., Bernatowicz T.J. and Lebsack E. (2010a) Microanalytical investigations of presolar SiC of type AB, *41st Lunar and Planetary Science Conference* (abstract #2074).

Hynes K.M., Croat T.K., Amari S., Mertz A.F. and Bernatowicz T.J. (2010b) Structural and isotopic microanalysis of presolar SiC from supernovae, *Meteoritics and Planetary Science* **45**; 596-614.

Iben Jr. I. (1975) Thermal pulses; p-capture, α-capture, s-process nucleosynthesis; and convective mixing in a star of intermediate mass, *Astrophysical Journal* **196**; 525-547.

Iben Jr. I. and Renzini A. (1983) Asymptotic giant branch evolution and beyond, *Annual Review of Astronomy and Astrophysics* **21**; 271-342.

Ito M. and Messenger S. (2008) Isotopic imaging of refractory inclusions in meteorites with the NanoSIMS 50L, *Applied Surface Science* **255**; 1446-1450.

Jochum K.P., Dingwell D.B., Rocholl A., Stoll B., Hofmann A.W., Becker S., Besmehn A., Bessette D., Dietze H.J., Dulski P., Erzinger J., Hellebrand E., Hoppe P., Horn I., Janssens K., Jenner G.A., Klein M., McDonough W.F., Maetz M., Mezger K., Munker C., Nikogosian I.K., Pickhardt C., Raczek I., Rhede D., Seufert H.M., Simakin S.G., Sobolev A.V., Spettel B., Straub S., Vincze L., Wallianos A., Weckworth G., Weyer S., Wolf D. and Zimmer M. (2000) The preparation and preliminary characterization of eight geological MPI-DING reference glasses for in-situ microanalysis, *Geostandards Newsletter* **24**; 87-133.

Jochum K.P., Stoll B., Herwig K., Willbold M., Hofmann A.W., Amini M., Aarburg S., Abouchami W., Hellebrand E., Mocek B., Raczek I., Stracke A., Alard O., Bouman C., Becker S., Ducking M., Bratz H., Klemd R., de Bruin D., Canil D., Cornell D., de Hoog C.J., Dalpe C., Danyusshevsky L., Eisenhauer A., Gao Y.J., Snow J.E., Goshopf N., Gunther D., Latkoczy C., Guillong M., Hauri E.H., Hofer H.E., Lahaye Y., Horz K., Jacob D.E., Kassemann S.A., Kent A.J.R., Ludwig T., Zack T., Mason P.R.D., Meixner A., Rosner M., Misawa K.J., Nash B.P., Pfander J., Premo W.R., Sun W.D.D., Tiepolo M., Vannucci R., Vennemann T., Wayne D. and Woodhead J.D. (2006) MPI-DING reference glasses for in-situ microanalysis: New reference values for element concentrations and isotope ratios, *Geochemistry, Geophysics, Geosystems* **7**; 1-44.

Jones A.P., Tielens A.G.G.M., Hollenbach D.J. and McKee C.F. (1996) The propagation and survival of interstellar grains In: *Astrophysical Implications of the Laboratory Study of Presolar Materials*: Edited by T.J. Bernatowicz and E. Zinner (American Institute of Physics (AIP), Woodbury, New York).

Kagi H., Tsuchida I., Wakatsuki M., Takahashi K., Kamimura N., Iuchi K. and Wada H. (1994) Proper understanding of down-shifted Raman spectra of natural graphite: Direct estimation of laser-induced rise in sample temperature, *Geochimica et Cosmochimica Acta* **58**; 3527-3530.

Kashiv Y., Cai Z., Lai B., Sutton S.R., Lewis R.S., Davis A.M., Clayton R.N. and Pellin M.J. (2001) Synchrotron X-ray fluorescence: A new approach for determining trace element concentrations in individual presolar SiC grains, *32nd Lunar and Planetary Science Conference* (abstract #2192).

Kashiv Y., Cai Z., Lai B., Sutton S.R., Lewis R.S., Davis A.M., Clayton R.N. and Pellin M.J. (2002) Condensation of trace elements into presolar SiC stardust grains, *33rd Lunar and Planetary Science Conference* (abstract #2056).

Keller L.P., Messenger S. and Bradley J.P. (2000) Analysis of a deuterium-rich interplanetary dust particle (IDP) and implications for presolar material in IDPs, *Journal of Geophysical Research* **105**; 10397-10402.

Kerridge J.F., Chang S. and Shipp R. (1987) Isotopic characterization of kerogen-like material in the Murchison carbonaceous chondrite, *Geochimica et Cosmochimica Acta* **51**; 2527-2540.

King A., Henkel T., Rost D. and Lyon I. (2010) Determination of relative sensitivity factors during secondary ion sputtering of silicate glasses by Au^+, Au_2^+ and Au_3^+ ions, *Rapid Communications in Mass Spectrometry* **24**; 15-20.

Knauth D.C., Federman S.R. and Lambert D.L. (2003) An ultra-high resolution survey of the interstellar $^7Li/^6Li$ isotope ratio in the solar neighborhood, *Astrophysical Journal* **586**; 268-285.

Knight K.B., Sutton S.R., Newville M., Davis A.M., Dauphas N., Lewis R.S., Amari S., Steele I.M., Savina M.R. and Pellin M.J. (2008) Trace element determinations in presolar SiC by synchrotron X-ray fluorescence: Commencement of a coordinated multimethod study, *39th Lunar and Planetary Science Conference* (abstract #2135).

Krantzman K.D., Kingsbury D.B. and Garrison B.J. (2007) Cluster induced chemistry at solid surfaces: Molecular dynamics simulations of keV C_{60} bombardment of Si, *Nuclear Instruments and Methods in Physics Research B* **225**; 238-241.

Krantzman K.D., Webb R.P. and Garrison B.J. (2008) Simulations of C_{60} bombardment of Si, SiC, diamond and graphite, *Applied Surface Science* **255**; 837-840.

Lagadec E., Zijlstra A., Sloan G.C., Matsuura M., Wood P.R., van Loon J.T., Harris G.J., Blommaert J.A.D.L., Hony S., Groenewegen M.A.T., Feast M.W., Whitelock P.A., Menzies J.W. and Cioni M-R. (2007) Spitzer spectroscopy of carbon stars in the Small Magellanic Cloud, *Monthly Notices of the Royal Astronomical Society* **376**; 1270-1284.

Lattanzio J.C. and Boothroyd A.I. (1996) Nucleosynthesis of elements in low to intermediate mass stars through the AGB phase In: *Astrophysical Implications of the Laboratory Study of Presolar Materials*: Edited by T.J. Bernatowicz and E. Zinner (American Institute of Physics (AIP), Woodbury, New York).

Lee M.R. (2010) Transmission electron microscopy (TEM) of Earth and planetary materials: A review, *Mineralogical Magazine* **74**; 1-27.

Lewis R.S., Tang M., Wacker J.F., Anders E. and Steel E. (1987) Interstellar diamonds in meteorites, *Nature* **326**; 160-162.

Lewis R.S., Amari S. and Anders E. (1990) Meteoritic silicon carbide: pristine material from carbon stars, *Nature* **348**; 293-298.

Lewis R.S., Amari S. and Anders E. (1994) Interstellar grains in meteorites: II. SiC and its noble gases, *Geochimica et Cosmochimica Acta* **58**; 471-494.

Lodders K. and Fegley B. (1995) The origin of circumstellar silicon carbide grains found in meteorites, *Meteoritics and Planetary Science* **30**; 661-678.

Lodders K. and Amari S. (2005) Presolar grains from meteorites: Remnants from the early times of the solar system, *Chemie der Erde* **65**; 93-166.

Lugaro M., Zinner E., Gallino R. and Amari S. (1999) Si isotope ratios in mainstream presolar SiC grains revisted, *Astrophysical Journal* **527**; 369-394.

Lugaro M., Herwig F., Lattanzio J.C., Gallino R. and Straniero O. (2003) S-process nucleosynthesis in asymptotic giant branch stars: A test for stellar evolution, *Astrophysical Journal* **586**; 1305-1319.

Lyon I., Tizard J. and Henkel T. (2007) Evidence for lithium and boron from star-forming regions implanted into pre-solar SiC grains, *Meteoritics and Planetary Science* **42**; 378-384.

Lyon I., Henkel T. and Rost D. (2010) Formation of Si_m^+ and $Si_mC_n^+$ clusters by C_{60}^+ sputtering of Si, *Applied Surface Science* **256**; 6480-6487.

Maas R., Loss R.D., Rosman K.J.R., de Laeter J.R., Lewis R.S., Huss G.R. and Lugmair G.W. (2001) Isotope anomalies in tellurium and palladium from Allende nanodiamonds, *Meteoritics and Planetary Science* **36**; 849-858.

Malfait K., Waelkens C., Waters L.B.F.M., Vandenbussche B., Huygen E. and de Graauw M.S. (1998) The spectrum of the young star HD1000546 observed with the infrared space observatory, *Astronomy and Astrophysics* **332**; L25-28.

Matrajt G., Borg J., Raynal P.I., Djouadi Z., d'Hendecourt L., Flynn G. and Deboffle D. (2004) FTIR and Raman analyses of the Tagish Lake meteorite: Relationship with the aliphatic hydrocarbons observed in the diffuse interstellar medium, *Astronomy and Astrophysics* **416**; 983-990.

McKeegan K.D., Aléon J., Bradley J., Brownlee D., Busemann H., Butterworth A., Chaussidon M., Fallon S., Floss C., Gilmour J., Gounelle M., Graham G., Guan Y., Heck P.R., Hoppe P., Hutcheon I.D., Huth J., Ishii H., Ito M., Jacobsen S.B., Kearsley A., Leshin L.A., Liu M-C., Lyon I., Marhas K., Marty B., Matrajt G., Meibom A., Messenger S., Mostefaoui S., Mukhopadhyay S., Nakamura-Messenger K., Nittler L., Palma R., Pepin R.O., Papanastassiou D.A., Robert F., Schlutter D., Snead C.J., Stadermann F.J., Stroud R., Tsou P., Westphal A., Young E.D., Ziegler K., Zimmermann L. and Zinner E. (2006) Isotopic compositions of cometary matter returned by Stardust, *Science* **314**; 1724-1728.

Mendybaev R.A., Beckett J.R., Grossman L., Stolper E., Cooper R.F. and Bradley J.P. (2001) Volatilization kinetics of silicon carbide in reducing gases: An experimental study with applications to the survival of presolar grains in the solar nebula, *Geochimica et Cosmochimica Acta* **66**; 661-682.

Messenger S. (2000) Identification of molecular-cloud material in interplanetary dust particles, *Nature* **404**; 968-971.

Messenger S., Keller L.P., Stadermann F.J., Walker R.M. and Zinner E. (2003) Samples of stars beyond the solar system: Silicate grains in interplanetary dust, *Science* **300**; 105-108.

Messenger S., Sandford S. and Brownlee D. (2006) The population of starting materials available for solar system construction In: *Meteorites and the Early Solar System*: Edited by D.S. Lauretta and H.Y. McSween Jr. (The University of Arizona Press).

Meyer B.S. and Zinner E. (2006) Nucleosynthesis In: *Meteorites and the Early Solar System*: Edited by D.S. Lauretta and H.Y. McSween Jr. (The University of Arizona Press).

Millar T.J., Bennett A. and Herbst E. (1989) Deuterium fractionation in dense interstellar clouds, *Astrophysical Journal* **340**; 906-920.

Montes F., Beers T.C., Cowan J., Elliot T., Farouqi K., Gallino R., Heil M., Kratz K-L., Pfeiffer B., Pignatari M. and Schatz H. (2007) Nucleosynthesis in the early galaxy, *Astrophysical Journal* **671;** 1685-1695.

Montmerle T., Augereau J-C., Chaussidon M., Gounelle M., Marty B. and Morbidelli A. (2006) Solar system formation and evolution: the first 100 million years, *Earth, Moon and Planets* **98**; 39-95.

Mostefaoui S., Perron C., Zinner E. and Sagon G. (2000) Metal-associated carbon in primitive chondrites: Structure, isotopic composition, and origin, *Geochimica et Cosmochimica Acta* **64**; 1945-1964.

Muñoz Caro G.M., Matrajt G., Dartois E., Nuevo M., d'Hendecourt L., Deboffle D., Montagnac G., Chauvin N., Boukari C. and Le Du D. (2006) Nature and evolution of the dominant carbonaceous matter in interplanetary dust particles: Effects of irradiation and identification with a type of amorphous carbon, *Astronomy and Astrophysics* **459**; 147-159.

Muñoz Caro G.M., Dartois E. and Nakamura-Messenger K. (2008) Characterization of the carbon component in cometary Stardust samples by means of infrared and Raman spectroscopy, *Astronomy and Astrophysics* **485**; 743-751.

Nagashima K., Krot A.N. and Yurimoto H. (2004) Stardust silicates from primitive meteorites, *Nature* **428**; 921-924.

Nakamura-Messenger K., Messenger S., Keller L.P., Clemett S.J. and Zolensky M.E. (2006) Organic globules in the Tagish Lake meteorite: Remnants of the protosolar disk, *Science* **314**; 1439-1442.

Negri F., di Donato E., Tommasini M., Castiglioni C., Zerbi G. and Müllen K. (2004) Resonance Raman contribution to the D band of carbon materials: Modeling defects with quantum chemistry, *Journal of Chemical Physics* **120**; 11889-11900.

Nguyen A. and Zinner E. (2004) Discovery of ancient silicate stardust in a meteorite, *Science* **303**; 1496-1499.

Nguyen A., Zinner E. and Lewis R.S. (2003) Identification of small presolar spinel and corundum grains by isotopic raster imaging, *Publications of the Astronomical Society of Australia* **20**; 382-388.

Nguyen A., Stadermann F.J., Zinner E., Stroud R.M., Alexander C.M.O'D. and Nittler L.R. (2007) Characterization of presolar silicate and oxide grains in primitive carbonaceous chondrites, *Astrophysical Journal* **656**; 1223-1240.

Nguyen A.N., Nittler L.R., Stadermann F.J., Stroud R.M. and Alexander C.M.O'D. (2010) Coordianted analysis of presolar grains in the Alan Hills 77307 and Queen Elizabeth Range 99177 meteorites, *Astropysical Journal* **719**; 166-189.

Nicolussi G.K., Davis A.M., Pellin M.J., Lewis R.S., Clayton R.N. and Amari S. (1997) s-Process zirconium in presolar silicon carbide grains, *Science* **277**; 1281-1283.

Nicolussi G.K., Pellin M.J., Lewis R.S., Davis A.M., Amari S. and Clayton R.N. (1998a) Molybdenum isotopic composition of individual presolar silicon carbide grains from the Murchison meteorite, *Geochimica et Cosmochimica Acta* **62**; 1093-1104.

Nicolussi G.K., Pellin M.J., Lewis R.S., Davis A.M., Clayton R.N. and Amari S. (1998b) Strontium isotopic composition in individual circumstellar silicon carbide grains: a record of s-process nucleosynthesis, *Physical Review Letters* **81**; 3583-3586.

Nicolussi G.K., Pellin M.J., Lewis R.S., Davis A.M., Clayton R.N. and Amari S. (1998c) Zirconium and molybdenum in individual circumstellar graphite grains: New isotopic data on the nucleosynthesis of heavy elements, *Astrophysical Journal* **504**; 492-499.

Nittler L.R. (2003) Presolar stardust in meteorites: recent advances and scientific Frontiers, *Earth and Planetary Science Letters* **209**; 259-273.

Nittler L.R. (2006) Correlated microanalysis of presolar materials, *Meteoritics and Planetary Science* **41**; 133.

Nittler L.R. and Alexander C.M.O'D. (2003) Automated isotopic measurements of micron-sized dust: Application to meteoritic presolar silicon carbide, *Geochimica et Cosmochimica Acta* **67**; 4961-4980.

Nittler L., Alexander C., Gao X., Walker R. and Zinner E. (1994a) Interstellar corundum and spinel from the Tieschitz ordinary chondrite, *25th Lunar and Planetary Science Conference* (abstract #1005).

Nittler L.R., Alexander C.M.O'D., Gao X., Walker R.M. and Zinner E.K. (1994b) Interstellar oxide grains from the Tieschitz ordinary chondrite, *Nature* **370**; 443-446.

Nittler L.R., Hoppe P., Alexander C.M.O'D., Amari S., Eberhardt P., Gao X., Lewis R.S., Strebel R., Walker R.M. and Zinner E. (1995) Silicon nitride from supernovae, *Astrophysical Journal* **453**; L25-28.

Nittler L.R., Amari S., Zinner E., Woosley S.E. and Lewis R.S. (1996) Extinct ^{44}Ti in presolar graphite and SiC: Proof of a supernova origin, *Astrophysical Journal* **462**; L31-34.

Nittler L.R., Alexander C.M.O'D., Gao X., Walker R.M. and Zinner E. (1997) Stellar sapphires: The properties and origins of presolar Al_2O_3 in meteorites, *Astrophysical Journal* **483**; 475-495.

Nittler L.R., Alexander C.M.O'D. and Nguyen A. (2006) Extreme ^{13}C and ^{15}N enrichments in a Murchison presolar SiC grain, *Meteoritics and Planetary Science* **41**; 5316.

Nittler L.R., Alexander C.M.O'D., Gallino R., Hoppe P., Nguyen A.N., Stadermann F.J. and Zinner E.K. (2008) Aluminium-, calcium- and titanium rich oxide stardust in ordinary chondrite meteorites, *Astrophysical Journal* **682**; 1450-1478.

Nuth III J.A., Charnley S.B. and Johnson N.M. (2006) Chemical processes in the interstellar medium: Source of the gas and dust in the primitive solar nebula In: *Meteorites and the Early Solar System*: Edited by D.S. Lauretta and H.Y. McSween Jr. (The University of Arizona Press).

Ott U. and Begemann F. (2000) Spallation recoil and age of presolar grains in meteorites, *Meteoritics and Planetary Science* **35**; 53-63.

Ott U., Altmaier M., Herpers U., Kuhnhenn J., Merchel S., Michel R. and Mohapatra R.K. (2005) Spallation recoil II: Xenon evidence for young SiC grains, *Meteoritics and Planetary Science* **40**; 1635-1652.

Owen T., Mahaffy P.R., Niemann H.B., Atreya S. and Wong M. (2001) Protosolar nitrogen, *Astrophysical Journal* **553**; L77-79.

Pearce N.G.J., Perkins W.T., Westgate J.A., Gorton M.P., Jackson S.E., Neal C.R. and Chenery S.P. (1997) A compilation of new and published major and trace element data for NIST SRM 610 and NIST SRM 612 glass reference materials, *Geostandards Newsletter* **21**; 115-144.

Pearson V.K., Sephton M.A., Gilmour I. and Franchi I.A. (2001) Hydrogen isotopic composition of the Tagish Lake meteorite: Comparison with other carbonaceous chondrites, *32nd Lunar and Planetary Science Conference* (abstract #1861).

Pizzarello S., Huang Y., Becker L., Poreda R.J., Nieman R.A., Cooper G. and Williams M. (2001) The organic content of the Tagish Lake meteorite, *Science* **293**; 2236-2239.

Pizzarello S., Cooper G.W. and Flynn G.J. (2006) The nature and distribution of the organic material in carbonaceous chondrites and interplanetary dust particles In: *Meteorites and the Early Solar System*: Edited by D.S. Lauretta and H.Y. McSween Jr. (The University of Arizona Press).

Quirico E., Raynal P-I. and Bourot-Denise M. (2003) Metamorphic grade of organic matter in six unequilibrated ordinary chondrites, *Meteoritics and Planetary Science* **38**; 795-811.

Quirico E., Montagnac G., Rouzaud J-N., Bonal L., Bourot-Denise M., Duber S. and Reynard B. (2009) Precursor and metamorphic condition effects on Raman spectra of poorly ordered carbonaceous matter in chondrites and coals, *Earth and Planetary Science Letters* **287**; 185-193.

Remusat L., Palhol F., Robert F., Derenne S. and France-Lanord C. (2009) Enrichment of deuterium in insoluble organic matter from pritmive meteorites: A solar system origin?, *Earth and Planetary Science Letters* **243**; 15-25.

Remusat L., Guan Y., Wang Y. and Eiler J.M. (2010) Accretion and preservation of D-rich organic particles in carbonaceous chondrites: Evidence for important transport in the early Solar System nebula, *Astrophysical Journal* **713**; 1048-1058.

Reynolds J.H. and Turner G. (1964) Rare gases in the chondrite Renazzo, *Journal of Geophysical Research* **69**; 3263-3281.

Rietmeijer F.J.M. (1998) Interplanetary dust particles, *Reviews in Mineralogy* **36**; 2.1-2.95 (Mineralogical Society of America).

Robert F. and Epstein S. (1982) The concentration and isotopic composition of hydrogen, carbon and nitrogen in carbonaceous meteorites, *Geochimica et Cosmochimica Acta* **46**; 81-95.

Rolfs C.E. and Rodney W.S. (1988) *Cauldrons in the cosmos* (The University of Chicago Press, Chicago and London).

Rost D., Stephan T. and Jessberger E.K. (1999) Surface analysis of stratospheric dust particles, *Meteoritics and Planetary Science* **34**; 637-646.

Rotundi A., Rietmeijer F.J.M., Colangeli L., Mennella V., Palumbo P. and Bussoletti E. (1998) Identification of carbon forms in soot materials of astrophysical interest, *Astronomy and Astrophysics* **329**; 1087-1096.

Rotundi A., Baratta G.A., Borg J., Brucato J.R., Busemann H., Colangeli L., d'Hendecourt L., Djouadi Z., Ferrini G., Franchi I.A., Fries M., Grossemy F., Keller L.P., Mennella V., Nakamura K., Nittler L.R., Palumbo M.E., Sandford S.A., Steele A. and Wopenka B. (2008) Combined micro-Raman, micro-infrared, and field emission scanning electron microscope analyses of comet 81P/Wild 2 particles collected by Stardust, *Meteoritics and Planetary Science* **43**; 367-397.

Russell S.S. (2007) The formation of the solar system, *Journal of the Geological Society* **164**; 481-492.

Sadezky A., Muckenhuber H., Grothe H., Niessner R. and Pöschl U. (2005) Raman microspectroscopy of soot and related carbonaceous materials: Spectral analysis and structural information, *Carbon* **43**; 1731-1742.

Sandford S.A. and Allamandola L.J. (1993) Condensation and vaporization studies of CH_3OH and NH_3 ices: Major implications for astrochemistry, *Astrophysical Journal* **417**; 815-825.

Sandford S.A., Bernstein M.P. and Dworkin J.P. (2001) Assessment of the interstellar processes leading to deuterium enrichment in meteoritic organics, *Meteoritics and Planetary Science* **36**; 1117-1133.

Sandford S.A., Aléon J., Alexander C.M.O'D., Araki T., Bajt S., Baratta G., Borg J., Bradley J.P., Brownlee D.E., Brucato J.R., Burchell M.J., Busemann H., Butterworth A., Clemett S.J., Cody G., Colangeli L., Cooper G., D'Hendecourt L., Djouadi Z., Dworkin J.P., Ferrini G., Fleckenstein H., Flynn G.J., Franchi I.A., Fries M., Gilles M.K., Glavin D.P., Gounelle M., Grossemy F., Jacobsen C., Keller L.P., David Kilcoyne A.L., Leitner J., Matrajt G., Meibom A., Mennella V., Mostefaoui S., Nittler L.R., Palumbo M.E., Papanastassiou D.A., Robert F., Rotundi A., Snead C.J., Spencer M.K., Stadermann F.J., Steele A., Stephan T., Tsou P., Tyliszczak T., Westphal A.J., Wirick S., Wopenka B., Yabuta H., Zare R.N. and Zolensky M.E. (2006) Organics captured from comet 81P/Wild 2 by the Stardust spacecraft, *Science* **314**; 1720-1724.

Savina M.R., Davis A.M., Tripa C.E., Pellin M.J., Clayton R.N., Lewis R.S., Amari S., Gallino R. and Lugaro M. (2003) Barium isotopes in individual presolar silicon carbide grains from the Murchison meteorite, *Geochimica et Cosmochimica Acta* **67**; 3201-3214.

Savina M.R., Davis A.M., Emil Tripa C., Pellin M.J., Gallino R., Lewis R.S. and Amari S. (2004) Extinct technetium in silicon carbide stardust: Implications for stellar nucleosynthesis, *Science* **303**; 649-652.

Seitz H-M., Brey G.P., Zipfel J., Ott U., Weyer S., Durali S. and Weinbruch S. (2007) Lithium isotope composition of ordinary and carbonaceous chondrites, and differentiated planetary bodies: Bulk solar system and solar reservoirs, *Earth and Planetary Science Letters* **260**; 582-596.

Sephton M.A. (2002) Organic compounds in carbonaceous meteorites, *Natural Product Reports* **19**; 292-311.

Sephton M.A., James R.H. and Bland P.A. (2004) Lithium isotope analyses of inorganic constituents from the Murchison meteorite, *Astrophysical Journal* **612**; 588-591.

Slodzian G., Hillion F., Stadermann F.J. and Zinner E. (2004) QSA influences on isotopic ratio measurements, *Applied Surface Science* **231-232**; 874-877.

Srinivasan B. and Anders E. (1978) Nobles gases in the Murchison meteorite: Possible relics of s-process nucleosynthesis, *Science* **201**; 51-56.

Stadermann F.J., Hoppe P., Floss C., Heck P.R., Hörz F., Huth J., Kearsley A.T., Leitner J., Marhas K.K., McKeegan K.D. and Stephan T. (2008) Stardust in Stardust – The C, N and O isotopic compositions of Wild 2 cometary matter in Al foil impacts, *Meteoritics and Planetary Science* **43**; 299-313.

Stephan T. (2001) TOF-SIMS in cosmochemistry, *Planetary and Space Science* **49**; 859-906.

Stephan T. and Jessberger E.K. (1996) TOF-SIMS analysis of interstellar SiC grains, *27th Lunar and Planetary Science Conference* (abstract #1267).

Stephan T., Bischoff A., Cramer H.G. and Zehnpfennig J. (1991) TOF-SIMS applications in meteorite research, first results, *Meteoritics and Planetary Science* **26**; 397.

Stephan T., Zehnpfenning J. and Benninghoven A. (1993) Correction of dead time effects in time-of-flight mass spectrometry, *Journal of Vacuum Science and Technology A* **12**; 405-410.

Stephan T., Rost D., Jessberger E.K., Budell R., Greshake A., Zinner E.K., Amari S., Hoppe P. and Lewis R.S. (1997) TOF-SIMS analysis of SiC grains with high lateral resolution, *28th Lunar and Planetary Science Conference* (abstract #1282).

Strazzulla G., Cooper J.F., Christian E.R. and Johnson R.E. (2003) Ion irradiation of TNOs: from the fluxes measured in space to the laboratory experiments, *Comptes Rendus Physique* **4**; 791-801.

Stroud R.M. and Bernatowicz T.J. (2005) Surface and internal structure of pristine presolar silicon carbide, *36th Lunar and Planetary Science Conference* (abstract #2010).

Stroud R.M., O'Grady M., Nittler L.R. and Alexander C.M. O'D. (2002) Transmission electron microscopy of an in situ presolar silicon carbide grain, *33rd Lunar and Planetary Science Conference* (abstract #1785).

Stroud R.M., Nittler L.R., Alexander C.M. O'D., Bernatowicz T.J. and Messenger S.R. (2003) Transmission electron microscopy of non-etched presolar silicon carbide, *34th Lunar and Planetary Science Conference* (abstract #1755).

Suess H.E. (1965) Chemical evidence bearing on the origin of the solar system, *Annual Review of Astronomy and Astrophysics* **3**; 217-234.

Sugimoto D. (1971) Mixing between stellar envelope and core in advanced phases of evolution. III-Stellar core of intial mass $1.5M_s$, *Progress of Theoretical Physics* **45**; 761-775.

Sun S., Szakal C., Winograd N. and Wucher A. (2005) Energetic ion bombardment of Ag surfaces by C_{60}^+ and Ga^+ projectiles, *Journal of the American Society for Mass Spectrometry* **16**; 1677-1686.

Timmes F.X. and Clayton D.D. (1996) Galactic evolution of silicon isotopes: Application to presolar SiC grains from meteorites, *Astrophysical Journal* **472**; 723-741.

Tizard J. (2005) A laboratory study of circumstellar SiC as a new window on stellar nucleosynthesis, *Ph.D. thesis*, School of Earth, Atmospheric and Environmental Sciences, University of Manchester, Manchester, U.K.

Tizard J., Lyon I. and Henkel T. (2005) The gentle separation of presolar SiC grains from meteorites, *Meteoritics and Planetary Science* **40**; 335-342.

Travaglio C., Gallino R., Amari S., Zinner E., Woosley S. and Lewis R.S. (1999) Low-density graphite grains and mixing in type II supernovae, *Astrophysical Journal* **510**; 325-354.

Treffers R. and Cohen M. (1974) High-resolution spectra of cool stars in the 10- and 20-micron regions, *Astrophysical Journal* **188**; 545-552.

Tuinstra F. and Koenig J.L. (1970) Raman spectra of graphite, *Journal of Chemical Physics* **53**; 1126-1130.

Verchovsky A.B., Wright I.P. and Pillenger C.T. (2004) Astrophysical significance of asymptotic giant branch stellar wind energies recorded in meteoritic SiC grains, *Astrophysical Journal* **607**; 611-619.

Virag A., Wopenka B., Amari S., Zinner E., Anders E. and Lewis R.S. (1992) Isotopic, optical, and trace element properties of large single SiC grains from the Murchison meteorite, *Geochimica et Cosmochimica Acta* **56**; 1715-1733.

Vollmer C., Brenker F.E., Hoppe P. and Stroud R.M. (2009) Direct laboratory analysis of silicate stardust from red giant stars, *Astrophysical Journal* **700**; 774-782.

Wilson R.G., Stevie F.A. and Magee C.W. (1989) *Secondary ion mass spectrometry* (Wiley, New York).

Winograd N. (2005) The magic of cluster SIMS, *Analytical Chemistry* **77**; 143-149.

Wirth R. (2004) Focused Ion Beam (FIB): A novel technology for advanced application of micro- and nanoanalysis in geosciences and applied mineralogy, *European Journal of Mineralogy* **16**; 863-876.

Wood B.E., Müller H-R., Zank G.P. and Linsky J.L. (2002) Measured mass-loss rates of solar-like stars as a function of age and activity, *Astrophysical Journal* **574**; 412-425.

Wopenka B. (1988) Raman observations on individual interplanetary dust particles, *Earth and Planetary Science Letters* **88**; 221-231.

Wopenka B. and Pasteris J.D. (1993) Structural characterization of kerogens to granulite-facies graphite: Applicability of Raman microscope spectroscopy, *American Mineralogist* **78**; 533-557.

Wucher A. (2006) Molecular secondary ion formation under cluster bombardment: A fundamental review, *Applied Surface Science* **252**; 6482-6489.

Yang J. and Epstein S. (1983) Interstellar organic matter in meteorites, *Geochimica et Cosmochimica Acta* **47**; 2199-2216.

Yin Q-Z., Aeoulus Lee C-T. and Ott U. (2006) Signatures of the s-process in presolar silicon carbide grains: Barium through hafnium, *Astrophysical Journal* **647**; 676-684.

Zega T.J., Nittler L.R., Busemann H., Hoppe P. and Stroud R.M. (2007) Coordinated isotopic and mineralogic analyses of planetary materials enabled by in situ lift-out with a focused ion beam scanning electron microscope, *Meteoritics and Planetary Science* **42**; 1373-1386.

Zhukovska S. and Gail H-P. (2008) Condensation of MgS in outflows from carbon stars, *Astronomy and Astrophysics* **486**; 229-237.

Ziegler J.F. (2004) SRIM-2003, *Nuclear Instruments and Methods in Physics Research B* **219-220**; 1027-1036.

Zijlstra A.A., Matsuura M., Wood P.R., Sloan G.C., Lagadec E., van Loon J.T., Groenewegen M.A.T., Feast M.W., Menzies J.W., Whitelock P.A., Blommaert J.A.D.L., Cioni M-R.L., Habing H.J., Hony S., Loup C. and Waters L.B.F.M. (2006) A Spitzer mid-infrared spectral survey of mass-losing carbon stars in the large Magellanic cloud, *Monthly Notices of the Royal Astronomical Society* **370**; 1961-1978.

Zinner E. (1998) Stellar nucleosynthesis and the isotopic composition of presolar grains from primitive meteorites, *Annual Review of Earth and Planetary Science* **26**; 147-188.

Zinner E., Tang M. and Anders E. (1987) Large isotopic anomalies of Si, C, N and noble gases in interstellar silicon carbide from the Murray meteorite, *Nature* **330**; 730-732.

Zinner E., Ming T. and Anders E. (1989) Interstellar SiC in the Murchison and Murray meteorites: Isotopic composition of Ne, Xe, Si, C and N, *Geochimica et Cosmochimica Acta* **53**; 3273-3290.

Zinner E., Amari S., Wopenka B. and Lewis R.S. (1995) Interstellar graphite in meteorites: Isotopic compositions and structural properties of single graphite grains from Murchison, *Meteoritics and Planetary Science* **30**; 209-226.

Zinner E., Amari S., Guinness R., Nguyen A., Stadermann F.J., Walker R.M. and Lewis R.S. (2003) Presolar spinel grains from the Murray and Murchison carbonaceous chondrites, *Geochimica et Cosmochimica Acta* **67**; 5083-5095.

Zinner E., Nittler L.R., Hoppe P., Gallino R., Straniero O. and Alexander C.M. O'D. (2005) Oxygen, magnesium and chromium isotopic ratios of presolar spinel grains, *Geochimica et Cosmochimica Acta* **69**; 4149-4165.